Naval Research Laboratory
Stennis Space Center, MS 39529-5004

NRL/FR/7401--96-9663

Dredged Material Isolation on the Abyssal Seafloor: A Feasibility Study

PHILIP J. VALENT
DAVID K. YOUNG
Editors

Marine Geosciences Division
Oceanography Division

December 1, 1997

REPORT DOCUMENTATION PAGE

Form Approved
OBM No. 0704-0188

1. AGENCY USE ONLY *(Leave blank)*	2. REPORT DATE	3. REPORT TYPE AND DATES COVERED
	December 1, 1997	Final

4. TITLE AND SUBTITLE

Dredged Material Isolation on the Abyssal Seafloor: A Feasibility Study

5. FUNDING NUMBERS

Job Order No. 5745914A6

Program Element No. 0603226E

Project No.

Task No.

Accession No.

6. AUTHOR(S)

Philip J. Valent and David K. Young, eds.

7. PERFORMING ORGANIZATION NAME(S) AND ADDRESS(ES)

Naval Research Laboratory
Marine Geosciences Division and Oceanography Division
Stennis Space Center, MS 39529-5004

8. PERFORMING ORGANIZATION REPORT NUMBER

NRL/FR/7401--96-9663

9. SPONSORING/MONITORING AGENCY NAME(S) AND ADDRESS(ES)

Defense Advanced Research Projects Agency/Tactical Technology Office
3701 North Fairfax Drive
Arlington, VA

10. SPONSORING/MONITORING AGENCY REPORT NUMBER

11. SUPPLEMENTARY NOTES

12a. DISTRIBUTION/AVAILABILITY STATEMENT

Approved for public release; distribution unlimited.

12b. DISTRIBUTION CODE

13. ABSTRACT *(Maximum 200 words)*

This report is the result of an examination of the feasibility of isolating contaminated dredged material on the abyssal seafloor. The focus is on the technical and environmental factors that constrain the considerations of feasibility. The sources of the materials are assumed to be in U.S. coastal waters. A thorough conceptual design of a *dredging-to-abyssal deposition* system is analyzed with regard to each subsystem and to the entire operational concept. These subsystems include: a low-leakage dredge, equipment for material handling and loading into geosynthetic fabric containers (GFCs), the barge for transport and navigation, and the subsystem for releasing the GFCs to sink to the abyssal seafloor isolation site. Particular consideration is given to the exclusion of dredged material from the ocean's productive zone in the upper 1000 m; this exclusion requires highly stable, reliable navigation and sea-keeping by the barge transporter and control of the configuration of GFCs within it. New theoretical models and previous empirical results are used to predict GFC motion through the water column and response to impact on the abyssal seafloor, including the case of potential release of contaminated, turbid water at impact. A geochemical model of the temporal and spatial evolution of the post-deposition geochemistry of the water column, the GFC contents and the sediments below is developed and analyzed; the results show that release of metals into the ocean waters would be insignificant. A model of the biological impacts of the introduction of dredged material in the abyssal environment is used to infer that: biological diversity in the vicinity of the deposition site will be diminished, biomass will be increased by dominance of a few fast-growing, opportunistic benthic species, and concentrations of trace elements and organic contaminants returned from the abyss to surface waters will be trivially small.

14. SUBJECT TERMS

dredged material, isolation, disposal, relocation, deep ocean, monitoring

15. NUMBER OF PAGES

123

16. PRICE CODE

17. SECURITY CLASSIFICATION OF REPORT	18. SECURITY CLASSIFICATION OF THIS PAGE	19. SECURITY CLASSIFICATION OF ABSTRACT	20. LIMITATION OF ABSTRACT
Unclassified	Unclassified	Unclassified	Same as report

INTRODUCTION AND OVERVIEW

This Report covers recent NRL research and development related to the AEC laser-pellet fusion program. The work covered in this report was primarily carried out under AEC Contract No. AT(04-3)-878 between July, 1973 and June, 1974. In some cases, for the sake of clarity, work not performed during this period has been included. In addition, the report discusses the large complementary program supported by the Defense Nuclear Agency at NRL on the study of laser produced plasmas in high atomic number materials. A significant part of the soft x-ray experimental studies (Chapter V) and all of the numerical modelling studies (Chapter VIII and Chapter IX) were supported by the DNA program. This work has been included in the present report for the sake of completeness and since many of the results obtained are of direct benefit to the AEC laser-fusion effort.

There is some overlap in time, with the period covered by the last NRL report, which was presented to the Laser-Fusion Coordinating Committee in November, 1973. However, it was felt useful to establish the precedent of fiscal year reporting starting with this Annual Report. In the future, a report on the AEC supported laser-fusion studies at NRL will appear on a semi-annual basis.

Studies of laser produced plasmas began at NRL in 1968. Development of a large Q-switched glass laser facility was carried out under ARPA sponsorship. Additional support for laser development was received as part of a DNA-supported program to study the interactions between an expanding laser-produced plasma and an ambient magnetized plasma background. The DNA program also provided NRL with the genesis of its expertise in the study of laser plasma generation and interactions. The glass laser system was developed under joint ARPA and DNA sponsorship to the point where, by FY 72, it represented the state-of-the-art in high power short pulse lasers. The system included an NRL designed mode-locked YAG oscillator system and a disc amplifier which became a prototype for those now in use and under development in the laser-fusion program.

When a large AEC supported laser-fusion effort began in FY 72, NRL was a logical place to turn to for support in building up the programs of the AEC laboratories. Shortly after the start of AEC-supported work at NRL, a DNA program at NRL was initiated to study laser produced high atomic number plasmas. The aim of this program was to develop a new source of soft x-rays for weapons effect simulation. The combined AEC and DNA supported programs have been known within NRL as the Laser-Matter Interaction (LMI) Program and Dr. John Stamper has served as Program Manager since its inception. The LMI Program has included contributions from a number of divisions at NRL and has involved both experimental and theoretical studies. The funding of the program during FY 74 consisted of $500,000 from the AEC for laser-fusion studies as well as additional funding from DNA for x-ray source investigations.

One of the unique features of the NRL laser-fusion program has been the availability of a reliable Nd:glass laser system which produces exceptionally clean pulses (i.e., spatially, temporally and spectrally pure) at sufficient power levels ($\lesssim$ 0.5 TW) for many studies of interest to laser fusion. Over 1500 laser shots were put on target in FY 74 for our AEC

CONTENTS

DREDGED MATERIAL ISOLATION ON THE ABYSSAL SEAFLOOR: A FEASIBILITY STUDY

Edited by: Philip J. Valent and David K. Young

with contributions by: John C. Bajus, Oceaneering International, Inc., Upper Marlboro, MD
LaMont Berger, Mississippi State University
Frederick A. Bowles, Naval Research Laboratory, Stennis Space Center, MS
Surya P. G. Dinavahi, Science Applications International Corp., Annapolis, MD
James C. Fitzpatrick, Science Applications International Corp. Arlington, VA
Peter Fleischer, Naval Research Laboratory, Stennis Space Center, MS
Martin J. Fritts, Science Applications International Corp., Annapolis, MD
Patrick C. Gallacher, Naval Research Laboratory, Stennis Space Center, MS
Albert W. Green, Jr., Naval Research Laboratory, Stennis Space Center, MS
John E. Hollister, Global Associates, Inc., Arlington, VA
Richard Jahnke, Skidaway Institute of Oceanography
Richard A. Korpus, Science Applications International Corp. Annapolis, MD
Michael J. Meinhold, Science Applications International Corp. Annapolis, MD
Robert Moorhead, Mississippi State University
John Palmerton, U.S. Army Corps of Engineers Waterways Experiment Station, Vicksburg, MS
Andrew Palowitch, formerly Oceaneering International, Inc., Upper Marlboro, MD
Michele Reed, Oceaneering International, Inc., Upper Marlboro, MD
Paul Rosenstrach, Volpe Center, Cambridge, MA
Gilbert T. Rowe, Texas A&M University
William B. Sawyer, Naval Research Laboratory, Stennis Space Center, MS
Michael Skrab, Oceaneering International, Inc., Upper Marlboro, MD
Thomas D. Wright, Environmental Consultant, Vicksburg, MS

sponsored by: Defense Advanced Research Projects Agency
(Allan Steinhardt and CAPT Bruce Dyer, USN (retired))

DREDGED MATERIAL ISOLATION ON THE ABYSSAL SEAFLOOR: A FEASIBILITY STUDY

1.0 INTRODUCTION

1.1 Background

The U.S. Environmental Protection Agency has estimated that 1 to 3% of the national annual total of dredged material, or 2–9 × 10^6 m^3 (3–9 × 10^6 yd^3), is sufficiently contaminated to require special management procedures (EPA 1994). The proportion of contaminated dredged material varies markedly from location to location for the United States Army Corps of Engineers (USACE) New York District, 60 to 75% of the navigation dredged material (Greges 1994), or 2–4 × 10^6 m^3 (3–5 × 10^6 yd^3) from the Port of New York/New Jersey alone (Del Vicario 1996), must be managed as contaminated material. Inaction in the timely removal of these sediments results in shoaling of navigation channels, turning basins, and berthing areas with a strong negative impact on local economies (Munson 1996) and may pose an impediment to timely projection of U.S. military force overseas. Further, there are continuing negative impacts to the resources of the coastal zone if contaminated sediments remain in place in harbors, bays, and estuaries. Relocation of these materials to the deep-ocean floor is a potentially viable option to present practices that expose valuable seafood products and humans to contaminants released by dredged materials in continental shelf and estuarine environments (Spencer 1991; Chryssostomidis 1991; Hollister 1992; Graham 1993; NRC 1985, p. 132; Edmond 1992; Ballard 1992; Rubin 1992). Consequently, there is a need for a better understanding of effects of emplacement of dredged material on the abyssal seafloor (water depths greater than 3000 m).

Suspended particulate materials in fresh, estuarine, and marine waters have natural affinities for sorbing large amounts of contaminants, including natural and anthropogenic derived compounds, from solution. The sediments thereby become long-term reservoirs of large quantities of stored contaminants, reflecting past and ongoing activities in the coastal zone and adjacent watersheds. Fluxes of contaminants from the sediments contribute to continued degradation of water quality and seafood products. Natural events, such as storms, and man-produced effects, such as dredging and dredged material disposal, may introduce large amounts of these stored contaminants into the water column, producing fish kills or other catastrophic effects in violation of State and Federal environmental and health standards. The fate, transport, and impact of contaminants released into the coastal zone by present dredged material disposal practices must be taken into consideration and balanced against the concept of deep ocean relocation (DOR) of dredged material.

In coastal zone environments, it is well known that many environmental factors affect the chemical concentrations and speciation, reaction kinetics, availability and, thus, toxicity of contaminants from dredged material. Of all the factors that affect early diagenetic changes to dredged material deposited in the coastal zone, the most important are associated with biogeochemical reactions that influence dissolved concentrations, pH, and the oxidation-reduction (redox) potential causing depletion or enrichment of products in both the fluid and solid phases of a deposit. The effects of toxicants and their reaction products within dredged material may include drastic reductions of

population densities and species diversity of organisms living within or near the sediment-water interface. Therefore, just as sediments integrate the temporal variability that commonly characterizes contaminant inputs from anthropogenic sources, benthic communities integrate the long-term effects as evident from the numbers, sizes, types, and activities of benthic animals present at any given time. The rates of mobilization, advective transport, and diffusion of contaminants, their reaction products, and the resulting sediment chemistry are widely acknowledged to be profoundly affected by the sediment reworking activities, or bioturbation, by coastal benthic animals. Bioturbation influences biogeochemical reactions by moving particles between reaction zones, altering solute diffusion geometries, adding metabolic products as new reactive organic substrates, and effecting changes to microbial populations by feeding and mechanical disturbances.

Physical, chemical, and biological processes in deep-ocean sediments, particularly in abyssal depths greater than 3000 m, are far less well understood than those in coastal zone sediments. The processes affecting the fate and transport of dredged material disposed of in deep-ocean depths are virtually unknown. Two recent studies have addressed this problem.

1.2 Prior Research

Two recent studies have addressed the deep-ocean option for disposal of various waste materials. The first study resulted from several workshops hosted by the Woods Hole Oceanographic Institution (WHOI) (Spencer 1991) and the Massachusetts Institute of Technology (MIT) (Chryssostomidis 1991) under the sponsorship of the Sloan Foundation. This study concluded that it was potentially possible, without detriment to humans and their environment, to dispose of sewage sludge from municipal treatment plants, fly ash from municipal incinerators, and contaminated dredged material by emplacement of these materials on the abyssal seafloor. The WHOI-MIT workshop participants did allow that many technical and potential environmental impact questions required answering before proceeding with the abyssal seafloor waste management option. A demonstration scale experiment was suggested as the means by which these questions could be answered. The more recent study was conducted by the Naval Research Laboratory (NRL) under sponsorship of the Strategic Environmental Research and Development Program (SERDP).

In the NRL study (Valent and Young 1995), engineers and economists evaluated and costed preliminary concepts for transporting to abyssal seafloor sites the same spectrum of wastes as in the WHOI-MIT study. NRL and academic scientists developed preliminary models of predicted hydrodynamic, chemical, and biological processes affecting potential pathways of contaminants potentially emanating from the emplaced waste deposits. Protocols for selecting sites optimized for waste isolation were established and a plan for surveying and monitoring such sites was developed.

Conclusions from the NRL study were that technologically achievable and economically feasible concepts for transfer of wastes from the ocean surface to the abyssal seafloor are (with the least costly and less complex first): (1) transfer in geosynthetic fabric containers (GFCs) free-falling from a platform at the ocean surface, (2) transfer to near the seafloor in a disk-shaped, free-fall submersible that would release its payload of GFC-bagged waste about 100 m above the seafloor and then would return to the ocean surface for another payload, and (3) transfer to near the seafloor in a glider submersible performing much like the disk-shaped submersible but capable of transporting a much larger payload (Hightower et al. 1995a). The NRL study further concluded that, given available data and modeling predictions, abyssal seafloor sites can be identified at which bottom currents will not be strong enough to resuspend dredged material once placed on the seafloor, thus ruling out the physical dispersal mechanism for transport of included contaminants (Valent and

Young 1995). While the NRL study made significant progress in developing analytical models of seafloor chemical and biological processes, study participants found that available data were inadequate to properly parameterize and validate all models.

1.3 Objective of This Work

The present study was undertaken to improve scientific understanding and technological concepts as inputs to and validation of pertinent numerical models. The SimDOR project (Simulation of Deep Ocean Relocation of Dredged Material) integrated visualizations of the numerical model results into a video explaining the abyssal seafloor dredged material management option. (Note the text of this video is presented in Sec. 9.0 of this report.)

1.4 Approach

The project was divided into one technical task and one scientific task:

(1) Relocation/placement technology model development and simulation, and

(2) Oceanographic and environmental model development and environmental impact simulation.

1.4.1 Relocation/Placement Technology Modeling and Simulation Task

The Relocation/Placement Technology Modeling and Simulation Task developed an end-to-end assembly of models predicting throughout (and thereby efficiencies and costs) for practical combinations of subsystems for accomplishing the process of dredging through dredged material isolation on the abyssal seafloor (see Sec. 2.0 of this report). The sophistication of the individual models and their connections varied. In the case of off-the-shelf models, those most descriptive of the processes taking place and having the better resolution were used. When existing models were found to be lacking, appropriate models were developed with the level of effort invested being commensurate with the impact of the modeled subsystem on overall system performance. The process of dredging was described by models of various clean dredging systems with consideration given to the variety of sediment properties encountered. The process of transporting the dredged material to the ocean-going transporter and altering of material properties for filling of the GFCs used existing solids handling and transport, dredged material/slurry pumping, and material mixing/blending models. The process of transporting the bagged waste by specialized ocean-going barge were described using Simulation Based Design technology when appropriate, but also used other commercially available design-visualization packages when dictated by project cost considerations (see Sec. 3.0).

This project assumed the position that all dredged-material-filled GFCs would pass intact through the upper productive water column. Engineers assumed that sufficient investment would be made in the design of the GFC release system on the transporter and design of fabric containers/bags to ensure that no contaminant loss to the overlying water column occurred.

The technology modeling and simulation task included technology development work in those technical areas for which NRL's SERDP study has shown understanding to be inadequate to support the modeling, simulation, and design of systems for the isolation of contaminated dredged materials on the abyssal seafloor. Effort emphasized those topic areas directly supporting the least costly and least complex waste emplacement concept, i.e., "emplacement from the surface" via containment of the dredged material in geosynthetic fabric bag-like containers and free-fall of these filled GFCs from the sea surface to the abyssal seafloor (Hightower et al. 1995a).

The technology modeling and simulation task included in its scope all dredging systems and techniques potentially applicable to the dredging of contaminated sediments from navigable waterways, turning basins, and berthing areas. Flexibility was incorporated to facilitate the addition of improved and/or new clean dredging technologies to evolve from USACE and industrial initiatives. The characteristics of the dredged material exiting the dredging system were be quantified, including modifications to the character of the material necessary to facilitate loading into geosynthetic fabric bag containers lining cells of a transporter barge. The physical plant and equipment necessary to modify the character/mechanical properties of the dredged material for bagging were identified. The transporter cell size and shape and the GFC type were evaluated for risk of rupture or tearing of the GFC during filling, release from the transporter, fall through the water column, and impact on the seafloor. Each of these functions were described in models where waste mass/volume throughput and cost need to be quantified, and where these models are suitable for interconnection to produce the capability to simulate the dredging and dredged material isolation process end-to-end. (Note that all processes required to be simulated were identified in the SimDOR project, as shown in Fig. 1; the end-to-end simulation was not completed during the first year of study as described in Sec. 10.0.)

The transporter optimization subtask included modeling of the transporter for release of the dredged, material-filled bags without bag tearing or puncture. Various concepts for release of the filled bags from the transporter were modeled to determine the influence of bag volume and shape on design efficiency. This modeling was performed without benefit of physical model tests because of inadequate budget and time, and, therefore, model results were not verified. (Note: to fully understand the filled-bag release process, physical model tests will be required, modeling the interactions between the transporter, the cell door(s), the bag shape, transporter speed at time of release, sea state, and very likely, additional parameters.)

Understanding of hydrodynamic performance and modeling capability for large fabric containers in free-fall were improved (see Sec. 4.0). The degree of instability in free-fall is a critical issue in predicting the size of the seafloor area over which one can expect the bags to land. The size of seafloor area, in turn, impacts the monitoring plan design. In predicting the size of the emplacement area, the free-fall velocity of the GFCs for different shapes and content densities must be known to predict the influence of current profile on the GFC descent. The influence of irregularities in bag shape and distribution of bag contents during the bag descent is extremely important in estimating the extent of horizontal movement and internal instabilities that may occur during free-fall. Improved predictions from these models eventually need to be developed from incorporating improved understanding of physical forcings acting upon and within containers.

Numerical simulations were conducted to test GFC integrity upon launch and impact with the seafloor. Experience of the USACE to date in the use of GFCs for the transfer of dredged material shows that the critical point for container tearing occurs at that point where the container is beginning to slide out the transporter cell through partially opened doors. From the SERDP study, NRL concluded that another point critical for container rupture may be upon impacting the seafloor. The USACE with Nicolon Corp. has performed some modeling of the fabric bag/cell doors problem for clean sand materials to better understand the mechanisms of the container tearing problem and to develop an empirical solution. The USACE effort to date has confined itself to consideration of existing bottom dump hopper barges and to varying the rate of opening the hopper doors. This SimDOR project built upon the USACE effort to include highly organic, fine-grained, dredged materials and to include alternate trap door release concepts. This study modeled stresses in the container fabric as a function of release system design. Further work, beyond the scope of the present study, is required to develop a simulation capability to optimize the selection of GFC design parameters.

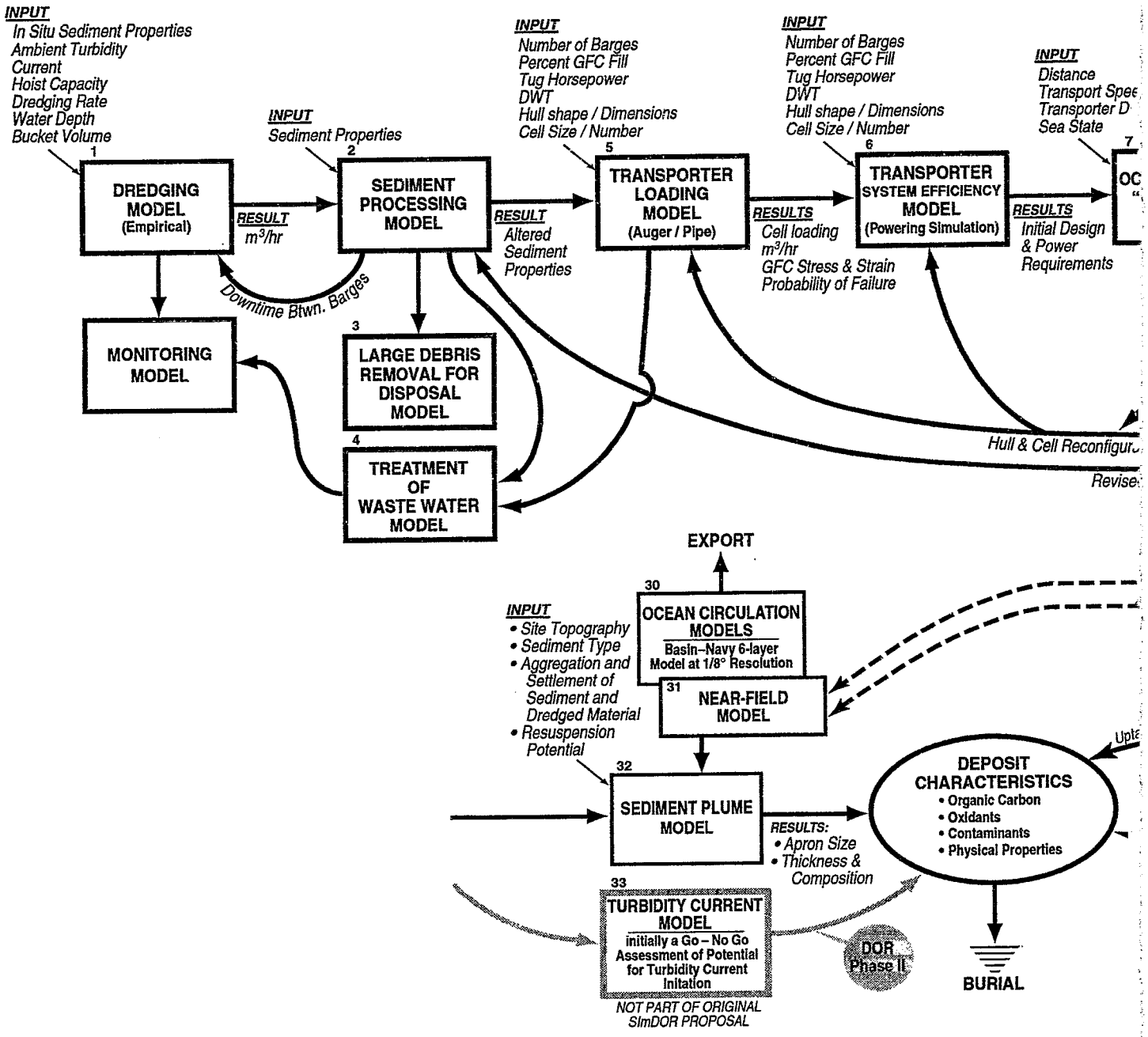

Fig. 1 — Model connection plan for SimDOR project

1.4.2 Oceanographic and Environmental Modeling and Simulation Task

The Oceanographic and Environmental Modeling and Simulation Task approached modeling of potential contaminant pathways from the viewpoint that a thorough understanding of biological, chemical, geological, and physical phenomena is necessary to assess and/or select the correct models and parameterizations of those models. For example, a good fit of modeled profiles of contaminant concentrations based on inaccurate simplifying assumptions of homogeneous, diffusion-dominated mass transfer may not accurately describe the dynamics of the interplay among water flow, organisms, substrates, pore water, and the early diagenetic environment of sediments.

Various scenarios come into play when dredged material is relocated from the coastal zone to the deep-ocean floor. Modeling and analysis for each scenario were accomplished in parallel and not in isolation of one another. Numerical simulations for all scenarios emphasized abyssal sites where isolation of dredged material would be maximized. In some cases, "open piles" were simulated as well as "bagged dredged material" scenarios to test the range of possible effects resulting from closed to ruptured containers. The potential for transport of dredged material and seafloor sediments by turbidity currents was examined from a phenomenological point of view (see Sec. 5.0).

The physical dispersion scenario examined influences of dispersal by diffusive and advective processes, including hydrothermal plume development (see Sec. 6.0). Physical dispersion models considered the effects of advection, both mean and episodic, in addition to anisotropic, turbulent diffusion. The model simulated the behavior of a strongly forced, buoyant plume and the behavior of a field of interacting plumes that may be caused by multiple disposal events. The mesoscale and basin-scale advection and diffusion of water from the dredged material relocation site were also modeled to determine the potential long-term fate of dispersed contaminants. The spread of potential contaminants were predicted as a function of distance and time in all directions around the relocation site.

The geochemical scenario examined effects of relocating organically rich, fine-grained, dredged material that may lead to mobilization of certain chemical contaminants (e.g., heavy metals, synthetic organic compounds). Emplacement of dredged material on the deep seafloor will lead to geochemical changes that may either enhance or minimize release of the sorbed contaminants to the overlying water column and into the food chain (see Sec. 7.0). The geochemical influence and fate of the relocated, dredged material were numerically simulated. These simulations included the influence of the method of emplacement and packaging on geochemical effects and the fate of redox-sensitive compounds and metals in the deposit.

The "deep freeze" scenario examined the possibility for methane hydrate formation within organic-rich dredged material under the high-pressure and low-temperature conditions of abyssal depths. This scenario was first raised as a possibility while considering the high organic contents of sewage sludge in the NRL study funded by SERDP. Because of the lesser organic carbon contents of dredged material, however, this possibility is viewed as being unlikely and was discarded early in the SimDOR study as a process that needed to be modeled and simulated (see Sec. 7.0).

The "enrichment" scenario examined the biotic and biogeochemical responses to a sudden input of varying amounts of material high in organic content to the deep seafloor, as represented by organic-rich dredged material. Models were based on three primary areas of biological response: (1) incorporation of natural compounds into resident food chain, (2) transfer of toxic materials in the food chain, and (3) biological recruitment (see Sec. 8.0). Initially, mass balance models and food chain transfer models simulated carbon flows in which the remineralization of organic matter

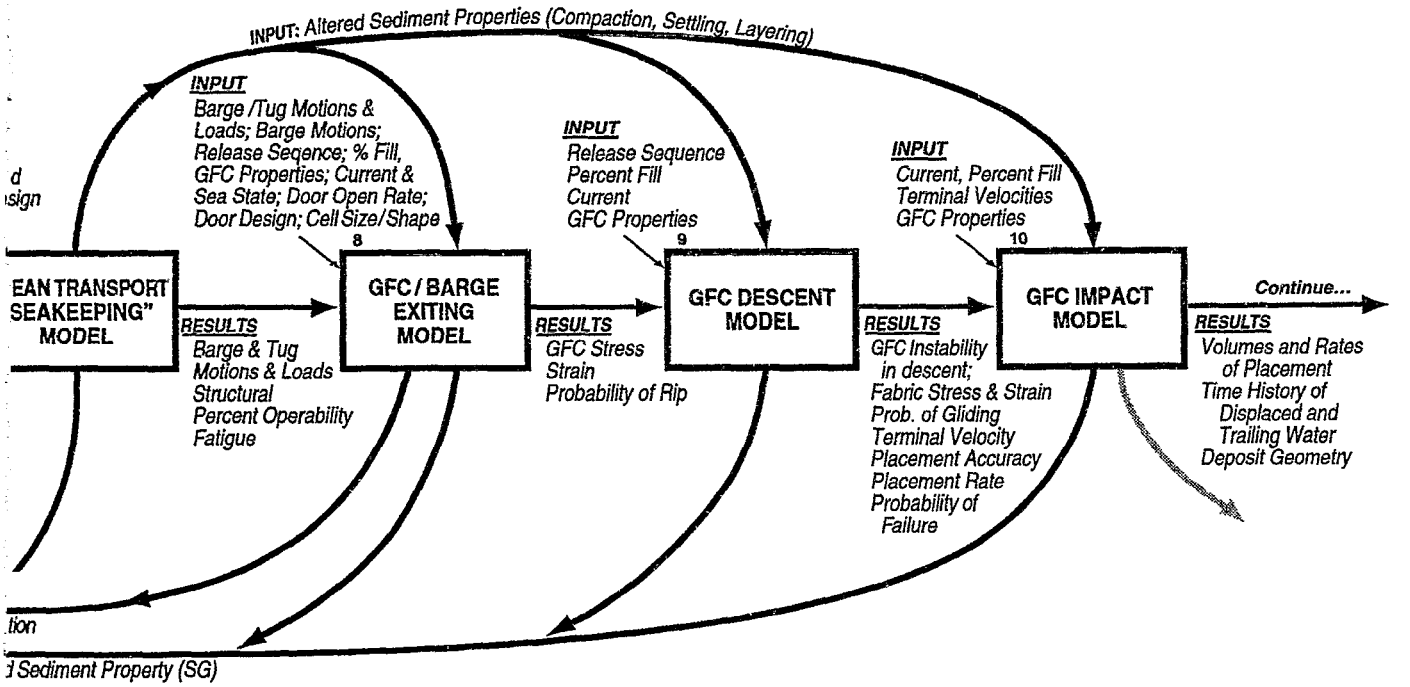
INPUT: Altered Sediment Properties (Compaction, Settling, Layering)
INPUT
Barge /Tug Motions & Loads; Barge Motions; Release Seqence; % Fill, GFC Properties; Current & Sea State; Door Open Rate; Door Design; Cell Size/Shape
8
INPUT
Release Sequence
Percent Fill
Current
GFC Properties
9
INPUT
Current, Percent Fill
Terminal Velocities
GFC Properties
10
d
sign
EAN TRANSPORT SEAKEEPING" MODEL
RESULTS
Barge & Tug Motions & Loads
Structural
Percent Operability
Fatigue
GFC / BARGE EXITING MODEL
RESULTS
GFC Stress
Strain
Probability of Rip
GFC DESCENT MODEL
RESULTS
GFC Instability in descent;
Fabric Stress & Strain
Prob. of Gliding
Terminal Velocity
Placement Accuracy
Placement Rate
Probability of Failure
GFC IMPACT MODEL
Continue...
RESULTS
Volumes and Rates of Placement
Time History of Displaced and Trailing Water
Deposit Geometry
tion
Sediment Property (SG)

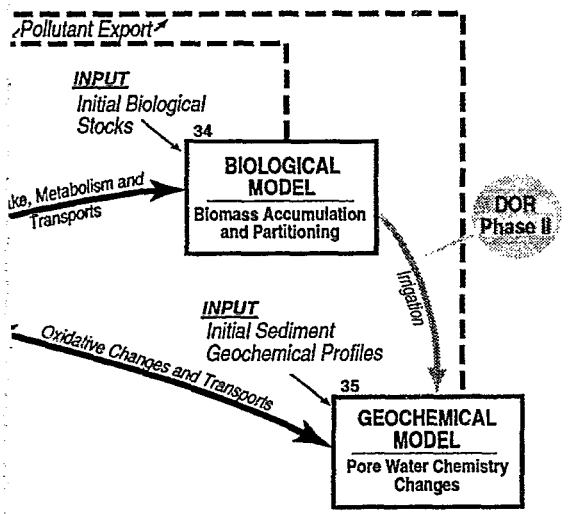
Pollutant Export
INPUT
Initial Biological Stocks
34
BIOLOGICAL MODEL
Biomass Accumulation and Partitioning
ke, Metabolism and Transports
DOR Phase II
Irrigation
INPUT
Initial Sediment Geochemical Profiles
Oxidative Changes and Transports
35
GEOCHEMICAL MODEL
Pore Water Chemistry Changes

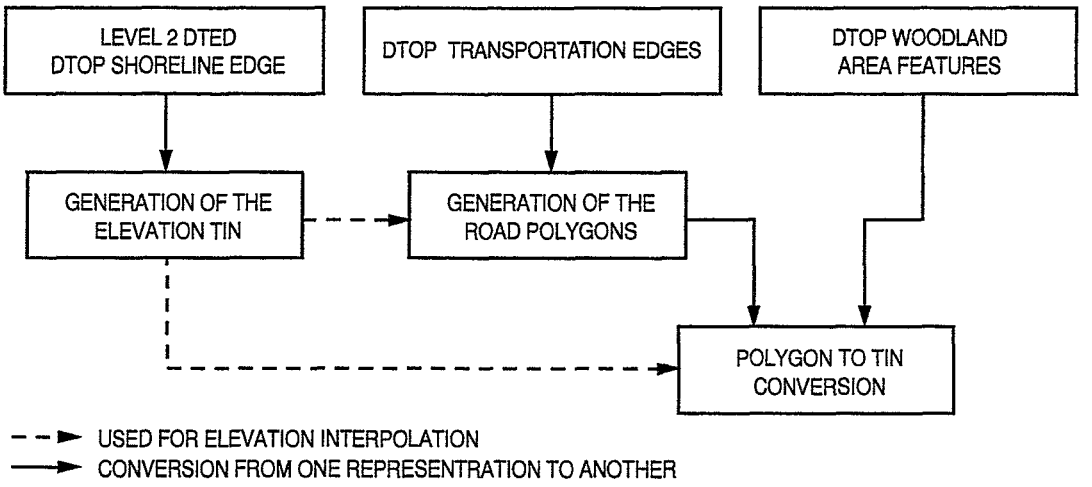

Fig. 3 — Overview of EVPF data generation procedure

values to the nodes in the remaining coverages. Once the coverages (i.e., primitive tables) are complete, TIN data can be converted to a second format and displayed using a 3-D rendering package.

TIN data can be generated from a variety of input sources, such as elevation grids, contour lines, arbitrary collection of edges, or previously generated TINs. This section will trace the populating of the elevation coverage of the MSEVP prototype using 90,300 nodes extracted from level 2 DTED and 639 nodes from five shoreline edges extracted from the hydrography coverage in DTOP.

The elevation points were used to create an ARC/INFO lattice, which serves as the foundation for building an initial TIN for the area. A z-tolerance of 10.0 m was chosen for the construction of this TIN in an effort to balance the need for a high-resolution surface representation while maintaining a manageable data set. The shorelines defined for the area in DTOP were added to the original triangulation as breaklines. The ARC/INFO *ungeneratetin* command was performed on the constrained TIN to create an ASCII file containing the TIN wire frame of the region.

Rendering values based on the elevation of the terrain were assigned for each triangle and each vertex to highlight the versatility of the TIN attribute and render-related attribute tables. The bodies of water, whose elevation can be determined by the color/elevation of the land surrounding it, were assigned a constant color of blue regardless of the elevation. In addition to the assignment of attribute values, a first_tin value for each connected node and adjacency relationships for each triangle side is computed before writing the EVPF primitive tables described in the previous section. Figure 4 provides a flow chart describing the complete procedure for the generation of the elevation TIN. The results of this process are shown in Fig. 5.

3.2 Generation of Road Polygons

With the elevation coverage completed, attention can be turned to the addition of other surface features to the surface model. The transportation network is represented by VPF edges in DTOP and all other current NIMA products. The transportation network has been converted from an edge

by the heterotrophic community, augmented by chemo-lithotrophic feedback, were investigated using parameterizations from well-sampled, deep sea ecosystems. Toxin pathways via food chain transfers were considered using these models.

2.0 ENGINEERING CONCEPT: DREDGING THROUGH RELEASE FROM TRANSPORTER *by Andrew Palowitch*

2.1 Scope

This section focuses on the description and selection of the engineering concept for the dredging, transfer and loading, transport, and deposit of contaminated material from harbors and waterways.

2.2 Concept of Operation

The engineering concept is divided into four functional areas: dredging, transfer and loading, transportation, and placement (see Fig. 2).

FUNCTIONAL AREA	DESCRIPTION
Dredging	Removes the contaminated sediment from the harbor or navigation channel floor and places it into the storage hopper on the dredging platform.
Transfer & Loading	Transfers and distributes the dredged material from the storage hopper on the dredging platform into the material containers on the transport vessel (transporter).
Transportation	Transports the dredged material to an ocean surface position over the abyssal seafloor isolation site.
Placement	Releases the containerized material from the transporter on the surface to free-fall through the water column and impact on the abyssal seafloor.

2.3 System Requirements

The system requirements for each of the SimDOR functional areas are outlined in App. A. The system requirements considered the following goals in their development:

- Maintain high percent solids of dredged material to increase the system efficiency by maximizing sediment solids content vs. water content and to increase deposit density to provide more than sufficient negative buoyancy at abyssal site
- Remain versatile to accommodate the majority of the dredging sites in the United States
- Reduce operational costs and environmental impacts
- Remain consistent between the requirements previously set during the Abyssal Plains Waste Isolation (APWI) program

One requirement in the Systems Engineering Report has changed since the report was issued. The cargo capacity was reduced from 25,000 DWT to 19,000 DWT. This cargo capacity is 6,000 DWT lighter than what was specified in the report. The original 25,000 DWT requirement was based on SERDP's previous requirements in the AWPI 94-01 Report, System Requirements Report for Abyssal

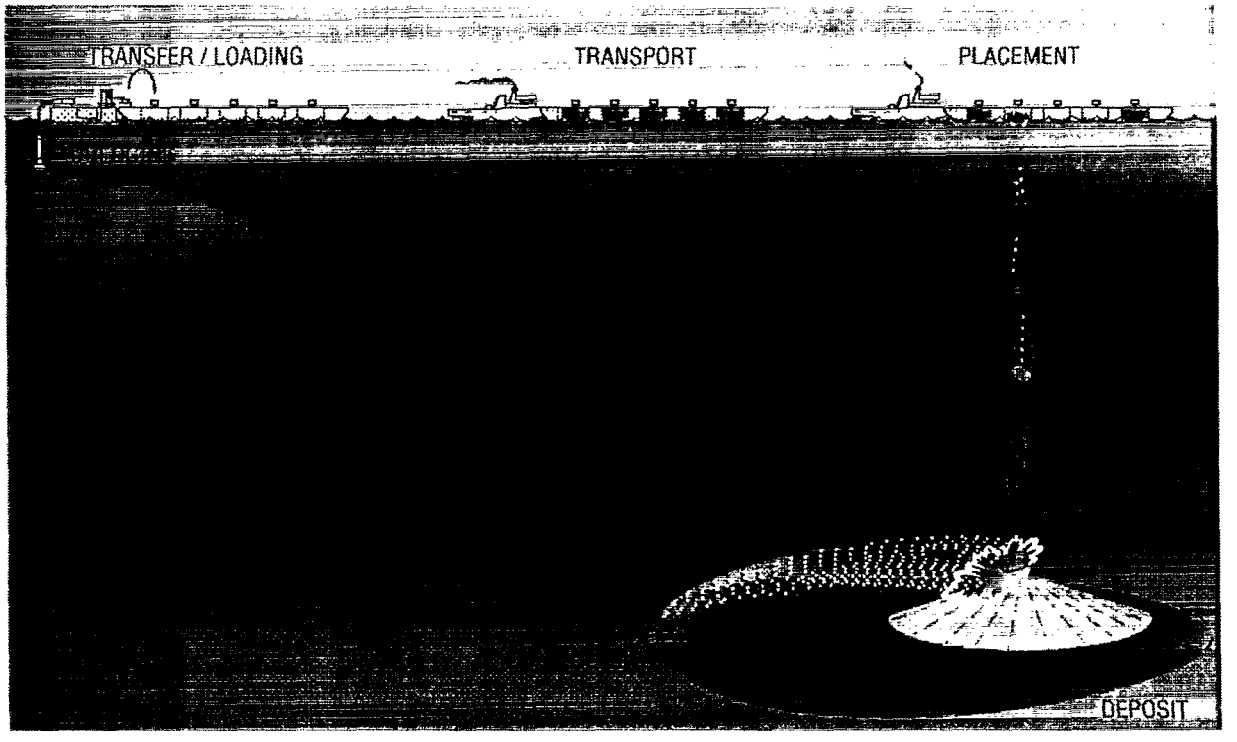

Fig. 2 — Engineering concept for Deep Ocean Relocation from clean dredging through loading and transport to placement of contained material on the abyssal seafloor

Plains Waste Isolation Project. In the SERDP project, the transported dredged material was slurried to a consistent bulk wet density of 1.25 Mg/m^3. In SimDOR, the bulk wet density of the material (as specified) is between 1.4 and 1.7 Mg/m^3. Incorporating the same cargo capacity (25,000 DWT) in SimDOR would achieve an average increase of 24% more deposited dredged material due to the increased in situ weight stored per unit volume. Reducing the cargo capacity by 24% allows the vessel to maintain its 5.5-m (18-ft) draft requirement and does not adversely affect cost effectiveness of the system.

2.4 Engineering Concept

The selection process and the resulting conceptual design for each functional area (dredging, transfer and loading, transport, and placement) of the system is described in this section. When appropriate, compliance of the design with the system requirements is also described.

2.4.1 Dredging

2.4.1.1 Selection of Dredging Method

The methods available for dredging contaminated sediments include special equipment in the following four main categories: mechanical, mechanical/hydraulic, hydraulic, and pneumatic. The dredging system selected for SimDOR is a mechanical dredge. This dredge system was selected after comparing the methods of equipment previously used or evaluated for environmental dredging projects. Table 1 illustrates which equipment meets the system requirements presented in Sec. 2.3 with a check mark. The typical performance of the categories is based on general representative

equipment. Specific equipment designs within these categories may be evaluated with different results than the general equipment results presented in the table.

Typically, the selection of dredging equipment is highly site- and project-specific. The SimDOR concept of operation is desired to be capable of accommodating a wide variety of site conditions to cover a majority of the dredging locations in the U.S. The dredged material among these sites in the U.S. varies from site to site. The dredged material characteristics are one of the main factors that determine the type of dredge equipment used in a dredging project. The dredging equipment selected in SimDOR is one possible method or approach for the dredging function of the system. The equipment was selected based on its ability to meet the requirements. The dredger system concept selected has the ability to contain and remove debris up to 0.75 m (2.5 ft) diameter.

The clamshell dredge concept is designed to remove the sediment at nearly its in situ density and to totally contain the material throughout the water column after it takes a bite. The concept has the following advantages over existing environmental clamshell bucket designs:

- The dredge does not require vent flaps or gates to allow water runoff at the water surface.
- The dredge removes a significant amount of water volume overlying the sediment surface prior to cutting.
  - Reduces the amount of surrounding water exposed to disturbed sediment
  - Reduces the amount of water taken by each cut
- The concept incorporates "hard silt curtains" preventing extruded material from escaping the clamshell.

Table 1 — Evaluation of Dredging Equipment Classifications Against Dredging Requirements for the SimDOR Project

DREDGING REQUIREMENTS	DREDGE EQUIPMENT CLASSIFICATIONS			
	Mechanical	Mechanical/ Hydraulic	Hydraulic	Pneumatic
(Including Requirement Reference Number from System Engineering Report)	Specialized Clamshell Dredge Concept	General Equipment	General Equipment	Pneuma Pump
1.2.1 Production Rate [≥150 m^3/h (≥200 yd^3/h)]	✓	✓	✓	✓
1.2.2 Debris Removal Capability	✓			
1.2.3 Depth Range [5–15 m (18–50 ft)]	✓	✓	✓	✓
1.2.4 Removal Efficiency (in situ density)	✓	✓		✓
1.2.5 Sediment Classification Range	✓	✓	✓	✓
1.2.6 Low Turbidity	✓	✓	✓	✓
1.2.7 Reliability	✓	✓	✓	✓

2.4.1.2 Dredging Operations

The dredging operation is accomplished with two 4-m^3 (5-yd^3) environmental clamshell dredges working side-by-side on a dredging platform (see Fig. 3). The dredging platform is a modified barge platform that incorporates a central storage hopper bin for short-term sediment storage in the intermediate stage of sediment transfer. The dredging platform is a representative model concept of the custom modified dredging platform.

The excavator equipment represented in Fig. 3 is capable of reaching depths of 7.3 m (24 ft). An extension between the clamshell and the excavator may be added to reach depths to 12 m (40 ft) (see Fig. 4). This depth is limited to 12 m with the shown extension due to clearance between the dredging platform and the clamshell that must be maintained during the swing to release a load in the storage hopper. Greater depths (up to 16 m (52 ft)) would be achievable by incorporating a telescoping extension.

2.4.1.3 System Requirements Verification

The clamshell dredge concept meets the system requirements listed in Sec. 2.3. One of the important aspects of the design is its ability to remove sediment at nearly in situ densities. Transporting sediment at high percent solids increases the amount of in situ dredged material deposited (therefore reduces the amount of deposited water) and increases the negative buoyancy of the deposit. The clamshell also has the ability to remove large debris commonly present at dredging sites. The production rate of one 4-m^3 (5-yd^3) clamshell is estimated at approximately 150 m^3/h

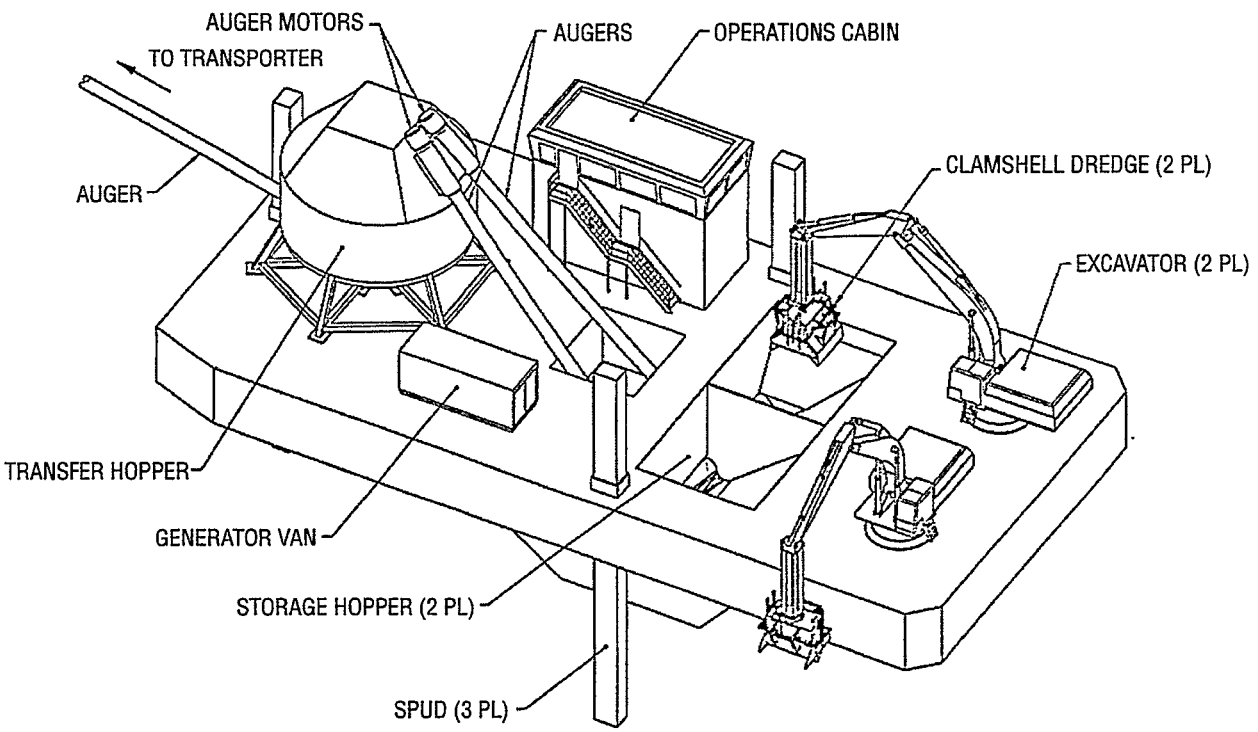

Fig. 3 — Dredging platform concept, oblique view

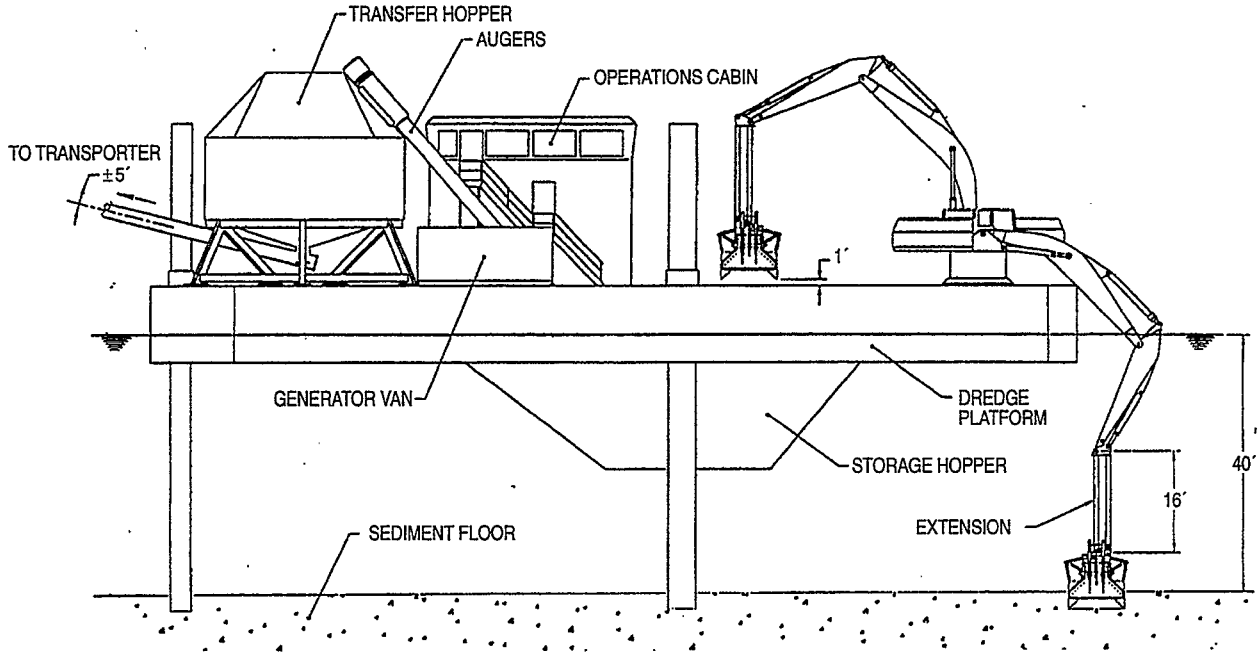

Fig. 4 — Dredging platform concept, side view

(200 yd^3/h) (based on a conservative cycle rate of 1.5 min). The system incorporates two clamshells for maintaining reliability and system production during operational downtimes.

2.4.2 Transfer and Loading

2.4.2.1 Selection of Transfer and Loading Method

The transfer and loading system provides the transfer of dredged material to the transporter vessel and distribution to the cargo cells. In maintaining the goal of high percent solids transported to the abyssal site, the sediment transport method must be capable of transporting slurries with a bulk wet density ≤1.7 Mg/m^3. The practical maximum in situ bulk wet density for hydraulic transport is 1.5 Mg/m^3 (Turner 1996). Commercial vendors recommended that a pumpable percent solids content by weight of sand/clay mixtures is approximately 35%. The dredged material properties listed in the system engineering report are in a range from 43 to 64% solids by weight. Therefore, hydraulic transport system capabilities were determined to be borderline.

A mechanical transport system was selected because of the capability to transfer materials of high percent solids. The mechanical sediment transfer and loading method utilizes augers and hoppers. Selecting the simplest method is most desirable for operation reliability. If hydraulic equipment is subsequently identified that can transport the material at its in situ density without adding water, that equipment should be utilized and should replace the more complex mechanical transfer and loading system option.

2.4.2.2 Transfer and Loading Operations

The transfer and loading system is illustrated in Figs. 3, 5, and 6. The system components remain installed on deck throughout the operation. The dredge clamshells release the dredged

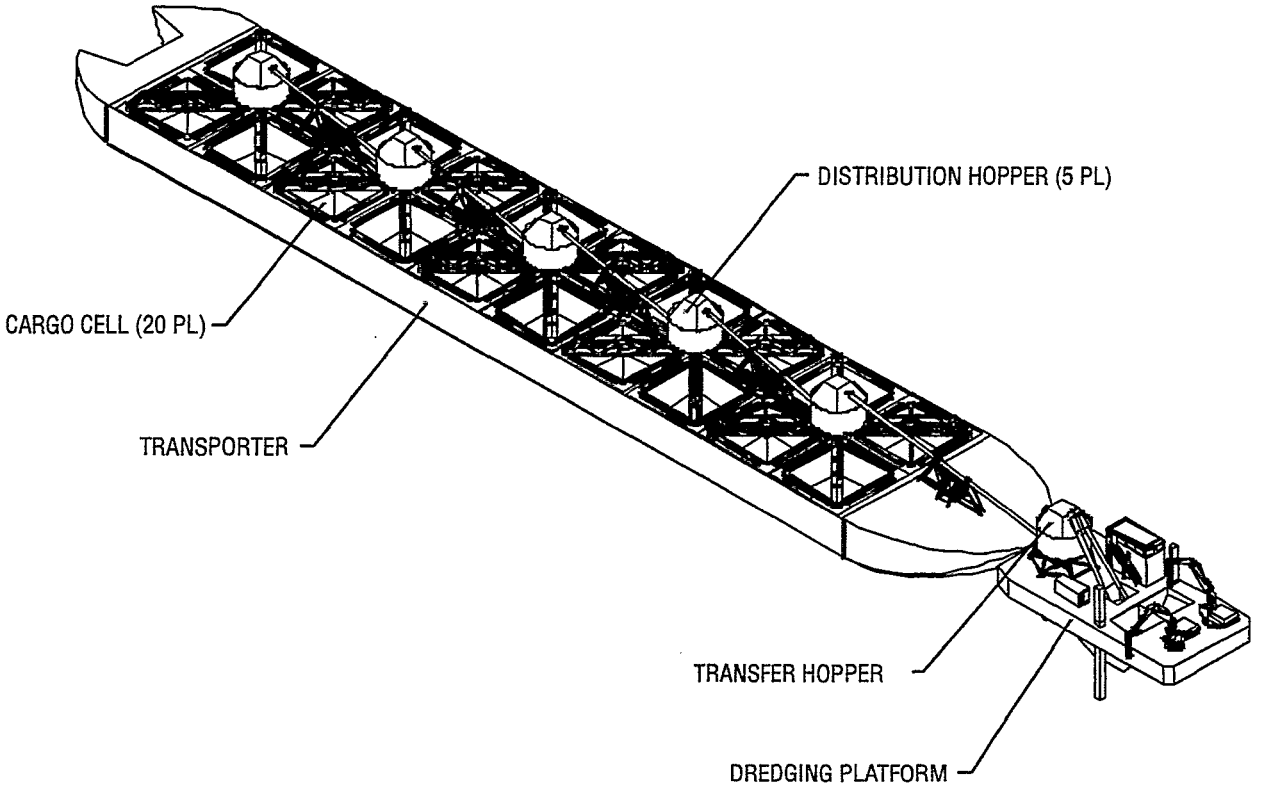

Fig. 5 — Concept for transfer of dredged material from dredging platform to transporter and distribution to transporter cells via screw auger feed system

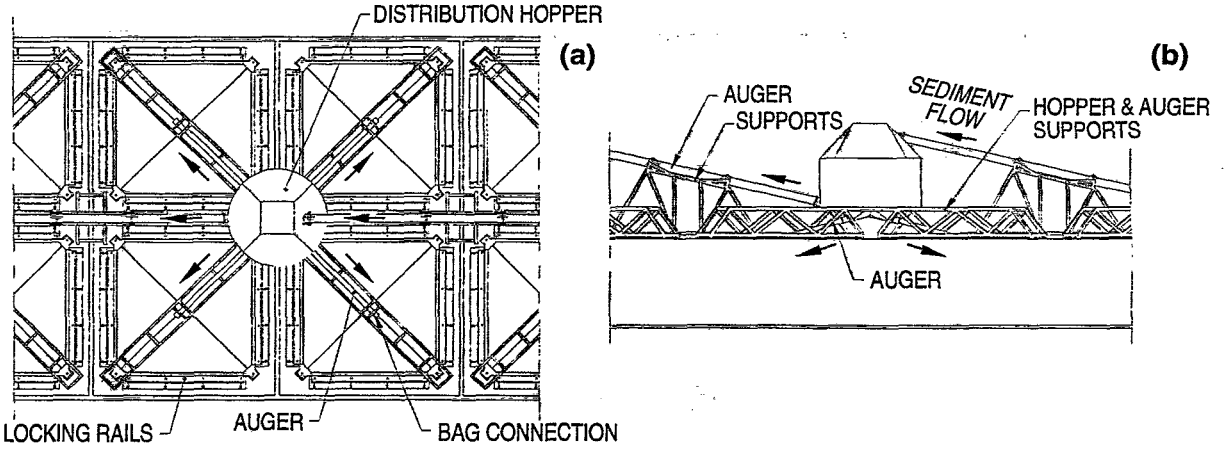

Fig 6. — Distribution system: (a) plan view and (b) side view

material into the dredging platform's storage hopper bin. On top of the storage hopper, large debris is removed by a debris separation system. The nature of debris at a site would be determined during a site investigation. After the site survey, the level of debris handling capability would be determined and a debris separation system selected. The material removed from the separation system could be mechanically loaded into containers with minimized operator intervention. Three separate systems previously used in similar cases include a slanted shaker-screen system, a conveyor screen system, and a grate/screen. For example, the shaker screen openings could be sized to limit the material to the size that is passable through the auger system and the grinding wheels. The shaker screen vibrates and is slanted toward debris containers. Material too large to fall through the screen bounces and shakes its way into the debris containers. Grinding wheels at the base of the storage hopper may also be added to increase the reliability of flow through the auger system.

The SimDOR system concept utilizes two dredges and two storage hopper bins. Each set is individually estimated to be capable of maintaining the required 150 m^3/h. The time required to fill the transporter, based on one dredge clamshell operating at 150 m^3/h, is 80.6 h (based on bulk wet density of 1.4 Mg/m^3).

At the base of the storage hopper in the dredging platform, two augers (one per hopper) transfer the material into the transfer hopper (see Fig. 3). The storage hopper has the capacity to store a total of 300 m^3 of material. The transfer hopper is the first hopper in the distribution series and serves in transferring the sediment from the dredging platform to the transporter vessel. The hoppers in the distribution series are oversized to accommodate the build-up of material in the event of equipment malfunction. The auger system has the maximum capability of transporting the dredged material at a rate of 450 m^3/h.

The distribution system can operate in several compartment-filling sequences. The distribution system can be controlled by a series of shut-off valves to continuously fill all cells, a set of four cells, or just one cell at a time. This gives the design the ability to be optimized during operations. The connection between the dredging platform and transporter (Fig. 5) is shown in a worst-case configuration requiring a long auger length between the transfer hopper and the first distribution hopper. If site space is available, the dredging platform can be positioned beside the transporter where the auger length would be reduced by approximately 10 m. The auger attachments at the transporter and the dredging platform have the capability to account for differential wave motions between the two bodies.

2.4.2.3 System Requirements Verification

The transfer and loading system meets the system requirements set forth in Sec. 2.3. The system is completely contained (with exception of the storage hoppers in the center of the dredging platform). The distribution system is contained and protected from the effects of rain and wind. The distribution system has the ability to shut down in less than 5 min in case of a malfunction via system power or shut-off valves. The distribution hoppers have adequate volume (300 m^3) to accommodate the build-up of material due to malfunctions.

2.4.3 Transport and Placement

The transporter concept design selected consists of a single vessel with a 10 × 2 array of cargo cells for containing the dredged material (Fig. 7). Each cargo cell (total of 20) has an inner compartment with bottom trap doors for releasing the material (Fig. 8).

The development of the transporter design focused on the following:

- Concept validation for structural configuration of vessel
- Compartment design for successful material release
- Compliance with the system requirements

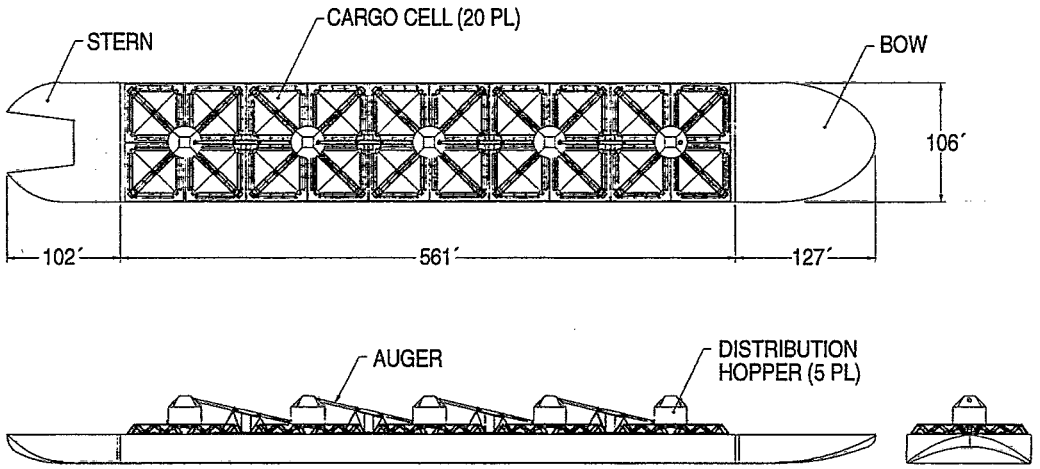

Fig. 7 — Transporter concept scale drawing

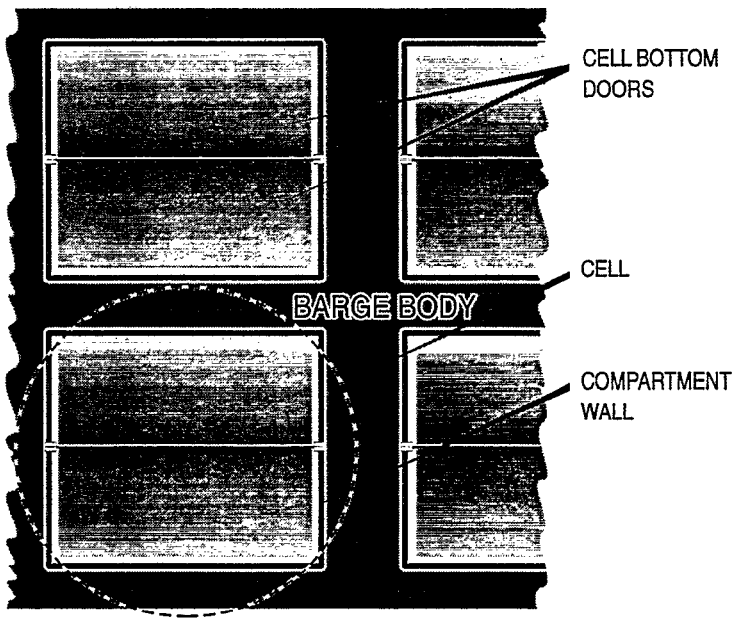

Fig. 8 — Plan view of transporter section (transporter terminology)

2.4.3.1 Structural Configuration of Transporter

The transporter overall dimensions are 241-m (790-ft) length, 32-m (106-ft) beam, and 5.5-m (18-ft) draft. The amount of freeboard added is based on the structural strength required and sea-keeping requirements for minimizing green water on deck. The cargo cells make up 171 m (561 ft) of the midbody (total midbody length is 202 m (663.5 ft). This leaves 21 m (67 ft) for the stern and 18 m (60 ft) for the bow. The length for the bow and stern is needed to transition the midbody dimensions from a block shape to a ship configuration capable of traveling at the required speed of 12 kt. The bow and stern design goals are to produce a vessel block coefficient below 0.8.

The structural configuration of the vessel has been validated as a successful approach to transporting 19000 DWT (between 10,000–12,000m^3 (13,000–16,000 yd^3)) of dredged material to the abyssal site. Structural steel can be placed in the approximately 2-m- (6-ft)-wide space surrounding the transporter and in the 4-m-(12-ft)-wide space along the longitudinal centerline of the vessel.

Only two factors of the structural configuration of the vessel require special considerations: (1) the girder structural strength and (2) incorporation of special structures to increase seaworthiness in sea state 8 to limit green water from coming onboard. These two considerations can be solved by a single design implementation of additional freeboard structure creating a wall around the transporter.

Several commercial integrated tug/barge connection systems available are: Intercon, Breit-Ingram, ARTUBAR, CATUG, Bludworth, and Articouple. The Intercon connection system is a single degree of freedom connection allowing free relative rotational pitch motion. The Intercon connection can offer higher average speeds and more control over the barge and operations in a larger range of sea states. The connection is capable of sea state 5 operations as required, but sea state 8 conditions would require disconnecting the tug and transporter and changing to a towed barge configuration.

2.4.3.2 Physics-Based Simulation of Transporter Design and Seakeeping

In a full-up, Simulation-Based Design (SBD) of the transporter system, most if not all of the critical design elements would be modeled with an appropriate level of fidelity to assess the performance of the system in its intended environment. Linked data bases would be used to not only assess performance, but to assess the cost and benefit of a design change. This was beyond the scope of SimDOR, but this effort did demonstrate the concept. Furthermore, useful transporter concept performance assessments have been developed.

Simulation-Based Design was applied in the sea-keeping analysis of the transporter and its connected tug. The transporter that would be appropriate for the transport and release of sediments contained in geotextile bags represents a unique ship design challenge. The performance and seaworthiness of such a vessel is a key element in the environmental safety of the DOR concept. Additionally, the sea-keeping properties of a transporter of a given payload determine the expected portion of the year that such a transporter might be able to operate between a given port and relocation site—having a first-order effect on the economic viability of the concept.

For SimDOR, two top-level transporter designs were evaluated. The first was an articulated design comprised of a number of smaller barges intended to accommodate sea surface motion. The second was a single large barge. The designs are described in Oceaneering International, Inc. (1996b). Sea-keeping analysis was performed using the Ship Motion Program model. It is a

two-dimensional, linear strip theory model developed by Dr. Nils Salvesen, and widely used by the Navy.

Both designs were evaluated for performance in sea states 5 and 8. In the articulated design, the individual units were allowed to move independently of any coupling. This preliminary analysis showed that at sea state 5 the design would probably be satisfactory. However, at sea state 8, the relative motions between barge sections were large enough that it was determined that potential coupling designs would be inadequate to withstand the resulting forces.

Attention was then focused on a conventional, rigidly framed barge concept. Integrated-tug-barge (ITB) designs are in current use (largely in near-coast operations), so it is believed that a satisfactory system could be developed for moderate sea states. The ITB system provides free relative rotational pitch motion between the two vessels. The barge was evaluated independently of the integrated tug since the tug would have little influence on the barge motions. However, the ITB design should be analyzed in any continuation of DOR system development since the barge would influence the tug motion. Due to a lower overall hydrodynamic drag for the system, the ITB configuration provides higher average speeds, better control, operation over a wide range of sea states, and better fuel economy.

Table 2 presents the barge design parameters and Table 3 the tug design parameters. To the midbody section of 202-m length, a bow section of 18 m and stern section of 21 m were added. A vertical or plumb bow was created with an approximate circular forefoot. It was not possible to design a fully hydrodynamic, satisfactory entrance given this short length and large beam. The stern section was simply contracted slightly in draft and beam. No cutout for the integrated tug was provided. Instead, the extra volume was assumed to approximately account for the presence of the tug.

The sea-keeping calculation was performed for long-crested (undirectional) head seas. Figure 9 shows a single frame from an animation of the ship motions for the conventional rigid construction alternative design in sea state 5, unidirectional (long-crested) head seas. Figure 10 shows a frame from the animation in sea state 8. Note in Fig. 10 that the barge would be under "green water" given the design freeboard (accurate flooding calculations are not performed, but the wave height above deck is shown when the freeboard is exceeded). The statistical results of these simulations are presented in Table 4.

Table 2 — Barge Simulation Design Parameters

PARAMETER	DIMENSION, m (ft)
Total Barge Length	241 (790)
Midbody Length	202 (663)
Total Barge Weight (Full Load)	34085 LTSW
Maximum Beam	32 (106)
Maximum Draft	5.5 (18)
Midbody Bilge Radius	0.23 (0.75)

Table 3 — Tug Simulation Design Parameters

PARAMETER	DIMENSION, m (ft)
LBP	37 (120)
Beam	14 (45)
Draft	3 (10)
CB	0.60
Displacement	926 LTSW (~2.3% of total configuration)

LBP – Length between perpendiculars, where herein foremost perpendicular is point where leading edge of bow meets the waterline and sternmost perpendicular is point where sternmost curve of hull meets waterline.

CB – Center of buoyancy.

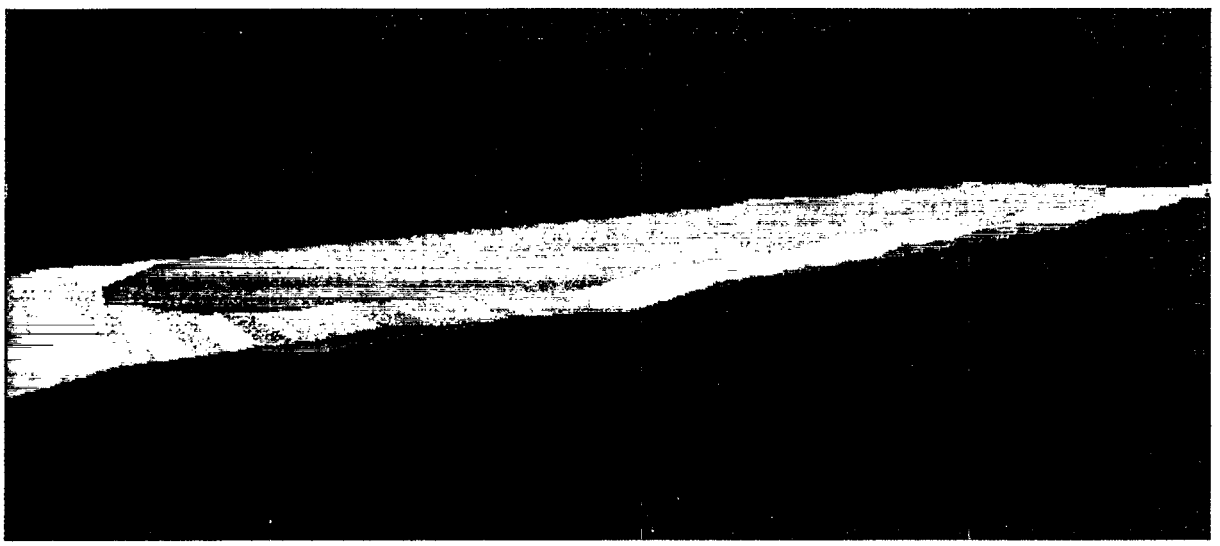

Fig. 9 — Frame from animation of loaded DOR transporter with tug decoupled in head seas, sea state 5, illustrating good performance

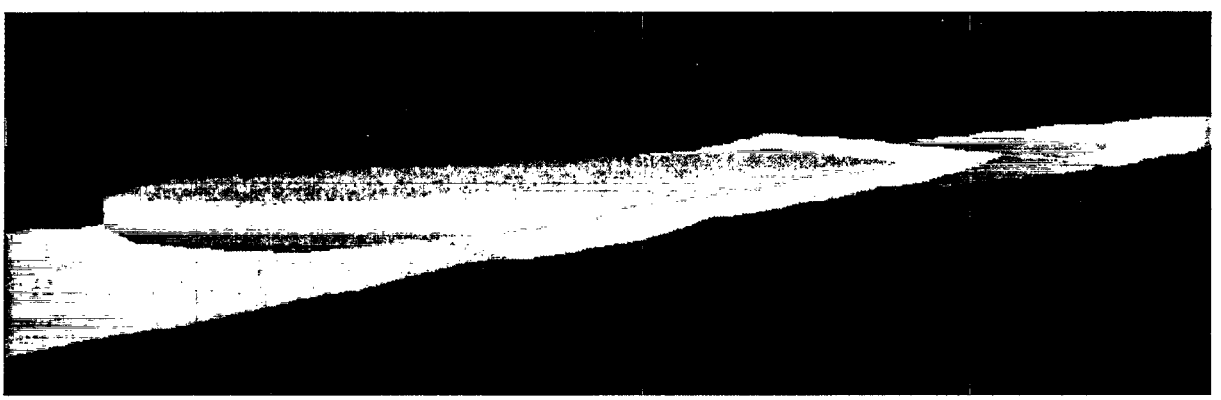

Fig. 10 — Frame from animation of loaded DOR transporter with tug decoupled in head seas, sea state 8, illustrating poor performance (green water over main deck)

Table 4 — Sea-Keeping Simulation Results

PARAMETER	RESULTS	
Sea State	5	8
Significant Wave Height, m (ft)	3.11 (10.2)	15.6 (51)
Modal Period, s	7	16
Significant Pitch, deg	0.25	5.9
Significant Heave, m (ft)	0.15 (0.48)	3.83 (12.6)

The large difference in transporter performance between these two sea states may seem surprising, but two factors contribute. First, the energy in sea state 8 is much greater than in sea state 5. Second, as wave heights increase, the energy is more concentrated at the low frequencies at which this large, heavy ship responds.

The sea-keeping analysis was only used to predict motions. No loads were calculated; a more refined, higher detailed geometry and mass distribution should be developed before this would result in a useful exercise. Multilevel, full three-dimensional Large Amplitude Motions Program codes should be used for load predictions.

An additional area to be explored if a three-dimensional code was used would be a higher fidelity coupling of the ship motion influence on the GFC release. As an example, in videos of the New York harbor GFC release experiments, significant sloshing of the container top surface can be seen. Barge roll is very apparent, and it can be seen that the barge motions will have significant impact on the GFC initial conditions at release.

It should be pointed out that a DOR dredged material transport barge represents a significant ship design challenge. Due to the desired high payload of dredged material, the barge would have very low buoyancy margin. Addition of equipment or strength members would have to be evaluated as the design was iterated. In summary, continued detailed design of a DOR transport barge would be an excellent candidate for the application of SBD design tools that would allow rapid evaluation of design modifications.

2.4.3.3 Compartment Design

The requirements set for the release of the containerized, dredged material aims at releasing the material quickly without physical restrictions to the fabric container. The release should minimize stresses on the dredged material container to minimize the risk of container failure. Stresses on the container during release include: hydrostatic pressure of the dredged material against the compartment walls, friction forces between the container fabric and the compartment wall, hydrodynamic drag against the water, forces due to physical deformation of the container due to obstacles, and the normal force of the dredged material on the container and bottom doors. These forces were reduced, if not eliminated, by incorporating a freely flooded compartment; fast, 100% opening compartment doors; and low-friction, high-density polyethylene (delrin) liners on compartment walls. The location of the water line above the dredged sediment reduces the effective hydrostatic pressure of the load on the compartment walls from 11 kPa (1.6 psi) to 4 kPa (0.6 psi). Reducing the load reduces the amount of stress on the container fabric due to dredged material weight. The

100% opening also eliminates restrictions from being applied on the container by eliminating a bag's need to alter its shape to exit the transporter.

The individual cargo compartments are approximately 12 m (40 ft) long by 12 m (40 ft) wide by 6 m (20 ft) deep for both designs. Each compartment can contain 500–620 m^3 (660–800 yd^3) of dredged material. The containerized, dredged sediment is released from the compartments through two bottom doors.

The compartment door design utilizes two doors configured similarly to a typical split-hull barge (see Fig. 11). The doors are held shut with a locking mechanism and a secondary hydraulic support system while in transit to the abyssal site. The doors are opened by releasing the lock and allowing the hydraulic cylinders to stroke open. The weight of the dredged material aids the opening of the doors.

2.4.3.4 Dredged Material Container

The container design for the dredged material must consider the following factors:

- Type of material for the container
- Shape and size of container
- Material and seam strength
- Density of material

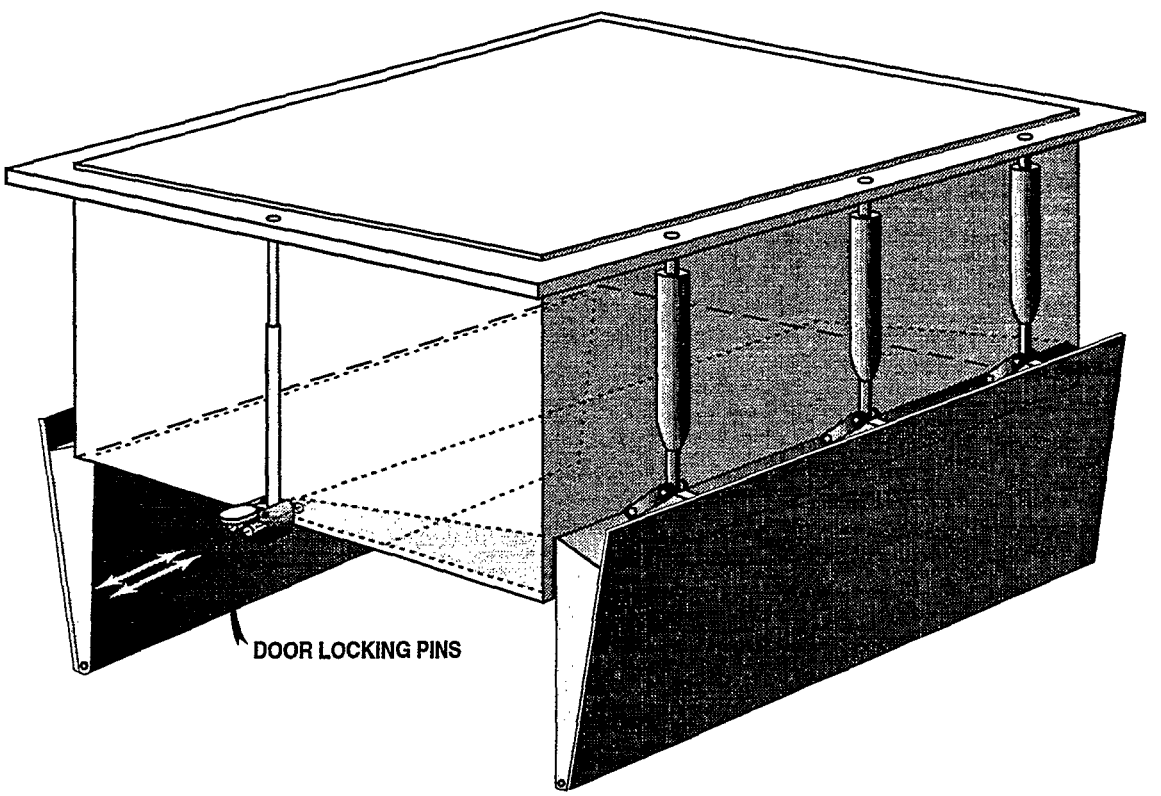

Fig. 11 — Cargo cell bottom door concept

The design of the transporter and compartments is versatile in regards to the type of container material used for containing the dredged sediment. The transporter does not restrict the container in regard to permeability of the container material. To avoid the possibility of container material floating to the sea surface, the specific gravity of the material should be greater than that of water. GFCs are currently being used for permeable containers of dredged material. GFCs are made from a polyester woven fabric with a specific gravity (SG) of approximately 1.3. Containers can be constructed using an outer permeable GFC with an inner impermeable polypropylene liner material (SG ≈ 0.91). Table 5 lists the possible container materials that were identified.

Work has been focused on the successful containment of dredged material in GFCs. Rupture of the container material is the highest risk factor in the SimDOR system. The method used to release the container significantly impacts the success of the release. Information on the use of GFCs to contain dredged material can be found in Fowler (1995), Fowler et al. (1994), and Fowler et al. (1995a).

The container configuration can be controlled to reduce the risk of container failure at the surface during release. Since the maximum allowable stresses are limited at the seams, the container construction should reduce the number of seams required. The size of the container should also be sufficient to allow the container increased mobility during the release. Extra container material also reduces tensile stresses on the container during impact. The recommended construction for the transporter compartments is a cylindrical "pill-shape," as shown in Fig. 12.

2.5 Design Factors

Two added factors to be considered during the design and investigation of deep-ocean relocation systems for contaminated, dredged material are minimization of costs and adverse environmental impact.

2.5.1 Cost Factors

The SimDOR concept of operation was evaluated in terms of the technical risks of the design that could significantly affect the cost of system operation. The technical risk evaluates the cost

Table 5 — Container Material Types Identified

MATERIAL TYPE	HISTORY OF USE	TENSILE STRENGTH kN/m (lbf/in)	SEAM STRENGTH kN/m (lbf/in)	SPECIFIC GRAVITY
Nicolon Polyester Woven Fabric (GFCs)	yes	175 (1000)	88 (500)	≈ 1.3
Nicolon Polyester Non-Woven Liner	yes	29–36 (166–206)	99% of tensile	≈ 0.91
GSE Ultraflex Impermeable, Polyethylene	none	18–88 (100–500)	70–90% of tensile	≈ 0.93
ChemFab ChemGlas PC PTFE/Fiberglass	none	~49 (~280)	70–90% of tensile	≈ 1.99

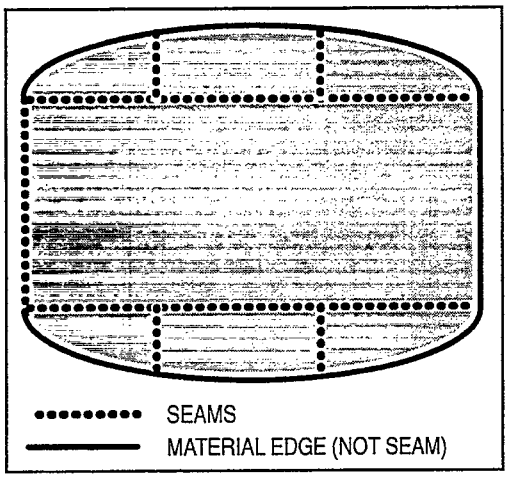

Fig. 12 — One concept for dredged material container construction

impact of an unsuccessful implementation of the particular subsystem of the design. In addition to the risk of GFC rupture during release from the transporter, free-fall, and impact on the seafloor, two added significant technical risk areas of the design are the selection of dredge system and the concept of operation for loading and transport. The technical approaches for the dredging method and the dredged material transfer and loading method could be changed from the selected mechanical methods to pneumatic and hydraulic, respectively. If a hydraulic method of sediment transfer was selected to replace the auger system, an estimated fixed cost savings impact of approximately $13,000 would occur. If a pneumatic dredging system was selected to replace the clamshell, an additional fixed cost impact of approximately $80,000 would occur. These cost factors associated with the technical methods are likely to be insignificant when compared to the cost of environmental impact assessments and environmental monitoring of the site.

Another cost factor associated with the SimDOR concept of operation is the technical approach chosen for the concept of operation. The concept of operation involves the dredge loading directly onto the transporter by a sediment transfer system. This requires the transporter to be able to dock next to the dredging platform. The transporter size and draft may restrict this concept of operation in some locations. If the transporter is not capable of accessing the dredging site, either a sediment transport line or lightering barge would be incorporated in the operation, increasing operation costs.

2.5.2 Environmental Factors

Environmental factors (as defined for SimDOR) are the key regulatory requirements, procedures, and/or restrictions and environmental impact concerns that apply to the operation of each component of the SimDOR system handling the contaminated sediment. The components included the environmental clamshell, the dredging platform hopper with grinders, sediment transfer and distribution system (augers, hoppers, and nozzles), geosynthetic fabric containers, and the transporter vessel. Each component of the concept of operation was evaluated for areas that may cause environmental concern (see App. B).

Several conclusions include (but are not limited to) the following:

- Dredging: The following steps may be required to assure minimized adverse environmental impact:
  - Evaluation under the National Environmental Policy Act (NEPA) for adverse environmental effects from incidental release of material during dredging
  - Estimation of the quantity and quality of the incidental release
  - Comparison of the incidental release estimate to state water quality standard or other criteria
  - Initial evaluation of water-column bioassays or more accurate actual time-concentration conditions
  - Implementation of control measures (silt curtains, dredge windows, equipment modifications, operational modifications) to reduce potential adverse effects
- Sediment Transfer and Loading
  - Minimization, if not prevention, of leakage or spillage of material
  - Implementation of secondary (back-up) control systems may be needed in the event of primary failures
  - Evaluation and validation of dredged sediment container material effectiveness
  - Evaluation and protection of personnel hazards on a case-by-case basis
  - Evaluation and compliance with Clean Air Act concerning release of volatiles
- Transport to Disposal Site
  - Prevention of spillage of material in transit (an unauthorized disposal)

The two most significant environmental factors are:

- Reducing the adverse impact due to dredging and the regulatory requirements to prove this protection process is being implemented.
- Eliminating or reducing leakage of dredged material contaminants through the container wall material. Environmental factors could restrict the type of material for the container to be an impermeable fabric for complete containment while on the sea surface.

2.5.3 Other Design Factors

The other factors associated with the SimDOR concept of operation are technology limitations and the sensitivity of the design's application.

The concept of operation is limited by the current technology available to accomplish several steps of the complete process. The operational areas that are limited by technology include:

- Pumping capacity of dredge pumps in regard to high bulk wet density sediment
- Tug/barge connection in high sea states
- Minimized environmental impacts during dredging
- Dredged material container fabric strength and seam strength

The most important factor to consider in the design of the SimDOR system is the system's sensitivity of its application. The SimDOR concept of operation demonstrates one applicable technology capable of delivering the dredged material to the abyssal isolation site. Accommodating the majority of the dredging sites and conditions is complex due to the fact that dredging sites have unique conditions pertaining to sediment characteristics and environmental conditions. These sediment characteristics are one major system driver in designing the complete system. The sediment characteristics determine the preferred dredging equipment, sediment transfer and loading equipment, the loading requirements of the transport vessel, and the characteristics of the hydrodynamic free-fall of the containerized material.

The most technical design factor associated with the highest risk is the successful release of the containerized material at the surface without rupture or tearing of the geosynthetic fabric container. The container's compartment design, material properties, and system operations are selected to reduce the risk of spills at the surface. The accidental spill of material at the surface during release is the most risky aspect of the DOR process.

2.6 Summary and Conclusions

There are several different systems that can complete the process of dredging through material disposal on the abyssal seafloor. One of the main factors driving the selection of a system is the dredged material characteristics/properties. The dredged material properties significantly impact performance of the dredging equipment, transfer and loading equipment, transporter capacity, and hydrodynamics of container release. One applicable design includes a mechanical clamshell dredge depositing material into a mechanical auger distribution and loading system filling releasable containers in a transport vessel. The transport vessel is an integrated tug/barge system that releases 20 500–620 m^3 (660–800 yd^3) containers from the sea surface over the abyssal site. The maximum and minimum required loading rate of the transporter is dependent on the dredging operations and is 300 m^3 and 150 m^3 (400 yd^3 and 200 yd^3)/h, respectively. These rates equate to a quickest and slowest transporter loading time of 33.2 h and 80.6 h, respectively. Both the dredging and transfer and loading system designs focus on minimizing adverse environmental impacts.

The aspect of the SimDOR design requiring special consideration is the successful release of the containerized dredged material from the transporter. The risk of container failure at the surface must be lowered by reducing container stresses with properly designed hardware and procedures. The transporter design includes carefully designed free-flooding compartments with 100% opening bottom doors. The containerized material release is controlled by sensors and is accomplished in less than 2 s.

The system requirements implied a worst-case engineering design scenario. The accommodation of clamshell dredges vs. hydraulic dredges and an auger distribution system vs. a hydraulic system is more complex and challenging in terms of maintaining production rates, economic viability, and systems engineering.

The design described in this report is a valid, applicable method of depositing dredged material on the abyssal seafloor. Since the system is highly dependent on the dredged material properties, it is recommended that specific evaluations of dredged material handling equipment be conducted on a site-to-site, project-to-project basis for actual operations of DOR. It is also recommended that the container release design be fully validated by scale model demonstrations. The validation could reduce the risk factor associated with the most risky engineering aspect of the SimDOR concept of operation design.

3.0 GFC DYNAMICS: RELEASE, FALL, AND IMPACT

by Albert W. Green, Jr. and Martin Fritts

3.1 Introduction

A brief description of material selection for GFC fabrication has been given in Sec. 2.4.3.4. Further, a brief summary of polyester fabric performance in the abyssal ocean environment is to be found in Valent and Young (1995), Sec. 1.4.2. GFCs have been used in the Netherlands for coastal construction (Ockels 1991; Jagt 1988), in the U.S. for groin construction for channelizing river flow (Fowler 1994), and for containment of contaminated dredged materials (Mesa 1995; Fowler et al. 1995; USACE 1996). To date, problems have been experienced with abrading and/or tearing of the GFC fabric; these problems have been substantially addressed in Secs. 2.4.3.3 and 2.4.3.4. To date, the GFCs have been dropped in water depths to 20 m (60 ft) (USACE 1996; Mesa 1995) and are known to have experienced rupture or tearing problems during transport in hopper barges, GFC fall to the ocean or harbor bottom, or during impact on the bottom. The relocation of contaminated, dredged material from harbors and navigation channels to the abyssal seafloor poses a problem of considerably different magnitude in that the filled GFCs will be free-falling through a 5000–6000-m water column over a time duration approaching 20 min and may impact on the seafloor at terminal velocities considerably higher than the 5 m/s noted to date. During free-fall, the GFCs are predicted to assume the shape of an oblate spheroid flattened in the vertical direction. Further, dynamic forces acting on the GFC will cause changes of shape and redistribution of stresses that could exceed the limits of the GFC fabric. The above hypothesized shapes and physical behavior are extrapolated from the behavior of raindrops falling in air (Green 1975; 1976). Vortex shedding during free-fall is expected to cause second-order shape changes of the GFC, particularly near the periphery, which coupled with the vortex shedding, could result in significant tilt of the GFC from the vertical and accompanying lateral skating of the GFC as it free-falls. This lateral skating could result in considerable deviation of the GFC from its ideal free-fall path, resulting in the seafloor area being populated by impacting GFCs being larger than the 3000-m-diameter site size estimated in Valent and Young (1995).

Analyses of the GFC dynamics during release from the transporter, free-fall through the water column, and impact on the abyssal seafloor were conducted with finite difference codes. Closed-form solutions of the free-fall portion of the analyses were performed to better understand and validate the free-fall, finite-difference model.

3.2 Models and Results

3.2.1 Release of GFCs from Cargo Compartment

The simulation code used in calculations of GFC release from the two-dimensional code developed by Dr. John Palmerton of the Waterways Experiment Station (WES) for simulations of GFC contained sediment release from split hull barges. This code had been used for previous calculations by WES in support of demonstrations of the use of GFCs for shallow-water applications. Validations of the code by Dr. Palmerton included static GFC shapes, geotextile fabric stresses, and GFC fall rates as compared with the demonstrations and with theory.

After receiving the Fortran code, "nydrop.f," from Dr. Palmerton, the IBM-specific code was converted to run on an Silicon Graphics, Inc. (SGI) machine. Science Applications International Corp. (SAIC) also converted the post-processing code "nrlplay.f" to the SGI platform. Several new capabilities had to be added to nydrop.f for the purpose of using the code within a total design and system simulation loop:

- barge compartment doors that could open according to a prescribed motion as input from the detailed CAD simulations;
- an initial velocity that could be imparted to the GFC and its contents at release to accommodate the initial transporter compartment fall period prior to the compartment door opening, as well as initial conditions prescribed by the transporter motion calculations derived from sea-keeping calculations;
- provision for coupling the code to a hydrodynamic code for self-consistent calculation of the effect of the external flow, including boundary layer formation, unsteady wake effects, and vortex shedding;
- provision for coupling the GFC position and shape back to the automatic gridding codes for external hydrodynamics calculations;
- the ability to subiterate the Palmerton model in conjunction with the hydrodynamics codes;
- output of the forces in the GFC for post-processing, particularly for visualization of bag stresses induced during bag release, descent, and impact; and
- a restart capability that was necessary for more efficient use of computer and human resources.

The original Palmerton model was designed for use in a quiescent water column with an added capability for regions of constant current. It was assumed that GFC and contained sediment motions could be governed by constant drag coefficients, and there was no provision to couple in externally supplied forces in dynamic calculations of the GFC motion. For shallow-water releases in which the GFC lengths were on the same order as the ocean depths, these approximations were reasonable and could be bounded by experimentally derived error bars. For the calculations of GFC descent and impact, the external forces experienced by each disk comprising the GFC membrane would be different, and the resultant unsteady GFC shape changes and unsteady motions would be important factors in being able to determine the descent path of the GFC, as well as the stresses experienced by the GFC membrane. Therefore, provision was made through these code modifications to provide the new unsteady forces at each timestep to each of the disks comprising the GFC membrane, to iterate the Palmerton model until a new GFC shape was found, and to input the new shape and position of the GFC to the gridding routines prior to the calculation of the new hydrodynamic forces. The details of the full coupling between the codes is given in Sec. 3.2.2.1 on the Reynolds-Averaged Navier-Stokes (RANS) codes.

A new graphics program was written in C utilizing openGL to plot the tensile/compression forces along the GFC at selected time steps. This capability permits the tracking of stresses within the GFC membrane during GFC release, descent, and impact, and allows a correlation of GFC stress with the time-dependent forces applied to the bag during each of these phases. This option has also been added to the original program, nrlplay.f, allowing ability to plot the tensile forces at every time step during post-processing.

Two sets of calculations were performed to study GFC dynamics at the full scale. The parameters used in these calculations are presented in Table 6.

The difference between the two runs is that the permeability of the GFC in one run is zero and 1.0 in the other. In Fig. 13a, the shape of the GFC in the barge compartment is shown before release. The circumference of the GFC is colored by its tensile force. At this stage in the simulation, the tensile force along the GFC is not significant, but reflects how well the GFC has been iterated to equilibrium prior to release. After release the GFC dynamics relative to the changing (opening) compartment geometry and the frictional forces between the GFC and the compartment

Table 6 — Parameters for GFC Release

PARAMETERS	VALUE
Total number of disks	1372
Diameter of the disks representing the GFC	0.2 m (0.5 ft)
Bulk wet density	1.6 Mg/m^3
Height of water above base	6.58 m (21.6 ft)
Impermeable GFC	–
Friction angle between GFC and compartment walls and bottom	10°
Rate of opening of the compartment bottom door	138.5°/s
Tensile strength of GFC per unit width	48.0 kN/m (274 lb/in.)
Maximum tensile stress along the GFC	1.37 MPa (198 psi)
Maximum compressive stress along the GFC	27.6 MPa (4000 psi)

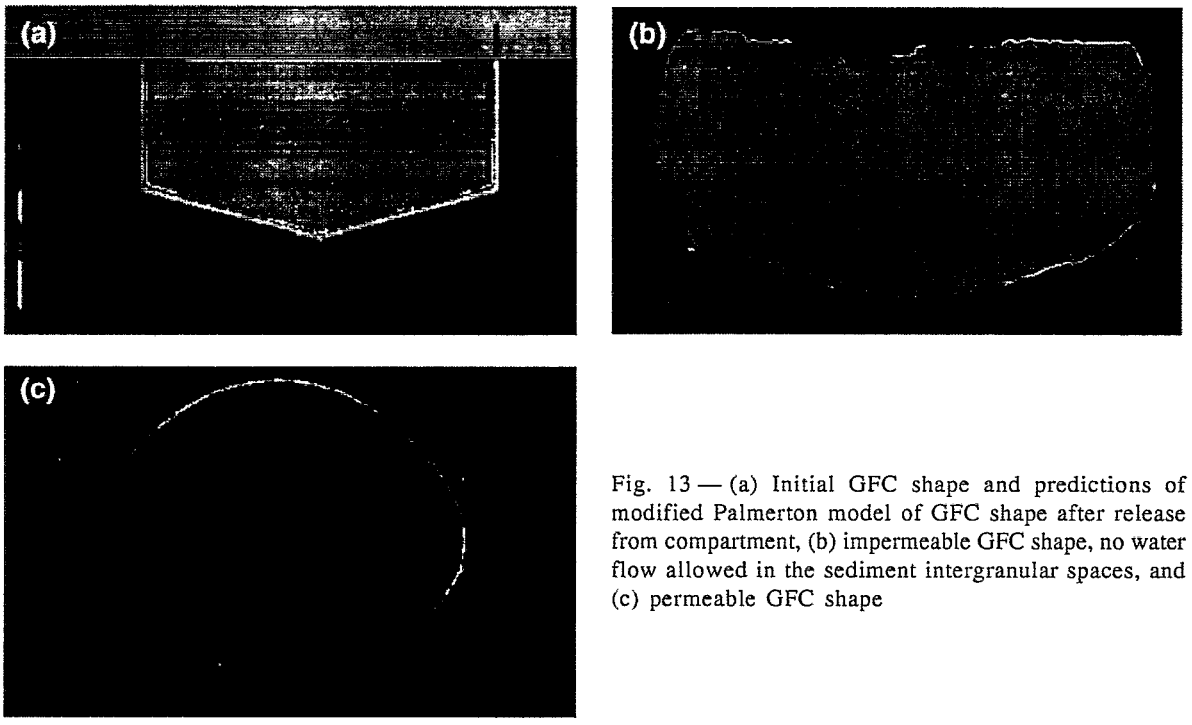

Fig. 13 — (a) Initial GFC shape and predictions of modified Palmerton model of GFC shape after release from compartment, (b) impermeable GFC shape, no water flow allowed in the sediment intergranular spaces, and (c) permeable GFC shape

give rise to significant tensile forces. In Fig. 13b and c, the shapes of the impermeable and permeable GFCs are shown after final GFC shapes have been attained. It is interesting to note the difference in GFC shape under the two assumed permeabilities. For the case of zero permeability, the GFC shape essentially remains similar to that of the cargo compartment even with a significant slumping in the top of the GFC due to the forces experienced in passing through the compartment doors. The

assumptions in the Palmerton model allow only for disk-to-disk forces so that the sediment can achieve a compacted shape that is fairly rigid. For a fluidized sediment, there would be an accompanying damping of these inter-disk forces, and the shape of the GFC could relax further. This type of behavior is shown at the other extreme in the permeable GFC simulation for which the GFC tries to attain the shape of an ellipse due to the passage of fluid into the GFC.

Figure 14a and b present the histories of the horizontal and vertical velocity vs. depth for the case of the impermeable GFC. There is very little horizontal velocity after the damping of the initial oscillations caused by the door opening and extending over the first 0.5 s. Similar initial oscillations are evident in the vertical velocity plot. The GFC attains a terminal velocity of 5 m/s. Figure 15 shows that the relationship between depth and time is linear after the first 2 s. This is consistent with the time at which the GFC attains terminal velocity. Detailed results of the release analysis are to be found in Dinavahi et al. (1997). The Discrete Element Method (DEM) of the release sequence identified corner points as being areas of high fabric tensions.

3.2.2 Free-Fall of GFC to Seafloor

The development of a predictive model describing the free-fall descent of a GFC enclosing 300 to 2000 m^3 of dredged material through a water column of ca. 5000 m, without benefit of model

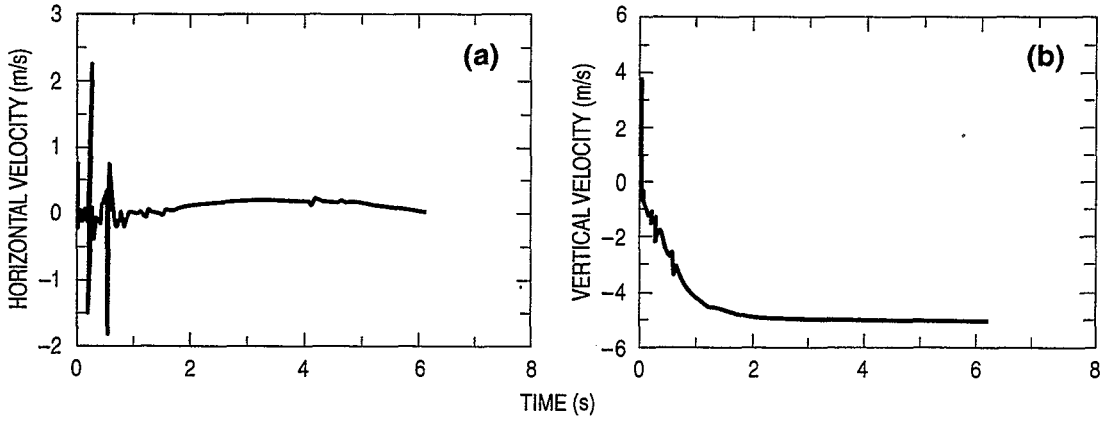

Fig. 14 — Predicted GFC velocity starting at compartment door opening: (a) horizontal and (b) vertical

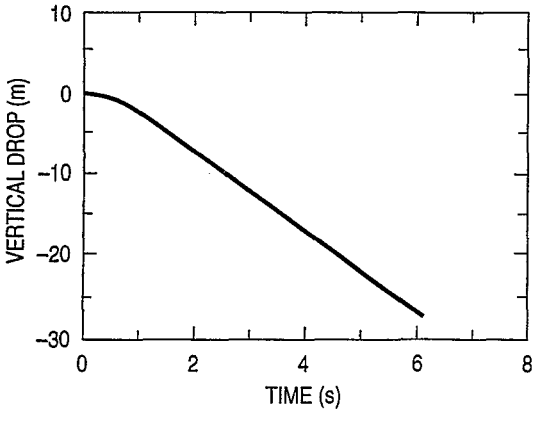

Fig. 15 — GFC vertical fall time history predicting GFC will attain terminal velocity 2 s after release

or prototype performance data of applicable scale, was undertaken along two paths. Dr. Martin Fritts of SAIC-Annapolis led one team examining applicability of a RANS solver, while Dr. Albert Green of NRL, Code 7330, examined a closed-form analytical approach combined with some empirical data used for some critical parameters.

3.2.2.1 Viscous Flow Simulations

3.2.2.1.1 Overview — A successful GFC drop simulation scheme must accurately account for (at least) three highly complex fluid-flow phenomena: GFC trajectory predictions, GFC stress prediction, and impact plume prediction. All three problems require solution of the complete, unsteady, turbulent flow around the GFC. Trajectory prediction, for example, requires unsteady integrated forces and moments caused by both attached boundary layers and separated turbulent wakes. GFC stress predictions, on the other hand, require a local distribution of forces. Plume prediction requires the ultimate level of flow knowledge; the complete flow field description around a GFC as it impacts the seafloor.

The minimum level of computational fluid dynamics (CFD) technology capable of providing all the necessary information for turbulent, vortical flows is the class of RANS solvers. This section describes the adaptation and application of one such solver, the SAIC Finite-Analytic Navier-Stokes (FANS) system to the SimDOR GFC drop problem.

FANS is a well-validated, three-dimensional, unsteady, incompressible RANS code with many user-friendly features. It has been extensively applied and validated to a wide array of both steady and unsteady problems, but required some extensions to handle bottom collisions. It was therefore decided that the initial SimDOR applications completed for FY96 would proceed using only two-dimensional geometries until the bottom collision capability has been validated. Thus, while the capability has been developed and incorporated into a three-dimensional code (with the ultimate goal of three-dimensional simulations in mind), this report presents results only for geometries of constant cross section.

3.2.2.1.2 Approach — SAIC's FANS Viscous Flow Prediction System was chosen for the SimDOR work because it already contained most of the functionality needed to simulate trajectories, GFC stresses, and bottom plumes. FANS is an unsteady, incompressible, three-dimensional, RANS solver that has been extensively validated on a wide range of high Reynolds number steady and unsteady flows (Korpus 1995; Chen and Korpus 1993; Weems et al. 1994). It utilizes the finite-analytic technique for primitive velocity and turbulence quantities and a SIMPLER/PISO nonstaggered Poisson solver for pressure. It supports body-fitted, multiblock, overset (a.k.a. Chimera) grids, and can therefore resolve any flow domain with maximum grid quality.

FANS currently employs three state-of-the-art turbulence models: a modified $k\varepsilon$ (Hanjalic and Launder 1990); a nonlinear algebraic Reynolds stress model (Gatski and Speziale 1993), and a fully implicit seven-equation Reynolds stress model (Speziale et al. 1991). Two techniques are available for solving the turbulent dissipation rate equation: a two-layer model that assumes a prescribed algebraic distribution in the near-wall region (Chen and Korpus 1993), and a low Reynolds number extension technique that solves ε all the way to the wall (So, et al. 1991). Either technique can be used with each of the three models to provide a full range of turbulence capability.

Communication between blocks in the Chimera scheme is handled by conservative second-order accurate interpolation and adjoining blocks are free to move relative to each other in any arbitrary time-dependent manner. Grid movement is treated by including grid velocities in each

of the governing equation convection terms, and time accuracy is maintained by updating the interpolation stencils at each time step.

Grids are normally generated using NASA Ames Research Center's HYPGEN code to maximize grid quality throughout the near field, and GRIDGEN to fill in the far field. Grid degeneracies and low-quality topologies such as "H" grids are completely eliminated, and the only requirement is that the union of all blocks spans the entire flow domain. The Chimera capability also eliminates the high cell skews usually associated with arbitrarily moving body problems by allowing a combination of body-fixed blocks and Earth-fixed blocks.

The only capability required for GFC drop simulations not included in the basic FANS system is stratified flow modeling. Such a capability is important for the proper handling of bottom collisions since the ocean floor is not generally a hard, flat surface. The presence of sediments causes the bottom to appear more as a finite density gradient than a hard floor. As the GFC penetrates the surficial sediments of the seafloor, the FANS system does treat and account for the increasing density of the sediment with depth of penetration, with the greater density of the sediment with respect to the seawater resulting in a corresponding increase in buoyancy. However, the FANS system will significantly overpredict depth of penetration and volume of seafloor sediment displaced by impact because this solution does not include the effect of inertia of the sediment mass being displaced and the sediment resistance to shearing in adding to the decelerating force (see Sec. 3.2.4). The FANS approach does have the advantage of being able to model the sediment-laden, turbid water plume generated by bag impact as part of the complete solution.

The approach was incorporated into FANS by treating density as an additional "passive" scalar dependent variable. The flow remains incompressible, but not necessarily with constant density. Density becomes a quantity advected with the surrounding flow providing a means to simulate plume upwelling. The advected distribution, in turn, modifies the surrounding flow through the density terms in the Navier-Stokes equations. An initial condition must be provided for the density distribution and can be taken from existing measurements of bottom makeup. The development, integration, and validation efforts required for this capability have now been completed, and production runs are ready to begin.

In addition to the stratification model described above, two additional aspects of the SimDOR work were unique: the need to couple fluid forces to GFC dynamics and to GFC shape. While these do not require complex capability development in the traditional sense, they do require the integration of capabilities that are complex in their own right. Coupling of GFC dynamics to the fluid forces, for instance, requires that the portion of grid that is fixed to the body is moved according to the equations of motion of the GFC. Thus, each time step requires solution of a solid-body dynamics equation for every degree of freedom of body motion. For the two-dimensional bodies studied here, the governing equations reduce to equations for two translational coordinates (x, y) and a rotational coordinate ϕ:

$$\rho_{GFC} V \frac{\partial^2 x}{\partial t^2} = F_x(t) \tag{1}$$

$$\rho_{GFC} V \frac{\partial^2 y}{\partial t^2} = F_y(t) + \rho g V - \rho_{GFC} g V \tag{2}$$

$$I\frac{\partial^2\rho}{\partial t^2} = M_z(t)\,, \tag{3}$$

where V is the volume of the GFC, ρ is the water density, ρ_{bag} is the density of the GFC plus its contents, I is the GFC's rotational moment of inertia, and g is the acceleration of gravity. The quantities $F_x(t)$, $F_y(t)$, and $M_z(t)$ represent the time-dependent forces and moment from FANS. Each equation requires two initial conditions, one for the magnitude of the particular degree of freedom (x, y, ϕ) and one for the time derivative of that degree of freedom ($\dot{x}, \dot{y}, \dot{\phi}$).

The simulations presented herein were performed using FANS' moving grid capability to simplify integration of these equations of motion. Three types of grid blocks were used to discretize the flow domain. That part of the domain closest to the body (i.e., boundary layers and wakes) were resolved using body-fitted curvilinear grids that translate and rotate with the body according to the solution of all three governing dynamics equations. The far-field flow is resolved with one large block spanning from the ocean surface to the floor and remaining Earth-fixed for all time. The portion of domain between these two scales is resolved using an intermediate level of refinement sufficient to capture such flow attributes as the GFC's vortical wake. This intermediate grid follows the GFC by translating according to the solution of Eqs. 1 and 2, but remains fixed in a vertical orientation without regard to the roll angle dictated by Eq. 3. Figure 16 shows the corresponding block structure with near-field in yellow, intermediate in green, and far-field in blue. A representative simulation using this technique is presented in a later subsection of this report.

The second code coupling task undertaken for this effort was the integration of FANS to John Palmerton's bag shape prediction software. This was accomplished using a shell script program to iteratively run FANS for predicting GFC surface forces and then Palmerton's code for predicting

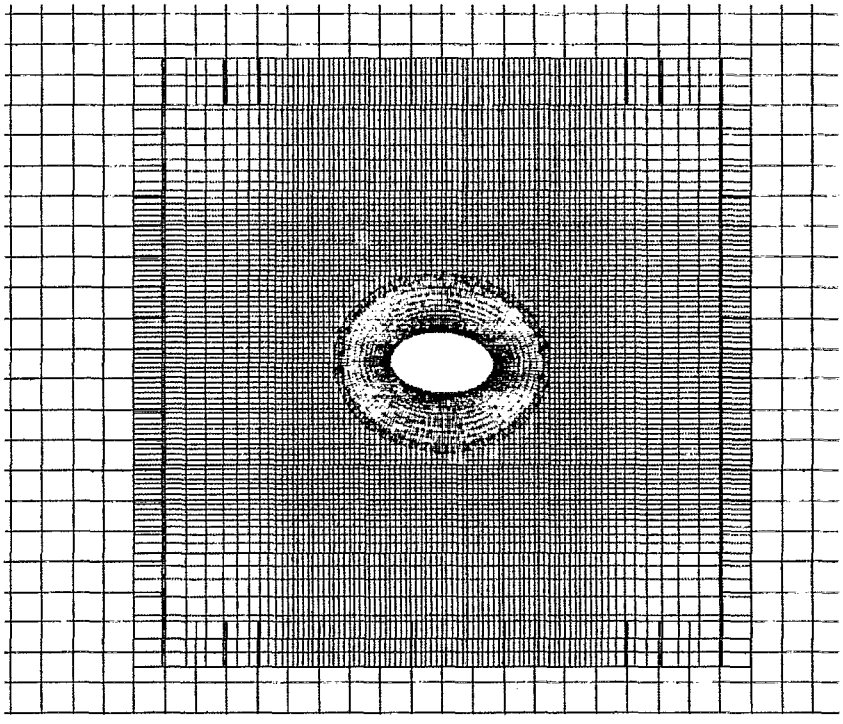

Fig. 16 — Typical moving grid block structure

GFC deformation under those forces. At each time step, the body is moved according to Eqs. 1, 2, and 3, and the near-field blocks regridded automatically using HYPGEN. Development of the required coupling has been completed, but demonstration cases were not completed in time for this report.

3.2.2.1.3 FANS Theory — The time-dependent viscous flow solutions presented in this study were obtained by solving the incompressible RANS equations in conjunction with $k\varepsilon$ turbulence model. When nondimensionalized by a characteristic length L, velocity V_0, and density ρ, the Cartesian form of these governing equations can be written:

$$U(i),_i = 0 \tag{4}$$

$$\frac{\partial U(i)}{\partial t} + U(j)\,U(i),_j + \left(p + \frac{2}{3}k\right),_i - \nu_{t,j}\,S_{ij} - \left(\frac{1}{Re} + \nu_t\right) U(i),_{jj} = 0 \tag{5}$$

$$\frac{\partial k}{\partial t} + U(j)\,k,_j - \left(\frac{1}{Re} + \nu_t\right) k,_{jj} - P + \varepsilon = 0 \tag{6}$$

$$\frac{\partial \varepsilon}{\partial t} + U(j)\,\varepsilon,_j - \left(\frac{1}{Re} + \frac{\nu_t}{1.3}\right)\varepsilon,_{jj} - \frac{\varepsilon}{k}\left[C_{\varepsilon 1}\,P_{sol} + C_{\varepsilon 3}\,P_{irr}\right] + C_{\varepsilon 2}\,\frac{\varepsilon^2}{k} = 0\,, \tag{7}$$

where $U(i)$ represents the Cartesian velocity components, p the static pressure, k the turbulent kinetic energy, and ε the rate of dissipation of turbulent kinetic energy. The quantity ν_t is defined as the linear eddy viscosity $0.09k^2/\varepsilon$, S_{ij} as the mean strain rate tensor $U(i),_j + U(j),_i$, and the Reynolds number as LV_0/ν. The rate of production of k is represented by P. In the dissipation rate equation, has been split into solenoidal and irrotational components following Hanjalic and Launder (1980):

$$P = P_{sol} + P_{irr} \tag{8}$$

$$P_{sol} = 4\left[S_{12}^2 + S_{13}^2 + S_{23}^2\right] \tag{9}$$

$$P_{irr} = 2\left[S_{11}^2 + S_{22}^2 + S_{33}^2\right]. \tag{10}$$

The modeling coefficients ($C_{\varepsilon\,1}$, $C_{\varepsilon\,2}$, $C_{\varepsilon\,3}$) are taken as constants set equal to (1.44, 1.92, 2.4), respectively.

The usual near-wall stiffness problem associated with Eq. 7 has been circumvented herein by using the two-layer approach of Chen and Patel (1988, 1989). The approach utilizes the $k\varepsilon$ model outlined above for most of the flow field, but a one-equation kl model in the viscous sub-layer and

buffer zone. Switching between ε and l dissipation models is performed automatically when the wall Reynolds number $Re_{wall} = Re\sqrt{k\delta}$ (δ being the normal distance to the closest wall) becomes less than 300 (Chen and Korpus 1993). Details of the l dissipation model can be found in Chen and Patel (1989) and will not be repeated here.

Discretization of the governing equations for $U(1)$, $U(2)$, $U(3)$, k, and ε is performed using the finite-analytic method of Chen et al. (1990). Each equation is first written in the form of a general convection/diffusion equation. Using ϕ to represent one of the conserved quantities, the generic form becomes:

$$\frac{\partial \phi}{\partial t} + U(j)\,\phi_{,jj} - \left(\frac{1}{Re} + \frac{\nu_t}{\sigma_\phi}\right)\phi_{,jj} + S_\phi = 0\,, \tag{11}$$

where

$$S_{U(i)} = \left(p + \frac{2}{3}k\right)_{,i} - \nu_{t,j} S_{ij}$$

$$S = -P + \varepsilon$$

$$S_\varepsilon = -\frac{\varepsilon}{k}\left[C_{\varepsilon 1} P_{sol} + C_{\varepsilon 3} P_{irr}\right] + C_{\varepsilon 2}\frac{\varepsilon^2}{k}$$

and $\sigma_\phi = 1$ unless $\phi = \varepsilon$, in which case it is set to 1.3.

In the interest of making the RANS solver sufficiently general for arbitrary geometries, the independent variables of the governing equations are first transformed into body-fitted coordinates. Using (ξ^1, ξ^2, ξ^3) to represent a generally nonorthogonal curvilinear system, Eq. 11 becomes:

$$\frac{\partial \phi}{\partial t} + \left[(U(j) - V(j)_{\text{grid}})\,\xi^k_{,j} + \left(\frac{1}{Re} + \frac{\nu_t}{\sigma_\phi}\right) f^k\right]\frac{\partial \phi}{\partial \xi^k} \tag{12}$$

$$+ \left(\frac{1}{Re} + \frac{\nu_t}{\sigma_\phi}\right) g^{jj}\frac{\partial^2 \phi}{\partial \xi^j\,\partial \xi^j}$$

$$+ \left[S_\phi + \left(\frac{1}{Re} + \frac{\nu_t}{\sigma_\phi}\right)\sum_{i \neq j} g^{ij}\frac{\partial^2 \phi}{\partial \xi^j\,\partial \xi^j}\right] = 0\,,$$

where g^{ij} is the contravariant fundamental metric tensor $f^k = \nabla^2 \xi^k$, and $\xi^k_{,j}$ is the inverse of the covariant transformation tensor $\partial x^k/\partial \xi^j$. The extra convective term $V(i)_{\text{grid}}$ represents a Cartesian gridpoint velocity arising from the time derivatives in a moving coordinate system and has been

included to allow arbitrary grid movement. Note that the cross-derivative terms from the Laplacian in curvilinear coordinates have been lumped with the source term to preserve a form amenable to separation of variables and that the Schwarz-Christoffel terms (f^k) have been lumped with the convective velocities to speed convergence.

With the equations in their generic form, the discretization proceeds by linearizing Eq. 12 over each computational element and then solving analytically by separation of variables. Evaluation of the analytic solution at the interior node of a computational element provides a stencil for the center point in terms of its nearest neighbors. Time derivatives are handled by the Euler implicit method, and unknowns from the previous time step are lumped into the source term. The resulting implicit system of equations is solved by the Alternating Direction Implicit method in each cross-flow plane and then swept repetitively in the stream-wise direction. Detailed expressions for the coefficients of the finite-analytic stencil can be found in Chen et al. (1990).

Pressure coupling is supplied using a modified SIMPLER/PISO algorithm (Chen and Patel 1989) that uses the strong conservation form of Eq. 4:

$$\frac{1}{\sqrt{g}}\left(\sqrt{g}U^i\right)_{,i}=0\,, \tag{13}$$

where U^i is the contravariant tensor $U(j)\xi^k_{,j}$ and g is the determinant of the covariant fundamental metric tensor. The technique defines pseudo-velocities from the discretized form of Eq. 12 as:

$$U^i=\hat{U}^i+E^{ii}\frac{\partial p}{\partial \xi^i}\,, \tag{14}$$

where $\hat{U}^i$ and E^{ii} necessarily involve the finite-analytic coefficients and will not be repeated here (see Chen and Korpus 1993). The technique is unique in that it introduces pseudo-velocities at the staggered grid locations, thereby leaving the pressure unknowns at the grid nodes. A discrete pressure Poisson equation is obtained using central differences and then substituting Eq. 14 into 13:

$$\begin{aligned}
&\left(\sqrt{g}E^{11}\right)_{i+1/2}\Delta^i p-\left(\sqrt{g}E^{11}\right)_{i-1/2}\Delta^i p \\
&\quad+\left(\sqrt{g}E^{22}\right)_{j+1/2}\Delta^j p-\left(\sqrt{g}E^{22}\right)_{j-1/2}\Delta^j p \\
&\quad+\left(\sqrt{g}E^{33}\right)_{k+1/2}\Delta^k p-\left(\sqrt{g}E^{33}\right)_{k-1/2}\Delta^k p \\
&\quad=-\left(\sqrt{g}\,\hat{U}^1\right)_{i+1/2}+\left(\sqrt{g}\,\hat{U}^1\right)_{i-1/2} \\
&\qquad-\left(\sqrt{g}\,\hat{U}^2\right)_{j+1/2}+\left(\sqrt{g}\,\hat{U}^2\right)_{j-1/2} \\
&\qquad-\left(\sqrt{g}\,\hat{U}^3\right)_{k+1/2}+\left(\sqrt{g}\,\hat{U}^3\right)_{k-1/2}.
\end{aligned} \tag{15}$$

Note that subscripts on the $\hat{U}^i$ and E^{ii} terms now represent discrete (staggered) grid locations and Δ^i and ∇^i represent forward and backward difference operators in the direction of the superscripted index.

For calculations around complex or moving geometries, the discrete solvers resulting from Eqs. 12 and 15 are embedded in a Chimera-like, multiblock environment. The solver works on one block at a time, and the only grid connectivity requirement is that the union of blocks spans the entire computational domain. Individual blocks are allowed to overlap arbitrarily and interblock communication is handled by conservative triquadratic interpolation. The overall approach has been extensively validated for both steady and unsteady three-dimensional applications (Korpus 1995; Chen and Korpus 1993; Weems et al. 1994).

3.2.2.1.4 Initial Certification — The first steps toward certification of FANS' moving-body capability for SimDOR applications were begun using a generic GFC shape and prescribed motions. The geometry was taken from one of John Palmerton's runs, since this was thought to give a realistic approximation to the actual shape. The motion was prescribed as purely vertical, accelerating linearly from rest to a terminal velocity of 4.6 m/s (15 ft/s). Terminal velocity was continued for a depth of about 20 GFC beams, after which a rapid deceleration to rest was prescribed to simulate bottom collision.

The Palmerton geometry was discretized using a two-block construction. Figure 17 shows the grid with near-field shown in green and far-field in blue. Since the purpose of this test was concept certification rather than validation, the intermediate resolution block described previously has been neglected in the interest of run-time efficiency.

The resulting simulation produced an enormous quantity of information. A grid of approximately 50,000 points was used and about 30,000 time steps were needed. Time histories of lateral velocity, vertical velocity, and pressure were saved at each time step, but turbulence quantities were discarded to preserve disk space. Time histories of the predicted forces and moments were also saved. Since the flow field is unsteady, data presentation in a report format was not feasible. Two movies were therefore produced to enable visualization: one showing the velocity deficit developing above the GFC and the other showing vorticity shed from the GFC. The movies were integrated into Oceaneering's Demo Video in September 1996.

Unfortunately, the unsteady aspect of these simulations cannot be adequately demonstrated here. A small number of "stills" could be presented, but would probably prove of limited utility. Accordingly, only two generic time steps will be included here for reference purposes, and the reader is referred to the Oceaneering video for further detail. Figure 18 shows contours of vertical velocity at two time steps: one about half way through the drop and the second after the GFC has reached the seafloor. Each figure represents the level of detail that RANS can yield about a complex viscous flow field—boundary layers, separation points, and wake formulation are all plainly shown. In each case, the waviness of the wake is indicative of the expected von Karman vortex street behind the bluff GFC. The bottom figure further indicates that the wake continues to move after the GFC is stopped, and can be expected to act to suppress any upwelling that may occur.

3.2.2.1.5 Ellipse Validation — Since unsteady validation is a prohibitively complicated process, it was thought prudent to perform a steady validation study before proceding with actual GFC drop simulations. The University of Manchester "lifting ellipse" wind tunnel tests were used for this purpose. FANS was used to simulate the experimental setup with the ellipse at a constant angle of attack and constant onset flow. Solutions were performed at 0°, 10°, and 20° angle of attack.

Figure 19 shows a typical FANS result, with the upper part showing contours of chord-wise flow and the lower showing pressure. Since the 6 to 10 Manchester ellipse is a fairly bluff body (even at zero degrees angle of attack), the expected von Karman vortex unsteadiness is visible in the wake. Figure 20 shows the FANS predicted lift and drag coefficients, also at 10 deg angle

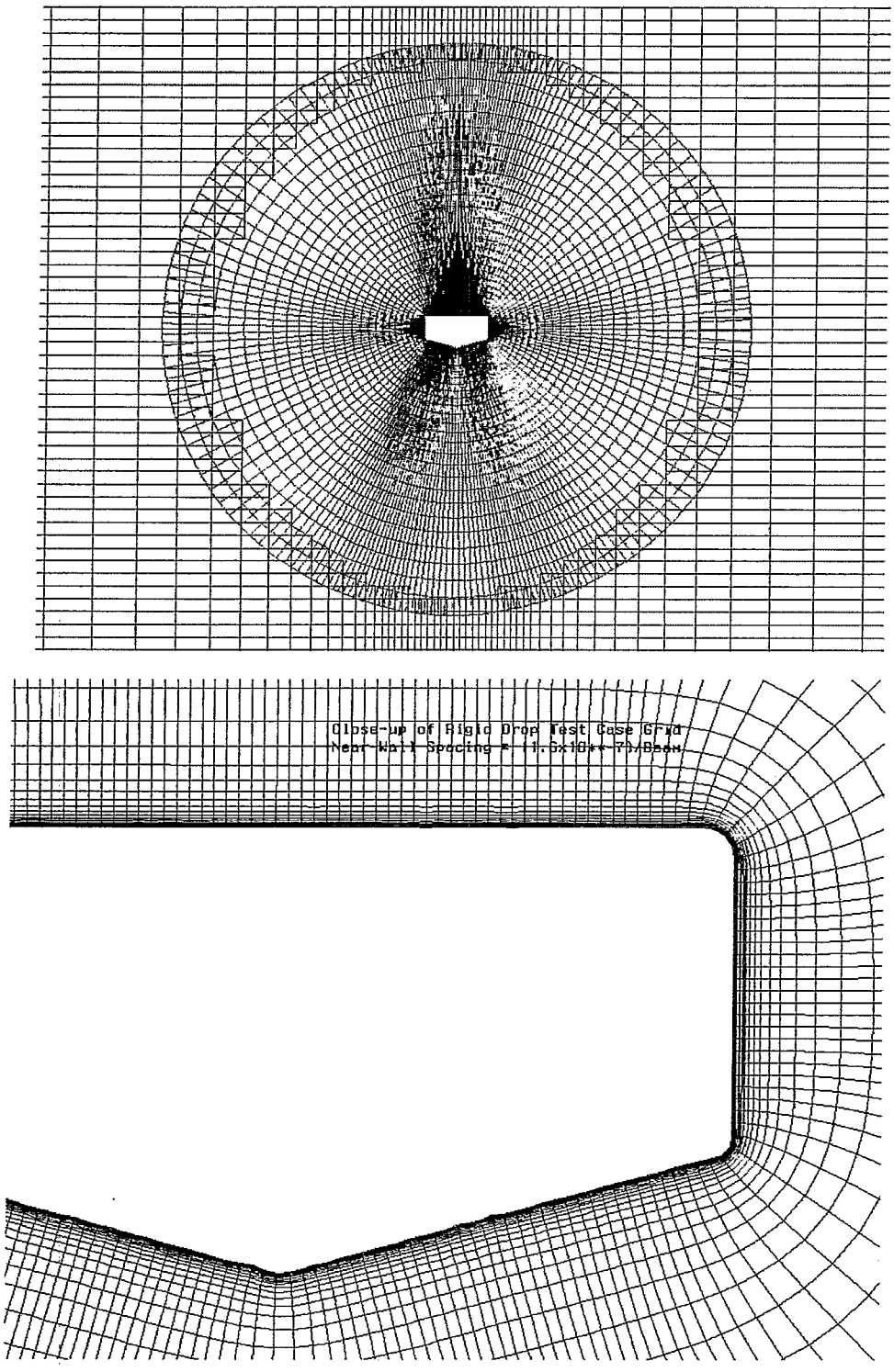

Fig. 17 — Moving grid block structure for initial certification studies

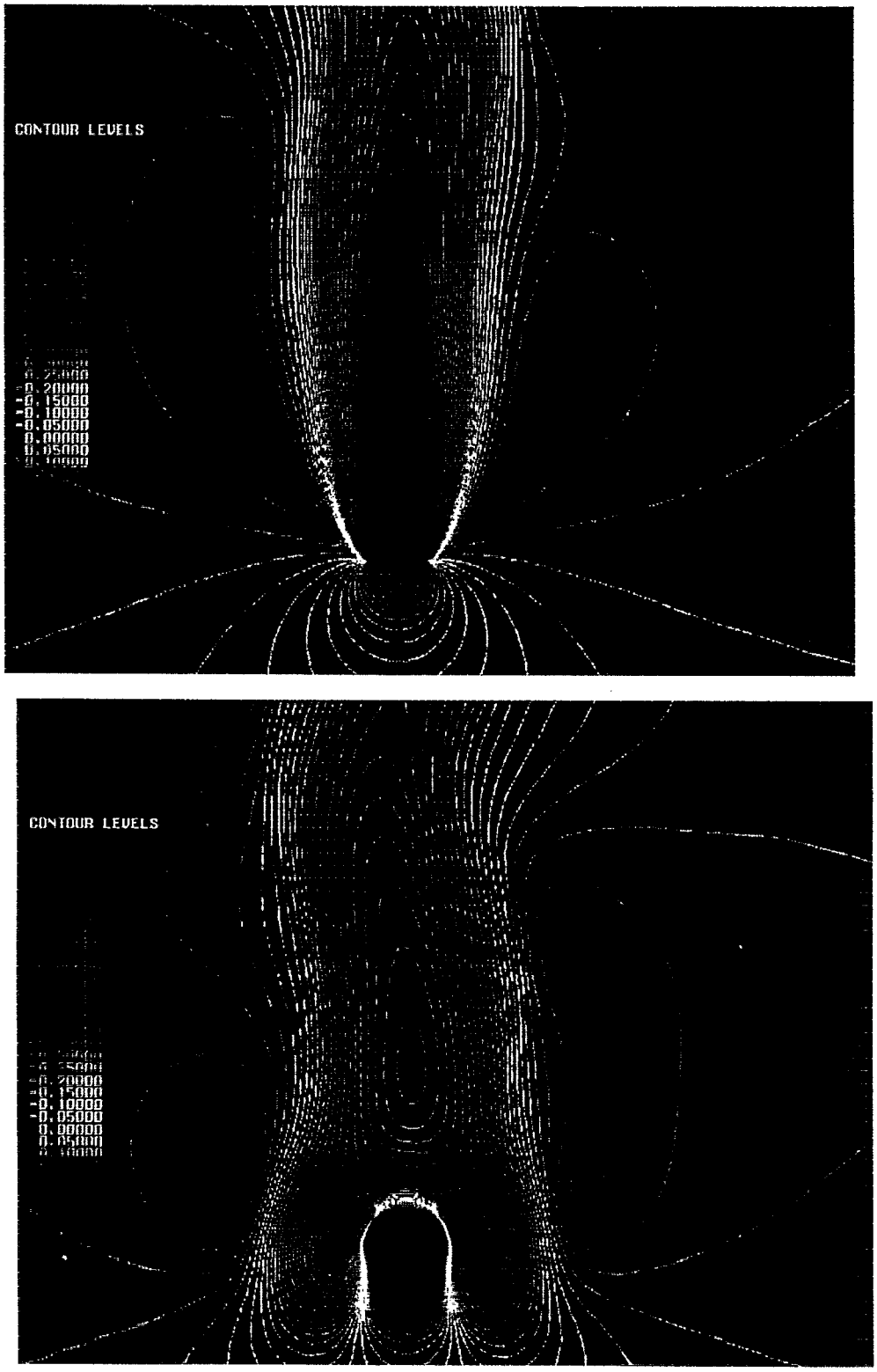

Fig. 18 — Contours of vertical velocity for initial certification studies (see text for explanation)

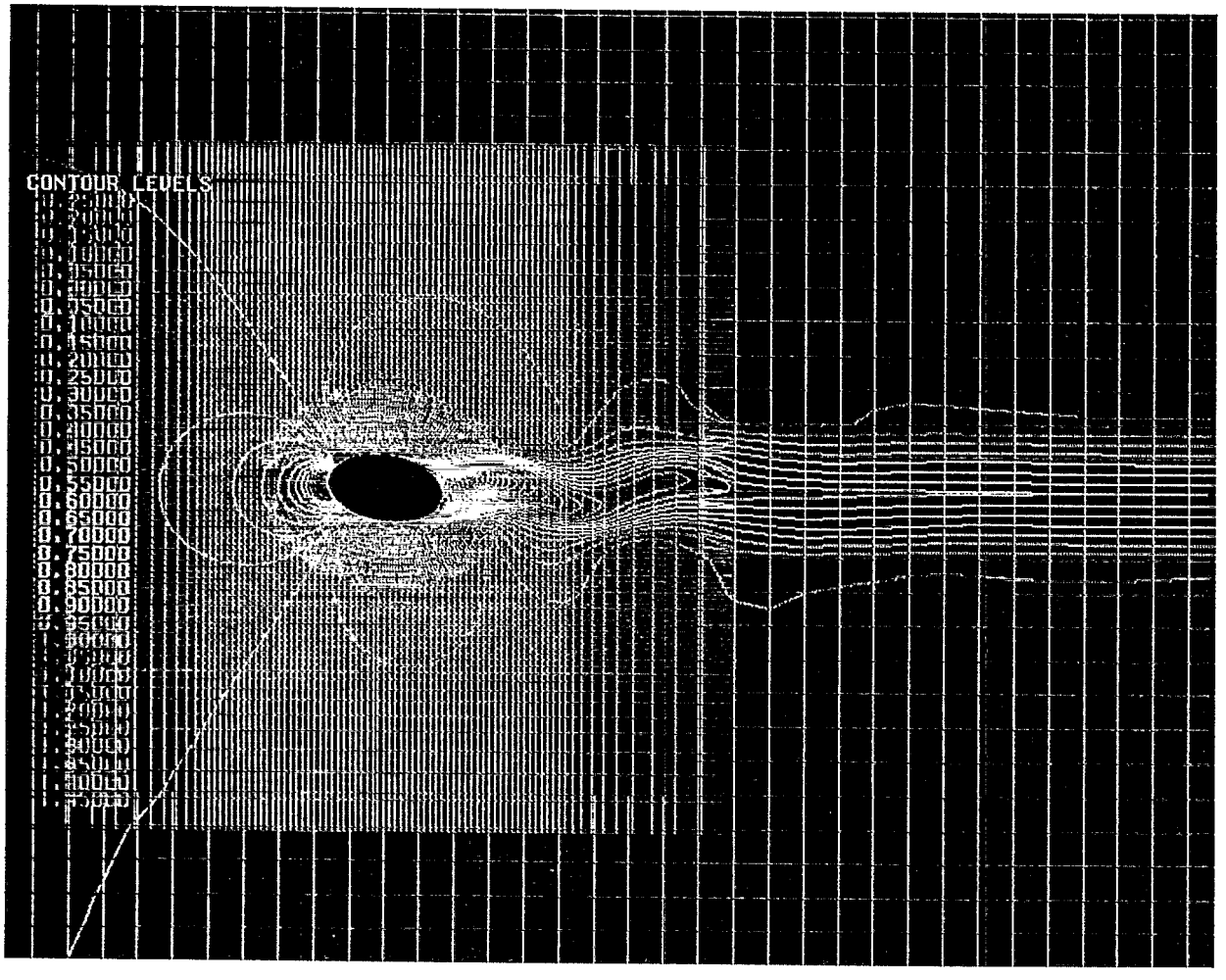

Fig. 19 — Manchester 6 to 10 ellipse at 10 deg angle of attack

of attack, and indicates how severe the unsteadiness really is. The amplitude of the lift and drag oscillations are on the order of magnitude of their respective means.

Finally, Fig. 21 shows the FANS predictions compared to Manchester's experiments. Unfortunately, the experimenters did not report the exact procedure used to obtain the reported force coefficients, so it has been assumed they were aware of the unsteadiness and chose to report the mean. The lines labeled "FANS" report the mean of the computational data. Although FANS has performed fairly well in previous force validation studies, the comparison here is poor at best. Only at 0° angle of attack is the comparison satisfactory—higher angles show that FANS is severely underpredicting both lift and drag. The cause of this discrepancy is still being investigated, with the first task being to more completely understand the Manchester test setup. In particular, an attempt is being made to ascertain which aspect of the unsteady forces were reported, how the nondimensionalization was performed, and whether or not wind tunnel blockage effects could be important.

3.2.2.1.6 Free-Fall — The final task undertaken during FY96 was a FANS simulation for free-falling GFCs where body motion is computed as part of the solution. In this simulation, FANS is used to compute the flow and resulting forces on the GFC, and Eqs. 1, 2, and 3 are integrated to update the GFC velocity and position. After each update, the grid is regenerated and the process

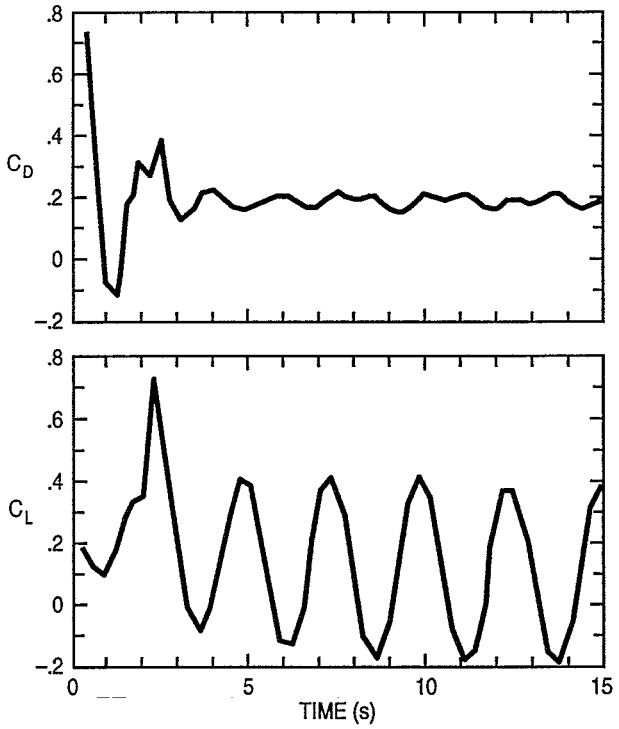

C_D = drag coefficient

$$= \frac{2 - D \text{ drag force}}{\frac{1}{2} \times \rho \times U^2 \times L}$$

where L = major diameter of ellipse

U = terminal velocity (15 ft/s for this case)

C_L = lift coefficient

$$= \frac{2 - D \text{ lift force}}{\frac{1}{2} \times \rho \times U^2 \times L}$$

Fig. 20 — Forces on Manchester 6 to 10 ellipse at 10 deg angle of attack, where C_D is the drag coefficient and C_L is the lift coefficient

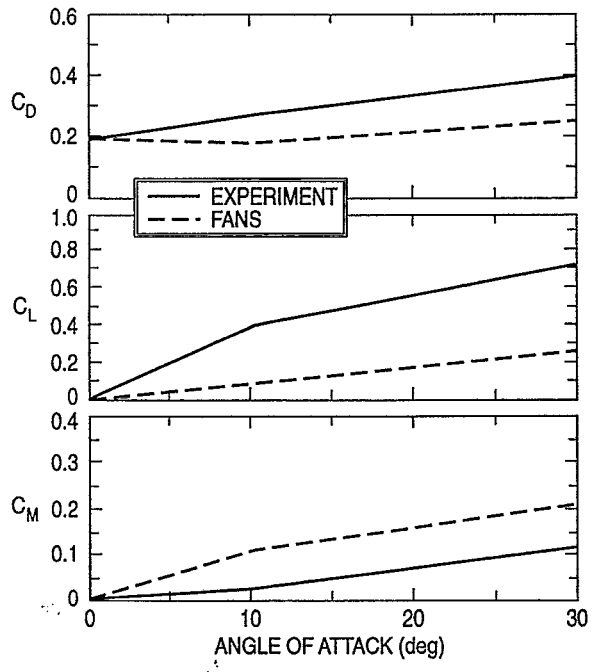

C_M = moment coefficient

$$= \frac{2 - D \text{ moment}}{\frac{1}{2} \times \rho \times U^2 \times L^2}$$

Fig. 20 — Forces for Manchester 6 to 10 ellipse vs. angle of attack compared to experiment

repeated. Since experiments at the WES have indicated that GFC shape is fairly constant and fairly elliptical, it was decided to use a 6 to 10 ellipse to represent the idealized GFC. A further advantage of this decision is that the Manchester steady-state ellipse data could be used as a "sanity" check.

The simulation was performed using a GFC of 12.5-m beam and 7.5-m depth. Its density was assumed uniform at 1.7 Mg/m^3. The initial attitude of the GFC was $x = y = 0$ with zero roll angle, and its initial horizontal, vertical, and roll velocities were specified as 0.3 m/s, 0 m/s, and 0 rad/s, respectively. The test domain was limited to a section of ocean 300 m wide and 300 m deep to keep CPU times at reasonable levels. The computation was nondimensionalized using a characteristic length of 12.5 m and characteristic velocity of 4.6 m/s.

The grid contained about 80,000 points in four blocks, and 10,000 time steps were used to complete the 36-s long drop time. Records of velocity and pressure were kept for every 40th time step for a total archive size of 209 megabytes. Movies were generated for pressure, vertical component of velocity, and vorticity. Two frames from the movie, one 10 s into the drop and one 30 s into the drop, are shown in Fig. 22. As before, the unsteady wake expected from the von Karman vortex street is visible, but this time the asymmetric forces cause the body to pitch and translate horizontally. The 30-s frame shows that the GFC leaves behind some significant "down-drafts" as it cycles through its periodic horizontal motion.

Histories of the GFC's motion are given in Figs. 23, 24, 25, and 26. Each history is plotted with its dependent variable on the x-axis and depth on the y-axis. This format allows the histories to be viewed as a function of depth as the GFC drops from the surface. The FANS forces are all encompassing, and include viscous, vortical, and pressure-induced effects.

Figure 23 presents histories of horizontal translation and rotation, which can be thought of as x vs. y trajectories and roll vs. depth histories, respectively. For the stated initial condition, FANS predicts a horizontal translation of 30 m to the left (the initial horizontal velocity was to the right). The FANS simulation shows roll as much as plus or minus 40°.

Figure 24 presents histories of horizontal and vertical velocities. As expected from its large horizontal translations, the FANS simulation predicts large horizontal velocities. Terminal velocities in the 9 m/s range (on average) are predicted.

Figures 25 and 26 show depth histories of horizontal force, vertical force, and roll moment, respectively. The high-frequency oscillations seen about halfway down were caused by a "near instability" with the numerics and was eliminated by reducing the time step for the latter half of the GFC's trajectory. The problem was noticed and corrected early enough that it is believed not to have affected the reliability of the overall results. The final result shown in Fig. 26 is the time vs. depth plot.

3.2.2.2 Closed-Form Solution for Simplified Shape for Free-Falling GFC

3.2.2.2.1 Introduction — To better understand results being produced by the Finite Element Modeling approach, the free-fall problem was approached in parallel with closed-form solution techniques.

The conceptual model for a dredged, material-filled GFC is a fluid-filled membrane that has a shape determined by the local balances of hydrodynamic, hydrostatic, and membrane forces. The "real" case should take account of local force balances at all points on the container and the variability

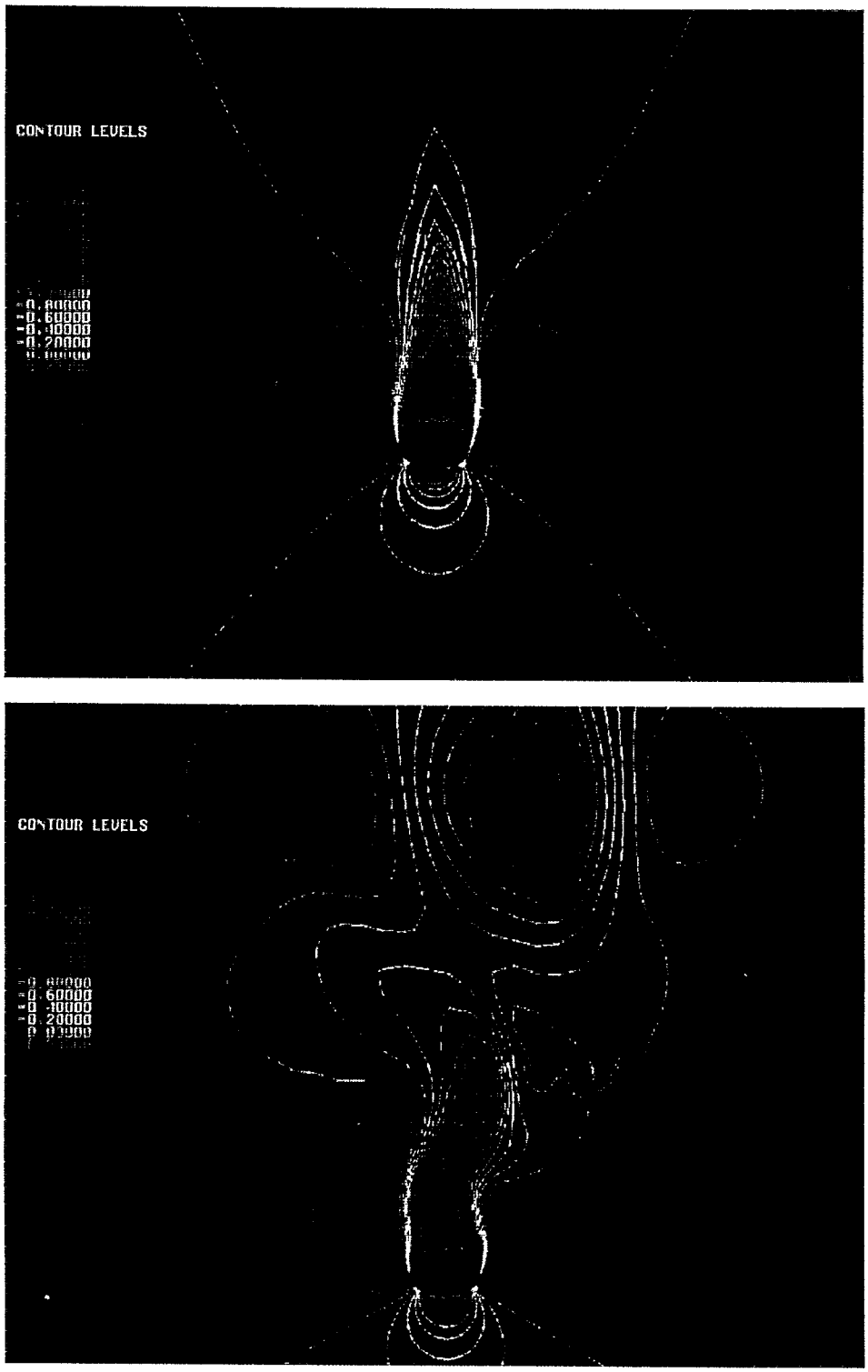

Fig. 22 — Contours of vertical velocity during free drop of rigid GFC model (see text for explanation)

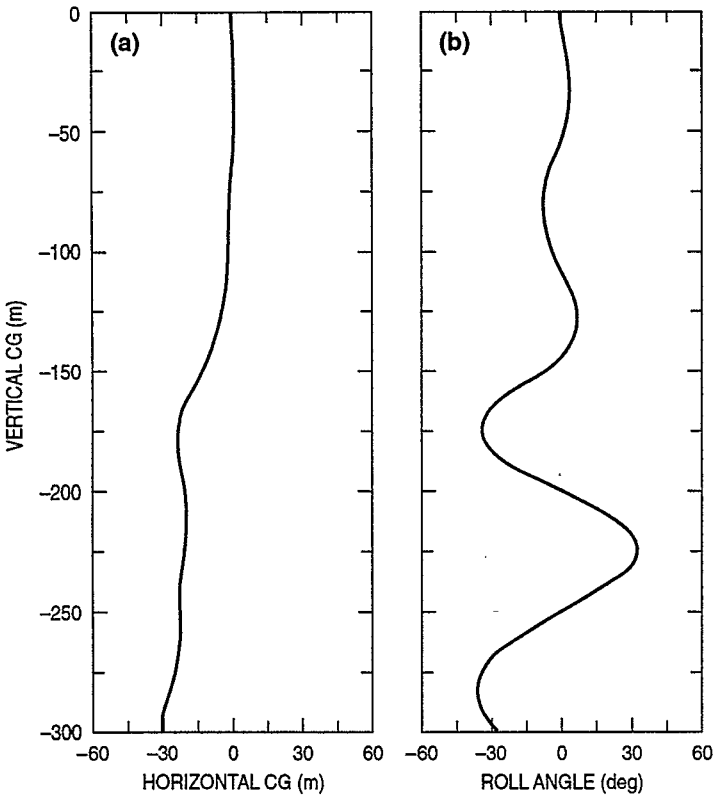

Fig. 23 — Predicted trajectories and roll angles for rigid GFC in free-fall, (a) lateral trajectory and (b) roll history

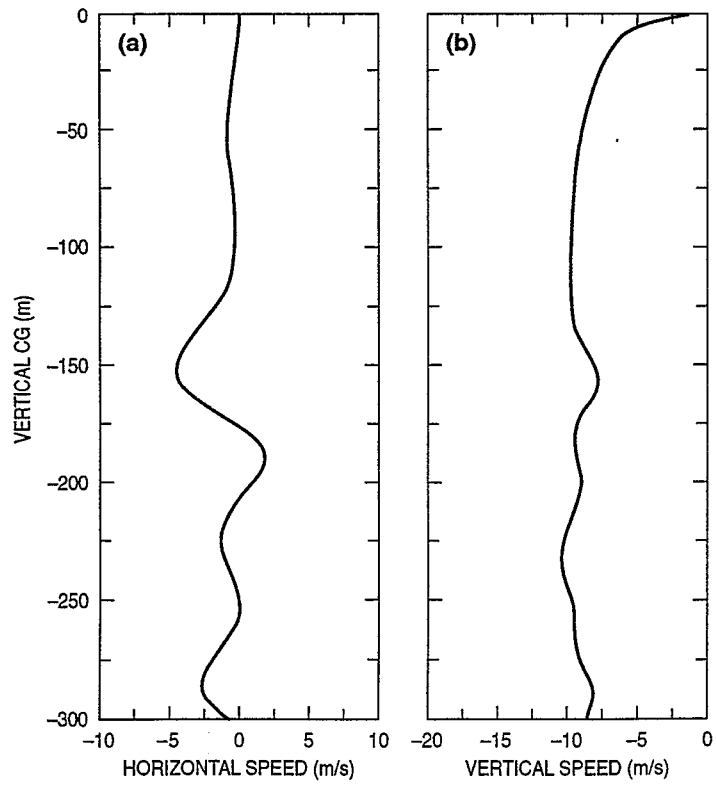

Fig. 24 — Predicted horizontal and vertical velocities for rigid GFC in free-fall, (a) lateral and (b) vertical velocity

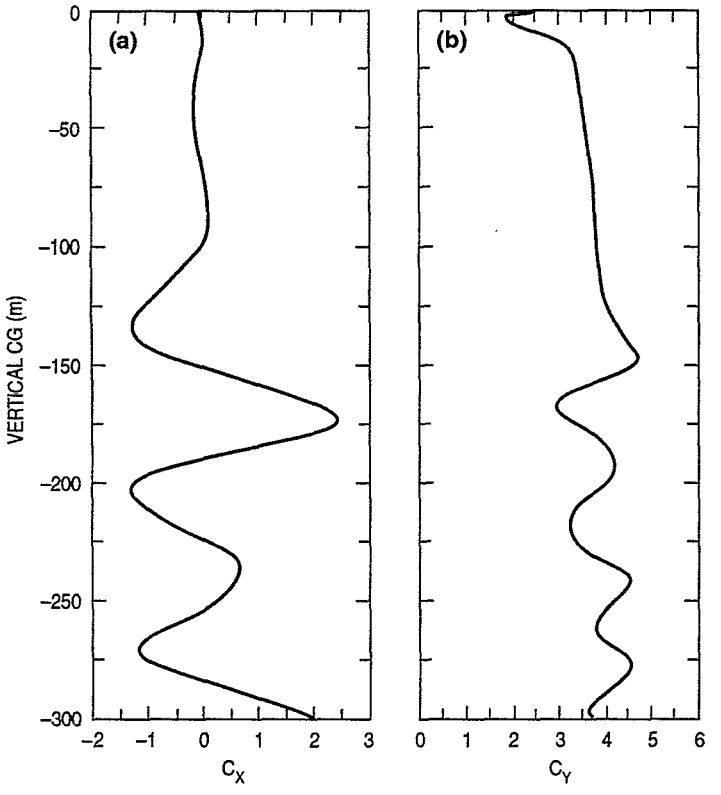

Fig. 25 — Predicted horizontal and vertical forces for rigid GFC in free-fall, (a) lateral and (b) vertical force

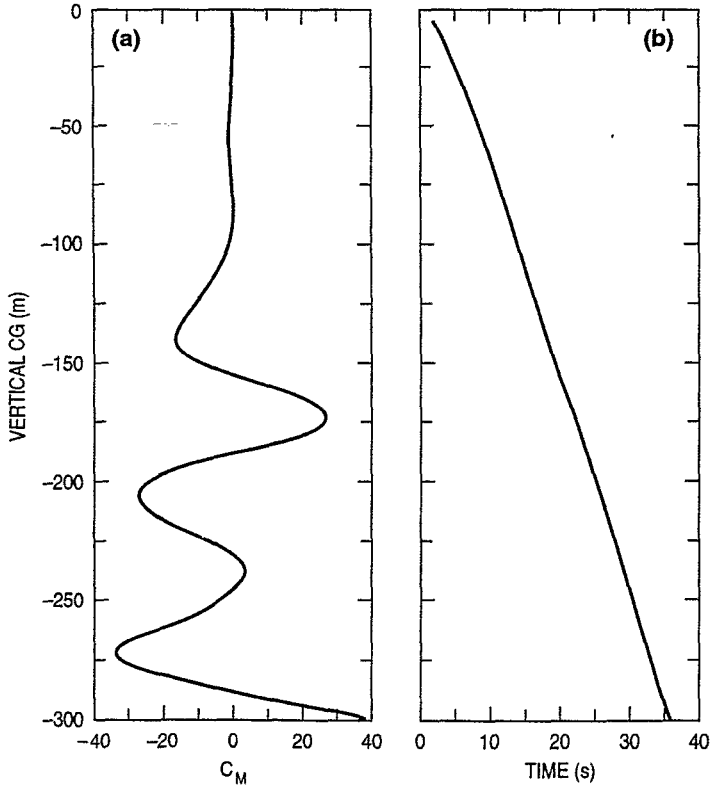

Fig. 26 — Predicted roll moments and drop times for rigid GFC in free-fall, (a) roll moment and (b) drop time

of these balances due to deformation of the container by fluctuations in the turbulent wake. The pressure at the bottom flow separation zone will tend to flatten the container, and the shape will be roughly ellipsoidal if there is sufficient membrane stress to keep the interior fluid mass intact. Further, it is known that the hydrodynamic pressure must equal the ambient far-field value somewhere between the base of the container and its trailing edge. The most basic assumption in this model is that the shape is an oblate ellipsoid; this is an approximation of what we may expect to be the equilibrium shape of the GFC.

3.2.2.2.2 The Model for the Equilibrium Shape of the Ellipsoid — The following analysis is based on the assumption that the fluid-filled flexible container is constrained to the shape of an oblate ellipsoid that is deformed by the hydrostatic forces. Measurements of the pressure distributions around oblate ellipsoidal bodies at high Reynolds numbers and terminal fall speed show that the pressure is near the far-field ambient value in the vicinity of the equator. For the case of a fluid-filled membrane, this allows an additional assumption: the hydrostatic force and intrinsic pressure force are balanced by a membrane tension force evaluated at the equator. In the observed cases of low Bond number, fluid-filled bodies are flattened, or concave downward, and are not symmetric about the equatorial plane. These surfaces would be described in terms of variables at somewhat higher degrees than quartics; however, their thickness-to-width ratios are similar to oblate ellipsoids. The intrinsic pressure is the residual pressure inside the container if there is no hydrostatic pressure, i.e., $\frac{2\sigma}{a_0}$. The total balance is assumed to be:

$$\sigma\left(\frac{1}{R_1}+\frac{1}{R_2}\right)=\frac{2\sigma}{a_0}+\left(1-\frac{\rho_w}{\rho_c}\right)g\,b\,. \tag{16}$$

For the general case of a surface of revolution, Eq. 16 would be expressed as a nonlinear differential equation:

$$\sigma\left(\frac{\frac{\partial^2}{\partial r^2}\phi}{\left(1+\left(\frac{\partial}{\partial r}\phi\right)^2\right)^{\left(\frac{3}{2}\right)}}+\frac{\frac{\partial}{\partial r}\phi}{r\left(1+\left(\frac{\partial}{\partial r}\phi\right)^2\right)^{\left(\frac{1}{2}\right)}}\right)=\frac{2\sigma}{a_0}+\rho_c\left(1-\frac{\rho_w}{\rho_c}\right)g\,\phi\,, \tag{16a}$$

where σ is the membrane tension parameter, g is gravity, $R_{1,2}$ are the principal radii of curvature, a_0 is the radius of a sphere with volume equal to the ellipsoid, $\rho_{w,\,c}$ are the density of water (w) and the container (c), and b is the semi-minor axis of the ellipsoid. In Eq. 16a, ϕ is a function of (r), the distance from the axis of symmetry. Equation 16a would be the appropriate model for the GFC shape when it is settled on the bottom. We take the more rudimentary assumption that the shape is a simple quartic surface. At the equator of the ellipsoid, $R_1 = a\ b^{(-2)}$ and $R_2 = a^{(-1)}$. The following analysis is aided by transforming the ellipsoid parameters in terms of a spheroid of equivalent volume:

$$\frac{4\pi a_0^3}{3}=\frac{4\pi a^2 b}{3}\,. \tag{17}$$

The new parameter is the relative difference equatorial of the cross-section areas of the equivalent sphere and the ellipsoid that is defined as $\eta = 1 - \frac{a_0^2}{a^2}$.

The equatorial force balance (Eq. (16)) in terms of the tranformed variables is:

$$B\,(1-\eta)^3 + 2\,(1-\eta)^2 - (1-\eta)^{5/2} - \frac{1}{\sqrt{1-\eta}} = 0\,. \tag{18}$$

The Bond Number (B) scales the internal hydrostatic pressure to wall tensile stress:

$$B = \sigma^{(-1)}\left(1 - \frac{\rho_w}{\rho_c}\right)\rho_c\, g\, a_0^2\,. \tag{19}$$

Next, Eq. 18 is expanded through $O(\eta^4)$ in a "small B" (B < ~100) assumption. **Note that for B > 200, primary balance of force is maintained by the first curvature** ($ab^{(-2)}$); for B > 200, $\frac{a}{a_0} \sim B^{\left(\frac{1}{7}\right)}$. For 0 =< B < ~200 the following equation gives a good approximation of Eq. (18):

$$B + (-3\,B - 2)\,\eta + \left(-\frac{1}{4} + 3\,B\right)\eta^2 - B\,\eta^3 - \frac{15}{64}\,\eta^4\,. \tag{20}$$

This quartic equation has only one positive real root:

$$\eta = -\frac{16}{15}B - \frac{1}{15}\sqrt{2}\,\sqrt{\%2} + \frac{1}{15}\sqrt{2}\,((256\,B^2\%1^{1/3}\sqrt{\%2} - 40\,\%1^{1/3}\sqrt{\%2} + 480\,B\,\%1^{1/3}\sqrt{\%2} \tag{21}$$

$$- 5\sqrt{\%2}\,\%1^{2/3} + 3300\,\sqrt{\%2}\,B - 20\,\sqrt{\%2} + 2220\,\sqrt{2}\,\%1^{1/3}\,B + 5760\,\sqrt{2}\,\%1^{1/3}\,B^2$$

$$+ 1800\,\sqrt{2}\,\%1^{1/3} + 2048\,\sqrt{2}\,\%1^{1/3}\,B^3)\,/\,(\%1^{1/3}\sqrt{\%2})^{1/2}\,,\ \text{with}$$

$$\%1 := 17172\,B^2 + 19080\,B + 6488$$

$$+ 12\sqrt{6547080\,B^3 + 4039188\,B^2 + 179540\,B + 292320 + 2047761\,B^4}$$

$$\%2 := \frac{128\,B^2\,\%1^{1/3} - 20\,\%1^{1/3} + 240\,B\,\%1^{1/3} + 5\,\%1^{2/3} - 3300\,B + 20}{\%1^{1/3}}$$

Figure 27 shows that the equatorial cross-section area of the ellipsoid increases relative to the equivalent sphere as a function of the hydrostatic force relative to the membrane tension, *the Bond number.* Figure 28 illustrates change of semi-minor/semi-major axis ratio as a function of Bond no. $B = \sigma^{(-1)}\left(1 - \frac{\rho_w}{\rho_c}\right)\rho_c\, g\, a_0^2$; Fig. 29 is a set of superimposed ellipses that represent the

meridional cross-sections of ellipsoids for the cases B = 0, 1, 2, 3, 4, 10, 150. The flattening of the ellipsoid increases the surface area and decreases height so that the internal hydrostatic pressure is balanced by the wall tension.

The formula for the ratio of the surface area of the deformed oblate ellipsoid to the area of a sphere of equivalent volume is:

$$sarf := \frac{1}{2}\frac{1}{1-\eta} + \frac{1}{4}\frac{(1-\eta)^2 \ln\left(\frac{1+\sqrt{3\eta-3\eta^2+\eta^3}}{1-\sqrt{3\eta-3\eta^2+\eta^3}}\right)}{\sqrt{3\eta-3\eta^2+\eta^3}} . \tag{22}$$

Figure 30 shows that the surface area of the ellipsoid must increase relative to a sphere of equivalent volume when the hydrostatic force increases relative to the membrane tension force (Bond number increases).

3.2.2.2.3 Terminal Fall Speed — The terminal fall speed of the container depends on its shape, volume, density relative to the water, and the ambient turbulence. For an oblate ellipsoid with axis of symmetry along the vertical equilibrium fall line, the terminal fall speed is:

$$W = \sqrt{\frac{8(\rho_c - \rho_w) g b}{3\rho_w C_D}} , \tag{23}$$

where C_D is the drag coefficient. Alternatively:

$$W = \sqrt{8\frac{\sigma B(1-\varepsilon)}{3\rho_w a_0 C_D}} , \tag{24}$$

which embodies the dependence of the thickness of the ellipsoid on the Bond number. For the assumed values of the parameters, $-\frac{\rho_w}{\rho_c} = 1.36$, $C_D = 0.67$,

$$W := \frac{2}{3}\sqrt{6}\sqrt{\frac{\sigma B(1-\varepsilon)}{\rho_w a_0 C_D}} \tag{25}$$

Figures 31 and 32 present terminal fall speed predictions for containers holding material of bulk wet density 1.4 and 1.7 Mg/m^3, respectively. Figure 33 presents a plot of speed difference for the two bulk wet densities.

3.2.2.2.4 Vortex Shedding — When a bluff body moves through a fluid rapidly enough that purely viscous forces are not significant (large Reynolds Number, Re = (*Length Scale of Body* × *Velocity through the Fluid/Kinematic Viscosity*), the wake becomes unstable and a stream of vortices are shed behind the body. The rate of vortex shedding is represented by the Strouhal Number (S). Considerable data exist about the shedding frequencies behind a variety of rigid body shapes, but there is no comprehensive analytical (or numerical) models that can accurately approximate the

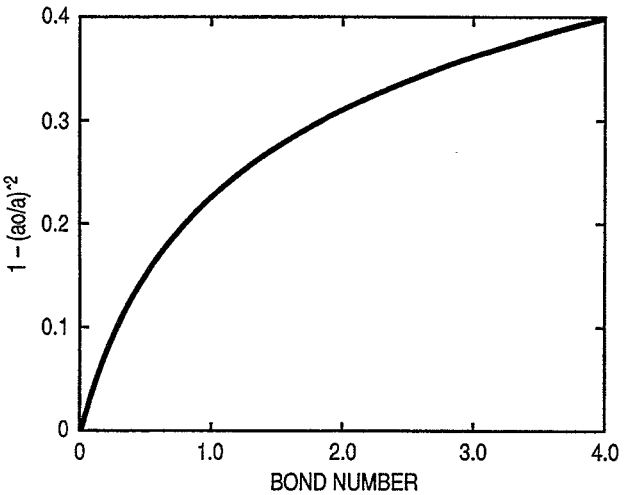

Fig. 27 — Relative equatorial area of ellipsoid as a function of Bond number

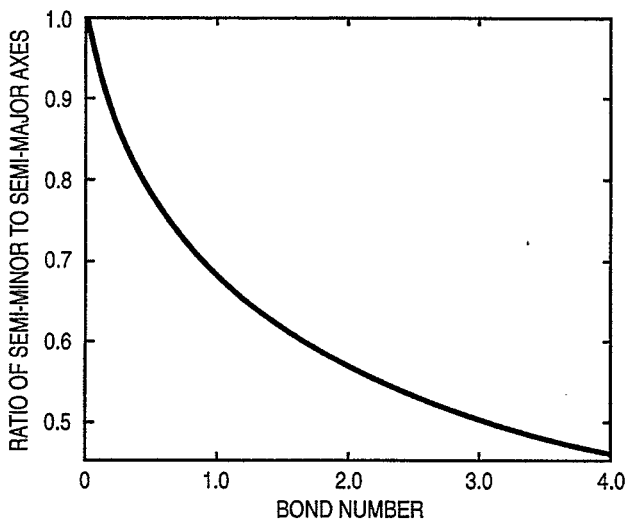

Fig. 28 — Variation of semi-minor/semi-major axes as a function of Bond number

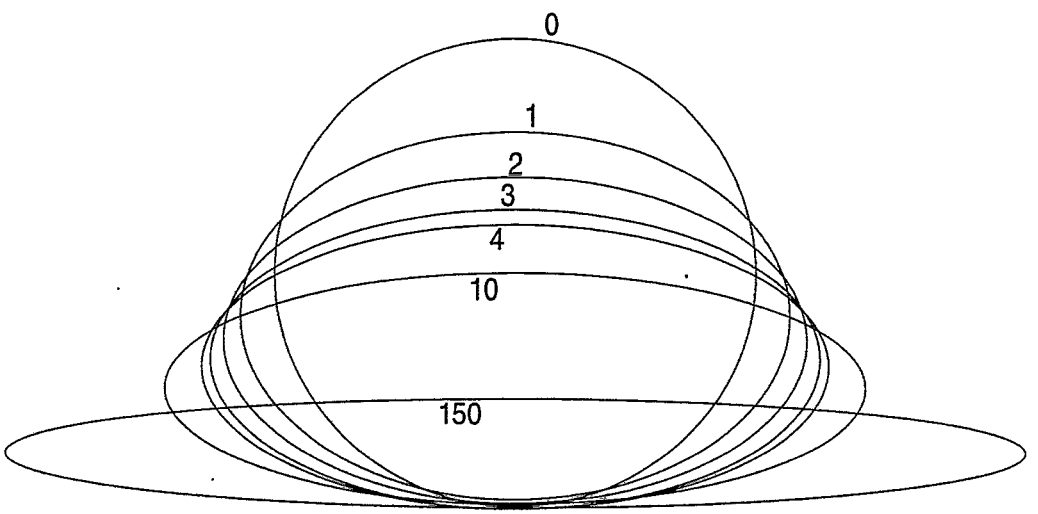

Fig. 29 — Shape of the ellipsoid with increasing Bond number 0, 1, 2, 3, 4, 10, 150

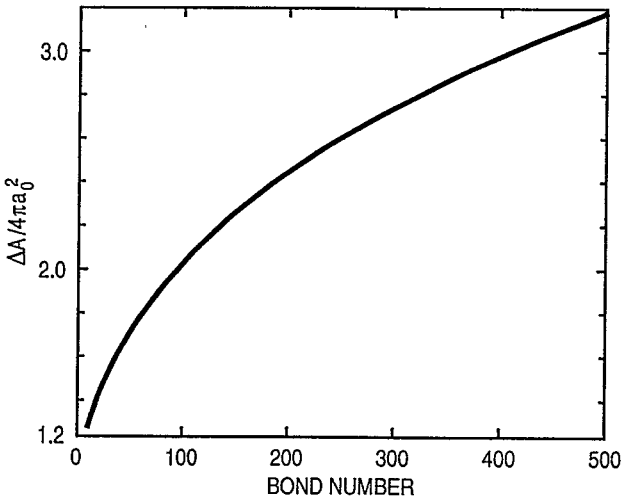

Fig. 30 — Relative change of total surface of the oblate spheroid with respect to a sphere of equal volume as function of Bond number

dynamics for arbitrary body forms. Therefore, the compilation of empirical results in *Fluid Dynamic Drag* by S. F. Hoerner (1965) is used here.

The Strouhal Number is a measure of the vortex shedding rate relative to the rate at which a fluid parcel traverses the length of the body. It is represented by:

$$S = \frac{f h}{W}, \tag{26}$$

where f is the shedding frequency and h is the "thickness" of the body along the direction of the ambient flow that has speed, W. For a massive body, such as the fluid-filled container, the Reynolds number is $O(10^6)$; consequently, it is in a flow regime in which the empirical results are stable. Hoerner (1965) found that the following formula gave consistent results:

$$\frac{f h}{W} = 0.2\, C_d^{\left(-\frac{3}{4}\right)} \quad . \tag{27}$$

From the present analysis, $h = 2\,b$ and W can be furnished by the terminal fall speed formula, i.e.,

$$\frac{f\,2b}{\sqrt{\dfrac{8\left(1-\dfrac{\rho_w}{\rho_c}\right) g\, b}{3C_D}}} \sim 0.2\, C_d^{\left(-\frac{3}{4}\right)} \tag{28}$$

Solving for f, $f = \dfrac{0.16\left(g\left(1-\dfrac{\rho_w}{\rho_c}\right)\right)^{\left(\frac{1}{2}\right)}}{b^{\left(\frac{1}{2}\right)} C_d^{\left(\frac{5}{4}\right)}}$.

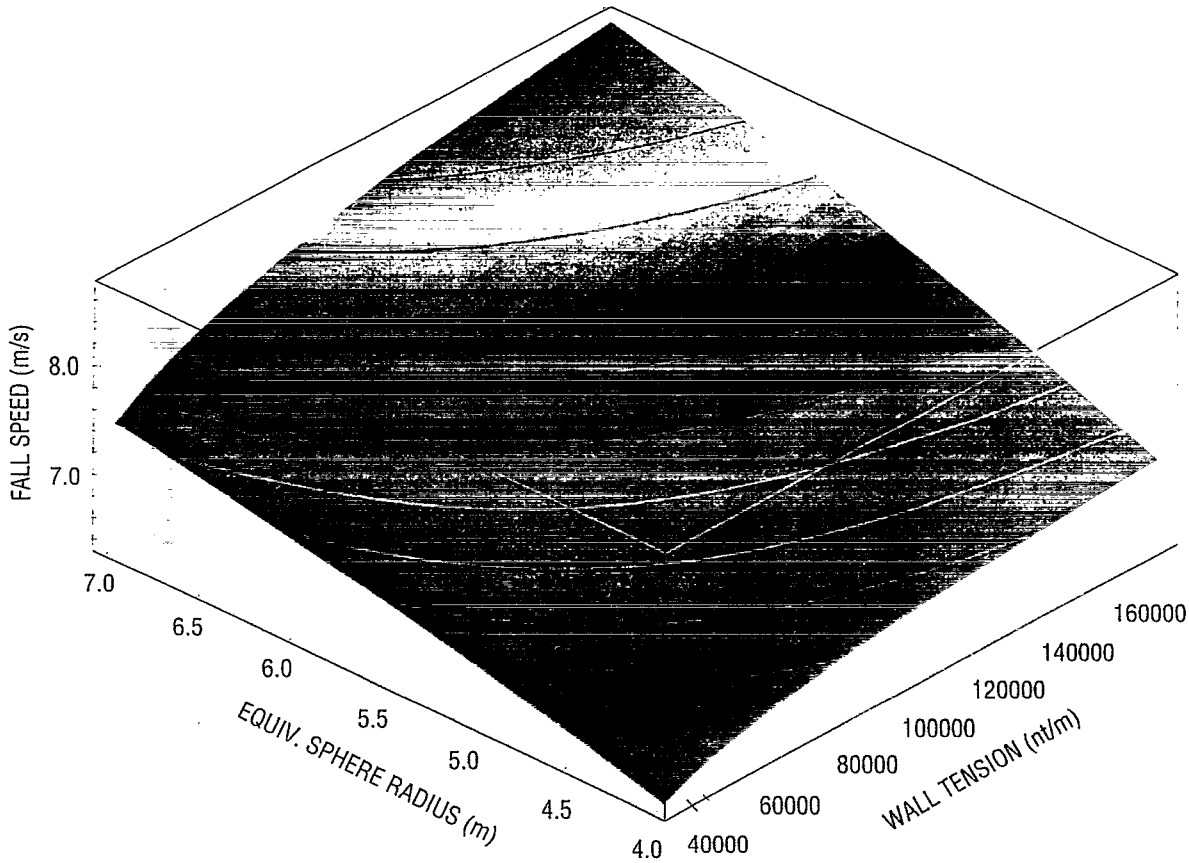

Fig 31 — Terminal fall speed vs. equivalent radius and bag tension with container density = 1.4 Mg/m^3

Assuming that $C_D = 0.67$, $g = 9.8 \frac{m}{\sec^2}$ and $\frac{\rho_w}{\rho_c} = 0.73$, the shedding frequency can be estimated as a function of Bond number:

$$f = 0.16 \frac{\sqrt{g\left(1 - \frac{\rho_w}{\rho_c}\right)}}{\sqrt{b} C_d^{5/4}}, \tag{29}$$

where $b = a_0 (1 - \eta)$ and with η defined in Eq. (21).

This yields a closed-form solution for the shedding frequency in terms of Bond number, but additional substitutions are needed to obtain the function in terms of GFC wall tension and equivalent spherical radius.

The results of the combination of Hoerner's empirical model with the hydrostatically deformed ellipsoid and terminal fall speed models are self-consistent. The interpretation is simple: (1) the higher the Bond number, the flatter the ellipsoid; (2) the flatter the ellipsoid, the slower it falls; and (3) shedding frequencies from low-tension, smaller ellipsoids are higher than larger, stiffer ones.

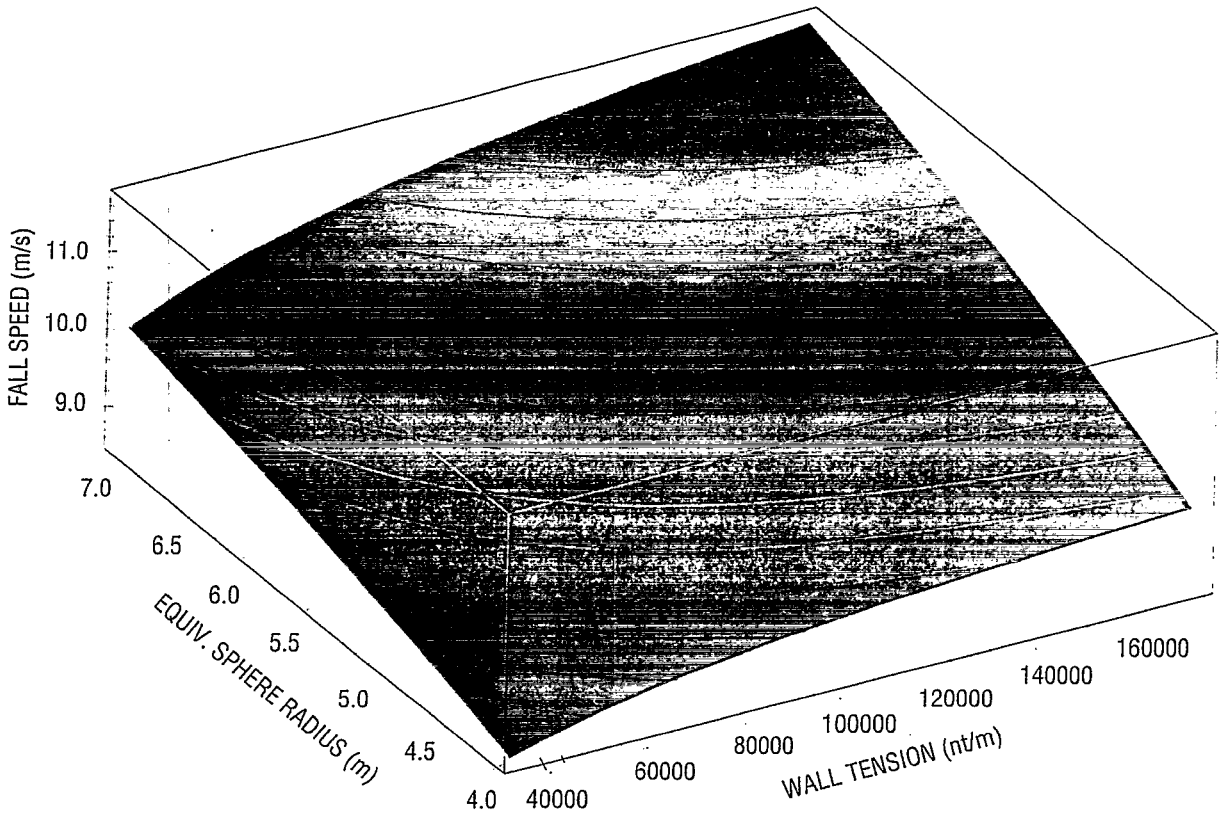

Fig 32 — Terminal fall speed vs. equivalent radius and bag tension with container density = 1.7 Mg/m^3

The shedding frequencies range from about 0.2 Hz for a small (4.8 m equivalent radius), lower density (1.4 Mg/m^3), less stiff (800 Nt/m) tension bag to 0.32 Hz with the flaccid, smaller bag with higher density (Figs. 34, 35, and 36).

These models do not take into account the fact that the dynamics of the flow will distort the container into non-symmetrical shapes and that these deformations may drastically affect the flight trajectory of the body. Fortunately, if the GFCs are flaccid, off-axis hydrodynamic lift will tend to redistribute the materials in the GFC. Modal oscillations are expected to have lower frequencies than the shedding frequency, so resonances would be unlikely. If the GFC is too flaccid (very high Bond number), it will not be able to maintain a predictable form, since the restoring force of wall tension will be ineffective. Twisted or isolated lobe shapes could result. In such cases, local stresses could rupture or tear the GFC, particularly at the time of bottom impact.

3.2.2.2.5 Discussion — This analysis has been based on empirical formulae, an axi-symmetric body shape and an approximation of wall, and dynamic and hydrostatic balance at a single latitude. The differential geometry of the system, even in this simplified case, produced highly nonlinear expressions that had to be approximated. However, the model does yield results, that appear to be reasonable. These models do not take into account the fact that the dynamics of the flow will distort the container into non-symmetrical shapes and that these deformations may drastically effect the flight trajectory of the body. Fortunately, the GFCs will not be too flaccid; consequently, non-symmetric,

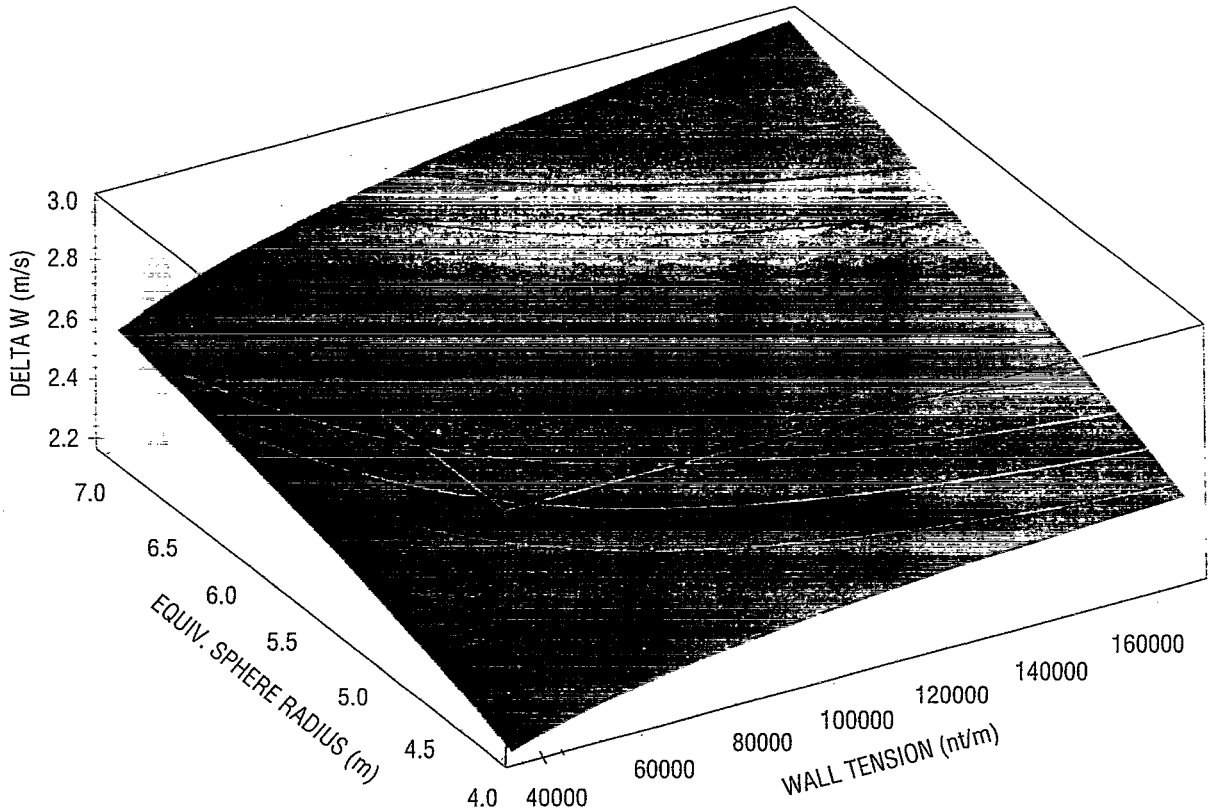

Fig 33 — Difference in fall speed (W (1.7 Mg/m^3) – W (1.4 Mg/m^3)) vs. equivalent radius and bag tension

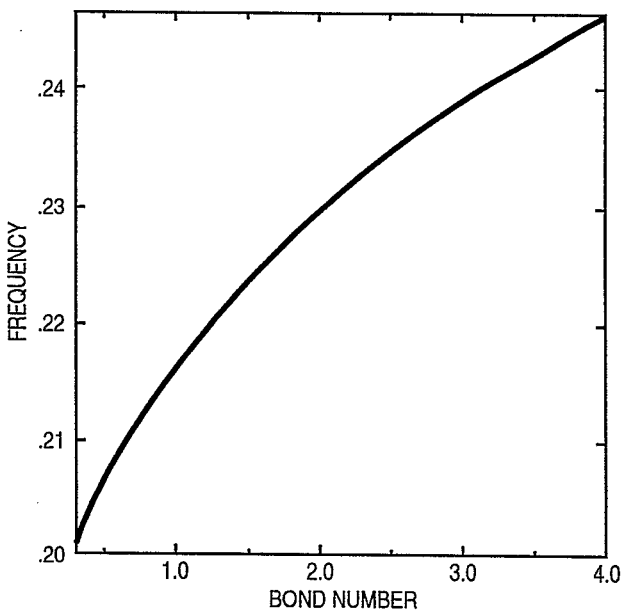

Fig 34 — Shedding frequency (1/s) with ao = 5 m, density = 1.4 Mg/m^3

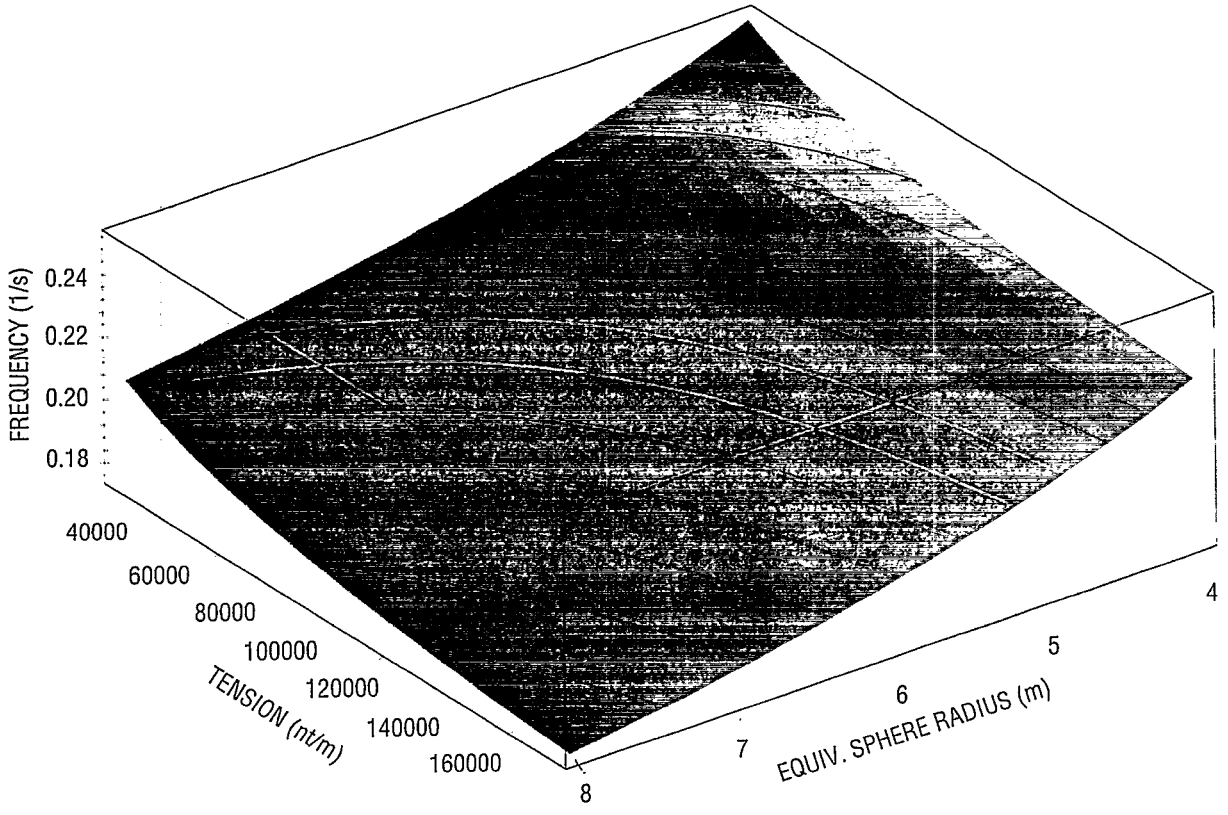

Fig 35 — Shedding frequency vs. equivalent sphere radius (m) and wall tension (Nt/m) drag coefficient 67, density 1.4 Mg/m^3

off-axis hydrodynamic lift will tend to be redistributed by shifting of the materials in the GFC, wall tension, and hydrostatic forces.

3.2.2.2.5.1 Shape and stability. In this model, the Bond number is the critical parameter in determining the shapes of the GFCs. If equivalent spherical radii are in the range 4–7 m, with the container density 1.4 Mg/m^3 – 1.7 Mg/m^3, then the Bond numbers will be ~0.33–3.69. Over that range of *B*, the axis ratio of the ellipsoid decreases from ~5/6 to ~1/2. The lower values of *B* indicate a relatively "tight form" but the upper extreme values could be marginal for wake-induced shape instabilities. The turbulent wake will (1) disturb the internal static balance, which will (2) lead to internal mass redistribution and shape change that will (3) modify the flow regime around the GFC, *et ad terminus*. Modal oscillations of the container should be computed and compared with the shedding frequency so that resonances could be anticipated and avoided. (This is currently a low priority, since it is expected that the normal modes of the containers will have lower frequencies than the vortex shedding.)

If the GFC is too flaccid (very high Bond number), it will not be able to maintain a predictable form, since the restoring force of wall tension will be ineffective. Twisted or isolated lobe shapes could result. In such cases, local stresses could tear the GFC particularly at the time of bottom impact. The GFCs may have tendencies to glide laterally due to lift forces that will occur when the GFC shape is severely non-axisymmetric, but internal redistribution of mass should minimize

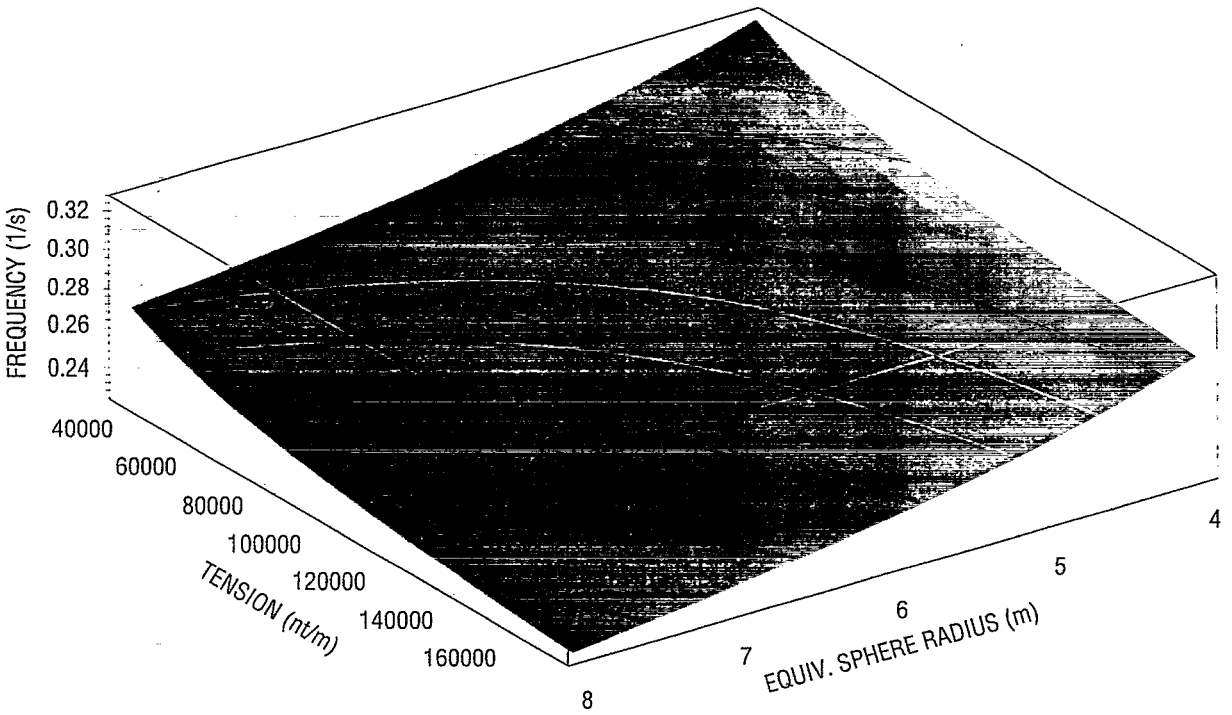

Fig 36 — Shedding frequency vs. equivalent sphere radius (m) and wall tension (Nt/m) drag coefficient 67, density 1.7 Mg/m^3

the glide in a given direction. If very large deformations occur, high stresses on the wall material may rupture the container.

3.2.2.2.5.2 Fall speed predictions. For the projected container densities, volumes, and wall materials, the balances of hydrodynamic, wall tension, and hydrostatic forces will produce shapes that are more oval than those included in numerical simulations to date. The Reynolds number $Re = \frac{DW}{v}$ (where D is the bag diameter, W is the fall speed, and v the kinematic viscosity) is the critical parameter in estimating the hydrodynamic drag on the GFC. For the conditions assumed so far, the $Re \sim 10^7$; this is in the super-critical regime of flow, at which the flow separation of the boundary layer and wake from the body stabilizes and the drag coefficient (C_D) also stabilizes at a near-constant value for a given shape (note Hoerner 3–11). Measurements of the pressure directly aft of bodies in super-critical flow appear to agree with potential flow computations according to Hoerner. For a sphere in the super-critical regime, C_D is ~0.2 and for a thin disk ~1.17 @ $\frac{b}{a} \sim 0.05$. Assuming that the C_D in the super-critical range of R is a linear function of $\frac{b}{a}$, then $C_D = 1.17 - 0.97\,\frac{b}{a}$. This approximation allows estimation of C_D as a function of B.

It is particularly important to note that for $B \sim 0.33$, the C_D is about half of nominal value of 0.67 used in Figs. 29–31. The 0.67 value was derived for the case in which the hydrostatic pressure at the base is exactly balanced by the dynamic pressure of the flow. Under the current approximation

$C_D \sim 0.67$, when $\frac{b}{a} \sim 0.52$, which corresponds to $B \sim 2.7$, a moderately small value that could easily be attained for the container volume/densities and wall tension, presently under consideration. At Bond numbers <10 the GFC shapes would have higher axis ratios and would have shapes that would be "rounder" with lower drag coefficients. However, if the GFCs are allowed to remain flat, without folding, the fall speed is smaller by roughly half and the bottom impact will be smaller. The C_D would be ~0.7 for the round body, but would be ~1.1 for the very flat GFCs.

3.2.2.2.5.3 Tradeoffs. At some stage, the costs/risks must be assessed for the GFC volume/surface, internal density, and structural materials properties. Accurate, high-resolution numerical hydrodynamic models of the GFC's interactions with the flow around it must be exercised enough to understand the extent to which these simple bulk dynamic models give reliable, robust results. Ultimately, laboratory tests that consistently represent the critical parameters should be executed before these containers are dropped 4000+ m into the ocean. A thorough study of the GFC dynamics was beyond the computer resources available for this project.

3.2.3 Close Approach to the Seafloor

The capability to interface the sediment disk model used within the Palmerton code with a CFD code such as RANS permits the flexibility to track the passage of individual sediment "particles" as well as the GFC shape and dynamics. Since the forces on the particles are no longer restricted to constant drag forces and currents, the individual sediment particles can be subjected to the hydrodynamic forces in the flow field and the drag on the particles can be adjusted to reflect the size and composition of the sediment particle. This capability was developed into a particle tracking code for the purpose of tracking the sediment plume generated upon impact as a dilute sediment suspension is lifted into the flow field about the impacting GFC.

Figure 37 illustrates the use of this code to visualize the paths of neutrally buoyant sediment particles using the computational results of a flow field from a RANS calculation. In this figure, the GFC position is shown at two different times. Ten particles had been seeded just below the GFC at different transverse locations. These locations, as measured from the GFC center line and non-dimensionalized by the GFC width, are: 0.1 to 0.6 in 0.1 increments and at 0.8, 1.0, 1.5 and 2.0. The particles away from the GFC have a tendency to move up and away initially. The particles that are in the path of the GFC, however, tend to move down and away from the bag. These particles tend to move downward with the GFC for a considerable distance downstream. This particle pattern compares favorably with the potential flow caused by a submerged sphere approaching a rigid wall (Milne-Thomson 1969).

3.2.4 Penetration/Embedment in the Seafloor

The seafloor at likely abyssal sites for dredged material isolation will be hemipelagic or pelagic clays with a thin surficial layer, 5–15 cm thick, of bioturbated sediments with a steeply increasing undrained shear strength profile with depth (Rocker 1985, Ch. 2). This surficial layer will be underlain by sediments with a profile of gradually decreasing water content and gradually increasing undrained shear strength (Rocker 1985, Figs. 2.2-4 thru 2.2-8). The impact on and penetration of the 400 m^3 of dredged material contained in the GFC will be resisted by the inertia of the seafloor sediment mass being displaced and by the undrained shear strength (dynamic undrained strength) along shear zones developed.

A predictive model for this impact/penetration phenomena is available (Rocker 1985, Ch. 8), but was not used and validated because effort was concentrated on the GFC release and free-fall

Fig. 37 — Particle trajectories about rigid GFC in free-fall

phenomena model validation. The penetration prediction model was developed for rigid objects penetrating into a seafloor of unconsolidated sediments, either cohesive (clays, silts, muds) or cohesionless (sands). The application of the technique/model to the description of penetration of a flexible (but incompressible), fluid-like, dredged material-filled bag would be considerably more involved than the method described in Rocker, to account for the deformation of the bag contents and associated redistribution of bag–seafloor contact pressures during penetration. The method in Rocker (1985, Ch. 8), accounts for decelerating forces due to the density difference between the penetrator and the media being displaced, the inertial forces generated in accelerating sediment during penetration, and the resistance of the sediment to shearing.

4.0 CONTAINER IMPACT-GENERATED TURBIDITY CURRENTS

by Frederick A. Bowles and Peter Fleischer

This section explores the potential for a turbidity current to be initiated by the impact of a waste-filled GFC with the seafloor. Such a turbidity current could potentially result in unintended dispersal of contaminants into the water column and over the bottom. To approach this concern, this section reviews the conditions that define the turbidity-current phenomenon.

A naturally occurring turbidity current is a gravity-driven, bottom-following density current laden with suspended sediment. Most workers recognize two principal types: high density and low density, with 1.1 Mg/m^3 being the approximate separation (Pickering et al. 1989).

A high-density turbidity current is a powerful, high-velocity flow that is capable of transporting all sizes of terrigenous sediment from shallow to deep water. Typically, it is a product of submarine slope failure and arises from a submarine slide, slump, or debris flow caused by loading of an oversteepened slope. Rapid sediment accumulation, an earthquake, or interaction of storm waves with the seafloor usually produces the loading. As it moves downslope, it becomes more fluid and turbulent by entrainment of water. Turbidity currents of this type are typically short-term events and are called surge flows. Speeds, inferred from largely indirect measurements, range from about 28 m/s on steep, upper continental slopes to about 2.5 m/s on the flat portions of basins (Kuenen 1952; Menard 1964; Ryan and Heezen 1965; Krause et al. 1970; Karlsrud and Edgers 1982; Piper and Savoye 1993). Kirwan et al. (1986) suggest that velocities between 20–25 m/s can be quickly generated on slopes of less than 1° given a sufficiently dramatic initiating event.

Low-density turbidity currents flow slowly (a few cm/s to about 0.3 m/s) and, thus, can transport only silt- and clay-sized material. Mud turbidity currents often evolve from high-density flows that have lost their coarse-grained component during transport. Alternatively, they can occur as density underflows (beneath less dense surface waters) resulting from the input of sediment-laden river water into a standing water body. Densities rarely exceed 1.05 Mg/m^3, and these turbidity currents typically correlate with density maxima in river inflow (Mulder and Syvitski 1995).

Einsele (1991) states that the slope failure of large sediment accumulations is probably the most important prerequisite for turbidity currents. Only very large, surge-type turbidity currents deposit extensive sand and mud layers over large areas of the abyssal seafloor. For this reason, they have been reviewed for their potential ability to damage waste-filled GFCs placed on the seafloor and to disperse their contents (Bowles 1995). Not considered, however, is the possibility that small turbidity currents may be generated by the GFCs themselves as a result of pre-impact, impact, and post-impact effects with the seafloor.

Turbidity currents generated by GFC impact will have initially high velocities and will consist mostly of silt- and clay-sized materials. The initiating force results from the water being rapidly squeezed from the diminishing volume between the descending GFC and the seafloor. The estimated terminal velocity for a filled, 380 m^3 GFC descending through 5000 m of water is about 5 m/s (Hightower et al. 1995a). Calculations by Green (1995) show that the velocity of the water being forced from beneath the GFC as it nears the bottom increases exponentially from nearly zero at 3 m stand-off to as much as 65 m/s at less than 1 m. This rapid flow of water will undoubtedly erode sediment from beneath and immediately around the GFC and transport it laterally in all directions. In addition, the entrainment of water by the turbulent wake behind the GFC creates a post-impact downwash that will augment the dispersion of sediment eroded during the pre-impact phase.

Using a simple approach (i.e., no fluid mechanics, no suspended sediment), the water forced from beneath the GFC will spread out and dissipate inversely as the square of the propagation distance or

$$D_x = (R_0)^2 \, V_0/V_x \,, \tag{30}$$

where D_x is distance from the GFC, R_0 the diameter of the GFC, V_0 the initial velocity, and V_x the ending velocity. If the initial velocity is 65 m/s and the GFC diameter is 6 m, it would take 342 m for the water to slow to 0.02 m/s. This value probably represents a minimum propagation distance.

In reality, because bottom sediment will be eroded and because the settling velocity of the resuspended sediment (predominantly fine-grained) will be much less than the forward propagation of the surge, a well-mixed, low-concentration suspension will result that will probably flow even farther. Fine-grained, low density (dilute), low-velocity flows in marine and fresh-water environments are known to travel considerable distances (Gould 1951; Lambert et al. 1976; Stanley and Bowen 1980). Hence, the dispersal of natural sediment around a waste site will encompass a substantially greater area than predicted by a simple plume model based on buoyancy (i.e., thermal effects).

The above scenario becomes critical in the case of a GFC rupture upon impact. At impact, the kinetic energy of the GFC and contents is absorbed by the seafloor and the GFC wall. Thus, should the internal hydrodynamic stresses rupture the fabric of the GFC, the contents will be released into the water column at nearly the same instant that water is being forced from beneath the GFC. More importantly, should the GFC break in only one place (e.g., along a seam), the result would be the jetting of concentrated (i.e., high-density), fine-grained GFC contents in one direction. Once again, using a simple approach, the speed of a buoyancy-conserving surge (i.e., jet) is inversely proportional to the square root of the propagation distance (Dade et al. 1994), or

$$(D_x)^{1/2} = (R_o)^{1/2}\ V_o/V_x\,. \tag{31}$$

Applying the same set of values as above, the surge will travel 64 km before slowing to 0.02 m/s. Intuitively, a 64-km travel distance seems unlikely. However, because the contents of the GFC are a dense mixture of sediment and water (1.4–1.7 Mg/m^3), the resulting flow will have substantially more momentum than a simple water jet. Thus, it is reasonable to expect that the waste material will propagate as a turbulent flow under its own impetus for a substantial distance (several kilometers) along a flat abyssal seafloor.

Clearly, the biggest difficulty in comparing natural turbidity currents with GFC-generated turbidity currents is scaling. It is notable, however, that naturally occurring turbidity currents have the poorly understood ability to sustain flow momentum for extraordinarily long distances (hundreds of kilometers) along bottoms that slope less than 1°. Middleton (1966; 1969), Bye (1971), Chu et al. (1979), Pantin (1979), and Dade et al. (1994) have addressed this issue. According to Middleton, an important factor is the stability and mixing characteristics of the upper (fluid-fluid) interface of the flow relative to bottom drag. The degree of mixing across this interface depends on the densiometric Froude Number which, in nature, is controlled mainly by slope. Where the Froude Number is less than one (i.e., on abyssal plains), there will be little mixing; consequently, little dilution and hydraulic resistance at the upper interface. As a result, flow can be maintained over long distances.

The dispersal of normal seafloor sediment by GFC impact is of little significance to a waste isolation and containment scenario. Most of the excavated material will settle and repose as a thin layer around the impact site; it will have no unusual effect on the bottom fauna, vis-à-vis natural turbidity currents, which can obliterate all bottom life. On the other hand, should GFCs rupture on impact, the problem becomes critical because the GFC contents may be widely dispersed. Just how wide remains to be determined and should be the focus of a concerted modeling effort.

5.0 PHYSICAL OCEANOGRAPHIC SIMULATIONS

by Patrick C. Gallacher

5.1 Introduction

There are two aspects of the hydrodynamics of the deep ocean that affect the SimDOR Project. The first is the potential spread of the dredge material into the benthic boundary layer where it is

susceptible to dispersion by bottom currents. The second is the speed, direction, and temporal variability of the basin-scale deep currents. These variables will determine the extent of the dispersion. Given present computer resources, the boundary layer and basin-scale dynamics cannot be simulated in one model because of the huge disparity of scales. The problem of the dispersion of dredged materials from the isolation site was separated into two parts: 1) an investigation of the plume that would result if a GFC were to rupture on impact with the seafloor and subsequently disperse the dredged material into the benthic boundary layer and 2) an examination of the basin-scale currents that would advect and diffuse material from the benthic boundary layer throughout the basin and potentially throughout the water column.

If the GFCs rupture or leak, the dredge material may enter the water column primarily in two phases. The solids in the dredge material can be injected into the water column. The larger particles will fall out fairly quickly due to their size and the finer particles will tend to flocculate on contact with seawater; this will hasten their deposition of solids on the seafloor. An apron of material will be formed surrounding the GFCs. Unless a turbidity flow occurs, the spread of solid particles by hydrodynamical processes will be confined to a relatively small area. However, the dissolved material can remain in suspension much longer and may be removed from the isolation site by the larger scale processes of advection and diffusion.

The choice was made to look first at the worst-case scenarios. If these are determined to have acceptable levels of risk, then more complex simulations that include chemical and biological interactions that may further limit the spread of contaminants from the dredged spoil are unnecessary. With this in mind, the GFCs were assumed ruptured on impact with seafloor releasing warm, fresh water containing significant concentrations of dissolved material. Then the dispersion of the dissolved substances by buoyant plumes was simulated.

To examine the potential for large-scale dispersion of the material and for the material to enter the upper ocean, hence, potentially to man's food chain, the large-scale deep circulation of the North Atlantic basin was simulated. To accomplish this, a model with very high horizontal resolution was used. The horizontal resolution is required to obtain realistic energy levels in the abyssal ocean circulation. With lower resolution, the energy to fuel this circulation remains trapped in the upper ocean. The discussion follows.

5.2 Plume Simulations

5.2.1 Introduction

Certain assumptions were made in the numerical simulations. The GFCs each have a capacity of 760 m^3 (1000 yd^3). They are filled to 75% of their capacity with a slurry that is 60% water. Of this total volume of water, only 10 to 20% can be released (the remainder is retained as pore water). Typically, the released water has a temperature of 18°C and a salinity of 32 psu; thus, the density at sea level is 1.023 Mg/m^3. This equates to a density of 1.036 Mg/m^3 at 3000 m where the ambient temperature, 3°C, and the salinity, 35 psu, yield an ambient density of 1.042 Mg/m^3. This density deficit is equivalent to a temperature difference of 35°C. If the GFCs rupture on impact, the buoyant acceleration that results from this density deficit is 5.5 cm/s^2.

In the scenario where some number of GFCs rupture on contact with the seafloor, dissolved and suspended material will be released into the benthic boundary layer. This will be accomplished through the action of vigorous plumes generated by the strong buoyant forcing produced by the large density deficit of the GFC-contained free water relative to the ambient water. The suspended

particles will fall out of the water column rapidly. Thus, the primary issue of concern was viewed as the potential spread of the dissolved contaminants.

Only very limited direct simulations were conducted; however, these simulations indicated that nonlinearities in the plumes cause the dispersion of dissolved material to be very asymmetric and nonuniform. This result raises questions about the validity of dispersion estimates from two-dimensional, radially symmetric models. Further work is required to validate the two-dimensional, radially symmetric results of previous investigators and to determine the fate of the dissolved material over the complete lifetime of the plume.

Ammonia was chosen as the first contaminant to simulate because of its potential to attract abyssal scavenging megafauna. A very probable pathway into the upper ocean for the contaminants is in the gonads of demersal fishes; thus the attraction of fauna to the site may play a pivotal role in the dispersion of the contaminants, particularly into the upper ocean. Further research should include a model for the dispersion of ammonia and a parameterization of the attraction of abyssal fauna.

5.2.2 Model Description

To study the behavior of individual plumes, a high-resolution, nonhydrostatic boundary layer model was used (McWilliams et al. 1993). This model is capable of simulating turbulent flows and flows where the hydrostatic assumption breaks down. The model is augmented for this simulation to include tracers and to incorporate a solid bottom boundary. The bottom boundary condition is changed from a heat flux (Dirichlet) boundary condition to a temperature (Neumann) boundary condition. The horizontal boundary conditions are periodic and the top boundary condition radiates waves out of the domain. The model utilizes a variable diffusivity based on the subgrid scale energy that allows the simulation of high Reynolds number flows.

5.2.3 Simulation

A set of preliminary simulations were designed to test the inclusion of tracers in the model. These simulations covered a domain of 300×300 m in the horizontal and 200 m in the vertical using 75 gridpoints in each direction. The heat sources from two ruptured GFCs were parameterized by prescribing a surface heat flux of 500 W/m^2 over a box of 6×7 gridpoints (approximately the size of a GFC) at the bottom of the model domain. The concentration 12 min after starting the heat flux is shown in Fig. 38.

After 7000 s (just less than 2 h) of plume development, the tracer that simulated dissolved contaminants rose to a height of roughly 150 m and was dispersed over an area roughly 200 m wide (Fig. 39). The dispersion had reduced the concentration of the tracer but a significant amount remained in suspension. Despite the fact that there was no external forcing, e.g. mean flow, large-scale turbulence, or tides, the dispersion was quite asymmetric and nonuniform. This pattern is a result of the inherent nonlinearities in the processes governing the formation and development of the plume. The two plumes interact, which further enhances the asymmetric pattern.

5.2.4 Conclusions

The results of the simulation described above are in agreement with experiments and field observations of buoyant plumes. These results are very preliminary. Further work needs to be done

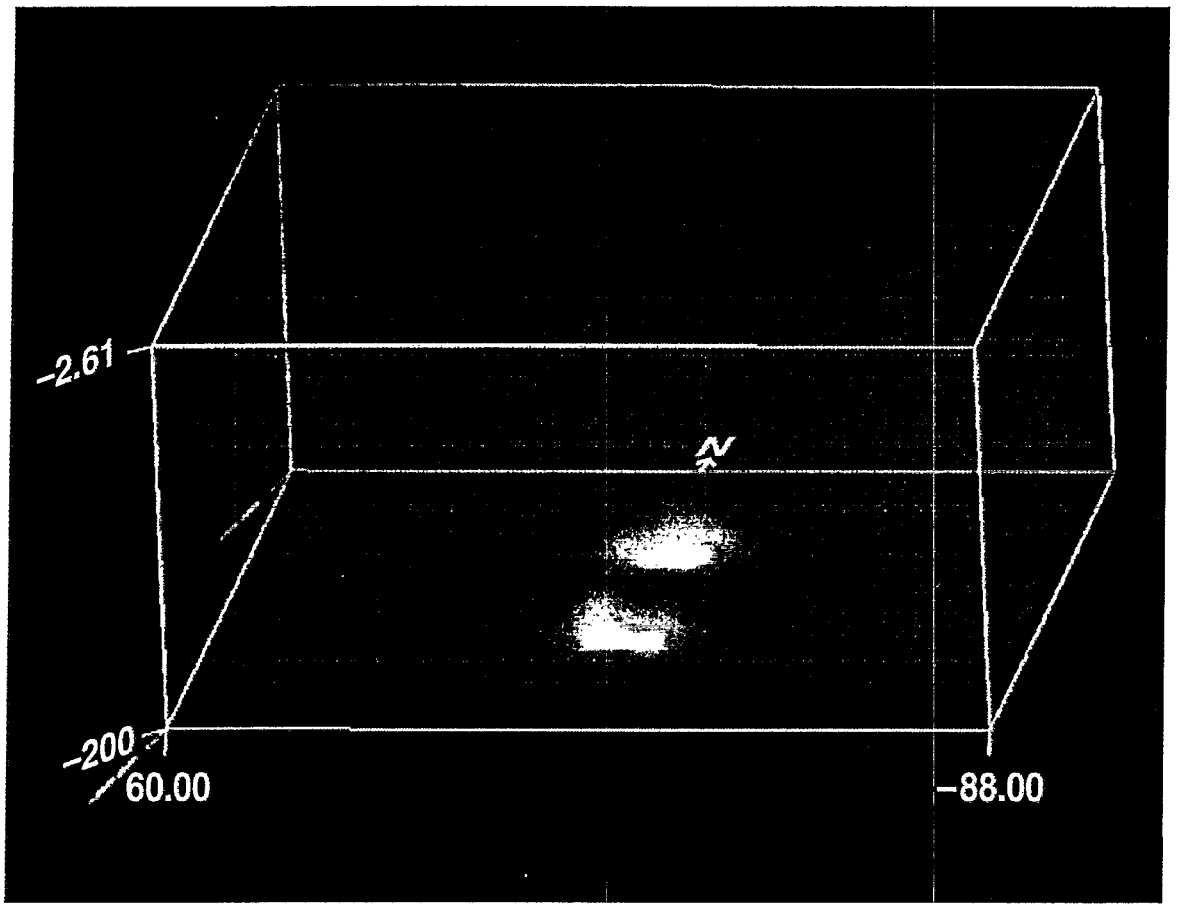

Fig. 38 — Distribution of tracer concentration from two hot spots 12 min after the start of the simulation

to determine the life cycle of the plumes and the effects of plume interactions. The change of boundary conditions must be completed and more exact simulations using the temperature boundary conditions with the correct temperature difference need to be completed. The existing results are qualitatively correct, but they do not quantitatively predict the extent of the dispersion of the contaminants.

The time required for water to cycle from the surface into the deep ocean and back to the surface through the oceanic thermohaline conveyor belt can be centuries. If a sufficiently quiescent site on the abyssal seafloor is chosen as the waste isolation site, water parcels that originate at that site may never enter the upper reaches of the ocean for periods as long as thousands of years. It has been shown that such sites probably exist in the western North Atlantic ocean.

5.3 Abyssal Ocean Flow Simulations

5.3.1 Introduction

The mean deep currents and their temporal variability are important criteria for site selection and an important consideration in designing the monitoring plan. Furthermore, it is the basin-scale circulation that ultimately determines if contaminants enter the upper ocean where they could

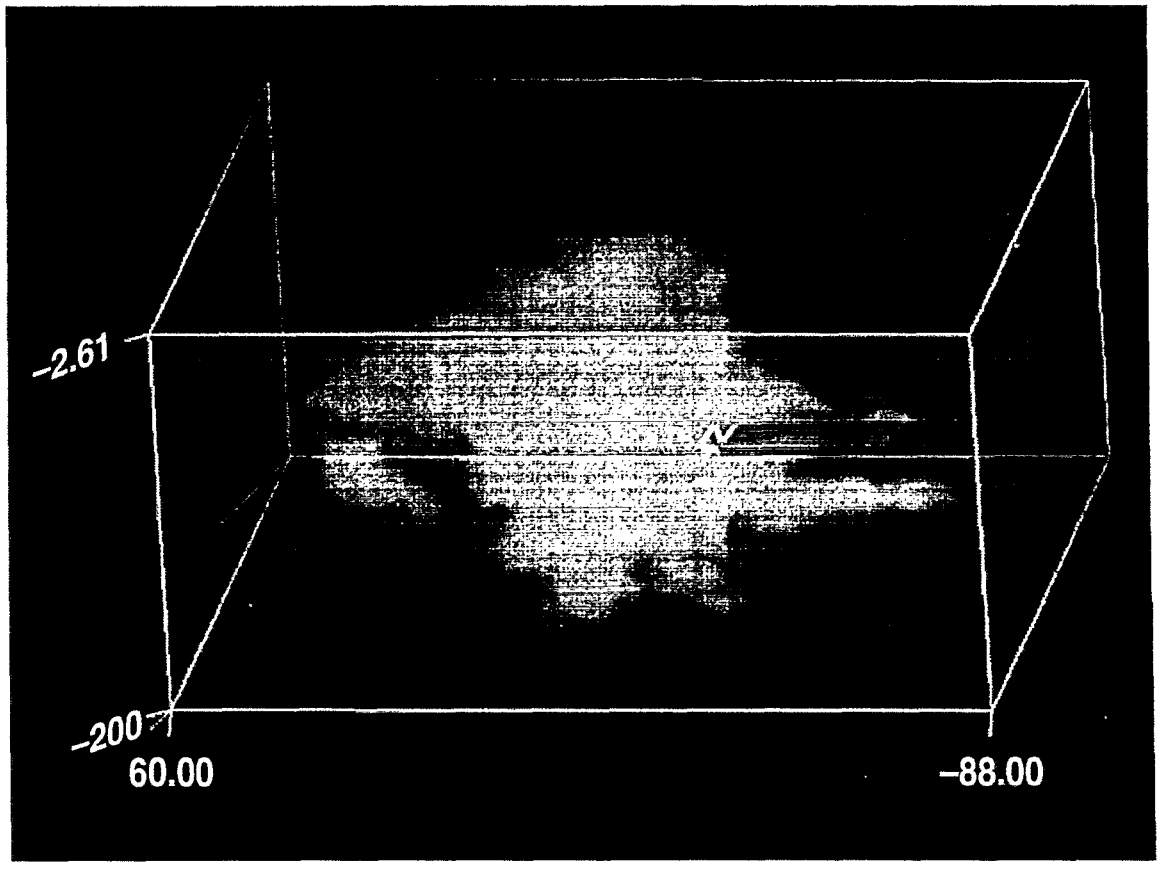

Fig. 39 — Distribution of tracer concentration from two hot spots 2 h after the start of the simulation

become incorporated into man's food chain. The thermohaline circulation of the oceans links the surface and deep waters on time scales of years to centuries. Surface water sinks primarily in polar regions and in concentration basins such as the Mediterranean Sea. The water then flows throughout the deep ocean until it resurfaces primarily in tropical regions and in the interior of ocean gyres. Recent observations suggest that upwelling of deep water also occurs around seamounts. It is uncertain whether this could result in significant entrainment of deep water into the upper ocean. This is an issue that should be researched in the future.

5.3.2 Model Description

The basin-scale models used in this study are finite depth versions of the NRL multilayer ocean model. The NRL multilayer ocean model is a primitive equation representation of a Boussinesq, hydrostatic ocean with a free surface. The equations are solved in spherical coordinates in a layer-averaged framework that allows momentum, but not density, to mix between layers. The model is similar to the hydrodynamical model described by Hurlburt and Thompson (1980), but it has been substantially augmented by Wallcraft (1991).

Those changes include an inter-layer mixing of momentum that is similar to the formation used by McCreary and Kundu (1988) as it depends on the layer thickness. The velocity in each active layer thus varies horizontally and temporally as a result of horizontal advection and diffusion, vertical mixing due to entrainment and detrainment and, in the surface layer, due to surface momentum

fluxes based on the Hellerman and Rosenstein (1983) monthly wind climatology and daily European Centre for Medium-Range Weather Forecasts' operational winds from 1981–1993.

5.3.3 Simulation

The animation developed is derived from numerical experiments done with the North Atlantic Subtropical Gyre model. The North Atlantic Subtropical Gyre model extended from 9° N to 47° N and from 95° W to 10° W so it also included the Gulf of Mexico and the Caribbean Sea. The North Atlantic Subtropical gyre model had 1/16° horizontal resolution with five levels in the vertical. The model was forced with the Hellerman and Rosenstein (1983) monthly wind climatology. Three vertical layers were used to describe the upper ocean and thermocline, one layer was used to describe the flow of intermediate water, and one for the deep-water flow. The interface between the intermediate and deep layers was initially 1000 m. Thus, the bottom layer included all depths from approximately 1000 m to the seafloor.

The model cannot distinguish between deep and bottom water flows and there is no benthic boundary layer in the model. However, the increased horizontal resolution that is achieved by using relatively thick vertical layers allows the energy put in the upper ocean by wind and surface cooling to be distributed correctly in the vertical through the action of baroclinic and barotropic instabilities. The current and eddy kinetic energy magnitudes and distributions in the deepest model level (Fig. 40) are in good agreement with observations (Gallacher 1997). This cannot be achieved with coarser horizontal resolution. In fact, a version of the NRL model with 1/4° horizontal resolution underestimated the magnitude of the eddy kinetic energy in the deepest layer by a factor of between 10 and 100 (Gallacher 1995).

Fig. 40 — Velocity of the current in the bottom layer of the simulation of the north Atlantic gyre. Size of the point is the speed of the flow (0–25 cm/s)

Fig. 41 — An enlarged portion of Fig. 40 showing the area surrounding the surrogate sites, located southwest of Bermuda in the region of very low velocities of bottom currents

5.3.4 Conclusions

The animation developed demonstrates that the mean currents and their temporal variability are small in the area of the SimDOR surrogate sites optimal for contaminant isolation (Fig. 41). Thus, any contaminants from the dredged material that may be swept into the benthic boundary layer either by plumes or by resuspension will most likely remain in the near vicinity within 20 km of the isolation sites. The time scales for diffusion beyond that region are very long and the probability of the material entering the upper ocean by means of advection or diffusion is small.

The velocities are larger, as are their temporal variability, closer to the continental United States. This is the region of the western undercurrent beneath the Gulf Stream and the subpolar gyre. This simulated current pattern is in good agreement with observations and is one of the strong reasons why the isolation sites cannot be located close to the continental margin.

6.0 GEOCHEMICAL SIMULATION

by Richard A. Jahnke

6.1 Introduction

This assessment of the geochemical impacts of relocating dredged materials to the abyssal seafloor was to build on the numerical simulation developed during the APWI Project. Based on the initial simulations, a variety of issues were identified including examination of:

- the influence of deposit geometry on the three-dimensional distribution of the geochemical characteristics of the deposit and underlying sediments and pore waters;

- the influence of bacterial inoculation rates;
- the fate of redox-sensitive trace metals within the deposit; and
- the possibility of forming gas hydrates within the deposit.

In addition to these topics, it was noted that focusing exclusively on the geochemical changes that occurred within the deposit did not provide an overall assessment of the geochemical impacts of the deposit to the deep ocean. It was decided, therefore, to also estimate the magnitude of the potential impacts of the dredged material deposit on ocean chemistry.

6.2 Three-Dimensional Distribution of Sediment and Pore Water Characteristics

To determine whether the anoxic zone that develops beneath the deposit extends significantly beyond the area covered by the deposit itself, the numerical simulations were expanded to assess the three-dimensional distribution of major redox chemical species in the pore waters beneath and adjacent to the deposit. To accomplish this calculation, the one-dimensional numerical simulation (described in detail in the APWI Final Report and Jahnke (1997)) that was developed during the APWI Project was rewritten in two dimensions. Because this system is symmetric with distance from the central axis of the deposit cone, this system could then simulate the full three-dimensional distribution by simply scaling element volume as distance from the center multiplied by 2*pi.

This calculation assumes that 5×10^6 m^3 (7×10^6 yd^3) of dredged material was deposited on the seafloor forming a cone-shaped deposit (a one-time deposit). The slope of the top is assumed to be 2°. The organic carbon content of the dredged material is set at 3.1%, consistent with measurements of dredged materials from New York Harbor.

A vertical section of the distribution of the anoxic zone is displayed in Fig. 42. The section extends laterally through the center of the deposit and vertically into the underlying sediments.

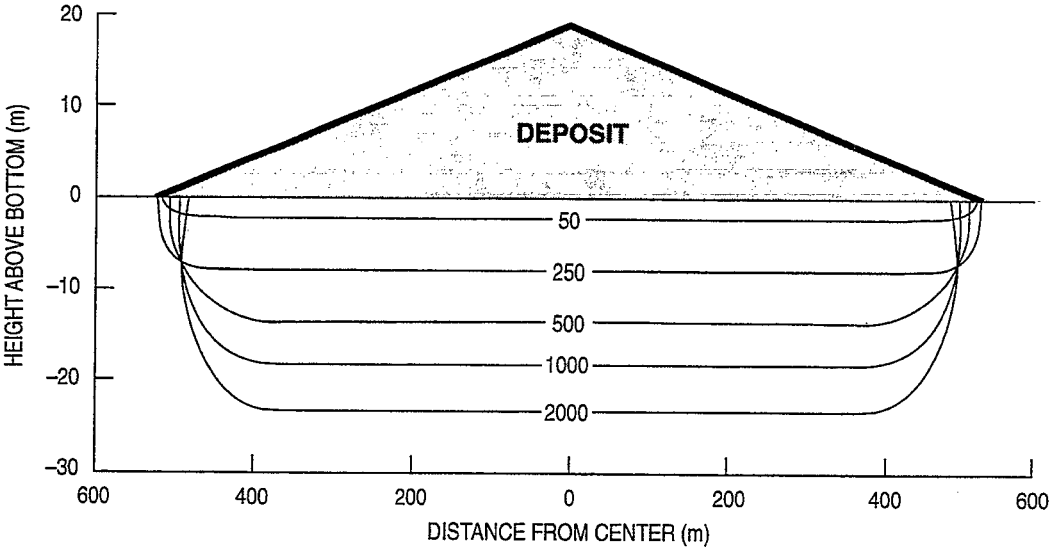

Fig. 42 — Vertical section of distribution of anoxic zone beneath cone-shaped deposit of 5×10^6 m^3 of dredged material with organic content of 3.1%. Numbers adjacent to profile lines indicate years since material was deposited.

Notice that the vertical and horizontal scales are different. Numbers adjacent to each line indicate the years since the material was deposited. It is important to note that this numerical simulation also estimates the pore water nitrate, ammonium, sulfide, sulfate, and methane concentrations. To simplify the visualization of the results, the distribution of these other solutes were not shown.

This simulation demonstrates that the anoxic zone within the sediments does not significantly extend laterally, beyond the dimensions of the deposit. The reason for this is simply that as the anoxic zone grows vertically and expands to greater depth, the organic carbon in the deposit is being oxidized. The deposit is very thin at its periphery. Thus, after a few hundred to a thousand years, the organic carbon at the outer edge of the deposit becomes exhausted and oxygen begins to diffuse back into this region. This can be seen by the fact that the zone of anoxia at the sediment-water interface (directly below the deposit) shrinks with increasing age. This is despite the fact that in the center of the deposit the anoxic zone continues to deepen. Thus, in the absence of any net lateral pore water advection, the anoxic zone formed by the decomposition of matter and the oxidation of reduced metabolites is basically restricted to the region beneath the deposit.

6.3 Bacterial Inoculation Rates

From the initial modeling studies, it was recognized that the rate of decomposition of the organic materials and, therefore, the development of reducing zones depends critically on the rate at which deep-sea bacteria can populate the deposit. It was also recognized that quantifying bacterial inoculation rates of the waste material would be an extremely difficult task. Any quantitative estimate would require detailed knowledge of the permeability of the GFC material, the containment integrity of the GFCs after impact with the bottom, and knowledge of the bacteria assemblages that would proliferate in the deposit. Because these aspects were either still evolving as the project started, or were simply not known, it was decided to again assume that the deposit materials were deposited in a loose, cone-shaped deposit and that deep-sea marine bacteria were present throughout. Thus, the influence of bacterial inoculation rates were not explicitly assessed in the SimDOR Project.

6.4 Redox-Sensitive Trace Metals

The distribution of redox-sensitive trace metals in the pore waters of the deposit was assessed in two ways during the SimDOR Project. A qualitative description of the concentration patterns to be expected within deep-sea sediments as a function of organic matter deposition and metabolite distributions has been developed previously (Shaw et al. 1990). The derived relationships are displayed in Figs. 43–46. Fig. 43 displays the pore water concentrations of oxygen, nitrate, manganese, and iron for several locations along the Southern California continental margin. For our purposes here, we will focus on the Patton Escarpment and Santa Monica Basin sites as they represent the depositional extremes for this region. For the Patton Escarpment, one should note that oxygen is present in the pore waters to a depth of 2 cm and that dissolved ferrous iron is not detectable, suggesting that this site is dominated by oxic and suboxic diagenesis. In contrast, at the Santa Monica Basin site, there is no detectable oxygen in the pore waters and reduced iron is measurable within the upper few millimeters of the pore waters. This pattern suggests that anoxic processes dominate sediment diagenesis.

The pore water distribution of selected redox-sensitive trace metals for these two sites are presented in Figs. 44 and 45. The down-core variations in redox state, as represented by the individual metabolites, exerts a major influence on the metal distributions. This can be clearly seen

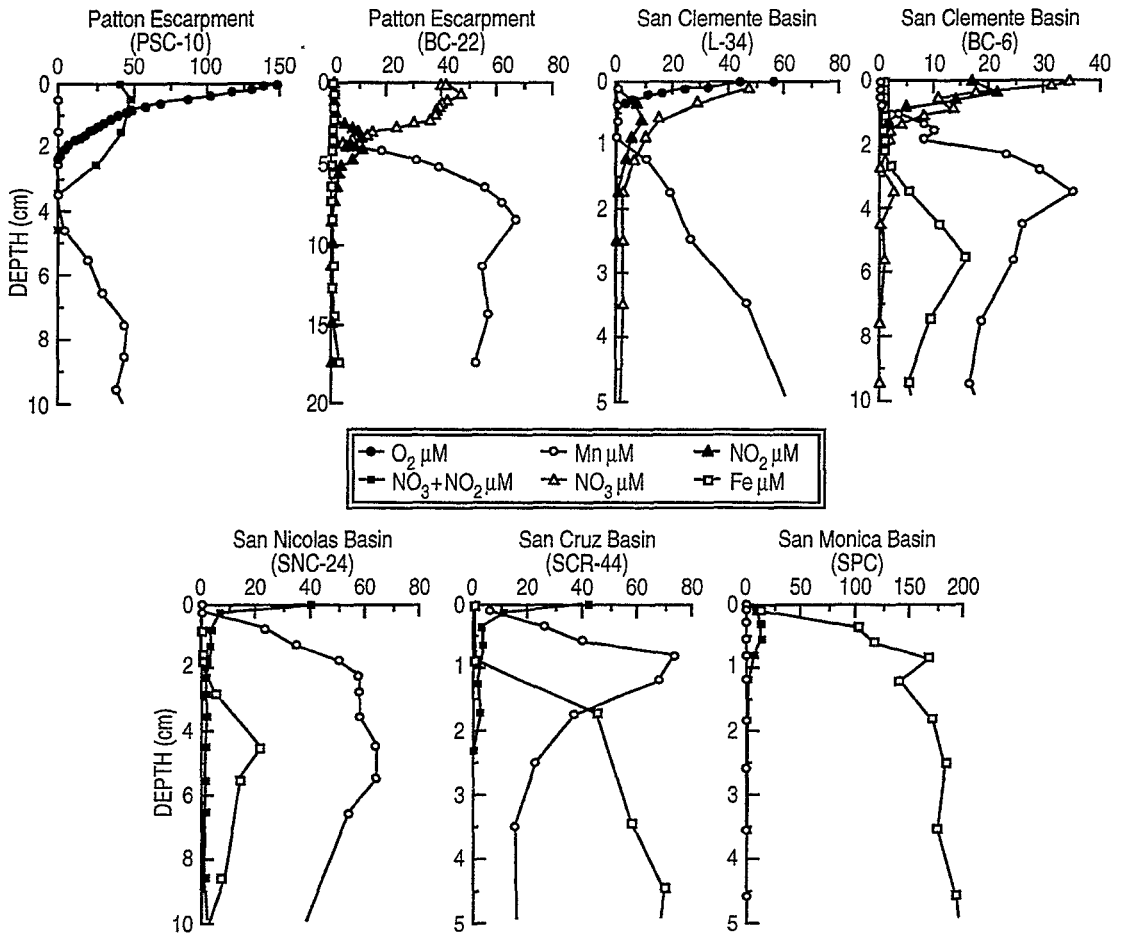

Fig. 43 — Pore water profiles of redox species. Only partial core sections are presented to show detail.

in the nickel, cobalt, and chromium distributions at the Patton Escarpment and the vanadium, nickel, and molybdenum distributions at Santa Monica Basin. One can also directly observe the influence of the diagenetic state on trace metal mobility by comparing the metal distributions between the two sites. These differences are most obvious for nickel and copper. Note the differences in the magnitude of the concentration axes.

Based on these distribution patterns, it is possible to construct the expected pore water metal distributions relative to the oxic, suboxic, and anoxic diagenetic processes (Fig. 46). Thus, from the results of the APWI and SimDOR numerical simulations, it is possible to predict, in relative terms, the mobility and chemical form of many redox-sensitive trace metals. In addition, the specific reactivities of these metals are being parameterized and incorporated into the numerical simulation.

6.5 The Possibility of Forming Gas Hydrates

Large quantities of methane may be produced by the microbial degradation of the organic matter in the deposit. Based on the simulations conducted during the APWI Project, the major factors controlling the pore water methane concentration are the rate of organic carbon oxidation

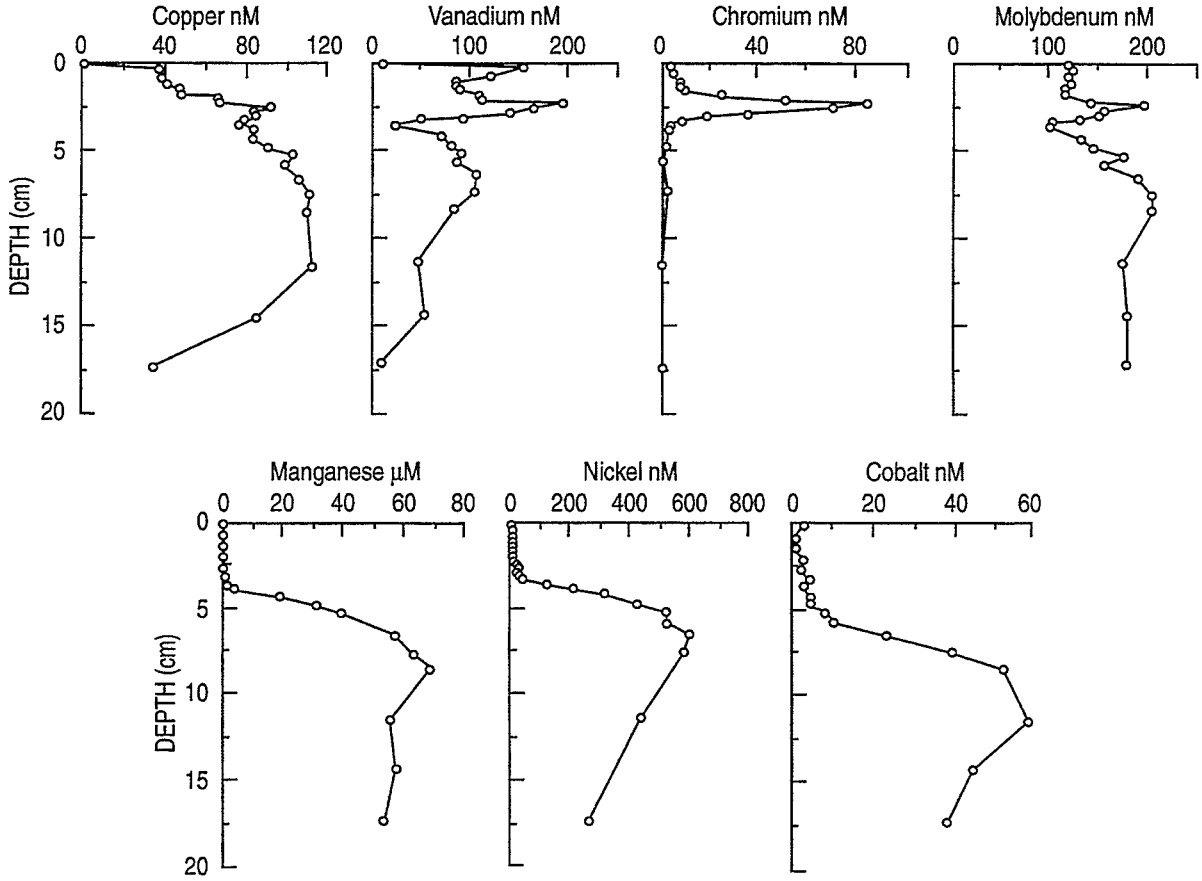

Fig. 44 — Pore water metal profiles from the Patton Escarpment (core BC-22)

and degradation, the thickness of the deposit, and the organic carbon content of the deposited materials. The faster the organic matter decomposes, the less time there is for other oxidants, such as oxygen, nitrate, and sulfate, to diffuse into the deposit. Thus, if organic matter reacts quickly, a greater proportion of the decomposition proceeds via methane fermentation increasing pore water methane concentrations. Similarly, because a thicker deposit has a smaller surface area to volume ratio, the diffusive influx of oxygen, nitrate, and sulfate is minimized by a thick deposit. This would similarly increase the role of methane fermentation and pore water methane concentrations.

Methane concentrations estimates in the APWI Project simulations reached very high values, easily exceeding the estimated threshold for the formation of a methane hydrate. However, these calculations were performed using an assumed organic carbon content of 7.9%, which represented a hypothetical mixture of organic-rich sewage sludge and dredged materials. In the SimDOR Project, we have focused exclusively on the relocation of dredged materials. In the calculation performed here, therefore, the organic carbon content was assumed to 3.1% as stated above. Because the other oxidants are used preferentially, this decrease in the organic carbon content dramatically reduces the predicted pore water methane concentration. In addition, because this calculation was performed in three dimensions, the area available to supply these other oxidants was also dramatically increased. The net result of these two factors is that predicted methane concentrations in the three-dimensional SimDOR calculations rarely exceeded 30 mM. At deep-sea temperatures and pressures, the thermodynamic threshold for methane hydrate formation is 50–60 mM. Thus, under these conditions, the

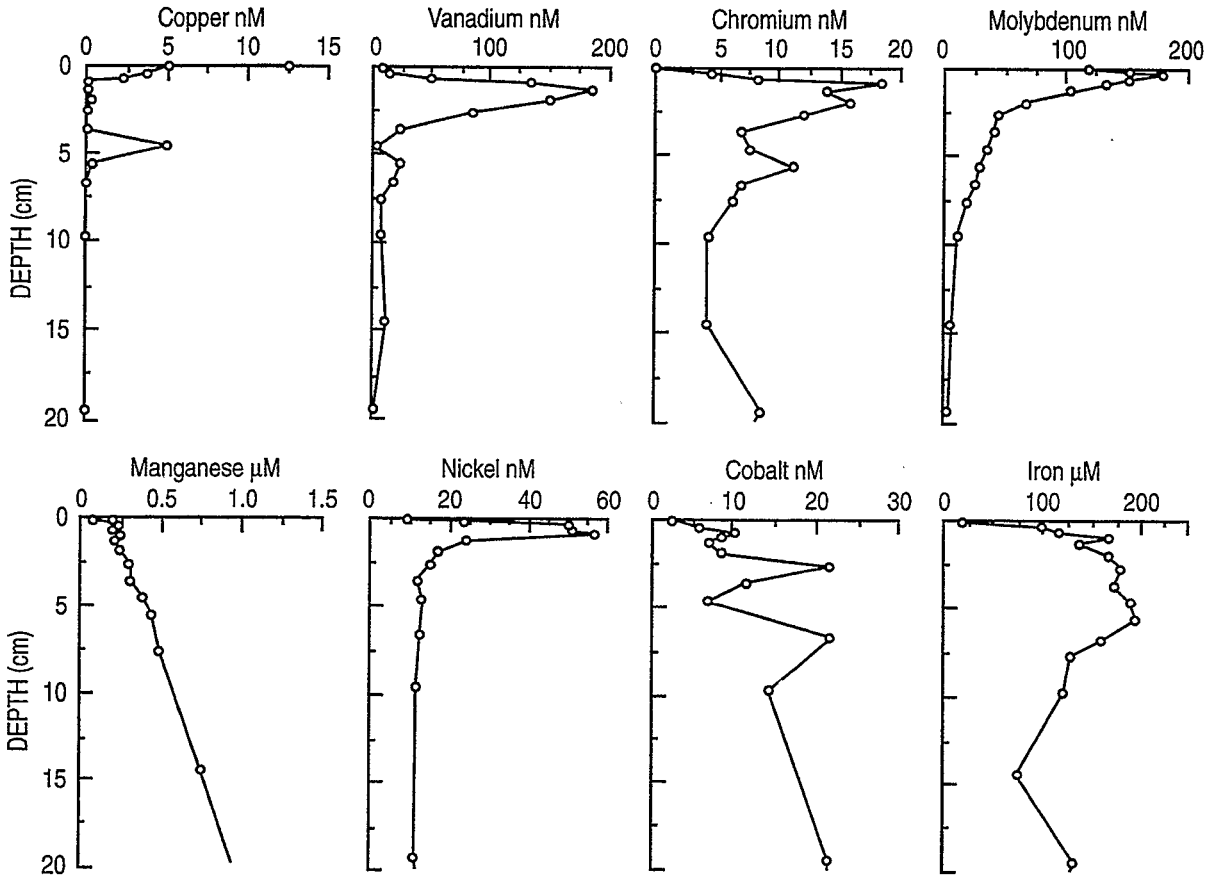

Fig. 45 — Pore water metal profiles from the Santa Monica Basin (core SPC)

formation of hydrate is not predicted to be important. However, it must be emphasized that this calculation is for a one-time deposit. If the isolation site were to receive repeated inputs of materials, increasing the thickness, or if the reactivity or organic content of the deposited materials is greater than assumed here, then the formation of hydrates may be expected.

6.6 The Relative Magnitude of Dredged Material Relocation to Deep-Sea Fluxes and Pools

To provide an assessment of the relative magnitude of relocating New York dredged materials to the abyssal ocean, the magnitude of the deposit is compared to estimates of ocean fluxes and pool sizes. To assess the size of the anticipated deposit, we assume that 5×10^6 m^3 (7×10^6 yd^3) are deposited on the seafloor in the shape of a cone with a 2° slope. This deposit would occupy 0.88 km^2. The area of the seafloor at water depths greater than 3 km is 2.72×10^8 (Menard and Smith 1966). Thus, the deposit would occupy much less than 1 millionth of the total area of the deep seafloor. To put this in a perspective that is easier to visualize, we make the following analogy: if the deep seafloor is represented by a football field (including the end zones), the area occupied by the relocated dredged material would be 16 mm^2 (0.025 in^2). Thus, an extremely small portion of the deep-sea habitat would be directly influenced by the deposit.

This is an important consideration when considering strategies to maintain global biodiversity. With the majority of the global population living near coastlines, the majority of coastal habitats

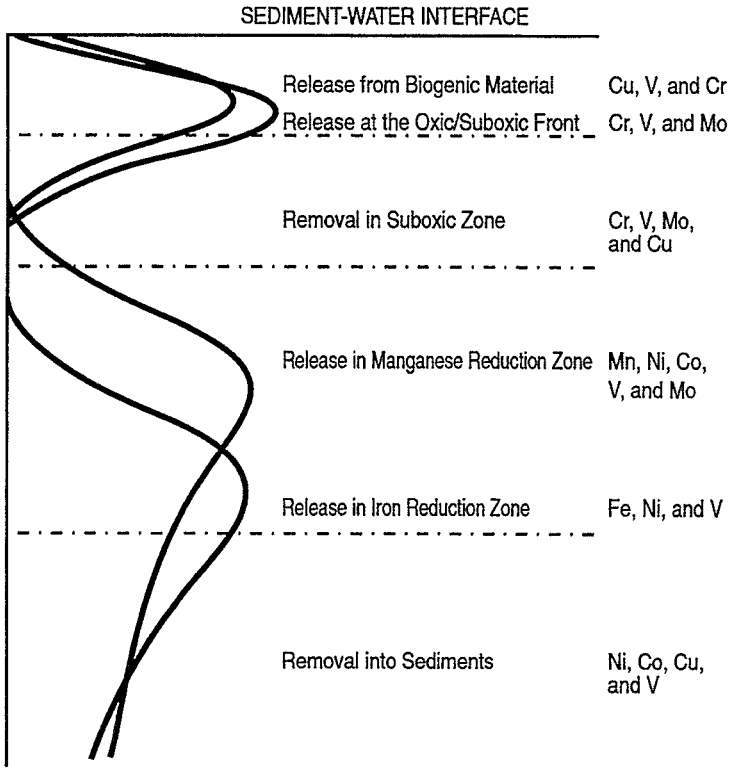

Fig. 46 — Schematic representation of characteristic zones of release and removal of trace metals in California Borderland Basin locations. Absolute profile concentrations are the sum of these processes at each sediment horizon.

have been impacted by man's activities to some degree. Relocating contaminated, dredged materials from the coastal zone to the deep sea will help to alleviate anthropogenic pressures on coastal habitats, the majority of which are impacted, while resulting in the direct impact to a miniscule portion of the deep seafloor.

One can also compare the magnitude of contaminant input to oceanic fluxes and internal pool sizes. For example, Table 7 lists the comparison between the amount of copper, zinc, and organic matter that is contained in 5×10^6 m^3 (7×10^6 yd^3) of New York dredged material and that which is estimated to enter the deep ocean annually through hydrothermal vents and the sinking of organic matter from the surface ocean. The hydrothermal input flux was estimated assuming that 15 km^3 of new crust is produced each year, of which the upper 0.3 km of the 5-km-thick section is altered. In the altering process, 17 and 30 ppm of copper and zinc, respectively, are leached from the basalt. The values obtained suggest that the amount introduced by relocating dredged material to the deep ocean is small compared to the natural hydrothermal input. Since the overwhelming majority of these metals will stay attached to the particles in the deposit, this calculation represents a maximal potential influence of the relocated material. Additionally, it must be noted that the hydrothermal value is an annual input. The biogenic carbon flux to the deep ocean has been estimated by Jahnke (1996). Again, the input associated with the relocated materials is much smaller than the natural flux rate. As shown in the earlier calculations, the organic carbon associated with the deposit requires thousands of years to be oxidized. Therefore, this calculation greatly exaggerates the potential impact of the relocation on bottom water carbon flux and, hence, oxygen consumption.

Table 7 — Deposit/Deep-Water Flux Comparison

CONTAMINANT	DEPOSIT (g)	HYDROTHERMAL INPUT (g/yr)	RATIO
Copper	8.2×10^8	3.4×10^{10}	0.024
Zinc	1.2×10^9	6.0×10^{10}	0.020
		BIOGENIC FLUX	
Organic Carbon	5.9×10^{10}	9.2×10^{13}	0.0006

Table 8 — Deposit/Deep-Water Total Content Comparison

CONTAMINANT (conc.– ppm)	DEPOSIT (g)	DEEP-WATER CONC. (ng/kg)	DEEP-WATER CONTENT (g)	RATIO
Cadmium (8.9)	1.7×10^7	70–117	$0.63–1.05 \times 10^{14}$	$1.6–2.7 \times 10^{-7}$
Copper (431)	8.2×10^8	120–130	$1.08–117 \times 10^{14}$	$7.0–7.6 \times 10^{-6}$
Mercury (95.1)	2.0×10^9	4–6	$3.6–5.4 \times 10^{12}$	$3.7–5.6 \times 10^{-4}$
Nickel (61.6)	1.2×10^8	480–566	$4.3–5.1 \times 10^{14}$	$2.3–2.8 \times 10^{-7}$
Zinc (619)	1.2×10^9	390–438	$3.5–3.9 \times 10^{14}$	$3.1–3.4 \times 10^{-6}$

The amount of trace metals in the relocated materials can also be compared to the total amount of trace metals in deep-sea waters (Table 8). The total amount of the indicated metals in deep-sea waters were estimated from their deep-water concentrations (Quinby-Hunt and Turekian 1983) and the volume of the ocean deeper than 1000 m. As listed in this table, the total amount of the indicated metals in seawater exceeds that in the relocated materials by approximately 10^4 to 10^7. Thus, if all of the metals were to escape the relocated materials, the deep-sea concentration would increase from 0.01 to 0.00001%. Since the vast majority of the metals would remain in the deposit attached to sediment particles, this calculation greatly overestimates the potential concentration change.

Since many organic contaminants do not occur naturally, their concentration in the deep sea is essentially zero. It is not possible to estimate the impacts of introducing these materials to the deep ocean directly. However, many of these compounds are transported to the surface ocean via atmospheric transport. Once in the surface waters, they primarily become attached to biogenic particles and are transported to the deep ocean on sinking particles. A comparison was made of the magnitude of atmospheric inputs of selected metal contaminants and total polychlorinated biphenols (PCB) to that contained in the relocated materials (Table 9). Atmospheric inputs are taken from Duce et al. (1991). With the exception of mercury, the atmospheric input exceeds the total amount contained in the deposit. Again, because the vast majority of each contaminant will stay attached to the particles within the deposit, these results suggest that any release from the deposit would be trivially small relative to the atmospheric input. Thus, these comparisons suggest that potential

Table 9 — Deposit/Atmospheric Input Comparison

CONTAMINANT (conc.– ppm)	DEPOSIT (g)	ATM. INPUT (g/yr)	RATIO (deposit/atm.)
Cadmium (8.9)	1.7×10^7	3.4×10^9	0.0049
Copper (431)	8.2×10^8	$1.6–6.0 \times 10^{10}$	0.013–0.05
Mercury (95.1)	2.0×10^9	1.7×10^9	1.2
Nickel (61.6)	1.2×10^8	2.5×10^{10}	0.0047
Zinc (619)	1.2×10^9	$0.44–2.7 \times 10^{11}$	0.0043–0.027
Σ PCB (1.84)*	3.4×10^6	2.4×10^8	0.014

*Boston Harbor Sediment (Silt Fraction) Concentration

releases of contaminants from the relocated materials is trivially small compared to the standing stock of trace metals in seawater to the natural hydrothermal input to the deep water, and to the atmospheric input of both trace metals and organic contaminants (using ΣPCB as an example) to the surface ocean.

7.0 SIMULATING THE RESPONSE OF THE BENTHOS TO DREDGED MATERIAL RELOCATED ON DEEP ABYSSAL PLAINS

by Gilbert T. Rowe

7.1 Introduction and Background

One salient weakness of previous "deep-ocean" options for waste storage and isolation has been an inability to predict biological effects. To a large degree, this is because of the remote and alien nature of the environment. Previously published "models" are limited to correlation or inverse analyses (Eldridge and Jackson 1993). Deterministic numerical simulations of a simplified carbon cycle in a natural deep-ocean ecosystem suggested that natural processes can be simulated reasonably well (Rowe 1997). Adding waste material as a forcing function in the deep-ocean ecosystem models suggests that deep-ocean communities will exhibit at least some responses that are parallel to those in shallow-water sediments. However, little direct evidence is presently available to validate the model results.

This project started out with a limited set of objectives. A primary goal was to construct a numerical simulation of a generic deep-sea, near-bottom food chain. The idea was to utilize the simulation to model the possible range of biological effects of disposal of dredged material on deep-ocean animal communities. A rather generic simulation was designed to also be able to predict potential transfer rates of toxic contaminants inside and outside a deep-ocean food chain. Conducting sensitivity analyses was also envisioned as an aid in the design of eventual experiments for model validation and verification. These initial goals were amended to include the possible effects of alien materials such as dredged material on a macrofaunal community structure. In this case, the different elements of a "population model" were explored to predict how animal densities would vary between "*r* vs. *K*" strategists.

7.2 Methods

The numerical simulations were run using software entitled STELLA II, authoring version and the hardware was a Macintosh Quadra 610 or a Macintosh PowerBook 150. The first step was to simulate the food chain in a deep, North Atlantic site based on available information (Smith 1992). After using data in the latter publication to determine a steady-state solution, the fluxes and the standing stocks were used to calculate first-order respiration rate coefficients for each functional group. The input of particulate organic carbon (POC) necessary to achieve steady state was estimated to be the sum of the respiration values over an annual cycle. Forward or Gaussian elimination was used to estimate the feeding rates necessary to maintain steady state. Following the steady-state calculations, the simulation of the natural system with a hypothetical seasonal cycle was allowed to run for as long as 10 yr to observe the oscillations that would possibly be created by the predator/prey relationships defined in the food chain (Rowe 1997).

Following the creation of an annual cycle that persisted for a number of years in what might be expected of a normal system, a new forcing was added to the input term that might simulate the addition of alien organic matter in the relocated, dredged material. After the responses of the biota to new material was observed, the calculations were made of possible concentrations and transfers of polycyclic aromatic hydrocarbons (PAH) through and out of a more complex food chain, using information from shallow-water organisms and information available from Deep Water Dump Site 106.

The present report is concerned with trying to make estimates of how adding alien sediments might alter the diversity of the macrofauna. It was presumed that many of the species in a deep-sea assemblage would have endogenous controls over reproductive rates or intrinsic rates of natural increase, but that some species would be able to respond to a new utilizable organic substrate substantially faster than others, e.g., they would be *r* strategists (Snelgrove et al. 1996). Deep-ocean tray experiments suggest that under some circumstances trays become dominated by individual species, thus displaying very low diversity. The models were therefore designed to explore what population parameters would most likely create such a relationship. Initially, these models were coupled directly to organic input, as with earlier ones above, simulating community carbon dynamics (Rowe et al. 1997). These were replaced with a simplified carbon model decoupled from individual population models for several different species, each of which acted independently of the others. That is, each population was subject to a suite of relationships that affected its numbers, but these populations were independent from the other populations. The justification for this is that all the populations were in sparse supply, on the order of 10–100/m^2, and as they all are presumed to be rather small, it was assumed that they did not interact in ways that limited their numbers. This approach is diametrically opposite to that proposed by Jumars and Gallagher (1982) who suggested that competition between species determined their relative abundances. But their construction assumes competition for limiting resources in a natural environment characterized by a mosaic of microhabitats. The approach taken here makes the assumption that competition in the steady state is relatively benign because there is so little for which to compete. When the input of organic matter is increased, then competition becomes important; some species respond, others do not. Those that can increase in numbers will then dominate the assemblage and lower its diversity by virtue of diminishing "evenness."

The basic model relies on the following relationship:

$$dN/dt = rN - mN, \tag{32}$$

where N is numbers of individuals (m^{-2}), r is the intrinsic rate of natural increase, and m is mortality. While r is assumed in these models to be a constant, m can vary as a function of several

parameters. This can be a decrease that could result when more food is available (increase in organic substrate) or an increase due to higher predation pressure. The result of this relationship is an "S-shaped" or von Bertellanfy growth curve. In general, this curve can be described by the following relationship:

$$dN/dt = rN(K - N/K), \tag{33}$$

where K is the "saturation value" at which rN equals mN. That is, K is a value on the y-axis where the population is no longer increasing because any new individuals are balanced by the loss or death of old individuals.

7.3 The Model

Sets of differential equations were solved numerically to simulate the range of responses of organisms to natural POC input, as well as being inundated with dredged materials. Codes were small (<50 lines each) and probably can be run in a variety of programming languages. In the different simulations, a variety of conditions that could exist in a dump site were utilized. Several of these have been previously reported Rowe (1997). These early simulations provide a list of variables and standing stocks that need to be experimented and/or monitored in an actual or pilot DOR operation.

The original conceptual model of Smith (1992) was simplified to a three-box model (Fig. 47). This was simulated under natural conditions of seasonal cycling (Fig. 48a). It was discovered that concentrations of organic matter in the sediments cannot be used in terms of bulk values (Rowe et al. 1997). Rather, it appears that it is the rain of fresh detritus that is important in controlling overall rates of metabolism and organic matter recycling. Initial values for organic carbon in the sediments were reduced to approximately 1% of the bulk values (Fig. 48b).

When a "pulse" of organic detritus in dredge spoils was added, then a pulse in the metabolic rates of the organisms was transferred through the food chain (Fig. 3 Rowe 1997). If it were presumed that a small fraction of the initial pulse of detrital carbon becomes gonad products that were exported from the near-bottom environment, then this "export" could be used to estimate how much contaminant material concentrated in the export will leave isolation (Fig. 4 Rowe 1997). By multiplying the rate of export times the concentration factor in a lipid-rich gonad, one can generate a possible rate of contaminant export. The rate will vary with the contaminant, of course, but in all cases in which it was considered in this investigation (PAHs, PCBs, pesticides, trace metals), the export value was trivially small.

The effects of pulses of organic-rich, dredged materials on species diversity or community structure is now also in the process of being investigated. In the present rendition, a simplified assemblage of three "generic" macroinvertebrates was considered: a segmented polychaete annelid worm, a protobranch bivalve mollusc, and a lysianassid amphipod crustacean. These were not meant to represent any particular species or assemblage, but rather to represent hypothetical species inhabiting a deep-sea sediment that had the depauperate nature of an oligotrophic abyssal plain.

Two net population parameters were varied as a function of the input of organic matter and resultant animal density: intrinsic rate of natural increase (r) and mortality. It was presumed that the net balance between the overall sum of these two rates resulted in either an increase or decrease in animal numbers. Therefore, the balance was tinkered with by various biological processes to

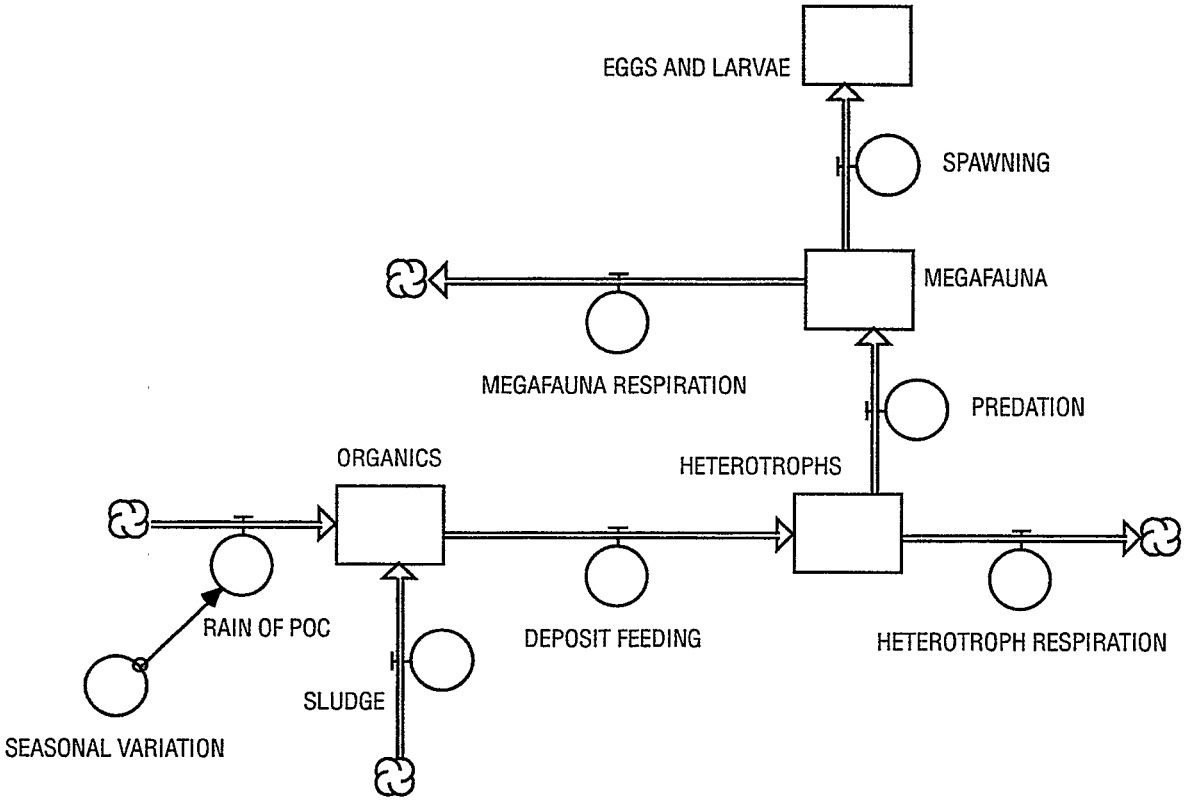

Fig. 47 — Conceptual model of simplified deep benthic food chain, based on Smith (1992), as modified by Rowe (1997a, 1997b)

result in different growth curves for each separate species. If the species had different growth curves, then the ultimate structure of the assemblage would be different under DOR conditions than it would be under "normal" oligotrophic conditions. It must be kept in mind that these three species are entirely hypothetical: we know little about the demographics of deep-sea species. While considerably more information is now slowly becoming available on shallow-water communities, actual numerical simulations designed to replicate species numbers in specific shallow-water environments have not been attempted (Zajac and Whitlatch 1985).

A basic assumption was that normal rates of mortality for juveniles on oligotrophic abyssal plains was relatively high due to starvation. Therefore, this starvation might, in some cases, be alleviated by DOR. The response to this alleviation, however, would vary with species, thus resulting in a net increase in numbers that varied between species. The net increases would continue in response to the DOR until the resources were depleted or until some other "density-dependent" process comes into play. Since the organisms in question in the environment under consideration have an initial condition of small individuals spread out over a relatively large area (several hundred individuals per square meter), any density-dependent decrease in net rate of increase is not assumed to be related to competition for space or for food. Something else must come into play if their "final" densities at the top of the growth curve are substantially different.

The solutions for the differential equations used in the simulation of "*r* vs. *K*" strategies follow:

Amphipod_Crustacean(t) = Amphipod_Crustacean(t – dt) + (Amphipod_Births – Amphipod_Predation – Amphipod_Deaths) * dt

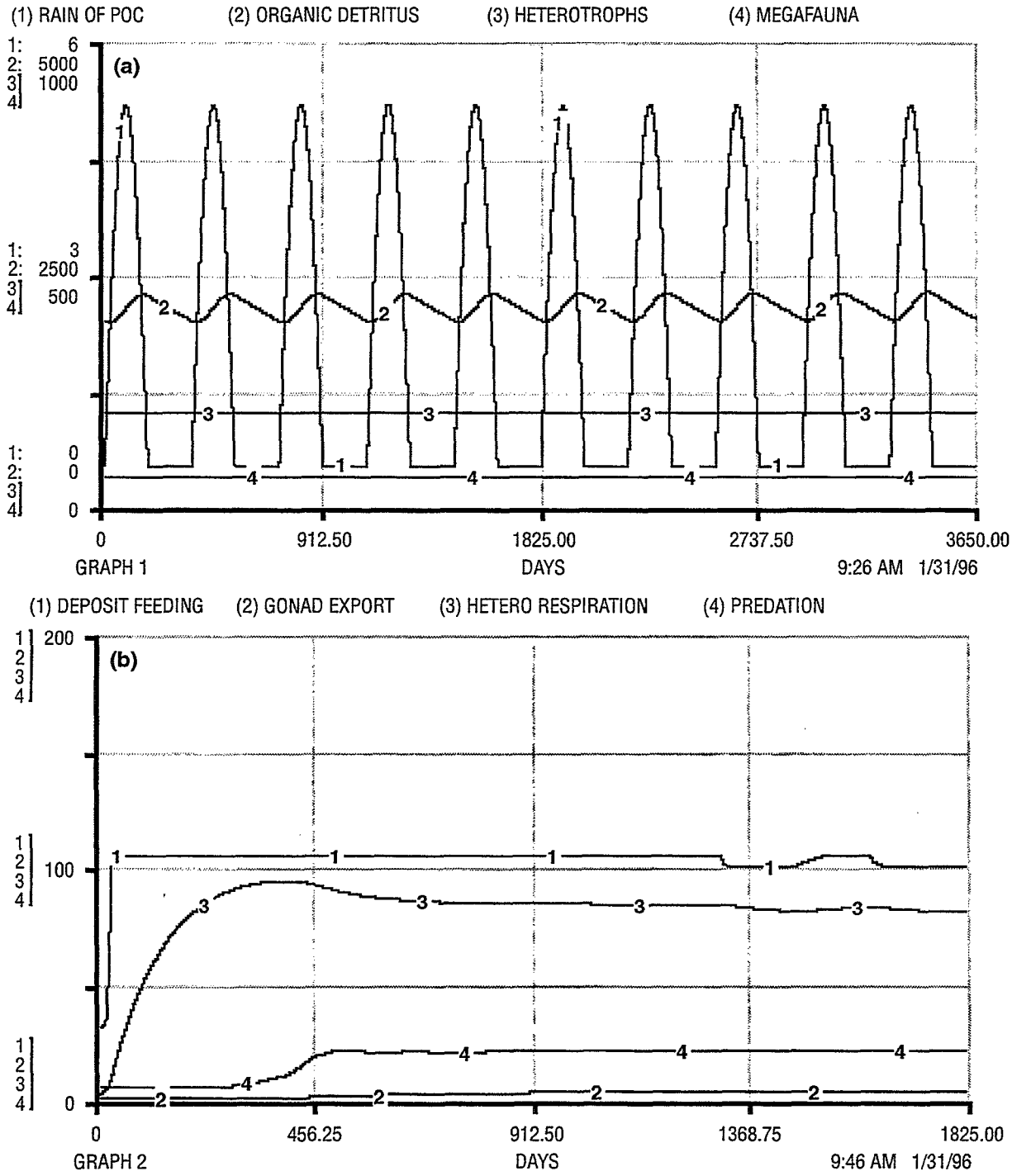

Fig. 48 — (a) Results calculated for the deep Pacific four-box model (Fig. 1) at steady state. Flux units (No. 1) are mg C m^{-2} d^{-1}. Stocks (Nos. 2, 3, and 4) are in mg C m^{-2} (from Rowe 1997b). (b) Results of time-dependent simulation of the four-box model (Fig. 1) from the deep Pacific (Smith 1992), but under DOR conditions. Fluxes (Nos. 1–4) are in units of mg C m^{-2} d^{-1}. This represents a DOR site in which 100 mg C $m^{-2}day^{-1}$ are being continuously released into the site for the entire simulation. This is reproduced from Rowe (1997b).

Clam(t) = Clam(t – dt) + (Clam_Births – Clam_Predation – Clam_Deaths) * dt

Polychaete_Worm(t) = Polychaete_Worm(t – dt) + (Polychaete_Births – Predation – Polychaete_Deaths) * dt

Organic_Matter(t) = Organic_Matter(t – dt) + (Rain_of_POC + Dredged_Materials – Respiration – Burial) * dt

Initial densities of organisms consisted of:

Amphipod_Crustacean = 8, Clam = 12, and Polychaete_Worm = 10,

with units of individuals per square meter of seafloor.

The initial condition for the organic detritus consisted of:

Organic_Matter = 2500, with units of mg. C m^{-2}.

(Note that this is approximately two orders of magnitude lower than the bulk value in Smith (1992).)

The fluxes into and out of the amphipod stocks were parameterized:

Amphipod_Births = Amphipod_Crustacean*Amphipod_Natality;
Amphipod_Predation=IF(Amphipod_Crustacean)>30THEN(Amphipod_Crustacean*Amphipod_Predation_Rate)ELSE(0);
and
Amphipod_Deaths = Amphipod_Crustacean*Amphipod_Mortality.

The fluxes into and out of the clam standing stocks were given the form:

Clam_Births = Clam*Clam_Natality;
Clam_Predation = IF(Clam)>20THEN(Clam*Clam_Predation_Rate)ELSE(0);
Clam_Deaths = Clam*Clam_Mortality.

Finally, the fluxes into or out of the living polychaete worm state variable box:

Polychaete_Births = Polychaete_Worm*Polychaete_Natality;
Predation=IF(Polychaete_Worm)>75THEN(Predation_Rate*Polychaete_Worm)ELSE(0);
Polychaete_Deaths = Polychaete_Worm*Polychaete_Mortality.

Two forcing functions (inputs of carbon) had the following forms:

Rain_of_POC=IF(Seasonal_Variation<0)THEN(3.5)ELSE(Seasonal_Variation*20)+3.5;

and

Dredged_Materials = IF(TIME>90)AND(TIME<450)THEN(500)ELSE(0).

Fluxes out of the organic carbon concentration box (exports or sinks) were zero-order flows with the following values:

Respiration = 9.5, and Burial = .5.

The units were mg C $m^{-2}day^{-1}$.

Constants used in the above parameterizations:

Amphipod_Natality = .03
Amphipod_Predation_Rate = .04
Clam_Natality = .04
Clam_Predation_Rate = .04
Polychaete_Natality = .04
Predation_Rate = .04
Seasonal_Variation = SIN(PI*TIME/182.5)

The following relationships define how mortality (other than predation) is a function of the input of natural organic matter, e.g., the rain of POC that varies seasonally. Nonlinear relationships were used to define the relationships between mortality and the input of natural organic matter into the system. Following each equation are pairs of numbers. The first number in each pair represents the input of organic matter and the second value is the "mortality constant." Note that as input increases, mortality decreases. In other words, with no input of POC, the mortality of each species is the constant given times the standing stock. The organisms are "starving," but at different rates. As the POC increases, the mortality rate of each species declines, but these decline at different rates. In other words, their survival varies.

Amphipod_Mortality = GRAPH(Rain_of_POC)
(0.00, 0.065), (2.00, 0.04), (4.00, 0.025), (6.00, 0.015), (8.00, 0.005), (10.0, 0.005), (12.0, 0.00), (14.0, 0.00), (16.0, 0.00), (18.0, 0.00), (20.0, 0.00)
Clam_Mortality = GRAPH(Rain_of_POC)
(0.00, 0.1), (2.00, 0.06), (4.00, 0.035), (6.00, 0.03), (8.00, 0.025), (10.0, 0.02), (12.0, 0.015), (14.0, 0.01), (16.0, 0.00), (18.0, 0.00), (20.0, 0.00)
Polychaete_Mortality = GRAPH(Rain_of_POC)
(0.00, 0.09), (2.00, 0.055), (4.00, 0.025), (6.00, 0.01), (8.00, 0.00), (10.0, 0.00), (12.0, 0.00), (14.0, 0.00), (16.0, 0.00), (18.0, 0.00), (20.0, 0.00)

Mortality that results from burial was defined to be negligible for both the clam and the worm; they can wriggle out of any sediment burden up to about 10-cm depth. However, an increased mortality or death was added to the amphipod crustacean:

Amphipod_Burial = IF(Burial)>3THEN(0.3)ELSE(0)

The "burial" term referred to is the flux out of the organic detrital carbon box. The units on these fluxes for the carbon are in mg C m^{-2} day^{-1}, but the loss from the amphipod standing stock is in individuals m^{-2} day^{-1}. That is, 0.3 amphipods (per amphipod) are lost per day when these organisms are being buried by greater than 3 mg C $m^{-2}day^{-1}$.

Finally, note that the predation rates are parameterized as threshold values. At low initial values of population density, nothing bothers to prey on these three species. However, when particular thresholds are reached, then "something" begins to prey on them at a rate that is proportional to their population size. The higher the threshold, the less ideal a prey item is to the predator and, therefore, the higher the ultimate value of the population. There is no evidence one way or the other that such a process operates in the deep ocean. However, such thresholds are often observed in other ecosystems.

7.4 Discussion of Model Results

There are a number of unanswered questions that plague the modeling of deep-ocean food chains. The growth rates, that is, the shapes of the growth curves of individual species in response to "new" carbon sources (the relocated sedimentary materials) have not been validated. The results in Fig. 48 suggest that deep-living communities will respond to new supplies of carbon and end up with a biomass similar to that in shallow water, but this needs to be tested. These species may not grow on relocated, dredged material.

Effects of shallow-water sediments (relocated) on species diversity in the deep sea is suspected based on "tray" experiments (Snelgrove et al. 1996), but the processes that contribute to control the rate and final outcome of the succession have not been quantified. The growth rates in response to new carbon sources have been varied in the model of three different species (Fig. 49) to illustrate

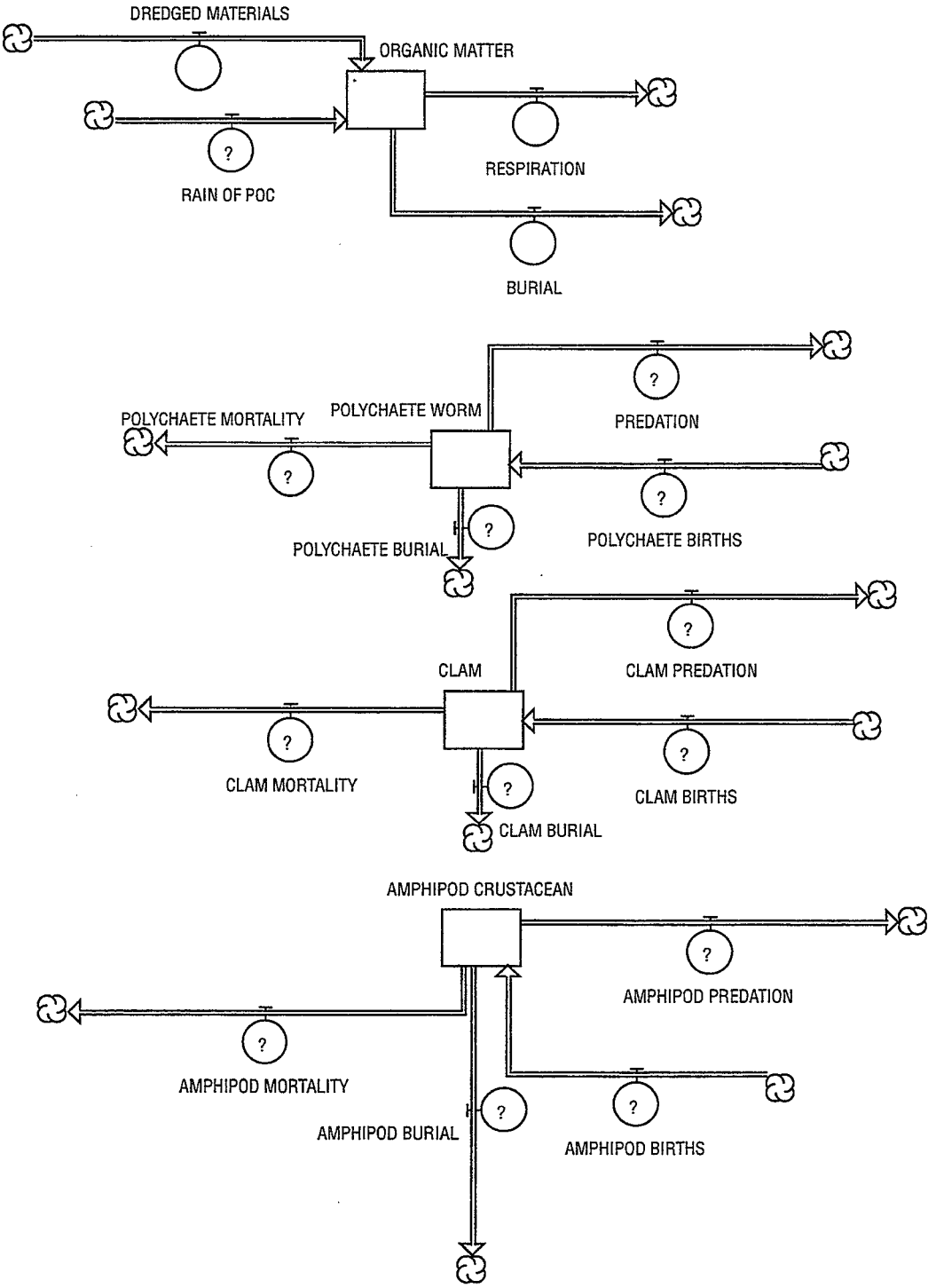

Fig. 49 — Conceptual diagram of three linked simulations. Top diagram represents simplified cycling of organic matter on the deep seafloor: inputs are natural rain of POC and organic carbon in dredge materials from shallow water relocated at an abyssal site. Sinks are community respiration and burial. Units are mg C $m^{-2}day^{-1}$ for the fluxes and mg C m^{-2} for the single stock. Bottom three diagrams are three hypothetical species in a deep-sea assemblage on an oligotrophic abyssal plain. The fluxes represent the processes controlling numbers of individuals at any given time: birth, death (by "starvation"), burial, and predation. Units are individuals m^{-2} for the stock size. Units for the fluxes are individuals $m^{-2}day^{-1}$.

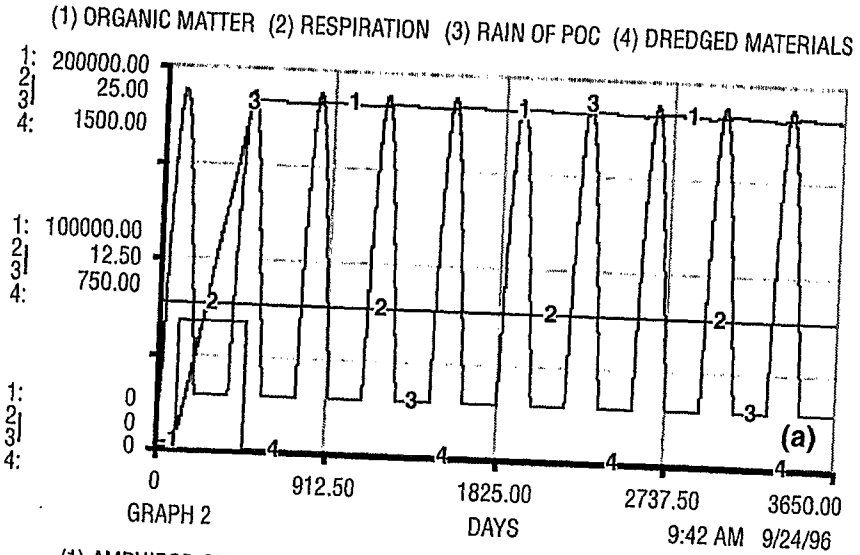

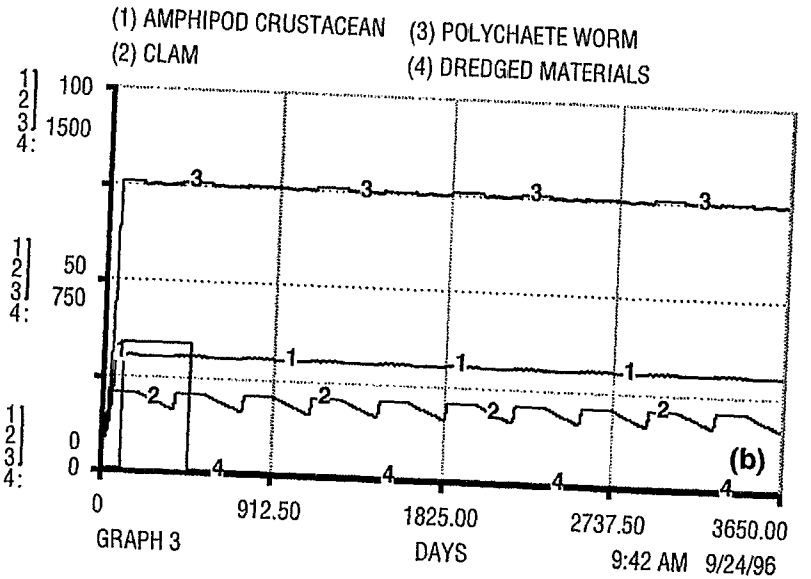

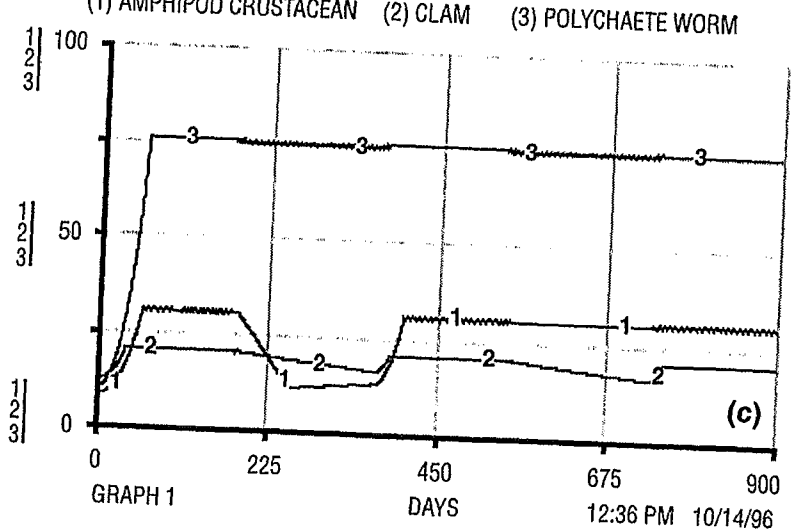

Fig. 50 — Results of a simulation of the effects of POC and DOR of dredged materials on a deep-ocean sediment community. (a) and (b) run for 10 yr, whereas (c) runs for just less than three. (a) Note variable values on the y axis. Concentrations (No. 1) and fluxes into a hypothetical deep-ocean relocation site (DOR). Input of material (No. 4) lasts for 1 yr and has a value of 500 mg C $m^{-2}day^{-1}$. (b) Variations in concentrations of variables at a DOR site in response to organic carbon concentrations. Variations over time are a function of births and deaths regulated by POC input, births, and predation. (c) As in (b), except with added mortality in amphipods due to burial by dredge spoils.

that "relief" from starvation could allow some to grow or reproduce faster than others. This would result in a "dominance" by the fast growers (Fig. 50), which would be reflected in a decline in apparent diversity and a decrease in evenness, but the species list would retain the same length. That is, no species were eliminated. Predation has been used as a control on the upper limit of a species' numbers (Fig. 50c). It is a death term that is density dependent because it "turns on" at some threshold above which it becomes profitable for the predator to utilize the prey.

Concentration factors of toxicants in shallow-water sediments are unknown for deep-sea organisms. The return of heavy metals and organic contaminants out of the deep ocean via reproductive products is only conjecture (Rowe 1997). Effects of burial on deep-ocean benthos is based on inferred effects of and responses to turbidity flows, not on dumping (Young and Richardson 1997); the response of the organisms to dredged material emplacement may be very different. Figure 36c illustrates an added mortality of amphipods due to burial with recovery at the end of the year; however, experiments to test these processes need to be conducted.

It must be stressed throughout this analysis that the variables introduced in the models were entirely hypothetical. They were introduced as possible sources of variation in animal numbers to explore how they might be responding to a relocation of dredged materials on the deep seafloor. Each result is simply one set of conditions that could diminish diversity and increase dominance. The value in the above analysis is that it provides a list of the kinds of information that might be necessary to determine by field sampling and experimentation if one needed to explain successional patterns in response to DOR.

8.0 SCRIPT FOR VIDEO

by Robert Moorhead, Lamont Berger, David K. Young, Philip J. Valent, and Andrew W. Palowitch

8.1 Background

Robert Moorhead and Lamont Berger, Mississippi State University, charged with producing a visualization of simulations for the SimDOR Project, stressed in the early stages of SimDOR that a working script was necessary to guide the actions necessary to produce a high-quality video within the time frame of the project. The first script, written in October 1995, bears little resemblance to the final version in August 1996, which became the audio accompanying the final video in September 1996. The script was a primary working document for each project meeting and helped define and direct the analyses and numerical simulations discussed in previous sections of this report. All project participants helped in editing and changing the script as it went through numerous drafts throughout the year. Although David Young and Philip Valent assumed primary responsibility for writing the initial drafts of the script, Robert Moorhead and Lamont Berger produced the final copy narrated in the video.

Development of that portion of the SimDOR visualization describing the dredging transfer and loading, transport, and release-fall-impact of material commenced with a standard engineering systems requirements analysis, but transitioned midway through the design effort to video presentation. As soon as CAD drawings were prepared in ProEngineer, the fundamental building blocks were available for incorporation into Alias/Wavefront animation. The standard engineering process continued as shown in Fig. 51, with the final design evolving after iterations through internal and external review cycles. With a final design captured in engineering drawings, solids rendering and animation of the equipment and platform was completed and set into the marine environment. Files were

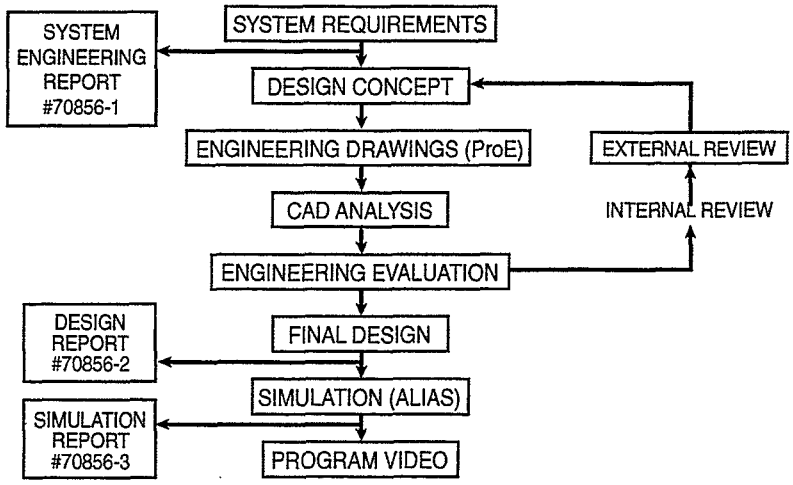

Fig. 51 — Process followed in reaching preliminary engineering design for DOR, collection and exercise of subsystem performance models, and assembly of performance visualizations into SimDOR video

developed and saved in .pix format at a resolution of 640 × 480 and then copied and transferred on CDROM to the Mississippi State University Television Center. At the Center the files were edited, compiled with the rest of video footage, and dubbed with audio to create the final product.

8.2 The Script

A version of the final script, modified slightly to improve its readability in absence of the video portion, is reproduced here as representing an accomplishment of the SimDOR Project. This reproduction serves to summarize the scientific and technical rationale behind the numerical simulations and analyses presented in this final SimDOR report. References and figures are included to provide primary sources of information and documentation, so this section of the report can stand alone as a SimDOR product. The text is written in present tense as is the video.

8.2.1 The Problem

With increased international trade and continued growth of port cities in the United States, keeping vital shipping ports dredged and continuously operating is of national importance. Finding a cost-efficient, environmentally safe, and politically acceptable alternative to land-based disposal of dredged material is becoming increasingly important to the welfare of our economy, our nation, and our national defense (NRC 1985).

Each year, 400 million cubic yards of sedimentary materials are dredged, of which 3 to 5 percent is contaminated and cannot be used beneficially or returned to the environment near dredging sites. Disposal of this contaminated, dredged material is a national problem (NRC 1989). Contaminated sediments in our nation's coastal waterways are a reservoir of toxins that can be passed through food webs potentially to man via bioaccumulation pathways. Removal of the contaminated sediments from harbors would remove this continued source of toxic material from the nation's productive coastal waters.

By law (Marine Protection, Research, and Sanctuaries Act 1972, Public Law 92-532), contaminated dredged materials, after removal from the ocean floor, either have to be isolated from the environment or be chemically altered, rendering them safe for disposal (EPA 1991). Remediation of contaminated

wastes, though technically feasible, is very expensive and is currently being tested and used only on a limited basis. Alternative solutions, such as shipping contaminated, dredged materials to inland sites remote from human habitation, are currently practiced.

The number of available disposal sites is steadily declining due to environmental, sociological, and political constraints. Rising landfill costs severely limit land-based disposal methods. The primary problem is to minimize environmental impacts upon humans and to our air, water, and food supplies by assuring that contaminants are isolated. But even if we can continue the expense of operating well-managed, contaminated waste material landfills, how much longer can we continue to consume valuable land space by this practice?

8.2.2 A Solution

A practical solution to this problem is to relocate and isolate contaminated, marine-dredged material on the seafloor of the abyssal ocean. The abyssal ocean encompasses those areas where the water is deeper than 3000 m. These isolated ocean regions contain most of the world's water and cover over half of the surface of the globe.

SimDOR, a project sponsored by the Defense Advanced Research Projects Agency and conducted by NRL, focuses on simulation of the scientific and technical issues involved with disposal of contaminated, dredged material in the abyssal ocean. SimDOR, which stands for Simulation of Deep Ocean Relocation, concentrates primarily on sites on the abyssal seafloor of the North Atlantic Ocean and dredged material coming from the eastern seaboard of the United States. Results from the SimDOR project are also generally applicable to west coast and Gulf of Mexico ports, as reported from an earlier study assessing suitability of deep-water sites within 1000 nmi of the continental United States for disposal of wastes (Young and Valent 1996). The SimDOR Project took advantage of recent advances in numerical modeling capabilities, simulation concepts, and visualization technology. Concepts and analytical models were developed and integrated to enable simulation of the dredging, transport, and isolation of dredged material in geosynthetic fabric containers to ensure that the contained material passes through the upper layer of the ocean without detrimentally affecting organisms in this productive region.

8.2.3 Containment and Delivery System

The containers, fabricated from geosynthetic fabrics of woven polyester or nylon fibers, have been used internationally in a range of beach replenishment, erosion prevention, island creation, and sediment disposal applications. The strength and durability of these fabrics assure long-term containment of sediments in marine environments (Valent et al. 1996). A system to dredge sediments, load the geosynthetic fabric containers, transport them to the ocean site, and ensure their safe descent to the seafloor has been proposed and extensively studied (Fig. 52).

During the dredging and disposal operation, potentially polluted dredged sediments must be contained. A specially designed clamshell dredge completely encapsules underwater sediments so that the amount of sediment released into the water at the dredge site is minimized. While maintaining the efficiency of commercial clamshell dredge operations, the total containment clamshell dredge head minimizes leakage while the crane arm moves out of the water and over to the storage hopper.

Large debris is removed from the dredged sediment in the storage hopper with separator screens and grinder rollers. Transfer augers lead up from the bottom of the storage hopper to control flow

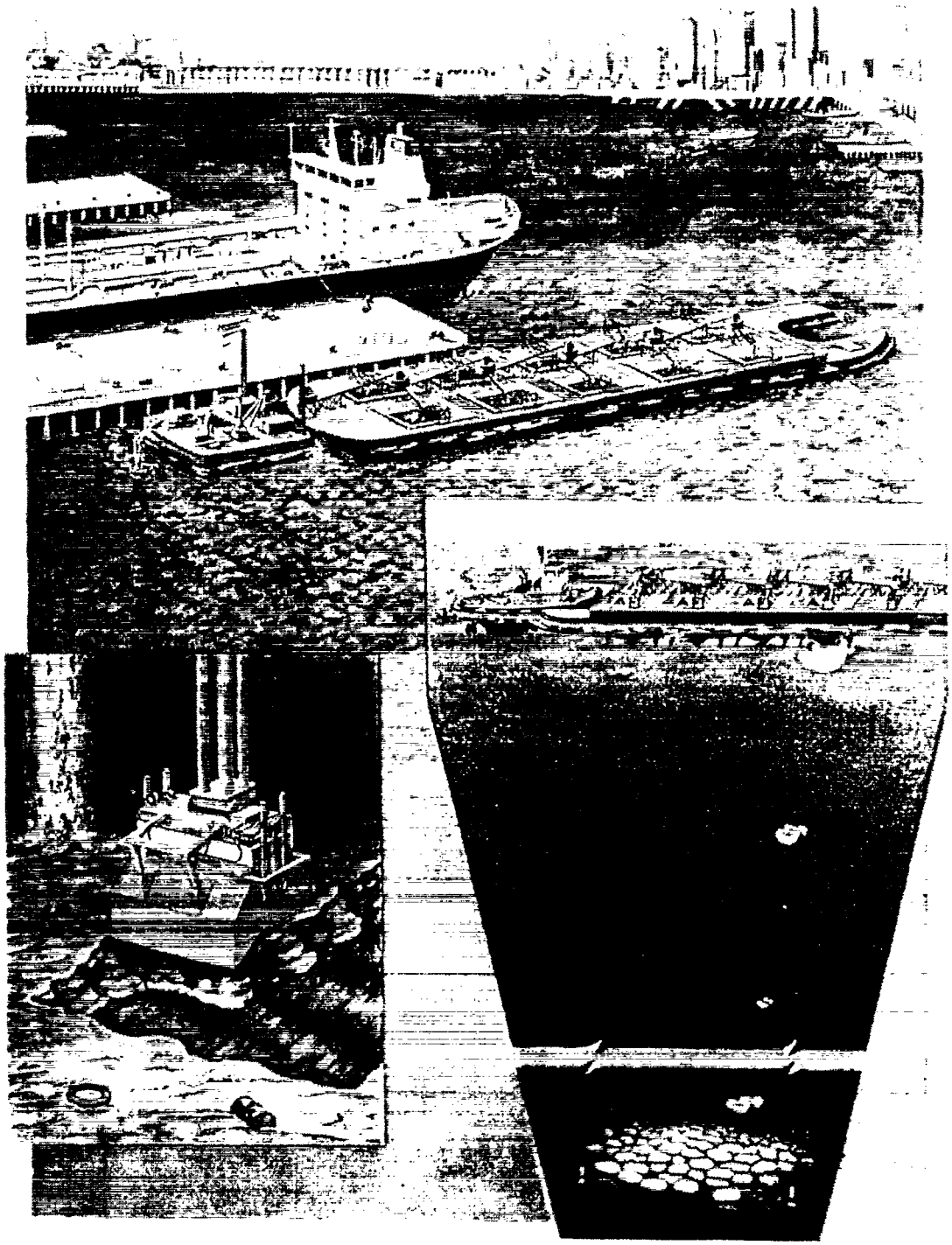

Fig. 52 — The deep-ocean relocation process for dredged materials involves the removal of contaminated sediments from harbors and navigation channels (lower left), the transfer and loading of the material into an ocean-going transporter (top), and the transport and free-fall of the material to the abyssal seafloor in geosynthetic fabric containers (lower right)

rates during sediment distribution to the transporter (Fig. 53). The totally enclosed auger pipes prevent the possible spread of pollutants from the sediments during container loading. Once on the transporter, a set of five distribution hoppers feed the 20 geosynthetic fabric containers that are positioned in segmented cells (Figs. 52b and Fig. 54). Each container is filled with roughly 800 cubic yards of sediment through a top central spout that is closed when loading is complete.

The transporter is then pushed by an ocean-going tug to the open-ocean disposal site during sea states less than four (Fig. 55). Physics-based dynamic modeling, also used to test the transporter for stability in heavy sea states, indicates that the transporter would have to be pulled in sea states greater than four. The design process considered not only the vessel's design, but the economic and operational viability of the entire process.

Using satellite positioning and ocean current measurement techniques, the transporter locates a release point such that the container will free-fall to a precise area on the abyssal seafloor. The containers are sequentially released from their individual cells by retracting the cell top locking rails. The weight of the sediment forces open the bottom doors and initiates the container's descent. Discrete element and numerical flow modeling techniques were used to assess risk during container release, descent, and bottom impact. Stresses within the container fabric during these periods

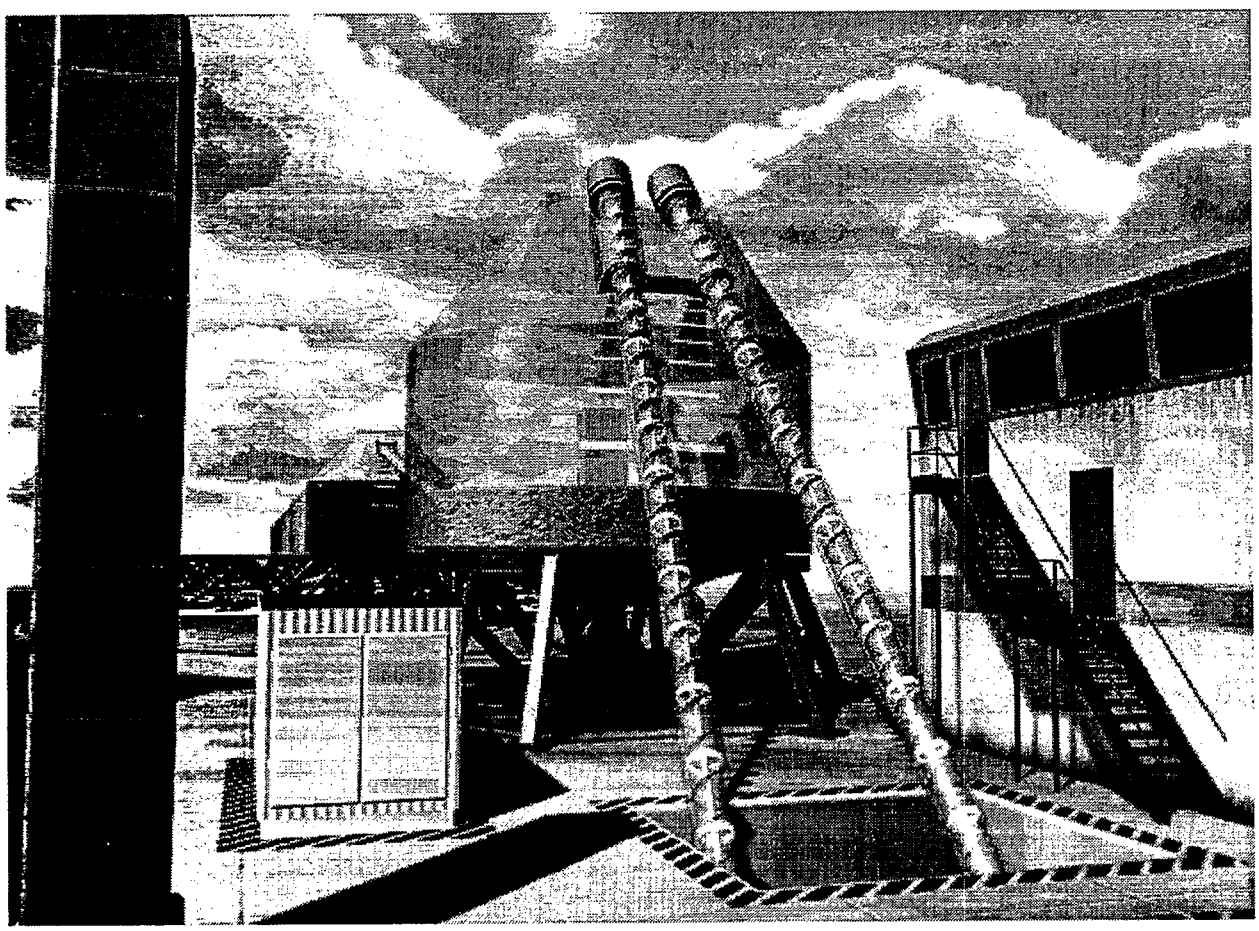

Fig. 53 — Contaminated sediment is transferred from the storage hopper beneath the dredge platform to the transfer hopper with the closed augers. Auger drive motors are positioned at the top of the auger screws.

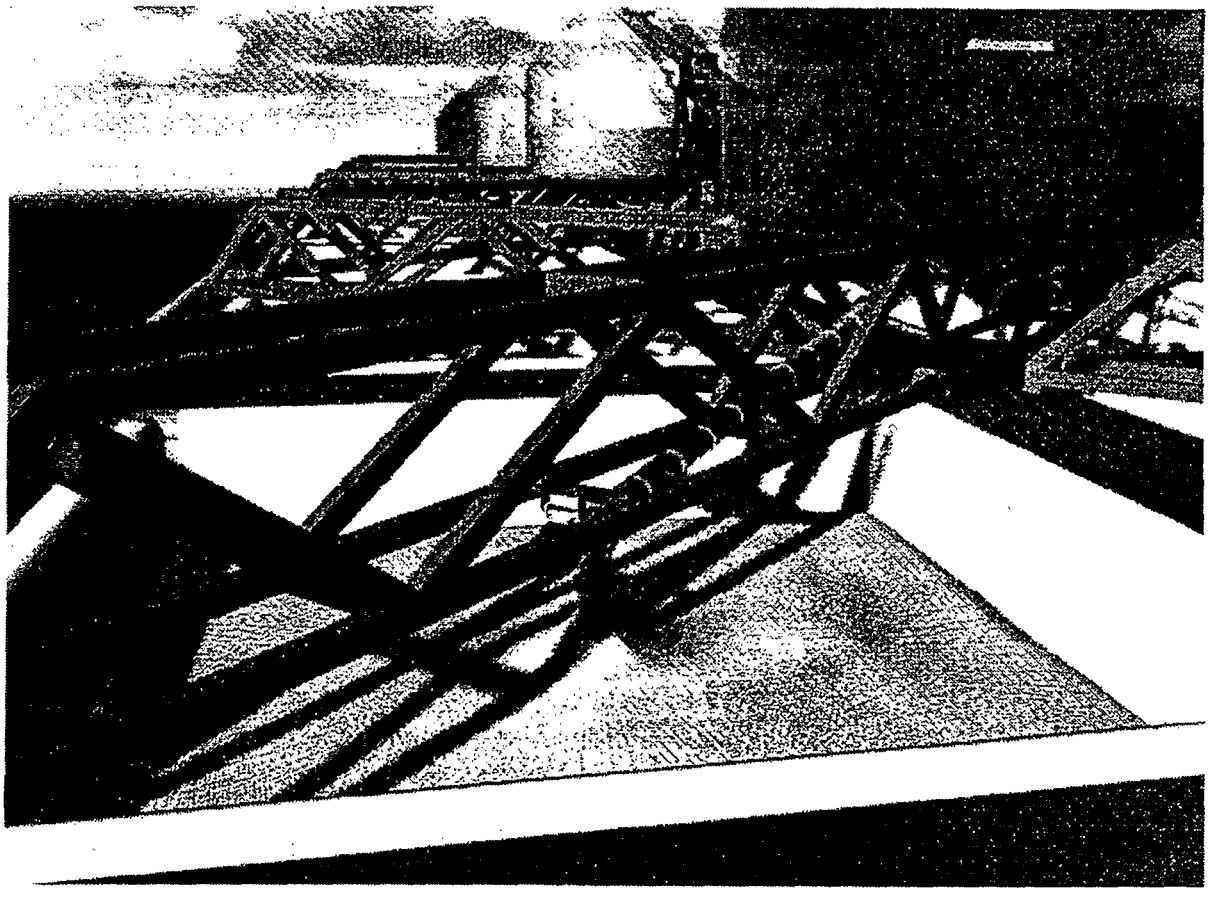

Fig. 54 — The sediment distribution system consisting of hoppers and augers delivers sediment to 20 geosynthetic containers located in cells on the transporter. The containers are filled through top center fill spouts that are sealed prior to the transporter's departure from port.

rapidly change, risking container rupture. The prediction of high stress areas assists in developing deployment hardware and operational procedures. During its descent, the container reaches a steady-state downward velocity of about 5 m/s. Upon reaching the bottom, the container settles into a slumped shape.

8.2.4 The Abyssal Environment

Once the containers are deposited on the seafloor, what is their long-term environmental impact upon the abyssal seafloor site? Scientists now know that many parts of the abyssal seafloor, far from continental land masses, are geologically stable and are not subject to frequent disturbances characteristic of shallower water and land masses that are exposed to the atmosphere (reviewed by Gage and Tyler 1991). The lack of seafloor relief in the abyssal ocean is contrasted with the steep slopes and roughness of continental margins.

As one progresses seaward from continental margins, the abyssal seafloor typically becomes progressively smoother without underwater mountains or hills. Abyssal plains are covered by a fine, thin layer of pelagic or hemipelagic sediment. These large, nearly flat abyssal plains are deposits of mud, silt, and dead marine organisms that have accumulated gradually over millions of

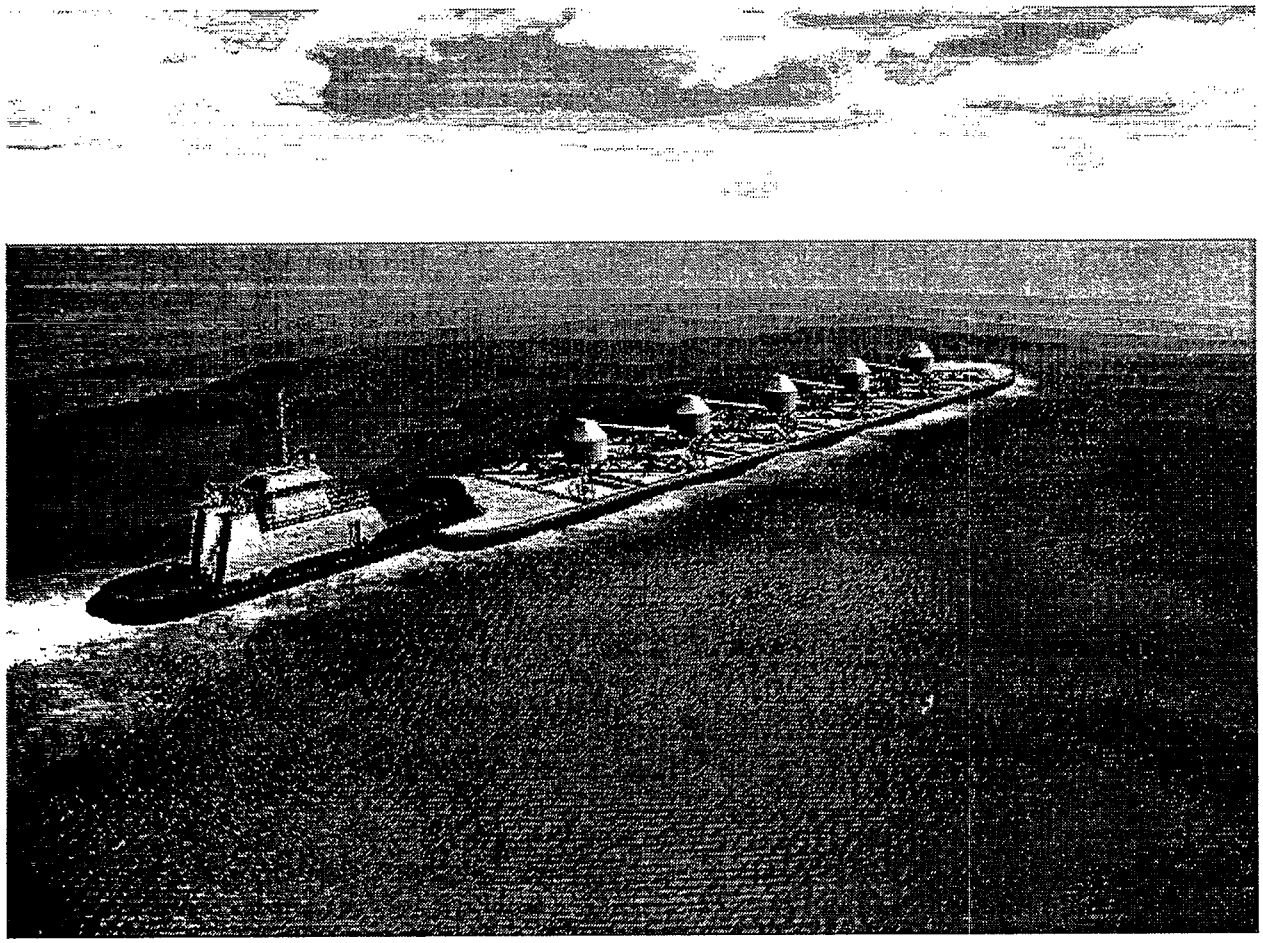

Fig. 55 — Transporter shown in transit from port to the ocean disposal site with a tug positioned in conventional ITB configuration

years. In the abyssal ocean there is no sunlight, the waters are constantly below 4°C, and the pressure is several hundred times greater than at the sea surface.

8.2.5 Site Selection

With so many variables, how does one find suitable sites for isolating materials on the abyssal seafloor? To answer this question, scientists turned to a site selection model that was developed at NRL to quantitatively compare the suitability of abyssal seafloor sites for waste isolation (Fleischer 1995). Areas were divided into 1-degree squares (latitude-longitude) and scorable factors were chosen that apply to the biologic, geologic, oceanographic, meteorologic, and anthropogenic criteria of significance to siting for waste isolation. Areas were excluded beyond 1600 km of the U.S. coastline, within foreign economic zones, and shallower than 3000-m depth. The entry of factors into the computer model and their weighting and scoring was carefully designed to maximize an effective environmental isolation plan.

The most favorable 1-deg squares in the North Atlantic for the isolation scenario are in the Hatteras Abyssal Plain. The characteristics of these areas are a nearly flat, uniform, muddy bottom,

tranquil water over the seafloor, and long distances from other human activities such as shipping lanes and submarine cables (Fig. 56).

8.2.6 Environmental Simulations

Simulations of the North Atlantic ocean circulation, conducted with the NRL basin-scale, multilayer model, show that average current velocities and kinetic energies of the mean flow of abyssal currents at the selected sites are very low (Gallacher 1995). This is part of a worldwide circulation pattern that cycles water from the surface through abyssal depths and back again on the time scale of centuries. Water that flows through the western North Atlantic in the region of the Hatteras Abyssal Plain may not come to the surface of the ocean for hundreds to thousands of years.

High-resolution computer simulations show that effects from impact of the geosynthetic fabric containers with the seafloor will remain local to the site (Gallacher 1997). Although sizeable plumes may result from this impact, the low levels of turbulent energy ensure that the dispersion of suspended and dissolved material will be minimal.

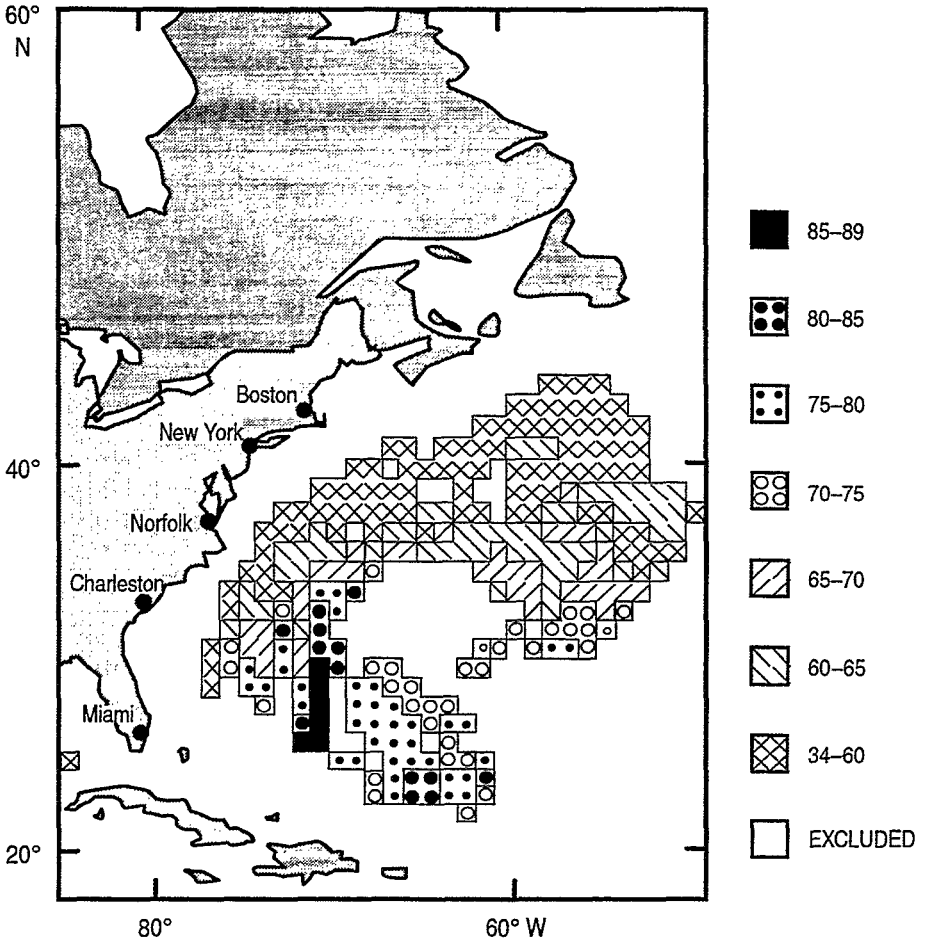

Fig. 56 — Map scores (percent) for isolation scenario using the site selection model for the North Atlantic Ocean (from Fleischer 1995)

Numerical simulations have been conducted to predict the rates and distributions of deposition and remineralization of a 1-yr disposal of 8.5 million cubic meters of dredged material on the abyssal seafloor (Jahnke 1995). As the organic matter within the deposit decomposes, oxygen and sulfate in the underlying sediments are depleted. Simulation results indicate that the oxygen-depleted zone does not significantly spread laterally into the surrounding sediments, but rather is essentially confined to the sediments directly below the deposit. Additionally, there is no significant anoxia of the overlying water affecting areas adjacent to or downstream from the site of deposition. Return to geochemical equilibrium conditions may take as long as thousands to tens-of-thousands of years. This should be no surprise because most turbidite deposits, which are natural analogs of the relocation process, have not yet reached geochemical equilibrium despite being laid down 10,000 years ago.

Ten-year numerical simulations of an abyssal food chain have been run to determine effects of increased organic matter on the organisms (Rowe 1995). At sites where animals are not buried, model results show increased growth rates and altered periods of growth. The food chain model was also used to simulate contaminant transport by incorporating PAHs into simulations. Results from these simulations suggest that the one hypothetical pathway for PAHs to leave abyssal depths is by transport in the yolks of eggs of certain of deep-sea invertebrates and fishes. The potential for measurable biological transport of contaminants by this pathway, however, is negligible.

8.2.7 Conclusions

These results show that potential environmental impacts resulting from relocating contaminated, dredged material to the abyssal seafloor would be localized at the disposal site, which would occupy less than one millionth of the deep-sea area. The local changes that would occur have to be balanced by the immediate detrimental effects occurring in many of our harbor areas posed by the *status quo*. Research and development for finding new and innovative alternatives to the disposal of contaminated, dredged materials must continue to determine safe, economical, and dependable isolation methods for the growing problem of managing these materials. The DOR program offers the potential for an economically sound and environmentally safe alternative to land-based waste isolation that can help reduce the amount of contaminated, dredged material deposited on an ever-decreasing amount of available land.

9.0 SUMMARY OF PROJECT RESULTS

by Philip J. Valent and David K. Young

9.1 Background

The SimDOR Project was designed to pick up where the SERDP-sponsored APWI Project left off, but was to focus only on the management of polluted, dredged material. SimDOR differed also from APWI in that the SimDOR scope was broadened to include the dredging operation rather than beginning the study as APWI with the loading of the ocean-going transporter. The SimDOR Project was proposed to include an analytical connection of models, physics-based wherever possible, to enable simulation of polluted, dredged material management via the abyssal seafloor isolation option. The project was to include the development of a video illustrating and clarifying the abyssal seafloor isolation option for the layman with physics-based modeling results giving credence to the technical and environmental projections presented wherever possible.

9.2 Findings

9.2.1 General

One finding was that the design, development, and production of the SimDOR video consumed significantly more time and funds than initially estimated. The emphasis on the video demanded of each project participant is responsible for the less-than-expected interconnection achieved between analytical, physical models describing the end-to-end process of applying the abyssal ocean option to dredged material management. However, the video product did turn out to be, potentially, an effective, high quality communication product meriting the investment of time, energy, and funds.

9.2.2 Dredging System

The technical subcontractor to SAIC, Oceaneering International, Inc., opted very early in the project for employing the Total Containment Clamshell Dredge (TCCD) concept for the SimDOR system. This concept, developed and tested by Oceaneering in a scale model under other funding, was judged by Oceaneering to be the best choice of the few "clean dredge" concepts from standpoints of minimizing pollutant quantities released to the environment at the dredging site, throughput of the system, etc. Review of the TCCD concept design and working model performance by the Principal Investigator indicates that the selected dredging system may well be the optimum; however, field performance comparison of a full-scale TCCD with existing systems, especially the Pneuma Dredge used in Europe, is required before a final decision on an optimum dredging system is rendered. It is likely that such a comparative study would find different systems to be optimum performers for different dredged material types and other environmental factors, including rubbish, water depths, currents, surface wave conditions, etc.

9.2.3 Dredged Material Transfer System

Oceaneering International applied the contained auger-feed system to the DOR concept to minimize the water content of the dredged material. (A pumped-material transfer system would require addition of water to make the material pumpable.) This design decision appears quite sound and quite consistent with experience in the bulk material transfer industry. The impact of the decision is far-reaching, resulting in a decrease in the transport barge dead weight tons (DWT) required from 25,000 to 20,000 for the same payload of dredged material, and results in a loaded barge draft of 5.5 m (18 ft) to enable the transport barge to be brought right up to most maintenance dredging sites for direct loading, eliminating the need for lightering of dredged material.

9.2.4 Dredged Material Transport System

Oceaneering continued their development of the integrated tug barge (ITB) concept resulting in a barge with two rows of cargo cells, each containing ten cells. (For a 20,000 DWT transporter, this design would result in 1,000 tons per cell and per GFC, which is probably close to the high side limit per GFC for minimizing fabric rupture potential.) Oceaneering contracted out a preliminary structural design study to ensure adequacy of the structural design up through sea state 8. This structural check is not integrated into the modeling for the simulation. SAIC performed a sea-keeping analysis of the transporter alone, i.e., tug not connected to the barge in the push mode. Output of the sea-keeping model is included in the video. This analysis does show that the ITB mode of transport would be in trouble above sea state 5; therefore, the tug operator would have to

switch to a towing mode of transport before getting into the sea state 5–8 regime. This required change in transport mode impacts on the overall economics of the abyssal seafloor isolation option because the Oceaneering International cost estimate is based on a 15-kt transport speed, whereas in the towed mode, the system would be slowed to 12 kt, increasing the transport costs by 20% and the overall cost per cubic meter by 10% for that time period when the system is required to operate in the towed mode.

Another item of concern regarding the Oceaneering transporter design is the GFC loading system mounted on the topside of the barge. The five distribution hoppers, the enclosed feed augers, and the drive motors are all exposed on the topside of the barge, subject to impact damage from any waves that may wash over the barge. Further, each of the cells is now open on the topside; these may require covers to exclude water from waves from temporarily filling the cells, driving the transporter deeper in the water, and making it easier for subsequent waves to wash over the transporter and damage the topside equipment.

9.2.5 Cargo Cell GFC Release Doors

The design and function of the cargo cell doors and their interaction with the GFCs is the most critical factor in the entire dredging, loading, transport, and placement operation. Most, and possibly all, GFC ruptures to date in USACE experience in the management of contaminated, dredged materials can be traced back to problems with the bottom door design/function. In their initial concept design under SimDOR, Oceaneering opted for four doors, one hinged on each side of the square cell and all meeting in the center of the cell (i.e., the edges of the doors describing the diagonals of the cell bottom). This design was seen as a way by which the doors would open very quickly before the contained material would have a chance to displace downward and stretch and abrade the GFC fabric against the door edges. However, analysis of the June 1996 partial rupture of a GFC at the New Jersey Mud Dump Site indicates that the GFC fabric may have abraded against the door edges during transport due to movement of the doors with heave, flexing, and torsional motion of the transport barge hull. To minimize potential for such door edge motions, Oceaneering changed the cell door design to a more conventional two-door design, with the opening edges of the doors restrained during transport by locking pins. Opening time duration for the new door design is about the same as the initial design. The dynamics of the door opening has not been coded into a software model.

9.2.6 GFC Exit from the Transporter Cell

NRL funded John Palmerton, U.S. Army Corps of Engineers Waterways Experiment Station (CEWES), to transition the CEWES two-dimensional discrete element model of the GFC exiting the transporter cell to the NRL Defense Advanced Research Project Agency (DARPA) Project. That transition was made exceptionally well. Exercise of the model showed some details in need of adjustment, including the occasional problem of elements of material contained within the "membrane" elements managing to extrude through the membrane (the modeled GFC wall). The model run result presented in the SimDOR video was "corrected" by simply washing over (erasing) an extruded element in the video editing. The GFC cell exit two-dimensional model is compatible for inclusion in an overall SimDOR simulation. Since Oceaneering has changed to a two-door concept, the two-dimensional model would likely simulate the prototype GFC-cell-seawater interaction reasonably well.

9.2.7 Free-Fall of the GFC

Bert Green, NRL Oceanography Division, bringing experience from earlier work on raindrop stability, has shown that the GFCs, during their 20-min, 5000-m, free-fall to the seafloor will approach the shape of a flattened ellipsoid with its short axis in the vertical direction. Further, because the pressure on the bottom surface of the GFC will be higher than that on the top surface (in excess of the potential head difference), the ellipsoid shape may dimple upward, approaching an umbrella shape. Martin Fritts, SAIC Annapolis, performed a finite element modeling of the hydrodynamics surrounding the GFC during free-fall. The vortices energy model result, is shown in the SimDOR video.

Fritts was not able to incorporate into his free-fall modeling for SimDOR an element of instability to account for nonsymmetry of GFC shape and distribution of material mass within the GFC. (This model development is important in predicting the distribution of GFCs resulting from any one surface release and important to predicting an eventual plan area covered by the deposit and deposit geometry; the work is programmed in DOR Phase II.) Both Green and Fritts believe they can add to our understand of the dynamics taking place within the GFC and the contained material during free-fall, but have not had the resources to approach the problem in SimDOR. Of particular concern are the strains and stresses developed in the GFC fabric walls due to the dynamics of the flattened ellipsoid.

Therefore, while a model is available to perform a two-dimensional simulation of the GFC free-fall without perturbations, the modeling of the perturbations is also needed for assessment of GFC fabric integrity and GFC distribution on the seafloor. This work is being transitioned to the DOR Phase II Project, and limited funding in FY97 will complete this numerical analysis by Green and Fritts.

9.2.8 Density Plume Model

In anticipation of that time when GFCs can be reliably released from a surface transporter with zero risk of rupture, the SimDOR Project has looked forward to the potential problem of GFC rupture on impact with the seafloor. Some small amount of water is added to the dredged material volume even when using the TCCD, and this free water is expected to work its way to the top of the dredged material contained in the GFC during transport. This free water would likely include some significant volume of particulate material from the dredged material with absorbed pollutants. If the GFC should rupture on impact, then this free water volume, consisting of less saline and warmer, and therefore less dense water, would rise as a plume in the denser abyssal water. Patrick Gallacher, NRL Oceanography Division, developed a three-dimensional model for this phenomenon showing that such a plume would likely not exceed 200 m in height above the seafloor and would dissipate rapidly, strongly indicating that this mechanism will not be a major contributor to pollutant dispersion from the immediate location of the isolation site. One illustration of Gallacher's model run results for a pair of GFCs impacting on the seafloor and both rupturing is also shown in the SimDOR video.

9.2.9 Plume Generation Resulting from Sediment Scour During GFC Impact

One mechanism of contaminant transport that has not been modeled is that of contaminated sediment scour due to high velocity exit of trapped water from beneath the GFC as it approaches the seafloor. It is assumed here that, over the time of operation of the isolation site, previously placed GFCs will deteriorate by some mechanism and their contaminated, dredged material contents

will be exposed on the seafloor. A newly released GFC could then cause scouring and suspension of these exposed materials and their absorbed contaminants. The suspended materials would move downcurrent beyond the perimeter of the placed GFCs and settle to the seafloor to form a thin apron of contaminated sediments. The volume and plan area of this contaminated apron must be modeled and verified. Martin Fritts, SAIC Annapolis, modeled the approach to and impact of the GFC on the seafloor for the SimDOR Project. However, the scour process and material parameters are different from those found in prior experience, and the results of extrapolation efforts were not convincing. Therefore, this very necessary link in the SimDOR simulation is not in place. (NRL has contracted with Martin Fritts, Bert Green and Phil Valent to assist, to complete this modeling effort and the description of the isolation site GFC deposit and apron in the DOR Phase II effort.)

9.2.10 Turbidity Flow Generation

In addition to the problem of scouring, suspension, and transport of contaminated sediments, the project team also considered the potential problem of contaminant transport via turbidity flows initiated by GFC impact on the isolation deposit. Turbidity flows, density currents entraining significant quantities of sediments and traveling at several kilometers per hour for hundreds of kilometers, are rare in the recent marine environment, but were the primary formative agents of the abyssal plains. The hypothesis of turbidity flows being a mechanism for contaminant transport in the abyssal isolation problem was not carried to a quantitative stage because of unknowns in scaling from the energy level of a GFC impacting on the seafloor as compared to that energy thought to initiate turbidity flows on the continental slope. Further, even though the exposed GFC fabric is expected to undergo deterioration with time, that fabric buried in the dredged material deposit may not, leaving the fabric as a very effective geosynthetic reinforcing material, greatly reducing the potential of initiating a turbidity flow. Therefore, the project team believes we have relegated the turbidity flow phenomenon to a non-problem for the abyssal isolation option WHEN GFCs ARE USED TO PLACE THE DREDGED MATERIAL.

9.2.11 One Isolation Site vs. Many

One of the first, and most significant, results of the SimDOR Project is the conclusion that one large isolation site would be a far better choice than opting for many small sites, such as would result from using a different site each year. This conclusion evolved from (1) the realization that each site would likely have an apron of contaminated, dredged material, probably very thin in the vertical dimension but of very significant areal extent and (2) the understanding that even a very thin layer of this highly organic material would alter the geochemistry and biology at such a location for hundreds of years. It is because of the large apron accompanying each isolation site that one is driven to consolidating deposits into one large deposit with one apron—granted, a large apron, but smaller in area than the collective area impacted by aprons from many individual sites.

9.2.12 Geochemistry of the Deposit

The geochemistry projections of Rick Jahnke, Skidaway, in the precursor APWI Project, addressed the deposit of waste material and the impacted subseafloor sediments beneath. The SimDOR environmental impact effort has focused on the deposit itself. The impact of bacterial inoculation rates and impact on the fate of heavy metal contaminants have been modeled. The potential of

methane hydrate formation in the dredged material deposit has been evaluated and found not to be a problem because of the relatively low biologically available carbon content (relative to available carbon believed necessary for methane clathrate formation). Similarly, the oxygen demand of the isolation deposit has been modeled and the resulting drawdown in available oxygen in the overlying water near the seafloor has been shown not to pose an environmental problem.

9.2.13 Biological Impact of the Deposit

The biological impact and contaminant transport projections by Gil Rowe, Texas A&M University (performed under the earlier APWI Project), assumed a linear relationship between carbon uptake and contaminant uptake. The SimDOR modeling effort is refining the parameters being used in the STELLA II model to include projected bioaccumulation of contaminants in the abyssal food chain. One new result is that certain fast-growing species in the presence of the new organic carbon source (relocated, dredged material) may dominate the benthic community, resulting in a decline in species diversity but not species richness. This prediction, of course, holds only for those benthic species not impacted and buried under the GFCs themselves.

9.2.14 Products Beyond Models, Simulations, and Video

The SimDOR Project has contributed support for closure of efforts initiated under the APWI Project. These are:

(1) The most notable is the finalization of peer-reviewed papers for the special issue of the Journal of Marine Systems, for which the Principal and co-Principal Investigators have collected and processed eight peer-reviewed papers. All papers were submitted to the journal editor in May 1997.

(2) The Principal Investigator presented testimony before a House Subcommittee Hearing in December 1995 on the topic of contaminated dredged material management on the abyssal seafloor.

(3) The Principal and co-Principal Investigators prepared and presented two papers describing the technical, economic, and environmental feasibility of contaminated waste management via isolation on the abyssal seafloor at the Oceanology International '96 Conference in Brighton, UK, in Mar 1996.

(4) The Principal and co-Principal Investigators presented the SimDOR project results at the 7th International Offshore and Polar Engineering Conference, Honolulu, 25–30 Mar 1997. A short paper was prepared for the published proceedings that provided further explanation of the science and technology issues behind the visualizations of numerical simulations.

(5) A paper on the SimDOR Project was submitted and presented at the 30th Texas A&M Annual Dredging Seminar, held in Charleston, SC, 28 Jun–3 Jul 1997.

(6) The Principal and co-Principal Investigators gave a keynote presentation for the afternoon session of a meeting of the Society of Underwater Technology in London, UK, on 26 Mar 1997. The session focus was "Deep Ocean Contaminant" of toxic wastes. The presentation material has been rewritten for a peer-reviewed paper and submitted to the Underwater Technology Journal.

10.0 CONCLUSIONS AND RECOMMENDATIONS

1. **Conclusion:** The technical feasibility of an end-to-end process of clean dredging of contaminated materials, transport, and placement at an abyssal seafloor isolation site has been demonstrated through analytical modeling and preliminary component and system design.

Recommendation: The demonstration of technical feasibility completed in this study should be extended into a comprehensive simulation of the dredging-through-placement process. The purpose of this simulation would be to identify those combinations of component selections yielding minimum cost per unit volume of dredged material to complete the relocation process for the range of contaminated dredged material types expected.

2. **Conclusion:** The Integrated tug-barge concept was shown in sea-keeping analyses to perform well in sea states up through 5. At sea state 8, the system performance was shown to be not acceptable, requiring the tug-pushing-the-barge arrangement be changed to a tug-towing-the-barge configuration.

Recommendation: Future projections of the cost per unit volume for management of contaminated, dredged material by the abyssal seafloor isolation option should factor in the impact of decreased tug-barge speed in the towed configuration when needed during periods of high sea states.

3. **Conclusion:** The finite difference solution employed to describe the descent of GFCs to the seafloor, using a fixed GFC shape and allowing no lateral skating of the GFC, predicts terminal velocity of the GFC to be about 5 m/s.

Recommendation: The solution for GFC shape for realistic bag designs, contained volumes, and bulk wet densities of contents should be exercised/expanded to allow reshaping of the GFC toward an equilibrium shape at terminal velocity to better estimate the terminal velocity and wall-fabric seam stresses and strains.

Recommendation: Model tests of GFC free-fall should be conducted as a means of validating analytical predictions of container shape and fabric stresses and strains at terminal velocity. The model test would help to develop an improved understanding of prototype GFC dynamics and instabilities leading to (a) an empirical statistical model of container lateral excursion/travel or skating during free-fall and (b) an empirical statistical model for deriving the corrected velocity vector at time of impact with the seafloor.

4. **Conclusion:** The plume of abyssal sediments generated by impact of dredged, material-filled GFCs with the abyssal seafloor would settle around the point of impact as a thin layer of sediment producing little probable effect on benthic fauna and geochemical processes. On the other hand, should the GFCs rupture upon impact, the lateral forces on released dredged material could widely transport abyssal sediments mixed with dredged material in a turbidity current.

Recommendation: Distances of transport of dredged material from a ruptured container should be modeled to be able to predict the dimensions and characteristics of the deposition footprint. Depths of deposited, dredged material should also be ascertained to determine effects of a ruptured container on biota and biogeochemical processes.

5. **Conclusion:** Hydrothermal plume effects alone would disperse dissolved contaminants released from a ruptured GFC locally near the point of impact. The overall range of dispersal is expected to be small, given the low current velocities modeled at the SimDOR surrogate sites, but exact distances are unknown.

Recommendation: Benthic boundary layer flow characteristics at the optimal disposal sites should be modeled together with simulations of turbidity current effects (noted in Conclusion 4) and their potential interactions with hydrothermal plume effects.

6. **Conclusion:** The sediments directly below a thick layer of relocated, dredged material would become anoxic and devoid of aerobic organisms. This anoxic zone would not, however, extend beyond the outer perimeter of the deposit.

Recommendation: Effects of bacterial inoculation of deposited, dredged material should be investigated as affecting rates and pathways of decomposition of organic matter. Dredged material, both enclosed in GFCs and in uncontainerized deposits, should be included in this investigation.

7. **Conclusion:** Trace metal concentrations and distributions in pore waters of deposited, dredged materials as affected by sediment diagenetic processes are dominated by redox conditions.

Recommendation: Specific reactivities of redox-sensitive trace metals should be investigated with regard to predicted effects from oxic, suboxic, and anoxic processes in relocated, dredged material and in abyssal sediments underlying the deposits.

8. **Conclusion:** Under predicted conditions at the abyssal seafloor, the organic content of most dredged material is sufficiently low that gas hydrates would not be expected to be produced.

Recommendation: If concentrations of organic matter in dredged material are unusually high and/or decomposition products are highly concentrated because of increased diagenetic activity, gas hydrates could possibly be formed under abyssal ocean conditions. Thus, the production of gas hydrates should not be entirely dismissed as a potential outcome from relocating dredged material with high organic content to the abyssal seafloor.

9. **Conclusion:** Potential releases of contaminants from dredged material relocated to the abyssal seafloor would be trivially small compared with the natural background of trace metals in seawater, to the inputs of trace metals from deep hydrothermal sources, and to the inputs of both trace metals and organic compounds to the surface ocean.

Recommendation: The impacts of dredged material deposition on the chemistry of the oceans should be considered only as a potential problem local to the relocation site and not on the magnitude of ocean-wide scales.

10. **Conclusion:** Modeled inputs of organic matter, either as a natural seasonal pulse of organic matter or in relocated dredged material, increase respiration and biomass of abyssal benthic organisms.

Recommendation: Experimental verification is needed for the modeled prediction of increased respiration and growth of abyssal benthic organisms in response to input of organic matter via relocated, dredged material.

11. **Conclusion:** Simplified food chain models predict numerical dominance by fast-growing, opportunistic benthic species in response to inputs of new organic matter contained in relocated, dredged material. This response, combined with selective predation, could result in diminished species evenness and, thus, decreased species diversity of macrofauna.

Recommendation: Experimental verification is needed for the modeled prediction of decreased species diversity of abyssal macrofauna in response to input of relocated, dredged material.

12. **Conclusion:** Return of trace metals and organic contaminants from abyssal depths to surface waters of the ocean via reproductive products of abyssal fauna is predicted to be trivially small. Other transport mechanisms by biological pathways are unknown.

Recommendation: Experimental verification of concentration of toxicants in reproductive products of abyssal fauna is needed to confirm that the predicted biological pathway is possible. If verified, further information on reproductive behavior and developmental biology of targeted species would be needed.

11.0 ACKNOWLEDGMENTS

The editors thank the participants of the SimDOR Project, many of whom are referenced in this report, for sharing results of their work summarized in this report. We acknowledge the help of many authorities—too numerous to mention here—in academia, government, and industry, who were consulted and gave freely their wealth of knowledge and experience. We appreciate support of this project by the Defense Advanced Research Projects Agency, Program Element 0603226E, Dr. Allan Steinhardt, Program Manager.

12.0 REFERENCES

Ballard, R. D., "Response to Waste Management Questions," in *Ocean Dumping Enforcement and the Current Status of Research Efforts*, hearing before the Subcommittee on Coast Guard and Navigation, House of Representatives, Serial No. 102-96, U.S. Government Printing Office, Washington, D.C., 1992, pp. 563–566.

Bowles, F. A., "Sedimentary Regime, Abyssal Seafloor Waste Isolation: Environmental Report," P. J. Valent and D. K. Young, eds., NRL/MR/7401--95-7576, Naval Research Laboratory, Stennis Space Center, MS, 1995, pp. 305–314.

Bye, J. A. T., "The Slope of Abyssal Plains," *J. Geophys. Res.* **76**, 4188–4194 (1971).

Chen, H. C. and R. A. Korpus, "A Multi-Block Finite-Analytic Reynolds-Stokes Navier-Stokes Method for 3D Incompressible Flows," Tr. of the ASME Fluids Engineering Spring Meeting, 1993.

Chen, H. C. and V. C. Patel, "Near-Wall Turbulence Models for Complex Flows Including Separation," *AIAA Journal* **26**(4), 641–648 (1988).

Chen, H. C. and V. C. Patel, "The Flow Around Wing-Body Junctions," Proceedings of the 4th Symposium on Numerical and Physical Aspects of Aerodynamics Flows, Long Beach, CA, (informal proceedings), 1989.

Chen, H. C., V. C. Patel, and S. Ju, "Solutions of Reynolds-Averaged Navier-Stokes Equations for Three-Dimensional Incompressible Flows," *Journal of Computational Physics* **88**(2), 305–336 (1989).

Chryssostomidis, C., "An Abyssal Ocean Option for Future Waste Management Monitoring: Engineering Systems and Research Needs," report of a workshop held at the Massachusetts Institute of Technology, Cambridge, MA, 12–14 Jun 1991, p. 71.

Chu, F. H., W. D. Pilkey, and O. H. Pilkey, "An Analytical Study of Turbidity Current Steady Flow," *Mar. Geol.* **33**, 205–220 (1979).

Dade, W. B., J. R. Lister, and H. E. Huppert, "Fine-Sediment Deposition from Gravity Surges on Uniform Slopes," *J. Sediment. Res.* **A64**, 423–432 (1994).

del Vicario, M., Presentation at the U.S. EPA Sediment Bioaccumulation Conference, Washington, D.C., 13 Sep 1996.

Dinavahi, S. P. G., R. A. Korpus, M. J. Meinhold, and M. J. Fritts, "Deep Ocean Relocation of Coastal Sediments, SimDOR Engineerings, Final Simulation Report," Contract No. N00014-96-C-6002, Science Applications International Corp., Annapolis, MD, for Naval Research Laboratory, Stennis Space Center, MS, 31 Jan 1997, pp. 11–15.

Duce, R. A., P. S. Liss, J. T. Merrill, E. L. Atlas, P. Buat-Menard, B. B. Hicks, J. M. Miller, J. M. Prospero, R. Arimoto, T. M. Church, W. Ellis, J. N. Galloway, L. Hansen, T. D. Jickells, A. H. Knap, K. H. Reinhardt, B. Schneider, A. Soudine, J. J. Tokos, S. Tsunogai, R. Wollast, and M. Zhou, M., "The Atmospheric Input of Trace Species to the World Ocean," *Global Biogeochem. Cycles* **5**, 193–260 (1991).

Edmond, J. M., Letter to Chair, Committee on Coast Guard and Navigation of 12 Nov 1992, reprinted in *Ocean Dumping Enforcement and the Current Status of Research Efforts*, hearing before the Subcommittee on Coast Guard and Navigation, House of Representatives, Serial No. 102-96, U.S. Government Printing Office, Washington, D.C., 1992, p. 467.

Einsele, G., "Submarine Mass Flow Deposits and Turbidites," in: *Cycles and Events in Stratigraphy*, G. Einsele, R. Werner, and A. Seilacher, eds. (Springer-Verlag, Berlin, 1991), pp. 313–339.

Eldridge, P. and G. Jackson, "Benthic Trophic Dynamics in California Coastal Basin and Continental Communities Inferred Using Inverse Analysis," *Mar. Ecol. Prog. Ser.* **99**, 115–135 (1993).

Environmental Protection Agency, "EPA's Contaminated Sediment Management Strategy," U.S. Environmental Protection Agency, Washington, D.C., 1994, p. 130.

Environmental Protection Agency, "Evaluation of Dredged Material Proposed for Ocean Disposal (Testing Manual)," EPA-503/8-91/001, U.S. Environmental Protection Agency, Washington, D.C., 1991, p. 196.

Fleischer, P., "Site Selection Model; Abyssal Seafloor Waste Isolation: Environmental Report," P. J. Valent and D. K. Young, eds., NRL/MR/7401--95-7576, Naval Research Laboratory Report, Stennis Space Center, MS, 1995, pp. 133–188.

Fowler, J., D. Toups, and P. Gilbert, "Geotextile Contained Contaminated Dredged Material, Marina del Rey, Los Angeles and Port of Oakland, California," *Fourteenth World Dredging Congress*, Amsterdam, The Netherlands, 14–17 Nov 1995.

Fowler, J., Soil and Rock Mechanics Division, U.S. Army Corps of Engineers, Waterways Experiment Station, Vicksburg, MS, 1994, pers. comm.

Fowler, J. A., "4000 cy Geotextile Container Filled with Maintenance Dredged Material," Port Authority of New York and New Jersey (interim report), 1995.

Fowler, J., C. J. Sprague, and D. Toups, "Dredged Material Filled Geotextile Containers, Environmental Effects of Dredging Technical Notes," U.S. Army Corps of Engineers, Waterways Experiment Station, Vicksburg, MS, 1994.

Fowler, J., D. Toups, and P. Gilbert, "Geotextile Contained Contaminated Dredged Material, Marina Del Rey, Los Angeles and Port of Oakland, California," *Fourteenth World Dredging Congress*, Amsterdam, The Netherlands, 14–17 Nov 1995a.

Fowler, J., D. Toups, F. Duarte, and P. Gilbert, "Geotextile Contained Dredged Material, Red Eye Crossing, Baton Rouge, LA," Western Dredging Association 16th Technical Conference, 28th Annual Texas A&M Dredging Seminar, *University of Wisconsin Sea Grant Dredging Workshop*, Minneapolis, MN, 23–24 May 1995b.

Gage, J. D. and P. A. Tyler, *Deep-Sea Biology: A Natural History of Organisms at the Deep-Sea Floor* (Cambridge Univ. Press, 1991), pp. 504.

Gallacher, P. C., "Physical Oceanographic Modeling; Abyssal Seafloor Waste Isolation: Environmental Report," NRL/MR/7401--95-7576, P. J. Valent and D. K. Young, eds., Naval Research Laboratory, Stennis Space Center, MS, 1995, pp. 254–276.

Gallacher, P. C., "Hydrodynamical Dispersion of Dredged Materials Sequestered on Abyssal Plains," *J. Mar. Sys.* (in press).

Gatski, T. B. and C. G. Speziale, "On Explicit Algebraic Stress Models for Complex Turbulent Flows," *Journal of Fluid Mechanics* **254**, 59–78 (1993).

Gould, H. R., "Some Quantitative Aspects of Lake Mead Turbidity Currents," *Soc. of Econ. Paleontol. Mineral. Spec. Pub.* **2**, 34–52 (1951).

Graham, D. M., "On Deep Ocean Waste Disposal," *Sea Technology* **7** (1993).

Green, A. W., "An Approximation for the Shapes of Large Raindrops," *J. Applied Meteorology* **14**, 1578–1583 (1975).

Green, A. W., "A Note on 'The Behavior of Large, Low-Surface-Tension Water Drops Falling at Terminal Velocity in Air,'" *J. Applied Meteorology* **15**, 1233–1236 (1976).

Green, A. W., P. Valent, D. K. Young, K. Hart, R. Ray, and W. Sawyer, "Dynamics of Sediment/ Water-Filled Containers," Second Project Mtg. DOR Phase II, Feb. 19–20, 1997.

Greges, M., U.S. Army Corps of Engineers, New York District, New York, NY, 1994.

Hanjalic, K. and B. E. Launder, "Sensitizing the Dissipation Equation to Irrotational Strains," *J. of Fluid Engineering* **102**(34), (1990).

Heezen, B. C. and M. Ewing, "Orleansville Earthquake and Turbidity Currents," *Am. Assoc. Pet. Geol. Bull.* **39**, 2505–2514 (1955).

Hellerman, P. J. and M. Rosenstein, "Normal Monthly Wind Stress Over the World Ocean with Error Estimates," *J. Phys. Oceanogr.* **13**, 1405–1413 (1983).

Herbich, J. B., "Removal of Contaminated Sediments: Equipment and Recent Field Studies, Dredging, Remediation, and Containment of Contaminated Sediments," ASTM STP 1293, K. R. Demars, G. N. Richardson, R. N. Yong, and R. C. Chaney, eds., American Society for Testing and Materials, Philadelphia, PA, 1995, pp. 77–111.

Hightower, J. M., W. R. Richards, S. Balinski, W. Briggs, T. Foster, D. Mauck, and A. Marcy, "Technical Assessment Report for Abyssal Plains Waste Isolation Project," NRL/CR/7401--95-0021, Naval Research Laboratory, Stennis Space Center, MS, 1995a, pp. 143.

Hightower, J. M., A. L. Marcy, and W. R. Richards, "Economic Viability Report for Abyssal Plains Waste Isolation Project," NRL/CR/7401--94-0016, Naval Research Laboratory, Stennis Space Center, MS, 1995b.

Hightower, J. M., A. L. Marcy, and W. R. Richards, "System Requirements Report for Abyssal Plains Waste Isolation Project," NRL/CR/7350--94-0007, Naval Research Laboratory, Stennis Space Center, MS, 1994.

Hoerner, S. F. and H. V. Borst, *Fluid-Dynamic Lift* (Hoerner Fluid Dynamics, Vancouver, WA, 1965).

Hollister, C. D., "Potential Use of the Deep Seafloor for Waste Disposal," in *Use and Misuse of the Seafloor*, K. J. Hsü and J. Thiede, eds. (John Wiley and Sons, Ltd., Chichester, NY, 1992), pp. 127–130.

Hurlburt, H. E. and J. D. Thompson, "A Numerical Study of Loop Current Intrusions and Eddy Shedding," *J. Phys. Oceanogr.* **10**, 1611–1651 (1980).

Jagt, H. J., "Bed Protection, Old Meuse, by Means of Geocontainers," Report No. VXT.HJ 88.168, Nicolon b.v., Almelo, The Netherlands, for Public Works Department of the Netherlands, Dordrecht, The Netherlands, 1988, p. 19.

Jahnke, R. A., "Geochemical Impacts of Waste Disposal on the Abyssal Seafloor," *Mar. Sys. Sci.* (in press).

Jahnke, R. A., "The Global Ocean Flux of Particulate Organic Carbon: Areal Distribution and Magnitude," *Global Biogeochem. Cycles* **10**, 71–88 (1996).

Jahnke, R. A. (1995). "Predictions of Near- and Far-Field Effects Resulting from Introduction of Wastes to Abyssal Environments; Abyssal Seafloor Waste Isolation: Environmental Report," NRL/MR/7401--95-7576, P. J. Valent and D. K. Young, eds., Naval Research Laboratory, Stennis Space Center, MS, 1995, pp. 326–351.

Jumars, P. and E. D. Gallagher, "Deep-Sea Community Structure: Three Plays on the Benthic Proscenium, in: *The Environment of the Deep Sea*, W. Ernst and J. Morin, eds. (Prentice-Hall, Englewood Cliffs, NJ, 1982), pp. 217–255.

Karlsrud, K. and L. Edgers, "Some Aspects of Submarine Slope Stability," in: *Marine Slides and Other Mass Movements*, S. Saxov and J. K. Nieuwenhuis, eds. (Plenum Press, New York, NY, 1982), pp. 61–81.

Kirwan A. D., Jr., L. J. Doyle, W. D. Bowles, and G. R. Brooks, "Time-Dependent Hydrodynamic Models of Turbidity Currents Analyzed with Data from the Grand Banks and Orleansville Events," *J. Sediment. Petrol.* **56**, 379–386 (1986).

Korpus, R., "Six Years of Progress Under the ARPA SUBTECH Program," SAIC Report #95/1143, 1995.

Krause, D. C., W. C. White, D. J. W. Piper, and B. C. Heezen, "Turbidity Currents and Cable Breaks in the Western New Britain Trench," *Geol. Soc. Am. Bull.* **81**, 2153–2160 (1970).

Kuenen, Ph. D., "Estimated Size of the Grand Banks Turbidity Current," *Amer. J. Sci.* **250**, 874–884 (1952).

Lambert, A. M., K. R. Kelts, and N. F. Marshall, "Measurements of Density Underflows from Walensee, Switzerland," *Sedimentology* **23**, 87–105 (1976).

Lamont, P. J., D. I. A. Poll, and R. Taghavi-Zenoz, "Reynolds Number Effects on the Flow Around 2-D Ellipses at Incidences," Manchester Univ., United Kingdom, AIAA, Aerospace Sciences Meeting and Exhibit, 33rd, Reno, NV, Jan. 9–12, 1995.

McCreary, J. P. and P. K. Kundu, "A Numerical Investigation of the Somali Current During the Southwest Monsoon," *J. Mar. Res.* **46**, 25–58 (1988).

McWilliams, J. C., P. C. Gallacher, C.-H. Moeng, and J. C. Wyngaard, "Modeling the Oceanic Planetary Boundary Layer," in: *Large Eddy Simulation of Complex Engineering and Geophysical Flows*, B. Galperin and S. Orszag, eds. (Cambridge University Press, New York, NY, 1993), pp. 441–452.

Menard, H. W. and. S. M. Smith, "Hypsometry of Ocean Basin Provinces," *J. Geophys. Res.* **71**, 4305–4325 (1966).

Menard, H. W., *Marine Geology of the Pacific* (McGraw-Hill Book Co., New York, NY, 1964), pp. 271.

Mesa, C., "Containerization of Contaminated Dredged Sediments, the Marina del Rey Experience," *World Dredging, Mining, and Construction*, Aug 1995, pp. 12–15, 24, 27.

Middleton, G. V., "Small Scale Models of Turbidity Currents and the Criterion for Autosuspension," *J. Sediment. Petrol.* **36**, 202–208 (1966).

Middleton, G. V., "Turbidity Currents," in: *The NEW Concepts of Continental Margin Sedimentation*, D. J. Stanley (convener), 1969, pp. GM-A-1–GM-A-20.

Milne-Thomson, L. M., *Theoretical Hydrodynamics, Fifth Edition* (The Macmillan Company, 1969).

Modi, V. J. and E. Wiland, "On the Fluid Dynamics of Elliptic Bodies," Proceedings of the Second International Offshore and Polar Engineering Conference, San Francisco, CA, Jun 1992.

Mulder, T. and P. M. Syvitski, "Turbidity Currents at River Mouths During Exceptional Discharges to the World Oceans," *J. Geol.* **103**, 285–299 (1995).

Munson, D., "Rising Mud," *NE-MW Economic Review*, Nov/Dec 1996, pp. 4–9.

National Research Council, "Dredging Coastal Ports, An Assessment of the Issues," Marine Board, National Research Council (National Academy Press, Washington, D.C., 1985), p. 212.

National Research Council, "Contaminated Marine Sediments—Assessment and Remediation," Committee on Contaminated Marine Sediments, Marine Board and Commission on Engineering and Technical Systems (National Academy Press, Washington, D.C., 1989), p. 493.

Oceaneering International Corp., "Systems Engineering Report: SimDOR (Simulation of Deep Ocean Relocation) System Requirements," Oceaneering Report No. 70856-01, Oceaneering International, Inc., Marlboro, MD, 1996a.

Oceaneering International Corp., "Design Report: SimDOR (Simulation of Deep Ocean Relocation) System Top Level Design," Oceaneering Report No. 70856-02, Oceaneering International, Inc., Upper Marlboro, MD, submitted to Science Applications International Corp., McLean, VA, 26 Aug 1996b, p. 20.

Ockels, R., "Innovative Hydraulic Engineering with Geosynthetics," *Geosynthetic World* 26–27 (1991).

Pantin, H. M., "Interaction Between Velocity and Effective Density in Turbidity Flow: Phase-Plane Analysis, with Criteria for Autosuspension," *Mar. Geol.* **31**, 59–99 (1979).

Pickering, K. T., R. N. Hiscott, and F. J. Hein, "Deep-Marine Environments," *Unwin Hyman*, (London, 1989), pp. 13–38.

Piper, D. J. W. and B. Savoye, "Processes of Late Quaternary Turbidity Current Flow and Deposition on the Var Deep-Sea Fan, North-West Mediterranean Sea," *Sedimentology* **40**, 557–582 (1993).

Quinby-Hunt, M. S. and. K. K. Turekian, "Distribution of Elements in Sea Water," *Trans. Am. Geophys. Union* 130–131 (1983).

Rocker, K., Jr., "Handbook for Marine Geotechnical Engineering," Naval Civil Engineering Laboratory, Port Hueneme, CA, 1985, Ch. 11.

Rouse, H., *Advanced Mechanics of Fluids* (Robert E. Krieger Publishing Company, Huntington, NY, 1976).

Rowe, G., "The Cycling of Organic Matter in Food-Limited Environments," *Biosystematics and Ecology* (1997a).

Rowe, G. "Numerical Simulation of Carbon Cycling in a Deep Ocean Benthic Food Chain and Potential Export of Contaminants from Abyssal Waste Isolation Sites," *Jour. Mar. Sys.* (in press, 1997b).

Rowe, G., G. Boland, E. Escobar Briones, M. L. Cruz Kaegi, A. Newton, D. Piepenburg, I. Walsh, and J. Deming, "Sediment Community Biomass and Respiration in the Northeast Water Polynya, Greenland: A Numerical Simulation of Benthic Lander and Spade Core Data," *Jour. Mar. Sys.* (1997).

Rowe, G. T., "Numerical Simulations of Deep-Sea Food Chains with an Estimate of Potential Export of Contaminants from Abyssal Waste Isolation; Abyssal Seafloor Waste Isolation: Environmental Report," NRL/MR/7401--95-7576, P. J. Valent and D. K. Young, eds., Naval Research Laboratory, Stennis Space Center, MS, 1995, pp. 356–366.

Rubin, A. B., Memorandum to Record, U.S. Environmental Protection Agency, Washington, D.C., dated 22 Apr 1992, pp. 211–214.

Ryan, W. B. F. and B. C. Heezen, "Ionian Sea Submarine Canyons and the 1908 Messina Turbidity Current," *Geol. Soc. Am. Bull.* **76**, 915–932 (1965).

Shaw, T., J. M. Gieskes, and R. A. Jahnke, "Early Diagenesis in Differing Depositional Environments: The Response of Pore Water Transition Metals," *Geochim. Cosmochim. Acta* **54**, 1233–1246 (1990).

Smith, K. L., Jr., "Benthic Boundary Layer Communities and Carbon Cycling at Abyssal Depths in the Central North Pacific," *Limnol. Oceanogr.* **37**, 1034–1056 (1992).

Snelgrove, P., J. F. Grassle, and R. Petrecca, "Experimental Evidence for Aging Food Patches as a Factor Contributing to High Deep-Sea Macrofaunal Diversity," *Limnol. Oceanogr.* **41**, 605–614 (1996).

So, R. M., H. S. Zhang, and C. O. Speziale, "Near-Wall Modeling of the Dissipation Rate Equation," *AIAA Journal* **29**(12), (1991).

Spencer, D. W., "An Abyssal Ocean Option for Waste Management," report of a workshop held at the Woods Hole Oceanographic Institution, Woods Hole, MA, 7–10 Jan 1991, pp. 111.

Speziale, C. G., S. Sarkar, and T. B. Gatski, "Modeling the Pressure-Strain Correlation of Turbulence: An Invariant Dynamical Systems Approach," *J. Fluid Mech.* **227**, 245–272 (1991).

Stow, D. A. and A. J. Bowen, "A Physical Model for the Transport and Sorting of Fine-Grained Sediment by Turbidity Currents," *Sedimentology* **27**, 31–46 (1980).

Technical Assessment Report for Abyssal Plains Waste Isolation Project (Attachment #1: Surface Emplacement Vessel Tradeoff Issues), NRL/CR/7401--95-021, Naval Research Laboratory, Stennis Space Center, MS, 1995.

Technical Assessment Report for Abyssal Plains Waste Isolation Project (Attachment #2: Dredged Material Filled Geotextile Containers), NRL/CR/7401--95-021, Naval Research Laboratory, Stennis Space Center, MS, 1995.

Turner, T. M., *Fundamentals of Hydraulic Dredging, Second Edition* (ASCE Press, New York, NY, 1996).

U.S. Army Corps of Engineers, "Dredged Material Management Plan for the Port of New York and New Jersey, Interim Report," U.S. Army Corps of Engineers, New York District, Sep 1996, pp. 10-4–10-11.

Valent, P. J. and D. K. Young, "Abyssal Seafloor Waste Isolation: Environmental Report," NRL/MR/7401--95-7576, Naval Research Laboratory, Stennis Space Center, MS, 1995.

Valent, P. J., D. K. Young, and A. W. Palowitch, "Technical and Economic Assessment of Waste Isolation on the Abyssal Seafloor," Proceedings Oceanology International 96 (Spearhead Exhibitions, Ltd. Publishers, Surrey, UK), Vol. 1, 1996, pp. 305–316.

Wallcraft, A. J., "The Navy Layered Ocean Model Users Guide," NOARL Report 35, Naval Research Laboratory, Stennis Space Center, MS, 1991.

Weems, K. M., R. A. Korpus, M. J. Fritts, W. M. Lin, and H. C. Chen, "Near-Field Flow Prediction for Ship Design," Tr. of the 20th Symp. on Naval Hydrodynamics, 1994.

Wright, T., U.S. Army Waterways Experiment Station, Vicksburg, MS, 1994, pers. comm.

Young, D. and M. Richardson, "Effects of Waste Disposal on Benthic Faunal Succession on the Abyssal Seafloor," *Jour. Mar. Sys.* (in press).

Young, D. K. and P. J. Valent, "Environmental Assessment of Waste Isolation on the Abyssal Seafloor," Proceedings Oceanology International '96 (Spearhead Exhibitions, Ltd. Publishers, Surrey, UK), Vol. 1, 1996, pp. 317–326.

Zajac, R. and R. Whitlatch, "A Hierarchical Approach to Modelling Soft-Bottom Successional Dynamics," Proceedings 19th Eur. Mar. Biol. Symp., P. E. Gibbs, ed., Cambridge Univ. Press, 1985, pp. 265–276.

Appendix A

SYSTEM REQUIREMENTS

The requirements for each of the four function areas of the system are listed in the following tables organized by areas: dredging, transfer and loading, transportation, and disposal. Support information, justification, and/or background for each requirement is presented in Table A5. The support information is found by the reference number listed in the right column of each requirement table.

Table A1 — SimDOR Dredging Process System Requirements

REQUIREMENT NUMBER	DESCRIPTION	REQUIREMENT	SUPPORT REF #
1.1	Dredging Location		
1.1.1	Dredging Depth	5.5 m–15 m (18 ft–50 ft)	1
1.1.2	Port to Disposal Site Transporter Distance	<1.9 and >1.2 km (<1,000 and >660 nmi)	2
1.2	Dredge Equipment		
1.2.1	Production Rate	≥150 m^3/h (≥200 yd^3/h)	3
1.2.2	Debris Removal Capability	Removal of large debris	4
1.2.3	Depth Range	5.5 m–15 m (18 ft–50 ft)	1
1.2.4	Removal Efficiency	Remove sediment at nearly its in situ density	5
1.2.5	Sediment Classification Range	Capable of removing a large range of sediment classifications	6
1.2.6	Low Turbidity	Must meet state and USACE requirements which vary site to site	7
1.2.7	Reliability and Availability	< the maximum amount of downtime that would result in reduction below the required production/processing rate	8
1.3	Dredged Material		
1.3.1	In Situ Material Properties		
1.3.1.1	% Solids by Weight	43 to 64%	9
1.3.1.2	Bulk Wet Density In Situ	(1.4 Mg/m^3–1.7 Mg/m^3)	9
1.3.2	Bulk Wet Density mixture	(1.4 Mg/m^3–1.7 Mg/m^3)	9
1.3.3	Particle Size		
1.3.3.1	Silt	3.9 μm–63.5 μm	2
1.3.3.2	Sand	625 μm–2,000 μm	2
1.3.3.3	Gravel	>2,000 μm	2
1.3.4	Contamination Level	Category III material	10

Table A2 — SimDOR Transfer and Loading Process System Requirements

REQUIREMENT NUMBER	DESCRIPTION	REQUIREMENT	SUPPORT REF. #
2.1	Contamination Containment	Contaminants shall be contained within the system	11
2.2	Transport Rate	≥150 m^3/h (≥200 yd^3/h)	3
2.3	Transfer Storage Capacity	≥230 m^3 (≥300 yd^3)	12
2.4	Sediment Transport Method	Capable of high % solids without the addition of water	13, 9
2.5	Maximum Particle Size	>2,000 μm and <auger component manufacturer recommendations	14,2
2.6	Distribution Hopper Capacity	≥11 m^3 (≥15 yd^3)	15
2.7	System Shut-Off	<5 min	15
2.8	Reliability and Availability	< the maximum amount of downtime that would result in reduction below the required production/processing rate	8
2.9	Container Loading		
2.9.1	Container Loading/ Closing Design	Nozzle with mechanical shutting mechanism	16, 11
2.9.2	Maximum Filling Pressure	1/3 of an atmosphere	17
2.9.3	Container Filled Capacity	760 m^3 (1000 yd^3)	18, 1
2.9.4	Cell Loading Rate	≥150 m^3/h (≥200 yd^3/h)	3

Table A3 — SimDOR Transporting Process System Requirements

REQUIREMENT NUMBER	DESCRIPTION	REQUIREMENT	SUPPORT REF. #
3.1	Operational Conditions		
3.1.1	Operations	Sea state 5	2
3.1.2	Survivability	Sea state 8	2
3.1.3	Transport Distance	<1.9 and >1.2 km (<1,000 and >664 nmi	2
3.2	Transporter System	Articulated tug barge system	19
3.2.1	Capacity Dead Weight	23,000 Mg (25,000 tons)	3
3.2.2	Maximum Draft	5.5 m (18 ft)	1, 18
3.2.3	Structural Strength and Stability	Per requirements established through certification agencies	20
3.2.4	Speed	>22 km/h (>12 kt)	2
3.2.5	Availability	< the maximum amount of downtime that would result in reduction below the required production/processing rate	8
3.2.6	Reliability (MTBF)	>720 h	2
3.3	Compartments		
3.3.1	Container Release	≤3 s	21, 3
3.3.2	Door Opening	100% of compartment size	21
3.3.3	Compartment Integrity	Free flooded	21
3.3.4	Wall Liner	Low friction surface	21

Table A4 — SimDOR Depositing Process System Requirements

REQUIREMENT NUMBER	DESCRIPTION	REQUIREMENT	SUPPORT REF. #
4.1	Descent/Operation Characteristics		
4.1.1	Minimum Terminal Velocity	>3 m/s (>10 ft/s)	22
4.1.2	Placement Accuracy	3000 m diameter	23
4.1.3	Release Sequence	Controlled release maintaining barge stability	24, 20
4.1.4	Maximum Release Interval	3 min and 6 min	3, 24
4.1.5	Maximum Surface Current	2.8 km/h (1.5 kt)	2
4.2	Container Requirements		
4.2.1	Minimum Strength of Container	Factor of safety of 2.5	22, 21, 25
4.2.2	Container Material Density	> density of seawater at abyssal depth water temperatures	22

Table A5 — SimDOR System Requirement Support Information

SUPPORT REF. NUMBER	JUSTIFICATION, BACKGROUND INFORMATION, AND/OR COMMENTS	REQUIREMENT NUMBER
1	The dredging depth was selected based on the following two port dredging plans: • *Final Environmental Impact Report/Statement, Boston Harbor: Massachusetts Navigation Improvement Project & Berth Dredging Project*, USACE and Massachusetts Port Authority, June 1995 • *New York Harbor: Dredged Material Management Plan: Phase 1 Report – Plan of Study*, USACE, July 1995 The planned dredging depth of 12 m (40 ft) in the above reports was increased by an additional 3 m to 15 m (10 ft to 50 ft) to anticipate an increase in requirements. The minimum depth of 5.5 m (18 ft) is the existing depth in the reports. The minimum depth can be decreased to zero meters by altering the selected system concept of operation by an addition of a lightering barge to transport the dredged material from the dredge to the transporter located in deeper water.	1.1.1 1.2.3 2.9.3 3.2.2
2	Requirements derived from the following tables in the APWI 94-01 Report, *System Requirements Report for Abyssal Plains Waste Isolation Project*: • Table 5: System Performance/Operational Requirements • Table 2: Physical and Chemical Properties The transporter MTBF is determined in the APWI 94-02 Report, *Technical Assessment Report for Abyssal Plains Waste Isolation Project*, Section 7.0, Comparison to System Requirements.	1.1.2 1.3.3.1 1.3.3.2 1.3.3.3 2.5 3.1.1 3.1.2 3.1.3 3.2.4 3.2.6 4.1.5
3	The process/production rate throughout the system is based on a previous result determined by the APWI 94-02 Report, *Technical Assessment Report for Abyssal Plains Waste Isolation Project*. The report determined that it was most economical to transport 25,000 DWT of disposal material. The report also determined the maximum amount of time (based on costs) the transporter could be on station during loading or unloading is 100 h. Based on the vessel's payload (equivalent to 20,000 yd^3) and station time limit of 100 h, the loading and unloading rate of the transporter is 200 yd^3/h. The transporter capacity and operation is also discussed in Attachment 1 (Surface Emplacement Vessel Tradeoff Issues) of the APWI 94-02 report.	1.2.1 2.2 2.9.4 3.2.1 3.3.1 4.1.4
4	The dredge equipment must be able to remove debris from the dredging site. The type, size, and proportion of volume of debris ranges from site to site. Large debris is not uncommon at dredging sites, especially at piers and berths.	1.2.2

Table A5 — Cont.

SUPPORT REF. NUMBER	JUSTIFICATION, BACKGROUND INFORMATION, AND/OR COMMENTS	REQUIREMENT NUMBER
5	The definition of removal efficiency of the dredging equipment is the ability to remove the sediment at its in situ density. It is desired to remove the sediment at high percent solids to reduce the amount of contaminated water disposal.	1.2.4
6	The dredge equipment must be able to remove a large range of sediment classifications. The dredge equipment should be versatile so that it can be used at a majority of the dredging sites in the United States, especially along the East Coast.	1.2.5
7	The dredging equipment shall be environmentally compliant with the state and USACE requirements. The dredging method must limit the amount of turbidity during dredging at the dredge head and throughout the water column. If the intended use of the water body is potentially impaired, the USACE requirements outlined in 40CFR-230 and 40CFR-220 through 228 apply.	1.2.6
8	The equipment throughout the system having an impact on the productivity rates must have a high reliability and availability percentage to reduce downtime and to lower the likelihood of reductions in the productivity rate. The systems should also have high reliability to limit malfunctions and the chance of exposure or spillage of the dredged material.	1.2.7 2.8 3.2.5
9	The dredged material properties were determined based on USACE supplied data and sediment transportation engineering assessment of possible dredged material properties. The USACE supplied sediment properties from the New York/New Jersey Harbor and Boston Harbor. The selected system concept accommodates sediment having an in situ bulk wet density of 1.4 to 1.7 Mg/m^3, and achieves optimum performance with the bulk wet density at 1.6 Mg/m^3. Hardware modifications to the system concept would allow performance in sediments outside the bulk wet density range of 1.4 to 1.7 Mg/m^3.	1.3.1.1 1.3.1.2 1.3.2 2.4
10	The contamination level of the dredged material is classified as Category III, the highest level of contamination for EPA Region, to design for worst-case conditions.	1.3.4
11	Equipment shall not allow contamination to escape the system by any method including water run-off, wind, and spillage. The system must be protected from environmental conditions (rain and wind) and include spill prevention features. The only location that permits possible contamination release is at the abyssal site on the ocean floor upon container impact.	2.1 2.9.1

Table A5 — Cont.

SUPPORT REF. NUMBER	JUSTIFICATION, BACKGROUND INFORMATION, AND/OR COMMENTS	REQUIREMENT NUMBER
12	The transfer and loading system shall have the capacity to store a sufficient volume of dredged material to prevent down time between barge replacement operations and possible system malfunctions. The transfer storage capacity of 300 yd^3 on the dredging platform allows 1.5 h of total transfer system down time without reducing the dredging operation below the required production rate.	2.3
13	The sediment transport method shall be capable of transporting material with a large range of percent solids without the addition of water to accommodate the range of materials along the United States. The addition of water is restricted to increase the amount of in situ dredged material deposited at the site.	2.4
14	The maximum particle size that the transfer and loading system shall accommodate is greater than the specified gravel content in the dredged material of 2,000 μm and less than the recommended maximum particle size for the systems' components. For mechanical auger screws, the maximum particle diameter is given by 40% of the difference of the auger shaft diameter and the blade diameter divided by 2. The maximum particle size is restricted to decrease the chance of clogging the system.	2.5
15	The distribution system on-board the transporter must also have the capability to store sediment in hoppers to avoid spillage during possible malfunctions. The storage capacity should be sufficient to allow a build-up of material during the time (<5 min) required to shut down the system due to malfunctions.	2.6 2.7
16	The container loading mechanism shall incorporate a sealing/closing design to contain the dredged material after the container is filled. The mechanism shall prevent material from escaping during transit and during the descent to the abyssal site.	2.91
17	The container loading mechanism(s) shall also allow the displaced air volume with the container to be vented as the container is filled with material. The amount of pressure experienced by the container during loading should be restricted. The filling pressure minimum requirement of 1/3 of an atmosphere is derived from the Nicolon Report, *Dredged Material Filled Geotextile Containers*, by Jack Fowler and C. J. Spraque.	2.9.2

Table A5 — Cont.

SUPPORT REF. NUMBER	JUSTIFICATION, BACKGROUND INFORMATION, AND/OR COMMENTS	REQUIREMENT NUMBER
18	The compartment capacity of each cargo bay is restricted to 1000 yd^3 based on preliminary designs of the container hydrodynamics during free-fall of various shaped containers and the draft requirements of the vessel. The transporter design is selected to allow access along side the dredging platform during operations. The minimum draft requirement of 5.5 m (18 ft) restricts the depth dimension of the compartment volume. The length and width dimension of the compartment is restricted by hydrodynamics and stability of the container. The length and width are restricted to reduce the possibility of "side-skating" and tumbling during free-fall.	2.9.3 3.2.2
19	Attachment number one of the APWI 94-02 Report, *Technical Assessment Report for Abyssal Plains Waste Isolation Project*, titled "Surface Emplacement Vessel Tradeoff Issues" recommended an Integrated Tug Barge (ITB).	3.2
20	The transporter's structural strength and characteristics shall be compliant with the following certification agencies' requirements: • United States Coast Guard – *Code of Federal Regulations*, Section 170.170, Subchapter S • American Bureau of Shipping (ABS) – *Rules for Building and Classing Steel Vessels*	3.2.3 4.1.3
21	The containerized, dredged material shall be released from the transporter without causing failure of the container at the water surface or through the water column. This can be accomplished by controlling several factors that contribute to the amount of stress imposed on the container by the release mechanism. These factors include but are not limited to: the shear strength of the material, vessel draft, coefficient of friction between the container and the compartment liner, and the amount of deformation required to exit. The USACE's past operations released containerized material from split-hull barges with a door opening of approximately 30% of the container size and required 3–8 min to release. The restricted opening size leads to potentially hazardous conditions including high material stresses and high frictional forces resisting container release. Allowing the compartments housing the containerized material to be free-flooded reduces the material effective stress and shear strength within the compartment. Increasing the door opening to 100% reduces the imposed stresses on the container by eliminating the conditions that required the containers to deform through a small opening. A door opening of 100% also increases the rate of release of the containers and reduces (1) the amount of contact with the releasing mechanism and (2) the risk of container failure by reducing the amount of time the container is at the surface.	3.3.1 3.3.2 3.3.3 3.3.4 4.2.1

Table A5 — Cont.

SUPPORT REF. NUMBER	JUSTIFICATION, BACKGROUND INFORMATION, AND/OR COMMENTS	REQUIREMENT NUMBER
22	The containerized, dredged material and the container fabric material shall remain deposited on the abyssal ocean floor. The bulk wet density of the container contents should be sufficient to promptly sink to the abyssal floor. Once the container has reached the abyssal floor, the container may fail on impact. The container material and the dredged material must remain negatively buoyant, deposited on the abyssal ocean floor.	4.1.1 4.2.1 4.2.2
23	Conclusions from the report *Engineering Concepts for the Placement of Wastes on the Abyssal Seafloor* by P. J. Valent, A. W. Palowitch, and D. K. Young state that the minimum feasible placement diameter at the abyssal depths is approximately 3000 m.	4.1.2
24	The release sequence of the material should include the simultaneous release of adjacent compartments to limit the unloading shock loads to the transporter. A ballasting system or a heave compensation system may be required to maintain stability and to accommodate the change in draft experienced when each compartment load is released.	4.1.3 4.1.4
25	The minimum design strength of the container material shall incorporate a design factor of safety of 2.5 over the maximum tensile strength determined during analysis. The design strength of the container material includes any portion of the container including seams.	4.2.1

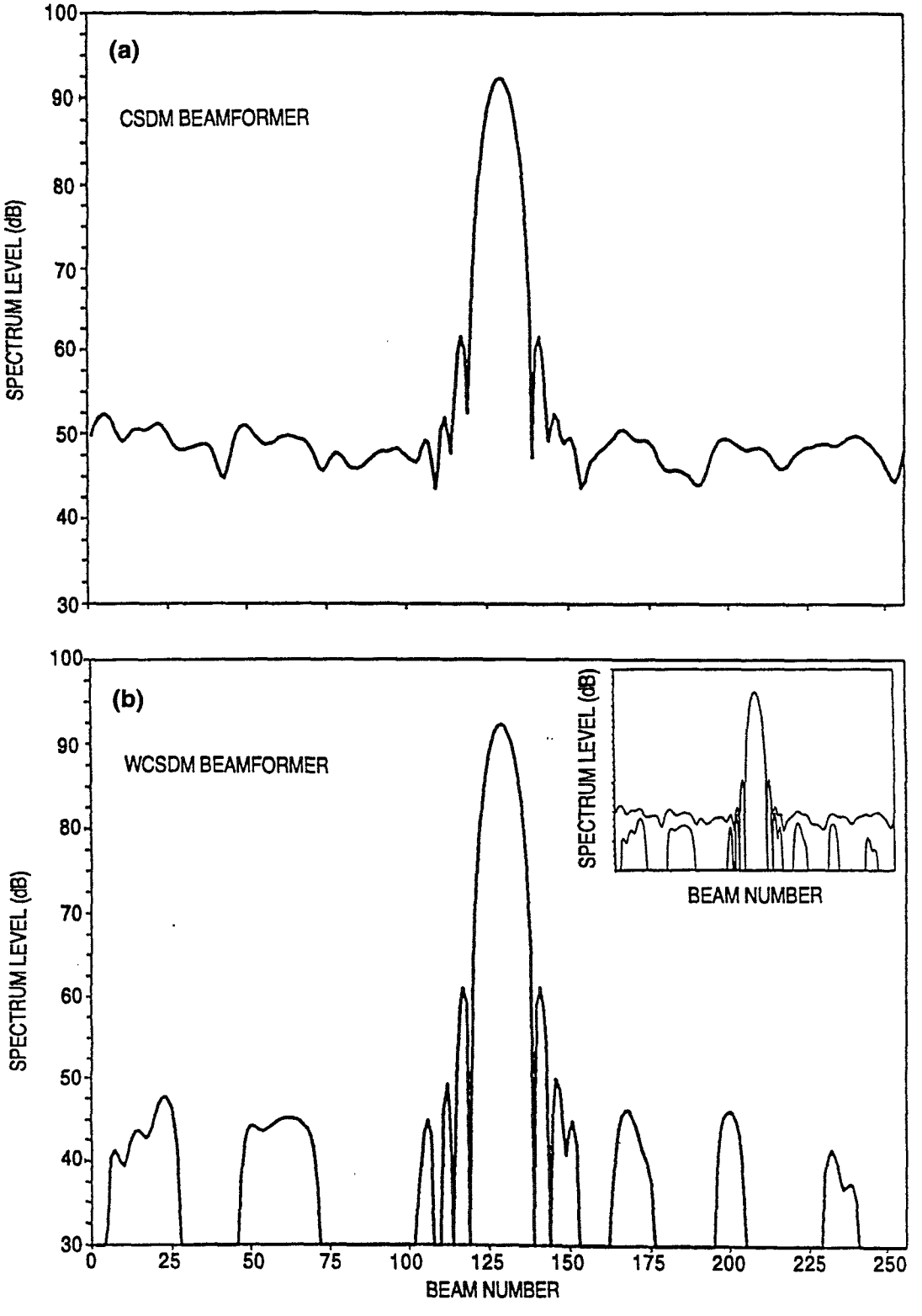

Fig. 8.2 — WISPR processing: WCSDM versus CSDM beamforming

Appendix B

SIMDOR ENVIRONMENTAL AND REGULATORY FACTORS

by Thomas D. Wright

1.0 INTRODUCTION

Deep Ocean Relocation consists of six distinct but related phases including material evaluation, the dredging operation, material handling and loading, transport for disposal, the disposal operation, and post-disposal monitoring. SimDOR only considers the second, third, fourth, and fifth phases (the dredging operation, material handling and loading, transport to the disposal site, and the disposal operation). This appendix will discuss the potential environmental effects and regulatory aspects of these four phases. Of necessity, this discussion will be generic, as specific considerations are a function of the dredging site, the particular project, and the nature of the material.

All phases of SimDOR are regulated by the National Environmental Policy Act (NEPA, PL 91-190). This is a broad "umbrella" under which it is appropriate to address all environmental concerns. Additionally, there are over 60 other laws, regulations, and executive orders that are applicable. The USACE, as the permitting agency for the discharge of dredged material into waters of the United States under the Clean Water Act (CWA, PL 95-217) or the transport of material for the purpose of disposal in the ocean under the Marine Protection, Research, and Sanctuaries Act (MPRSA, PL 92-532), will determine which of these are pertinent to a particular dredging and disposal operation and will ensure that they are met.

Although NEPA is broadly applicable to all aspects of SimDOR, the CWA and the MPRSA specifically address, through their implementing regulations (40 CFR 230 and 40 CFR 220228, respectively) potential environmental effects that may result from the discharge of dredged material. Further, under Section 10 of the River and Harbor Act of 1899, a permit from the USACE is required for the excavation and deposition of material in waters outside the established Federal lines.

In the following discussion, it is assumed, that in the evaluation phase the material will have been found unacceptable for open-water disposal under the Ocean Dumping Criteria at 40CFR 227.4, the CWA 404(b)(1) Guidelines at 40 CFR 230, or both. This being the case, dredging and associated activities may also have the potential for unacceptable adverse effects and will need to be addressed in NEPA documentation. It is further assumed that all other regulatory requirements have been met and environmental concerns other than those related to the dredging and associated activities will have been addressed.

Because of the recent revision of 33 CFR 320-30 (FR Vol. 58, No. 163, 25 Aug 1993), there has been a certain degree of confusion as to whether or not incidental discharges during dredging and associated activities are considered to be discharges of dredged material and would, therefore, be regulated by the CWA 404(b)(1) Guidelines at 40 CFR 230. In the revision, at 40 CFR 232.2(d)(1),

the term "discharge of dredged material" is defined and (d)(2) lists specific exclusions from the definition. Incidental discharges during dredging and associated activities are not among these. However, at 40 CFR 232.2(d)(3)(ii), it is stated that incidental movement of material during normal dredging operations does not require 404 authorization. Hence, such discharges do not require an evaluation under the 404(b)(1) Guidelines nor CWA Section 401 water quality certification.

It is important to note that navigation dredging poses a different set of issues than does remedial dredging. With navigation dredging, it is a given that the material needs to be removed. The primary issue is the potential environmental effects that the material may have when it is discharged, and secondly, any effects associated with removal. In contrast, remediation dredging is conducted because the material is causing adverse environmental effects. This requires a balancing of the effects that the material is having while in place with those that may occur at the disposal site to determine if removal will have a net benefit.

2.0 DREDGING OPERATIONS

The clamshell design proposed for SimDOR would appear to minimize the release of contaminants or suspended solids during dredging. Nevertheless, there will be some incidental release that may impact water column and benthic biota. This should be evaluated by NEPA to determine if there may be adverse environmental effects from this incidental release, will be project and material-specific, and will require an estimate of the quantity and quality of the incidental release. When this has been done, the contaminants and suspended solids may, after consideration of mixing, be compared to state water quality standards or other criteria to determine if the potential water column effects are unacceptable. Because dredged material often contains contaminants for which there are no water quality standards or criteria, or that may interact with each other to enhance or minimize toxic effects, it may be appropriate to conduct water column bioassays. As a worst case, the results of water column bioassays conducted during the initial evaluation of the material for disposal may be used. If these indicate unacceptability, it will be desirable to more closely approximate the actual time concentration conditions.

Estimating the potential effects of the released material upon benthic organisms is much more difficult. It will first be necessary to model the "footprint" of the settled material. Having done this, a determination of "how much is too much?" will be needed to decide whether the settled material might have an unacceptable adverse impact upon the benthic biota.

If it is indicated that there will be potential adverse effects, there are control measures that can be used to reduce these impacts. These include physical barriers such as silt curtains and operational modifications such as dredging windows, dredge modification, and changes in the dredging cycle.

3.0 SEDIMENT TRANSFER AND LOADING

The primary environmental concern with this phase of SimDOR is the leakage or spillage of material. It is very likely that it will be required that such discharges be minimized and that the hoppers, augers, and bag compartments be as watertight as possible. Back-up systems in the event of failure of the primary control measures may also need to be considered.

The bag compartments may pose a significant environmental problem. If there is spillage of material during the filling of the bags or if water is extruded from the bags through consolidation, it may have to be retained in the bag compartments. If it is desired to remove the spillage or extruded water prior to transport and it is intended to discharge it into waters of the United States, it may be subject to evaluation under the 404(b)(1) Guidelines if this action has not been clearly defined as a part of normal dredging operations. If it is not removed, it will become part of the disposal phase and should be evaluated under the MPRSA Ocean Dumping Criteria.

An auxiliary concern regards potential hazards to personnel and violations of the Clean Air Act. This will be project- and material-specific and will have to be evaluated on a case-by-case basis. In particular, volatile contaminants such as ammonia, hydrogen sulfide, and organics, if present, may pose hazards to personnel and contribute to violations of the Clean Air Act. In some areas, pathogenic organisms may be encountered. Hence, it may be necessary to provide protective gear to personnel and minimize the release of volatiles.

4.0 TRANSPORT TO DISPOSAL SITE

This phase is regulated by the MPRSA, which provides that dredged material may be disposed only at a designated ocean disposal site under the conditions of a permit issued by the USACE. The concern here is that spillage or leakage while the material is in transit would constitute unauthorized disposal. As previously noted, it is essential that the bag compartments be watertight so that this does not occur.

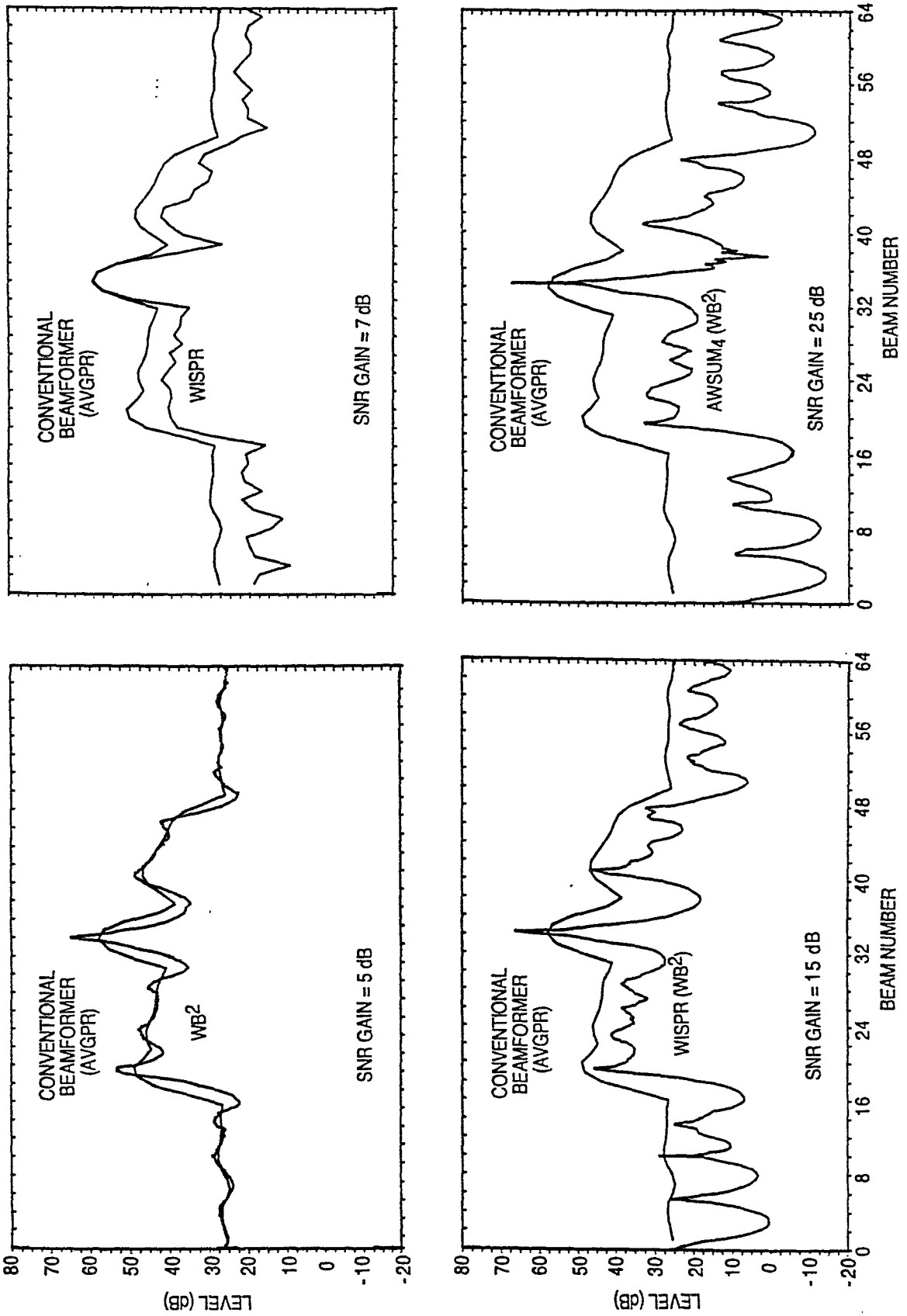

Fig. 9.1 — High resolution – high gain: WISPR (WB^2), $AWSUM_4$ (WB^2)

Appendix C

CLOSED-FORM SOLUTION FOR ELLIPSOIDAL SHAPE IN FREE-FALL, IN MAPLE V (RELEASE 4)

```
> desc:=l-epsilon;
> epeq:=B*desc^(3)+2*desc^(2)-desc^(5/2)-desc^(-1/2);
> convert(series(epeq,epsilon,5),polynom);
> ep4s:=solve(",epsilon);
> ep4:=allvalues(ep4s):
> plot([ep4[3]],B=04.0,labels=['BondNumber','1-(ao/a)^2'],title='Relative
  Equatorial
  > Area');
> e43:=ep4[3]:
> axrat:=(l-e43)^(3/2):
> plot(axrat,B=04,title='Variation of Semi-minor/Sem-major Axes as a Function of Bond
  #');
> bo:=evalf(subs(B=0,e43)):bl50:=evalf(subs(B=150,e43)):
> bl:=evalf(sUbs(B=lre43)):b2:=evalf(subs(B=2,e43)):b3:=evalf(subs(B=3,e43))
  :b4:=evalf(subs(B4,e43)):blO:=evalf(subs(B=lO,e43)):
> ba1:=(1-bl):aa1:=(1-bl)^(-1/2):bao:=(1-bo):aao:=(1-bo)^(-1/2):
> ba2:=(1-b2):aa2:=(1-b2)^(-1/2):ba3:=(1-b3):aa3:=(1-b3)^(-1/2):
> ba4:=(1-b4):aa4:=(1-b4)^(-1/2):ba1O:=(l-b1O):aa1O:=(l-b1O)^(-1/2):
> bal50:=(1-bl50):aal50:=(1-bl50)^(-1/2):
> with(plots):with(plottools):
> elli1 := ellipse(x0,-.17], aa1, ba1, filled=false, color=magenta):
> elli1O := ellipse([x0,-.48], aa1O, ba10, filled=false, color=cyan):
> elli2 := ellipse([x0,-.27], aa2, ba2, filled=false, color-black):
> elli3 := ellipse([x0,-.35], aa3, ba3, filled=false, color-blue):
> elli4 := ellipse([xO,-.38], aa4, ba4, filled=false, color=red):
> elli150 := ellipse([xO,-.75], aa150, bal50, filled=false, color=purple):
> x0 := 0: y0:=O:
  ellio := ellipse([xO,yO], aao, bao, filled=false, color=green):
  plots[display]([ellio,elli1,elli2,elli3,elli4,elli1O,elli150],
    scaling=CONSTRAINED,
  axes=none,title='Deformation of the Ellipsoid with Increasing Bond No. 0,
    1,2,4,10,150');
> ir:=l-e43:ecc:=sgrt(l-(1-e43)^3):ecf:=sgrt(l-(1-E)^3):
> sarf:=(1/2)*(1/(1-E)+(1-E)^2/2/ecf*ln((l+ecf)/(1-ecf)));
> W:=sgrt(8*(sigma/3/rho[w]*B/a[0]*(1-epsilon)/C[D]));
> sar:=(1/2)*(1/(1-e43)+ir^2/2/ecc*ln((1+ecc)/(1-ecc))):
> plot([sar],B=0 .500,title='Relative change of total surface of the oblate
  spheroid w.r.t.a sphere of equal volume');
> es4:=subs(B=sigma^(-l)*(l-rho[w]/rho[c])*rho[c]*g*a[0]^2,rho[c]=1400,
    rho[w]=1028,g=9.8,C[D]=.67,e43):
> Ws:=subs(rho[c]=1400,C[D]=.67,rho[w]=1028,B=sigma^(-l)*(1-rho[w]/rho[c])
```

```
      *rho[c]*g*a[0]^2,g=9.8,epsilon=es4,W):
    > w4:=subs(rho[w]=1028,rho[c]=1400,a[0]=ao,Ws):
> plot3d(w4,sigma=35000..175000,ao=4..7,title='Terminal Fall Speed vs Equiv.
  Radius and Bag Tension with Container Density=1400kg/m^3',labels=['Wall Tension
  (Nt/m)','Equiv. Sphere Rad.(m)',' Fall Speed (m/s)']);
    > es4h:=subs(B=sigma^(-l)*(1-rho[w]/rho[c])*rho[c]*g*a[0]^2,rho[c]=1700,
      C[D]=.67,rho[w]=1028,g=9.8,e43):
    > Wsh:=subs(rho[c]=1700,C[D]=.67,rho[w]=1028,B=sigma^(-l)*(l-rho[w]/rho[c])
      *rho[c]*g*a[0]^2,g=9.8,epsilon=es4,W):
    > w4h:=subs(rho[w]=1028,rho[c]=1700,a[0]=ao,Ws):
> plot3d(w4h,sigma=35000175000,ao=47'title= Terminal Fall Speed vs Equiv. Radius
  and Bag Tension with Container Densityz1700kg/m^3',1abels=['Wall Tension
  (Nt/m)','Equiv Sphere Rad.(m)','Fall Speed (m/s)']);
    > plot3d(w4h-w4,sigma=35000175000,ao=47,title=' W(1700kg/m^3)-W(1400kg/m^3) vs
      Equiv. Radius and Bag Tension ',labels=['Wall Tension(Nt/m)','Equiv. Sphere
      Rad.(m)','Delta W (m/s)']);
    > fq:=.16*(g*(1-rho[w]/rholc]))^(1/2)/b^(1/2)/Cld]^(5/4);
    > fgs:=subs(g=9.8,rho[w]=1028,rho[c]=1400,C[d]=.67,b=ao*(l-e4),fq):
    > fgs2:=subs(B=sigma^(-1)*(1-rho[w]/rho[c])*rho[c]*g*a[0]^2,fgs):
    > f:=subs(g=9.8,rho[w]=1028,rho[c]=1400,a[0]=ao,fgs2):
    > fao:=subs(ao=5,fgs):
    > plot(fao,B=.34,1abels=[ Bond Nunber','Frequency'],title='Shedding Frequency
      (1/sec) with ao=5m,densiLy-1400kg/m^3');
Plotting error, empty plot:
    > plot3d(f,ao=48,sigma=35000175000,title='Shedding Freq.vs Equiv. Sphere
      Radius(m) and Wall Tension(Nt/m),Drag Coef .67, Density
      1400kg/m^3',labels=['Eq.Sph.Radius','Tension','Frequency' (1/sec)']);
    > fh:=subs(g=9.8,rho[w]=1028,rho[c]=1700,a[0]=aoFfgs2h):
    > fgsh:=subs(g=9.8,rhotw]=1028,rho[c]=1700,C[d]=.67,b=ao*(1-e4),fq):
    > fgs2h:=subs(B=sigma^(-1)*(1-rho[w]/rho[c])*rho[c]*g*a[0]^2,fgsh):
    > fh:=subs(g=9.8,rho[w]=1028,rho[c]=1700,a[0]=ao,fgs2h):
> plot3d(fh,ao=48,sigma=35000175000,title='Shedding Freq.vs Equiv. Sphere
  Radius(m) and Wall Tension(Nt/m),Drag Coef .67, Density
  1700kg/m^3 ,labels=['Eq.Sph.Radius','Tension','Frequency (1/sec)']);
> plot3d(fh,ao=48,sigma=35000175000,title='Sho~ing Freq.vs Equiv. Sphere Radius(m)
  and Wall Tension(Nt/m),Drag Coef .67, Density
  1700kg/m^3',labels=['Eq.Sph.Radius','Tension ,' Frequency (1/sec)']);
```

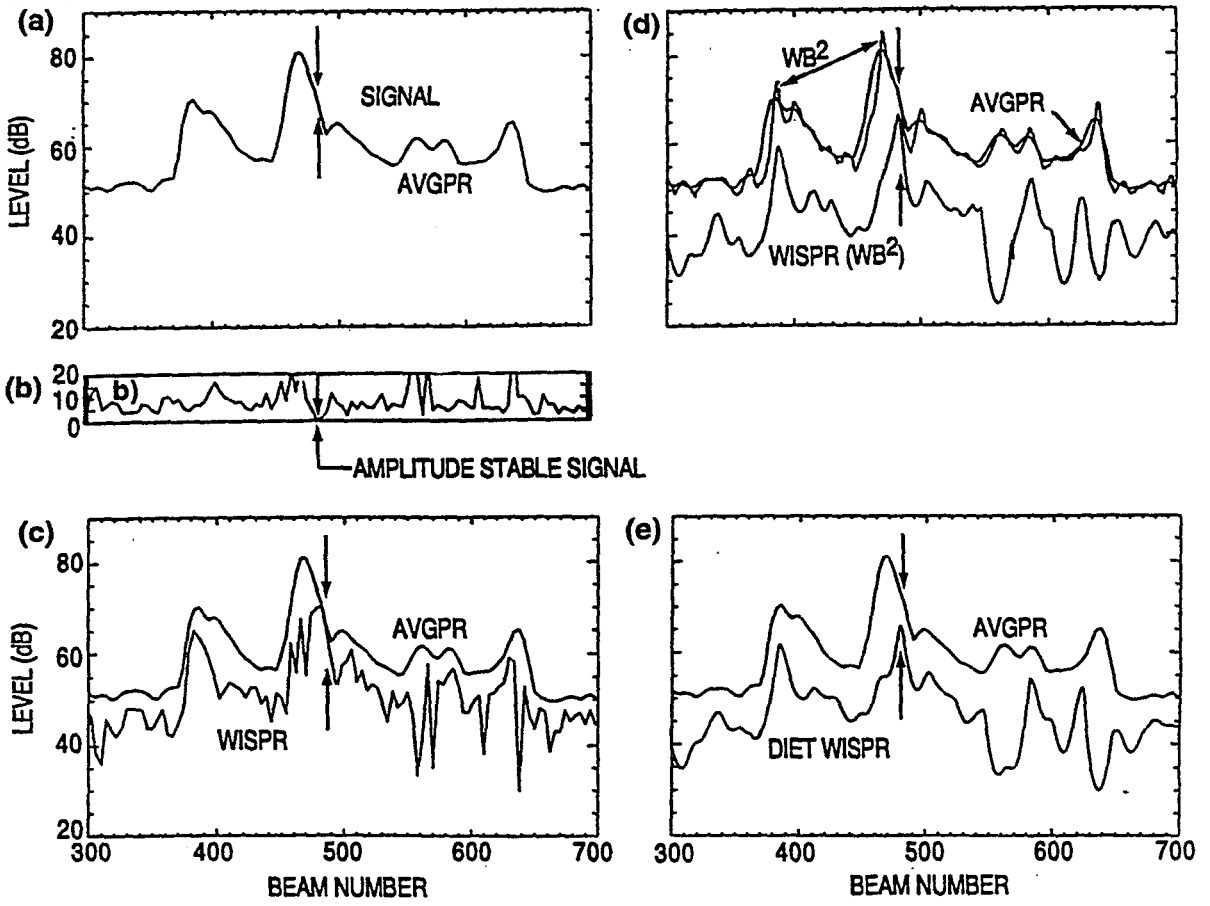

Fig. 9.3 — High gain – high resolution algorithms: WISPR (WB^2) and DIET WISPR

the SNR gain of the buried signal have not been improved by WB^2. Notice the lack of change in the immediate region of the two arrows that identify the location of the submerged source signal.

The bottom curve in Fig. 9.3d, designated WISPR (WB^2), was obtained by combining the WISPR and the WB^2 algorithms. That was accomplished by generating a WB^2 curve for every FFT output and then applying the WISPR algorithm across the set of WB^2 curves at each resolution point across the beam number plot. (Note that the resolution of the WB^2 output across the plot is a factor of four greater than the resolution in beam number.) In this case, the WISPR (WB^2) curve has about the same resolution as the WB^2 curve, but some of the peaks are at different places than in either the AVGPR curve or the WB^2 curve. The reason for this is that the WB^2 and AVGPR algorithms are not sensitive to the fluctuations, while the WISPR (WB^2) algorithm is sensitive to fluctuations. Hence, when a submerged source signal fluctuates less than clutter signals and noise, it will be attenuated less by the WISPR processor than will the clutter signals and the noise. The net effect is that there will be an enhancement in the SNR and a more accurate localization of the stable (i.e., less fluctuating) submerged source signals. For example, the peak in the WB^2 result that is close to the two arrows is actually co-located with the peak in the AVGPR curve. On the other hand, the peak in the corresponding WISPR (WB^2) curve is at the exact location of the arrows, where it needs to be. In addition, it has the approximate magnitude (level) that it should have. Furthermore, the SNR for the real submerged source signal peak (at the arrows) has been increased dramatically by the WISPR (WB^2) algorithm, compared to the AVGPR result where it is not visible at all. The SNR of the submerged source signal in the AVGPR result is obviously <0 dB.

It is still not readily identified in the WISPR results of Fig. 9.3c, but the main peak in the noise beam has been suppressed by about 15 dB. Furthermore, the level of the peak may not be much different from the WISPR result in Fig. 9.3c, but the resolution in the WISPR (WB^2) result has been significantly enhanced.

Figure 9.3e provides a comparison of a new algorithm called the DIET via the WISPR algorithm (DIET WISPR) with the AVGPR result. In this case, the location of the stable signal is identified correctly and the SNR gain has been increased sufficiently to produce a well defined peak where it should be. When the DIET WISPR curve in this figure is compared with the corresponding curve for WISPR (WB^2) in Fig. 9.3d, considerable similarities can be seen. The most important are that the signal has been correctly localized and the SNR gain enhancement has been sufficient to produce a well identifiable peak where there is not a peak in the AVGPR curve.

The similarities between the curves for the WISPR (WB^2) and the DIET WISPR algorithms are rather remarkable. Both algorithms are fluctuation-based signal processors. In other words, both algorithms have been devised or modified to exploit the fluctuations to enhance those algorithms' performances for signals that have lower fluctuation amplitudes. Furthermore, both algorithms correctly localize the stable signal and provide sufficient SNR gain to make it clearly identifiable. The similarity is even more remarkable when the $AWSUM_4$ algorithm is used instead of WISPR to produce the DIET $AWSUM_4$ algorithm. When that is done, the results, presented in Fig. 9.4, are very similar in SNR as the WISPR (WB^2) results, but the resolution is significantly greater. The DIET $AWSUM_4$ results are also enhanced compared to the DIET WISPR results in Fig. 9.3e.

The results in Figs. 9.3 and 9.4 illustrate the important role that fluctuations can play in detecting, identifying, localizing (Figs. 9.3 and 9.4), and enhancing the resolution and SNR of stable signals among clutter signals and background noise.

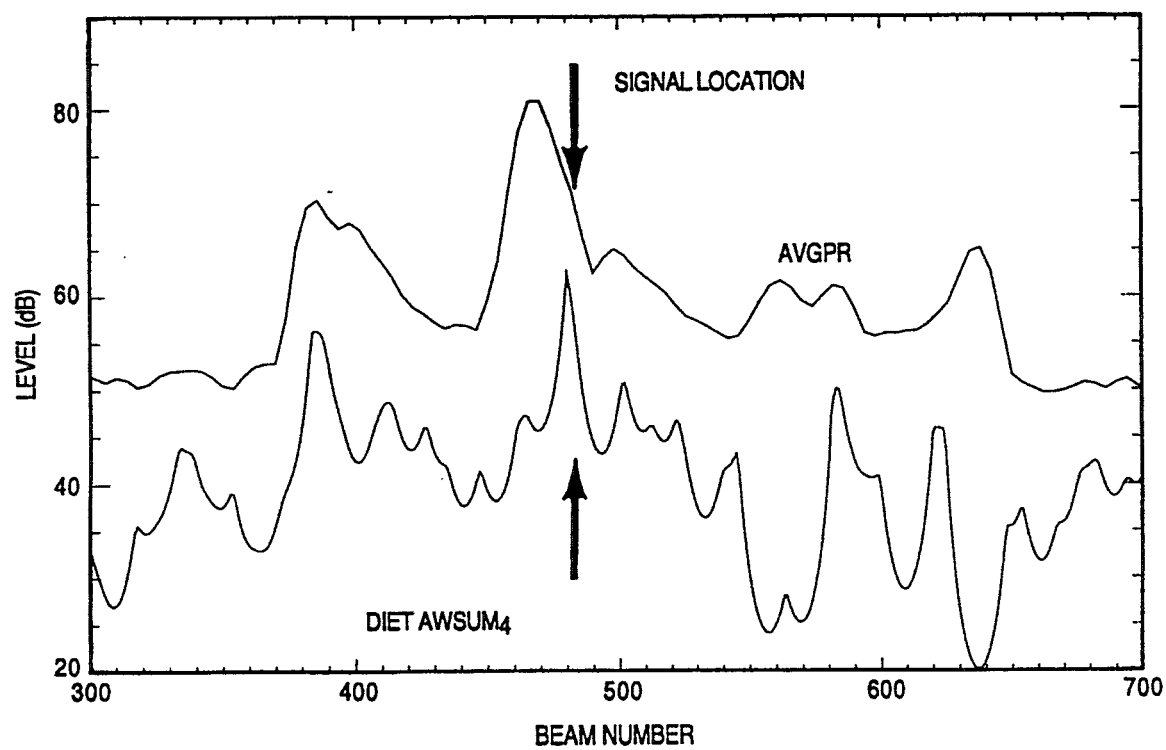

Fig. 9.4 — A comparison of DIET $AWSUM_4$ processing with conventional processing

10.0 MEASURES OF WISPR PROCESSOR PERFORMANCE

10.1 The Problem with the DI as a WISPR Performance Measure

10.1.1 Introduction

Throughout this report, the SNR gain increase has been defined as the signal excess of the fluctuation-based processors (e.g., WISPR, AWSUM, and WISPR II) compared to the signal excess that is achieved by the AVGPR processor. Some signal processing researchers may attempt to "put round pegs into square holes," e.g., try to evaluate an unconventional nonlinear processor such as WISPR according to standards developed to test conventional linear processors. An example is the measurement of the SNR gain of WISPR. A benchmark method that has become accepted by many signal processors for determining the SNR gain improvement of one processor relative to another is the DI, defined in Sec. 10.1.2. The relative SNR gain by this procedure is defined simply as the ratio of the DIs for the two systems to be compared. For example, with A and W for AVGPR and WISPR respectively, the SNR gain of WISPR compared to AVGPR would be

$$SNR_{(Gain:W/A)} = DI_W/DI_A \,. \tag{10.1.1}$$

The main fallacy of this method is that it is incapable of reasonably accounting for gain achieved through differences in signal fluctuations. In fact, when fluctuation gain must be taken into account, this index (at low SNR) can be shown to produce absurd and unusable results. Although not obvious, the evenly distributed noise assumption (locally white noise in the vicinity of the signal) is tacitly required by its definition. In addition, no distinction is made between signals which have variation in fluctuation levels. The main cause of failure is the structure of the index itself. It arises as a direct result of its definition in terms of expectations and implied statistical distributions.

10.1.2 Definition of the Detection Index

Detection Index, DI, as used herein, is

$$DI \equiv \left[\frac{<S+N>-<N>}{\sigma_f}\right]^2 , \tag{10.1.2}$$

where

$< >$ = expectation operator,

N = noise power,

S = signal power,

σ_f = is the power standard deviation, across a group of frequencies, centered around the frequency of signal S, exclusive of itself. It is usually estimated by

$$\sigma_f \approx \left[\frac{1}{n-1}\left[\sum_{j=f-(n/2)}^{j=f-1}(X_j - X_{avg})^2 + \sum_{j=f+1}^{j=f+n/2}(X_j - X_{avg_f})^2\right]\right]^{\frac{1}{2}} , \tag{10.1.3}$$

and

$$X_{avg_f} = \frac{1}{n}\left[\sum_{j=f-(n/2)}^{j=f-1} X_j + \sum_{j=f+1}^{j=f+n/2} X_j\right], \tag{10.1.4}$$

where

n = in this case, an even number of values in the vicinity of the fth item,

j = the index of a spectral bin,

X_j = the jth spectral power, taken in the vicinity of the fth frequency, excluding itself.

Other ad hoc ranges thought to be more typical of the ambient noise could be used with some loss of objectivity for this index.

10.1.3 Discussion of the DI Calculation

If the acoustic local white noise frequency domain world was from a statistically perfect universe, it could be assured that the $\langle N \rangle$ and $\langle S + N \rangle$ (expectations) could be determined easily. With a sufficiently large number of time realizations, by simply taking averages over noise frequency bins, the average would converge to $\langle N \rangle$. Since the idealized world is locally of white noise, the average for noise in a signal bin would also have to converge to $\langle N \rangle$. Additionally, the average for a purported signal bin should converge to $\langle S + N \rangle$. Close examination of Eqs. 10.1.2, 10.1.3, and 10.1.4 reveals that these conditions must be at least approximately true to obtain reasonable estimates for $\langle S + N \rangle$ and $\langle N \rangle$.

The authors are not trying to convince anyone that this is reality; clearly it is not. Yes, noise generated in the sea by many natural processes is broadly distributed in frequency. Yes, transient events, whose time domain signals are processed through the Fourier transform, also produce results broadly distributed in frequency (though hardly ergodic). Man-made signals obviously have some broadband structure. However, many signals of interest generated at power levels sufficient to reach distant receivers are chiefly discrete tonals. Admittedly, some of their power shows up after Fourier transformation as sidelobes in the frequencies near to the tonal frequency. In spite of all this, there is still plenty of opportunity for noise (on the average) to not be absolutely evenly distributed. Thus, some spectral bins may contain much less noise than that indicated by the estimated average value.

10.1.4 Detection Index Fluctuation-Based Performance Study for WISPR Processors

To demonstrate just what the DI would show for typical acoustic data of known characteristics, noise and tonal data have been artificially generated. The result of this simulation is shown in Table 10.1.1.

10.1.4.1 Data Set Generation Method

Typical signal and noise power levels, normally distributed in decibels (equivalent to a log-normal distribution before conversion to decibels), were generated separately for a mean of 70 dB and with the standard deviations (sigma) indicated in Table 10.1.1 (3, 4, 5, and 6 dB) for

Table 10.1.1 — WISPR Class Processor Detection Index Simulation Study

Processor	N-Avg. Across Freq.	% Noise in Bin				% Noise in Bin			
		10	40	70	100	10	40	70	100
		Total Power in Tonal Bins, dB				DI Ratio, Processor/AVGPR			
AVGPR	69.98	70.4	71.5	72.4	72.9	1	1	1	1
WISPR	67.92	70.4	71.4	72.1	72.5	50	8	5	4
$AWSUM_2$	66.90	70.4	71.3	72.0	72.3	63	8	5	3
$AWSUM_3$	65.95	70.4	71.2	71.9	72.2	56	7	3	2
$AWSUM_4$	65.14	70.4	71.2	71.8	72.1	52	6	3	2

Time Sequence Noise Standard Deviation, 3 dB–Time Sequence Tonal Standard Deviation, 1 dB

Processor	N-Avg. Across Freq.	% Noise in Bin				% Noise in Bin			
		10	40	70	100	10	40	70	100
		Total Power in Tonal Bins, dB				DI Ratio, Processor/AVGPR			
AVGPR	70.00	70.4	71.6	72.4	73.0	1	1	1	1
WISPR	66.32	70.3	71.3	71.8	72.2	297	23	12	8
$AWSUM_2$	64.55	70.3	71.2	71.6	72	328	22	11	7
$AWSUM_3$	63.04	70.3	71.1	71.5	71.8	327	20	9	6
$AWSUM_4$	61.90	70.3	71.0	71.4	71.7	375	22	10	6

Time Sequence Noise Standard Deviation, 4 dB–Time Sequence Tonal Standard Deviation, 1 dB

Processor	N-Avg. Across Freq.	% Noise in Bin				% Noise in Bin			
		10	40	70	100	10	40	70	100
		Total Power in Tonal Bins, dB				DI Ratio, Processor/AVGPR			
AVGPR	69.98	70.4	71.3	72.3	72.7	1	1	1	1
WISPR	64.30	70.4	71.0	71.6	71.9	767	102	33	26
$AWSUM_2$	61.70	70.3	70.9	71.4	71.7	799	98	29	22
$AWSUM_3$	59.76	70.3	70.9	71.3	71.5	1030	122	34	26
$AWSUM_4$	58.45	70.3	70.8	71.2	71.4	1424	164	45	33

Time Sequence Noise Standard Deviation, 5 dB–Time Sequence Tonal Standard Deviation, 1 dB

Processor	N-Avg. Across Freq.	% Noise in Bin				% Noise in Bin			
		10	40	70	100	10	40	70	100
		Total Power in Tonal Bins, dB				DI Ratio, Processor/AVGPR			
AVGPR	70.01	70.5	71.2	72.4	73.2	1	1	1	1
WISPR	61.82	70.4	70.9	71.3	71.7	2201	427	107	58
$AWSUM_2$	58.37	70.4	70.8	71.2	71.4	2914	538	126	66
$AWSUM_3$	56.10	70.3	70.8	71	71.2	4884	879	200	102
$AWSUM_4$	54.66	70.3	70.7	70.9	71.1	7496	1325	295	149

Time Sequence Noise Standard Deviation, 6 dB–Time Sequence Tonal Standard Deviation, 1 dB

300 time realizations. (This data set can be considered to apply to any frequency range, since the maximum frequency of real data would be determined by the time domain digital sampling rate.)

(a) The dB values generated were converted to arithmetic power levels and stored.

(b) The noise generated for each of 1024 frequency bins was averaged across time for each bin.

(c) The single tonal generated was averaged across time.

(d) The power level for the entire data set was adjusted so that the noise and tonal arithmetic averages when converted back to decibels would equal 70 dB, an initial SNR of 1.0.

(e) The arithmetic power level for the noise in bins 100, 400, 700, and 1000 was adjusted to 10%, 40%, 70%, and 100% of the former values, respectively.

(f) The single tonal set was then added to the noise in bins 100, 400, 700, and 1000. Note that only bin 1000, with 100% noise, has a 70-dB noise level and a 70-dB signal level, an initial SNR = 1.0 (0 dB).

10.1.4.2 Discussion

The results of processing these simulated data utilizing the AVGPR, WISPR, $AWSUM_2$, $AWSUM_3$, and $AWSUM_4$ processors are shown in Table 10.1.1. Several observations can be made concerning these results:

(a) The reduction in the processor result (Col. 2) systematically decreases as the noise sigma is increased from 3 to 6 dB and systematically decreases as the AWSUM processor order number increases, just as would be anticipated from the previously described properties of these processors.

(b) In contrast to observation (a), there is practically no suppression of the tonal in the 10% noise bin (Col. 3) and only 0.8- to 2.1-dB suppression of the tonal in the highest noise case, the 100% noise bin (Col. 6).

(c) The WISPR DI ratio (SNR gain from Eq. 10.1.1) progresses dramatically upward as the noise content in a signal bin is reduced, e.g., for the 5-dB noise case, the WISPR DI ratio at 100% noise is 26, increasing to 767 at 10% noise. In instances where the average noise and signal are approximately equal, but noise in a particular instance is not manifest in the signal bin, the numerator of Eq. 10.1.2 would become zero when the AVGPR processor is used, producing $DI_A \approx 0$. Since the fluctuation-based processors will dramatically suppress the noise (estimated $\langle N \rangle$) in all bins, but not the steady tonal (estimated $\langle S + N \rangle$) in the signal bin, this numerator would be far from zero. Therefore, the SNR gain would approach infinity, a very unreasonable result. One may think this cannot occur in reality. Examples demonstrating this possibility will be presented shortly for real data.

(d) In any case, an interpretation of the DI results from this data set, constructed to intentionally show its weakness for the evaluation of fluctuation-based processors, leaves one with the question, "Now that I have calculated the DI, how can it be used under similar field conditions in any reasonable manner to evaluate the processors being compared?" The implications are probably more subtle than a reader unfamiliar with these processors is initially willing to admit.

10.1.5 Processor DI Performance for Real Ocean Acoustic Data

10.1.5.1 The Fallacy of AVGPR when SNR = 1 (0 dB) for Real Data

From the point of view of fluctuation-based processors, any fluctuating signal is noise; whereas, steady tonals are viewed as those from submerged sources. In essence, the question to be answered

is, "How well do these processors identify those steady tonal submerged sources?" Note, as discussed earlier, that as a practical matter, the theoretical values for $<S + N>$ and $<S>$ are never known for real data but may only be estimated. With real data, calculation of the DI resorts to a determination of $<S + N>$ as the averaged value (determined with the processor under consideration) in that spectral bin where a signal is purported to be present. Then, from other nearby spectral bins where noise only is purported to be present, $<N>$ is estimated as the average for those bins of the value that was obtained by the processor, e.g., as determined by Eqs. 10.1.3 and 10.1.4.

Example 1: (Note: The figure referred to in the next paragraph was presented in Sec. 4.0)

Clearly, in Fig. 4.6a (with only 50 elements of the array), calculating the detection index for the signal near beam 68 for the AVGPR processor, $<S + N> \approx <S>$, which yields from Eq. 10.1.2 that $DI_A \approx 0$. Any reasonable person, examining the AWSUM$_4$ curve in that plot, would conclude that $<S + N>$ is about 42 dB and the $<N>$ is about 30 dB. Therefore, for the WISPR type processor, AWSUM$_4$ in this case

$$\frac{DI_W}{DI_A} = \left[\frac{<S+N>-<N>}{\sigma_f}\right]_W^2 \Big/ \left[\frac{<S+N>-<N>}{\sigma_f}\right]_A^2$$

$$= \left[\frac{42-32}{\sigma_f}\right]_W^2 \Big/ \left[\frac{\approx 0}{\sigma_f}\right]_A^2 = \rightarrow \infty ,$$

an absurd result. The signal peak at beam number 68, visible on the AWSUM$_4$ curve, is not visible on the AVGPR curve. However, it is difficult to deny that the two curves are actually quite reasonably related. That this peak actually exists, as indicated by the AWSUM$_4$ processor, is ultimately shown in the AVGPR curve when the number of array elements is increased to 100 and to 198 as shown in Fig. 4.6b and c.

Example 2:

Figure 10.1 identifies three tonals that are embedded in background noise at 43, 65, and 80 Hz. The top curve is for AVGPR, the middle curve is for WISPR, and the bottom curve is the difference between the previous two curves (noise suppression A_{01}), truncated at 10 dB. Where this last curve (or set of curves) approaches 0 dB, it indicates the presence of three tonals that are known to have been projected from submerged sources. For the signals at 43 and 65 Hz, it would be possible to calculate the DI. At those frequencies, DI may or may not (dependent upon the actual detailed values) numerically indicate that the AVGPR processor is superior to the WISPR processor. The situation is somewhat different at 80 Hz where there is no discernible signal in the AVGPR curve, but there is in the WISPR result. In this case, the ratio of the DIs approaches infinity as described in Example 1 just presented, indicating that WISPR is far superior. How does one reconcile this ambivalence using the ratio of the DIs for evaluating the two processors? One can't; he/she must simply conclude that the DI definition does not make much sense when applied to fluctuation-based processors; processors that can achieve gain through properties of signals and noise that simple conventional processors fail to utilize. WISPR is clearly better, but the ratio of the DIs can't quantify exactly how much better, or even that it is better.

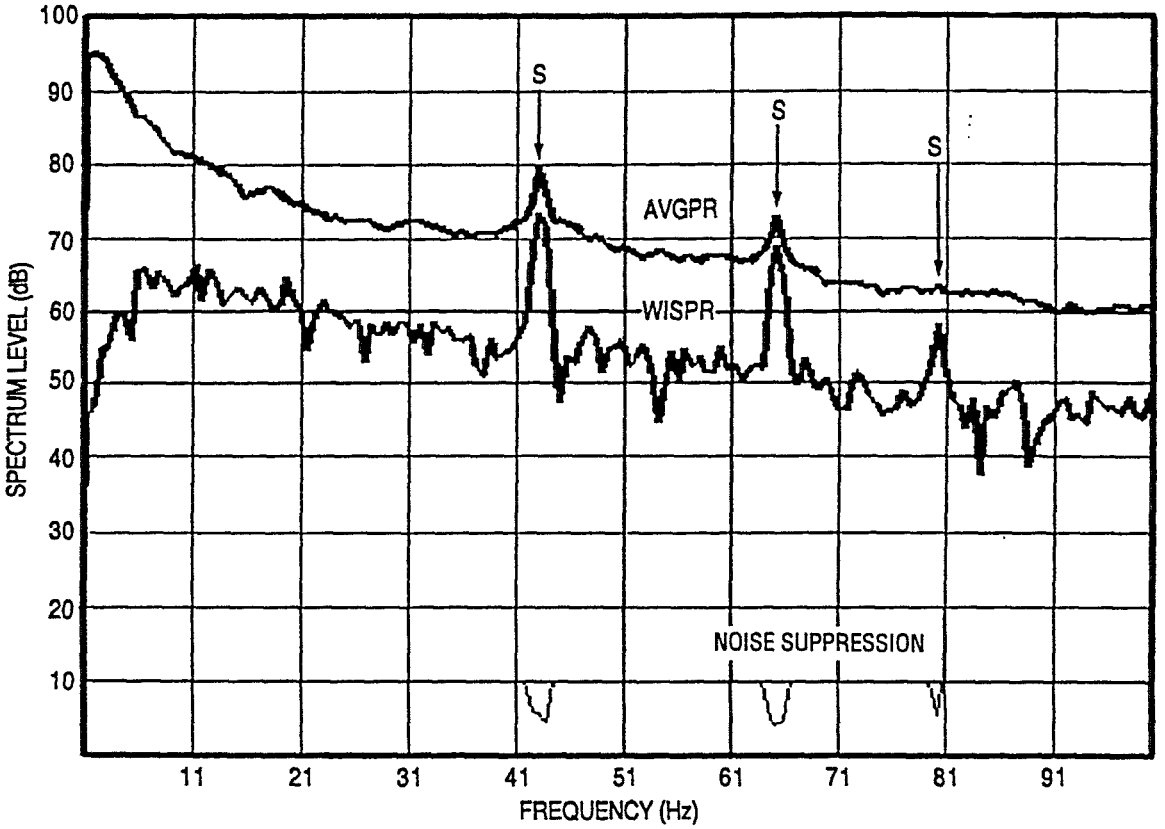

Fig. 10.1 — WISPR processing: SNR <0 at 80 Hz

10.1.6 Summary

It should be obvious from the simulation study and the two examples using real data that if the SNR is too low for the tonal to be detected by the conventional processor, the ratio of the DIs are not valid and cannot be used to compare the two processors. That being the case, the question naturally arises as to when can the ratio of the DIs be used? Furthermore, if it is not a valid measure at low SNR, what then makes it a valid one at higher SNR, and how high must it be? Until those questions are answered, it seems that other criteria need to be devised; criteria that recognize the uniquely different nature of the WISPR processor compared to classical/conventional processors. In devising such criteria, the most important thing to keep in mind is that the WISPR processor is driven by the magnitude of the fluctuations. The actual magnitude of the tonal, for the most part, is not a relevant parameter for the fluctuation-based processors such as the WISPR processor. By contrast, conventional signal processors are driven by the magnitude of the tonal and completely discard a key source of classification information encoded by nature in the acoustical fluctuations of signals and noise.

10.2 WISPR Performance Measured by ROC Curves and the Relationship to DI

Receiver Operating Characteristics (ROC) curves were generated to measure the performance of the WISPR Filter in noise that has a Gaussian distribution in power and in noise that has a Gaussian distribution in the log of power (a log-normal distribution). Figure 10.2, containing plots

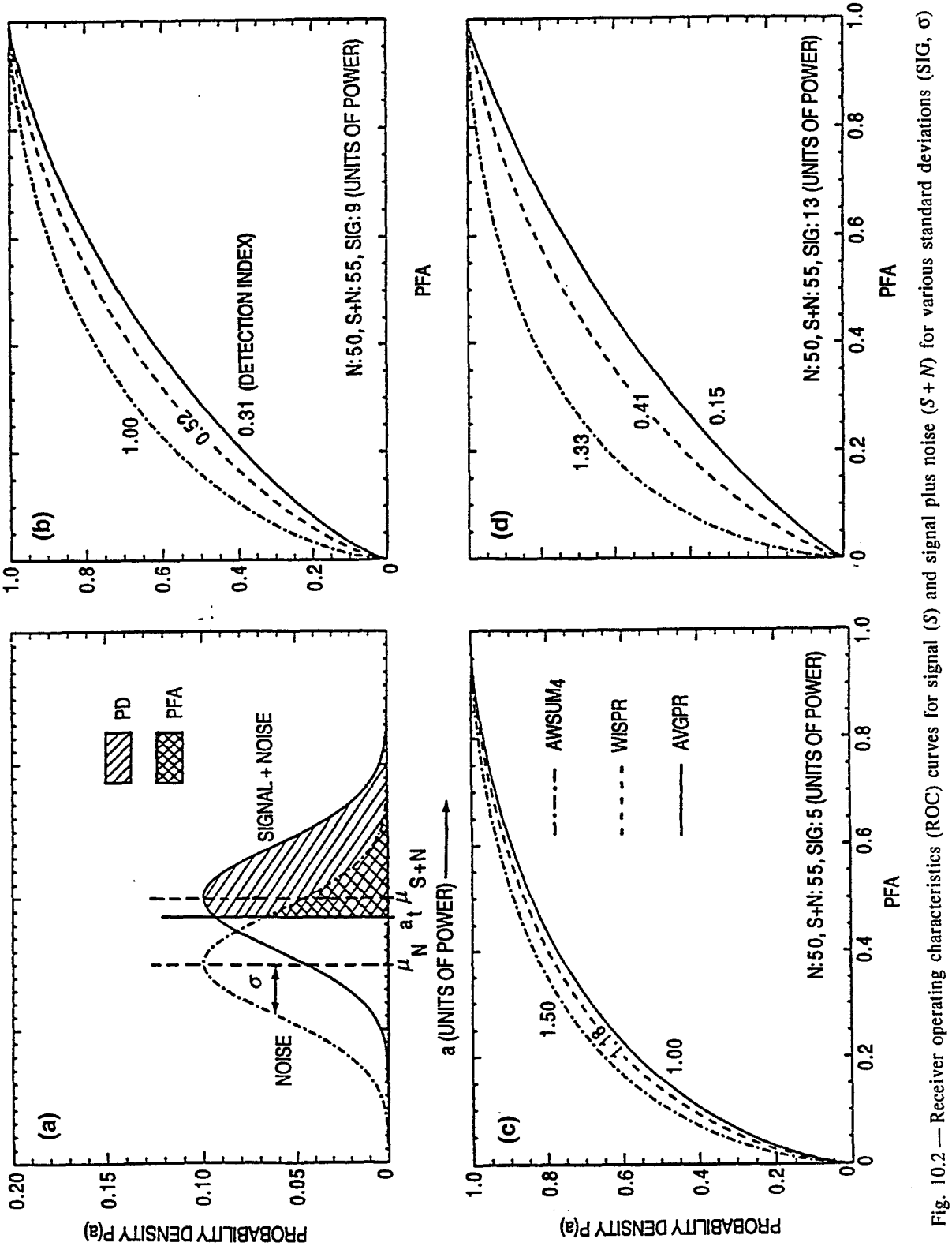

Fig. 10.2 — Receiver operating characteristics (ROC) curves for signal (S) and signal plus noise ($S+N$) for various standard deviations (SIG, σ)

(a), (b), (c), and (d), illustrates the results for the AVGPR (the solid curves), the WISPR Filter results (the dashed curves), and the AWSUM$_4$ Filter results (the dashed-dot curves).

Figure 10.2, plot (a), illustrates the process of generating the ROC curves and the regions under the noise and the signal plus noise curves that are important in the calculations. The mean noise power is μ_N and the mean signal plus noise is μ_{S+N}. The signal is assumed to be an ideal steady tonal with a standard deviation (variously labeled σ, SIG, or SIGMA) of zero and power a_t. The boxes show the type of shading under the noise and signal plus noise probability density curves that correspond to the areas that represent the probability of detection (PD) and the probability of false alarm (PFA). In this case, the signal plus the noise is five units of power more than the noise.

Figure 10.2, plots (b), (c), and (d), give the ROC curves for the three different methods when the standard deviations (units of power) are 9, 5, and 13, respectively. In each case, the WISPR Filter outperforms the AVGPR processor by achieving a larger DI (c.f., Sec. 10.1.2 for the definition of DI) and the AWSUM$_4$ Filter outperforms both of them. For example, in plot (b) the DIs are 0.31, 0.52, and 1.00 for the AVGPR processor, the WISPR Filter, and the AWSUM$_4$ Filter, respectively. The trend is for the DI of the WISPR Filter to exceed that of the AVGPR processor differences to grow as the standard deviation of the noise increases.

The previous illustration shown in Fig. 10.2 was for a highly idealized case where the equivalent standard deviation ranged from about 0.6 dB (plot (c)) to 1.5 dB (plot (d)). The standard deviations of noise in the ocean normally range from about 4.5 to 7 dB, and the probability density curves for the signal and the noise are more nearly log-normal than Gaussian (c.f., Fig. 3.20 and the discussion of that figure).

Results for the AVGPR processor and the WISPR Filter are given in the left and right plots in Fig. 10.3, respectively, for a mean noise level of 70 dB, a standard deviation of 6 dB, and for three different signal levels. The SNRs range from –5 dB to 1 dB.

The results in Fig. 10.3 indicate, as in Fig. 10.2, that the performance of the WISPR Filter, as measured by the DI, exceeds the performance of the AVGPR processor by substantial amounts for all three signal levels (and also SNR). The improvement is approximately a factor of 18 (12.8 dB),

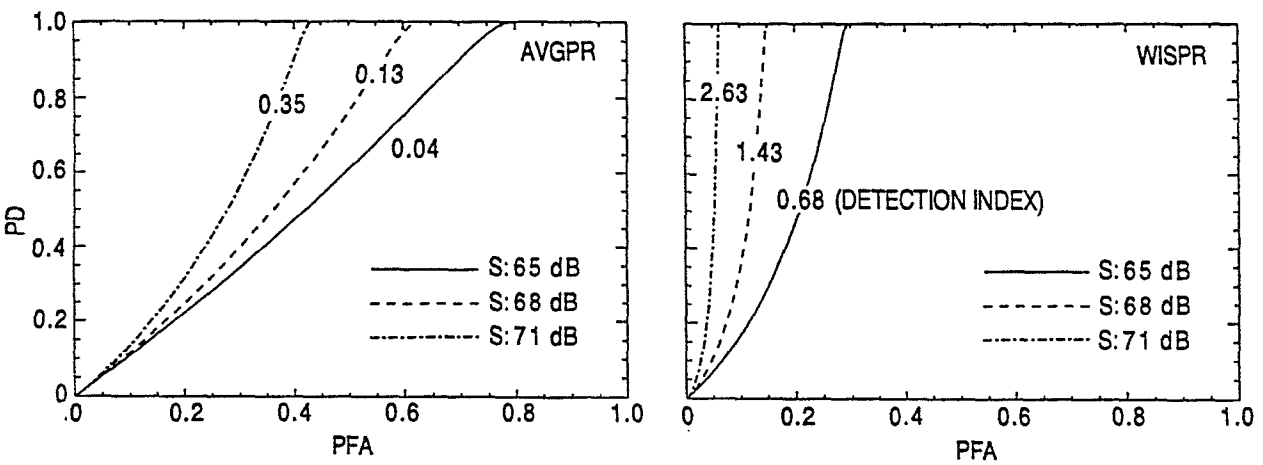

Fig. 10.3 — Sonar system performance for tonal (S) in log-normal noise (N): WISPR (right) versus conventional (AVGPR) processing (left), N: 70 dB, SIGMA: 6 dB

11 (10 dB), and 7 (8.5 dB) for signal levels of 71, 68, and 65 dB, respectively, and for SNR of 1, –2, and –5 dB, respectively. For the case of a steady tonal in noise that is characteristic of undersea ambient noise (Fig. 10.3), the gains in WISPR processing are of the order of 8 to 12 dB for SNR from 1 to –5 dB. However, when the standard deviations are small (Fig. 10.2) and the noise is normally distributed, not at all like the undersea noise, the gains are small enough to be considered insignificant. However, that turns out to be an advantage, since the distribution of an actual submerged tonal has a rather small standard deviation such as the "noise" in Fig. 10.2, and the attenuation by the WISPR Filter would also be small, less than about a decibel.

There is an important point that needs to be made in regard to the ROC curves in Figs. 10.2 and 10.3. They were produced with the assumption that the signal and the noise added in an incoherent manner. For some signals and noise that would not be a valid assumption and a coherent addition would be more appropriate.

11.0 ACKNOWLEDGMENTS

Mr. Tommy Goldsberry of the Office of Naval Research (ONR) Code 321 is gratefully acknowledged for his support under the WISPR Development and Evaluation Project Number 602314.

Appreciation is also expressed for colleagues at the Naval Research Laboratory who contributed to the research reported herein including Ms. Karen Dudley, Mr. Robert Fisher, Ms. Susan D. Gardner, Ms. Stephanie F. Kooney, Mr. Jackson Mobbs, Mr. Joal J. Newcomb, and Mr. E. J. Yoerger. Their contributions include figures used in the report, time contributed to acquire and process data, and contributions to the analysis efforts. For those contributions the authors are sincerely grateful.

The authors also wish to acknowledge with gratitude various forms of assistance provided by Dr. Marshall Bradley of Planning Systems Inc. (especially in modeling) and Laura Hart of Alliant Techsystems (especially in data acquisition and processing) and their highly competent and helpful staff.

12.0 REFERENCES

1. "Encyclopedic Dictionary of Mathematics," Volume II, 2nd Ed., Section 211, p. 807, English translation by the Massachusetts Institute of Technology (1987), United States Library of Congress ISBN 0-262-09026-0, MIT Press.

2. R. A. Wagstaff and J. George, "A New Fluctuation Based Digital Signal Processor Including Phase Variations," patent application submitted, Aug 1995.

3. R. A. Wagstaff and J.-L. Berrou, "A Fast and Simple Nonlinear Technique for High Resolution Beamforming and Spectral Analysis," *J. Acoust. Soc. Am.* **75**(4), 1133–1141 (1984).

4. S. D. Gardner, "A Method for Improving the Signal-to-Noise Ratio and Resolution of Stable Amplitude Signals," MS Thesis, Univ. of New Orleans, Dec 1995.

Appendix A

PROCESSING ALGORITHMS AND RELATED EQUATIONS

A-1.0 INTRODUCTION

To interpret data, particularly when in the form of rapidly acquired real-time data streams, it is both reasonable and necessary to develop methodologies (algorithms) that reduce the original data to more easily interpretable (derived) quantities. The statistical community commonly computes familiar quantities, such as measures of central tendency (e.g., average), standard deviation, and higher order statistics.

Some of the computational methods pertinent to this report are evolved from the generalized function

$$M_r = M_r(a) = \left[\frac{1}{n} \sum_{j=1}^{j=n} a_j^r \right]^{\frac{1}{r}}, \tag{A.1.1}$$

where the data stream is the sequence, a

$$a = (a_1, a_2, a_3, \ldots a_n), \; a_j \geq 0. \tag{A.1.2}$$

Because of the possibility of numerical overflow, use of Eq. A.1.1, when $r < 0$ is restricted to nonzero data values. Two practical approaches that avoid numerical overflow are: (1) Force values near zero to a small numerically convenient value. As A/D converters are not usually significant in the lowest order bits, a logical choice is to set this minimum value of a_j to the value implied by some small multiple of the A/D converter least significant bit. (2) Simply delete any data less than a small numerically convenient value from the original data set. This latter approach is preferred as it also provides for automated removal of data from periods of time where the data acquisition system is malfunctioning or otherwise unavailable without biasing the results obtained from the data actually processed.

Eq. A.1.1 can be used quite generally and for particular choices of r defines several familiar statistical quantities. For example, compare:

When $r = 1$, the average is: $a_{avg} \equiv M_1 = \left| \frac{1}{n} \sum_{j=1}^{j=n} a_j \right|$,

when $r = 2$, the root mean square is: $a_{rms} \equiv M_2 = \left[\frac{1}{n}\sum_{j=1}^{j=n} a_j^2\right]^{\frac{1}{2}}$,

when $r = -1$, the harmonic mean is: $a_{harm} \equiv M_{-1} = \left[\frac{1}{n}\sum_{j=1}^{j=n} a_j^{-1}\right]^{-1}$.

Consider Eq. A.1.1's relationship to the geometric mean.[1]

$$a_{geom} \equiv \left[\prod_{j=1}^{j=n} a_j\right]^{\frac{1}{n}} = M_{r\to 0} = \lim_{r\to 0}\left[\frac{1}{n}\sum_{j=1}^{j=n} a_j^r\right]^{\frac{1}{r}}. \tag{A.1.3}$$

Thus, though not initially obvious, the geometric mean, a_{geom}, is identically equal to M_0.

Another important property that can be shown by mathematical induction[1] is that M_r increases strictly monotonically with increasing r. This is illustrated in Fig. A.1.1 using the arbitrary data sequence $a = (1, 2, 3, \ldots, 10)$. It follows that

$$M_{-1} \le M_0 \le M_1 \le M_2, \text{ i.e., } a_{harm} \le a_{geom} \le a_{avg} \le a_{rms}. \tag{A.1.4}$$

The value of M_r for any particular sequence, a, $a_j \ge 0$, is also bounded

$$M_{r\to\infty} \to a_{max} \text{ and } M_{r\to-\infty} \to a_{min}. \tag{A.1.5}$$

In Fig. A.1.1, it is fairly obvious that $M_{r\to\infty}$ approaches 10, the maximum value, and $M_{r\to-\infty}$ approaches 1, the minimum value.

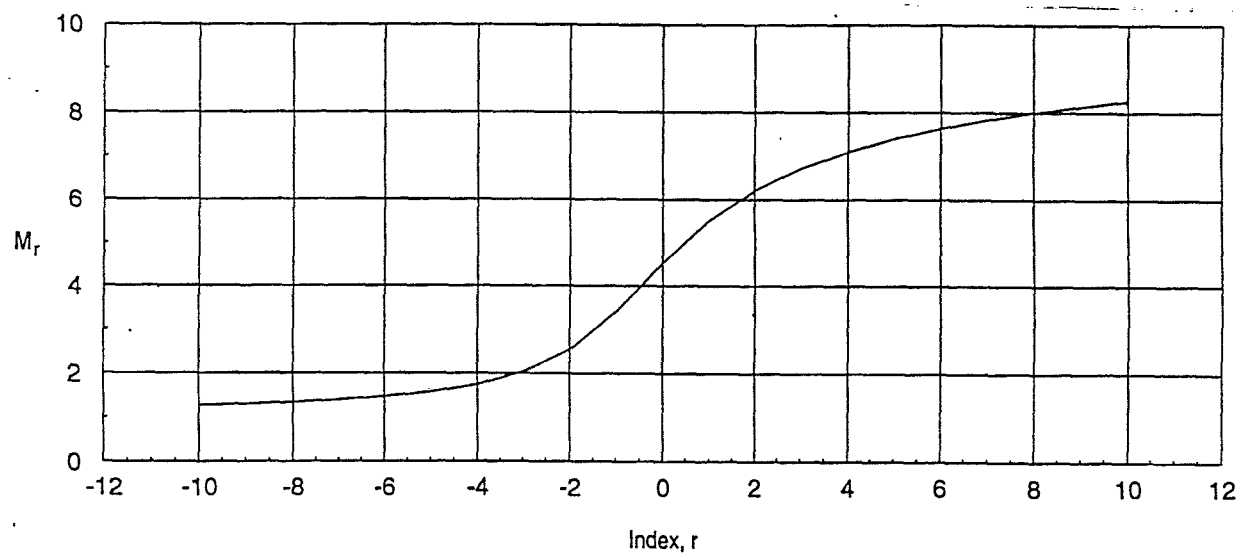

Fig. A.1.1 — The effect of index r on the sequence, $a = (1, 2, 3, 4, 5, 6, 7, 8, 9, 10)$

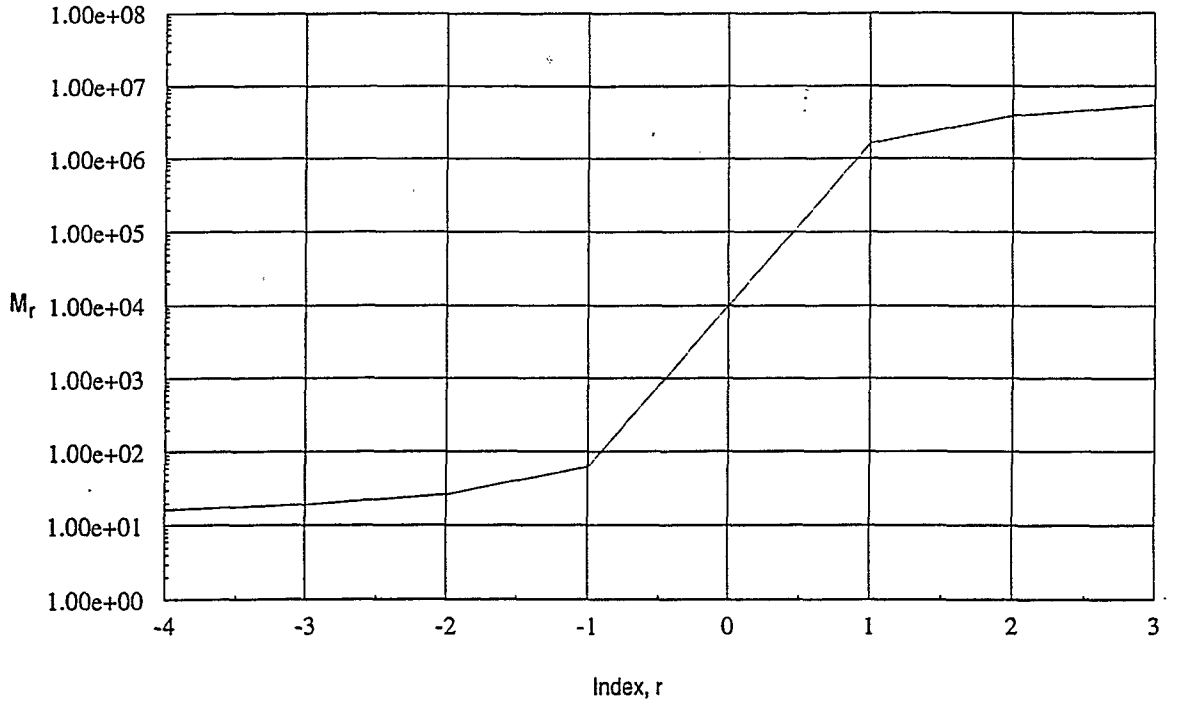

Fig. A.1.2 — The effect of index r on the sequence, $a = (10^1, 10^2, 10^3, 10^4, 10^5, 10^6, 10^7)$

The linearly distributed data shown used to prepared Fig. A.1.1 is not particularly representative of ocean acoustic data. Even though the trend is obvious, the example does not adequately illustrate what happens when data are distributed over a broad range in power. The logarithmically distributed data sequence $a = (10^1, 10^2, 10^3, 10^4, 10^5, 10^6, 10^7)$ used to prepare Fig. A.1.2 provides an example of what occurs for this type of data. With data distributed in this fashion, the negative order (exponent) processor results are almost captured (very strongly influenced) by the smallest two values, 10^1 and 10^2, whereas the positive order processor results are almost captured (very strongly influenced) by the largest two values, 10^6 and 10^7. It is quite simple to verify that if there is no variation in the data, i.e., there are no fluctuations, the result for M_r of all orders, $r = -4$, -3, -2, -1, 0, 1, 2, 3, 4 will be equal. In other words, the greater the fluctuation level, the greater that the negative order filters, M_r, will suppress the final result, whereas, nonfluctuating signals are not suppressed. It is this interpretation of the properties of these fluctuation-based processor algorithms/filters that is the key to successfully understanding the unusual and often very impressive results they achieve on actual measured data.

A.2.0 AVERAGING IN LOGARITHMS OR DECIBELS

A.2.1 Logarithms

Let X_j correspond to the original data values in power, then if

$$a_j = \log(X_j),$$

and noting that $a_{avg} = M_1$, this particular average yields

$$a_{avg\ in\ log} = \left[\frac{1}{n}\sum_{j=1}^{j=n} \log X_j\right].$$

Thus, from Eq. A.1.3

$$\log^{-1}(a_{avg\ in\ log}) = \left(\left[\prod_{j=1}^{j=n} X_j\right]^{\frac{1}{n}}\right) = (X_{geom}).$$

Upon taking the logarithm again

$$a_{avg\ in\ log} = \log\ (X_{geom}). \tag{A.2.1}$$

A.2.2 Decibels

Following the same steps for averaging in decibels, let X_j correspond to the original data values in power, then if

$$a_j = \mathrm{dB}(X_j) = 10\ \log\ (X_j),$$

and noting that $a_{avg} = M_1$, this particular average yields

$$a_{avg\ in\ dB} = \left[\frac{1}{n}\sum_{j=1}^{j=n} 10 \log X_j\right] = 10\left[\frac{1}{n}\sum_{j=1}^{j=n} \log X_j\right].$$

Thus, from Eq. A.1.3

$$\log^{-1}(a_{avg\ in\ dB}) = \left(\left[\prod_{j=1}^{j=n} X_j\right]^{\frac{1}{n}}\right)^{10} = (X_{geom})^{10}.$$

Upon taking the logarithm again and using the result from Eq. A.2.1

$$a_{avg\ in\ dB} = 10\ \log\ (X_{geom}) = 10 a_{avg\ in\ log}. \tag{A.2.2}$$

These results are important computationally, since the obstacles that M_0 cannot be calculated directly and the product, $\prod_{j=1}^{j=n} X_j$, can easily produce numerical overflow when n is large, are avoided.

A.2.3 Magnitude Order

The magnitude order is preserved in decibels, i.e., with the original data in power

$$\mathrm{dB}(a_{harm}) \le \mathrm{dB}(a_{geom}) = \mathrm{dB}(a_{avg\ in\ dB}) = 10a_{avg\ in\ log} \le \mathrm{dB}(a_{avg}) \le \mathrm{dB}(a_{rms}) \ . \qquad \text{(A.2.3)}$$

Similarly, the decibel magnitude order is preserved for other values of r, a property that is extensively utilized by fluctuation-based processors.

A.3.0 THE CONVENTIONAL PROCESSOR - FILTER

The average power is referred to herein as the conventional processor or filter. Thus, when the sequence, a, is power, average power is

$$AVGPR = M_1. \qquad \text{(A.3.1)}$$

A.4.0 FLUCTUATION-BASED PROCESSORS/FILTERS EQUAL TO M_r

A.4.1 The WISPR Filter (Wagstaff's Integration Silencing PRocessor)

When the sequence, a, is power, then

$$WISPR = M_{-1}. \qquad \text{(A.4.1)}$$

It may be noted that *WISPR* is notationally equivalent to $AWSUM_1$ below. It is also known in the literature as the harmonic mean.

A.4.2 The $\mathrm{AWSUM_k}$ Filters (Advanced WISPR SUMmations), Usually for $k = 2$, 3, or 4

When the sequence, a, is power, then

$$AWSUM_k = M_{-k} \ . \qquad \text{(A.4.2)}$$

A.5.0 FLUCTUATION-BASED PROCESSORS/FILTERS, DERIVED FROM M_r

Several processors that are related to the M_r class may be obtained by simple combination of those previously described.

A.5.1 The A_{0k} Processors

Examples for A_{0k} processors, for $k = 1$ and 4, are

$$A_{01} = AVGPR/WISPR = M_1/M_{-1}, \qquad \text{(A.5.1)}$$

$$A_{04} = AVGPR\ /AWSUM_4 = M_1\ /M_{-4}, \qquad \text{(A.5.2)}$$

or more generally,

$$A_{0k} = AVGPR/AWSUM_4 = M_1/M_{-k}. \tag{A.5.3}$$

A.5.2 The A_{jk} Processors

The A_{lk} processors for $j = 1$ and $k > 1$ are defined as

$$A_{1k} = WISPR/AWSUM_k = M_{-l}\ /M_{-k}\ , \tag{A.5.4}$$

and for $j > l$ and $k > j$ are defined as

$$A_{jk} = AWSUM_j/AWSUM_k = M_{-j}/M_{-k}\ . \tag{A.5.5}$$

A.6.0 THE WISPR II_k PROCESSORS

When the data exist in the form of a decibel power spectrum series, an additional statistic that can be used to achieve gain is the modified temporal standard deviation, σ, of the sequence, a, for the ith spectral bin. Care must be taken during overlapped processing to use only the results of the independent time series, i.e., only the nonoverlapped segments should be used to estimate a_j, otherwise the values will be correlated and a value that is lower than the true standard deviation will be found. In particular, σ is for a in decibels

$$\sigma = \left[\frac{1}{n-1}\sum_{j=1}^{j=n}(a_j - a_{avg})^2\right]^{\frac{1}{2}}. \tag{A.6.1}$$

Using this definition for the standard deviation, WISPR II_k becomes

$$WISPR\ II_k \equiv WISPR\,/\,10^{\left(\frac{k\sigma}{10}\right)}. \tag{A.6.2}$$

A detailed rationale for this processor was developed in Sec. 5.0.

A.7.0 WISPR III_k PROCESSOR OF ORDER k

The WISPR III_k processor has been developed to exploit fluctuations present in the signal phase information. Typically, complex spectra are obtained from an FFT or DFT on temporal sample sets where each is offset a fixed time, Δt, which is a function of the sample rate, FFT size, and the percentage overlap. In general, for steady tonal sources, i.e., those tonals with a steady frequency-generating mechanism, the initial phase of the tonal will systematically advance or delay at the beginning of each temporal sample set, a signal processing artifact associated with discrete sampling. The complex spectral results obtained by FFTs or DFTs for those frequency bins nearest to a particular tonal will reflect that systematic phase shift of the tonal. Therefore, to avoid cancellation of out-of-phase segments of the same tonal during a complex (or coherent) summation,

any systematic phase shift must be removed from the complex spectral value nearest the tonal frequency. This is necessary regardless of the type of coherent summation that is used; the conventional summation or ones based on the WISPR philosophy. In WISPR III_k processing, great care is taken to ensure that the processing is coherent. Once the systematic phase shift has been removed, the residual variations in phase are then considered to be fluctuations.

When a steady tonal, ζ, is generated, with time, t, equal to zero at the beginning of the first data set, it may be represented (even though several mechanisms may subsequently generate fluctuations in amplitude and phase prior to reaching a hydrophone) as

$$\zeta = r_0 e^{\left[j(\Theta_0 + 2\pi f t)\right]}, \tag{A.7.1}$$

where

t is the time since the onset of sampling,

f is the tonal frequency in Hz,

r_0 is the tonal hypothetical steady magnitude, and

Θ_0 is the phase at the onset of sampling.

Alternatively with time, τ, equal to zero at the beginning of each temporal data set

$$\zeta = r_0 e^{\left[j\left(\Theta_0 + 2\pi f(n-1)\Delta t + 2\pi f\tau\right)\right]} = r_0 e^{\left[j\left(\Theta_n + 2\pi f\tau\right)\right]}, \tag{A.7.2}$$

where

τ is the time since the beginning the temporal data set,

Δt is the sample offset time (time between temporal data sets), and

Θ_n is the phase at the beginning the temporal data set.

Defining signal summation as the addition (in the time domain) of the sampled tonal, after a sufficient number of samples, the summation would result in zero due to out-of-phase summations, not a very useful result. Even if fluctuations in magnitude and phase have been generated prior to reaching the sensor that samples the tonal, on the average, the effect of out-of-phase cancellations is still present. Coherent summation avoids the effect of cancellation by shifting the phase of the sample segment to Θ_0, i.e., by subtracting $(2\pi f(n-1)\Delta t$ from Θ_n. Normally, the actual phases would all be reduced numerically modulo 2π.

Discrete numerical operations, equivalent to those just presented, are more conveniently accomplished in the frequency domain. A somewhat subtle, and sometimes overlooked point, is that the complex spectral values generated by an FFT or DFT of even noise-free data, in general, (1) do not have bin boundaries that correspond exactly to the tonal frequencies actually present; thus, the tonal frequencies are not known exactly and (2) do not reproduce the phase of the tonal itself at the beginning of the temporal sample set, but rather the phase of the frequency corresponding to the frequency at the upper bin boundary. Therefore, it is not possible to achieve coherent

processing by simply using the frequency of the nearest spectral bin boundary to calculate the offset.

If the BW is sufficiently narrow to isolate tonals, the systematic phase shift of the tonal is reflected closely (though not exactly) for the frequencies of the nearest spectral bins. Any algorithm used must be capable of extracting a reasonable estimate of the required phase shift, even in the face of these obstacles and in the presence of noise. Although the success of the WISPR III_k processor, at least in part, depends on removal of the phase shift discrete sampling artifact, the actual technique used to determine the correct shift has little bearing the development of the WISPR III_k processor and, thus, is omitted from this discussion.

The discussion just presented from the point of view of time series data from a hydrophone would also apply to output from a beamformer with only minor modifications in terminology. Let the set $\{v_n\}$ $(n = 1,2,3, ..., N)$ denote the shifted phase (to ensure coherent summation) complex spectra values from a single hydrophone or a single beam at a particular frequency. Let Φ_n denote the new phase values determined by a suitable phase-shifting algorithm, then the estimate of the signal corresponding to a particular bin frequency for that sample period is represented by

$$v_n = r_n e^{\left[j\left(\Theta_n + 2\pi ft\right)\right]}, \tag{A.7.3}$$

and has the Fourier transformed value

$$z_n = (r_n \cos\Phi_n + j r_n \sin\Phi_n) . \tag{A.7.4}$$

The set average value, s_{avg}, is

$$s_{avg} = \frac{1}{N} \sum_{n=1}^{n=N} \frac{z_n}{r_n^k} .$$

Using these results, the WISPR III_k processor is defined by

$$WISPR\ III_k = \left[\left(\frac{1}{N} \sum_{n=1}^{n=N} r_n^{-k} \right)^{-1} \sqrt{s_{avg}\, s_{avg}^*} \right]^2 . \tag{A.7.5}$$

A.8.0 WISPR CROSS-SPECTRAL DENSITY MATRIX BEAMFORMING, A_kCSDM OF ORDER *k*

Beamformers that are based upon the cross-spectral density matrix (CSDM) are referred to as CSDM beamformers. Input data required are the complex spectral values for each hydrophone from FFTs or DFTs at several sequential temporal realizations. Let the complex spectral value for a particular frequency bin for hydrophones l and m, at time index, i, be represented by

$$z_{l,i} = x_{l,i} + jy_{l,i} \text{ and } z_{m,i} = x_{m,i} + jy_{m,i} ,$$

then the CSDM quantity, $Z_{l,m,i}$ for hydrophones l and m, is

$$Z_{l,m,i} = z_{l,i} z^*_{m,i} = (x_{l,i} + jy_{l,i})(x_{m,i} - jy_{m,i}) \ .$$

The typical CSDM beamformer uses averages of these complex data according to some specific procedure prior to beam steering and summation to form the beam output; e.g., the simplest average is

$$Z_{l,m} = \frac{1}{T} \sum_{i=1}^{i=T} z_{l,m,i} \ .$$

The A_kCSDM beamformer utilizes a new average resulting from the WISPR philosophy, substituting this "average" for the conventional ones. Let the magnitude of $Z_{l,m,i}$ be $r_{l,m,i}$, i.e.,

$$r_{l,m,i} = +\sqrt{Z_{l,m,i} Z^*_{l,m,i}} \ .$$

The A_kCSDM beamformer, for order k (typically, 1, 2, 3, or 4), is accomplished by the simple replacement of the quantity, $Z_{l,m}$, with the new average $A_kCSDM_{l,m}$, prior to beam steering and summation to form the beam output. $A_kCSDM_{l,m}$ is defined as

$$A_kCSDM_{l,m} \equiv \left[\frac{1}{T} \sum_{i=1}^{i=T} r_{l,m,i}^{-k} \right]^{-1} \left[\frac{1}{T} \sum_{i=1}^{i=T} \frac{Z_{l,m,i}}{r_{l,m,i}^{k}} \right] . \qquad \text{(A.8.1)}$$

WCSDM beamforming is the special case for k =1, i.e., $A_1CSDM_{l,m}$, analogous to WISPR being equivalent to $AWSUM_1$.

A.9.0 TIME AND FREQUENCY DOMAIN WISPR MATCHED FILTERS

These applications simply use the standard WISPR Filter processors. The only difference is the type of data that are actually processed. A description of the type of data processed is provided in Secs. 7.2 and 7.3.

A.10.0 WISPR(WB^2)

The WB^2 processor[1] is a processor that utilizes an iterative technique to enhance the spatial and spectral resolution from the output of a conventional processor. It is possible to enhance this technique by utilizing the output of other processors, e.g., the fluctuation-based processors described herein. When combined in this manner, the resulting processors are referred to as

$$\text{WISPR}(WB^2) \ ,$$

or more generally for the AWSUM higher order processors as

$$\text{AWSUM}_k(\text{WB}^2) .$$

This application is discussed in Sec. 9.2.

A.11.0 DIET WISPR AND DIET AWSUM$_k$

The DIET AWSUM$_k$ processor of order k is a self-consistent, high-resolution, high-gain estimate of the spatial density. The special case where $k = 1$ is referred to as DIET WISPR^2. The generalized form of the unnormalized processor is defined as

$$DIET\,AWSUM_k(x_i) \equiv \left[\sum_{t=1}^{T} \sum_{j=1}^{J} \left\{ B_{j,t} / R_{j,t}(x_i) \right\}^{-k} \right]^{-\frac{1}{k}} , \qquad \text{(A.11.1)}$$

where

i is the spatial density index,

j is the beam number index,

t is the time index,

k is the processor order, $k > 0$,

x_i is the spatial density variable,

$B_{j,t}$ is the beamformer output powers for the jth beam for time sample t,

$R_{j,t}(x_i)$ is the beam power spatial response of the jth beam at the ith location

in spatial density space for time sample t,

J is the number of beams, and

T is the number of time samples.

To compare the output of this processor to other accepted standards, normalization is required. However, as this process (though a little tedious numerically) is straightforward, it is omitted from this discussion.

The form of the DIET WISPR processor presented here applies to spatial beamforming applications similar to those described in Sec. 9.3. Using a rationale parallel to that which has resulted in defining Eq. A.11.1, a similar equation can be developed for improved spectral resolution. This remains an area needing additional research to fully develop its capability.

Appendix B

LIST OF RELATED PUBLICATIONS

B.1.0 PATENTS

1. R. A. Wagstaff, "Signal Processing for Increasing Signal-to-Noise Ratio," Navy Case No. 72548, Jan 1993.

2. R. A. Wagstaff, "Advanced WISPR Summation (AWSUM) Processor," Navy Case No. 74838, application submitted to NPO, Sep 1994.

3. R. A. Wagstaff and J. George, "A New Fluctuation Based Digital Signal Processor Including Phase Variations," application submitted to NPO, Dec 1996.

4. R. A. Wagstaff, "A_kCSDM: A General Fluctuation Sensitive Cross Spectral Density Matrix for High Gain Beamforming and Signal Processing," Navy Case No. 78,266, submitted Naval Research Laboratory, Jan 1997.

B.2.0 JOURNAL ARTICLES

1. R. A. Wagstaff, "The WISPR Filter: A Method for Exploiting Fluctuations to Achieve Improved Sonar Signal Processor Performance," submitted to *J. Acous. Soc. Am.*, Sep 1995.

2. R. A. Wagstaff and S. D. Gardner, "Exploitation of Acoustic Fluctuations to Enhance Signal-to-Noise Ratio and Resolution of Amplitude Stable Signals," submitted to *J. Acous. Soc. Am.*, Oct 1995.

3. R. A. Wagstaff, "WISPR Processing: The Key to Accessing a New Source of Signal-to-Noise Gain," unpublished manuscript, Oct 1995.

4. J. George and R. A. Wagstaff, "Enhanced Target Detection in the Dabob Bay Active Acoustic Barrier Using the WISPR Filter," unpublished manuscript, Oct 1995.

5. J. George and R. A. Wagstaff, "WISPR Filter Performance Measured in the Presence of Signal Fluctuations and Ambient Noise," unpublished manuscript, Oct 1995.

6. R. A. Wagstaff, "AWSUM: A Digital Filter for Achieving Increased Signal-to-Noise Ratio and Other Signal Processor Enhancements," unpublished manuscript, Apr 1996.

7. R. A. Wagstaff and K. J. Dudley, "Trend Removal to Improve the Performance of the WISPR Processor for Detecting Submerged Sources," unpublished manuscript, Oct 1995.

8. R. A. Wagstaff and S. F. Kooney, "The AWSUM Filter: A 20-dB Gain Fluctuation Based Processor,"*IEEE J. Oceanic Eng.* **22**, 119–127 (1996).

9. R. A. Wagstaff, "WISPR II and Other Enhanced Fluctuation Based Processors," submitted to *J. Acous. Soc. Am.*, Mar (1997).

10. S. D. Gardner and R. A. Wagstaff, "DIET AWSUM: A Technique for Exploiting Fluctuations to Enhance Signal-to-Noise Ratio and Resolution," *IEEE J. Oceanic Eng.* **22**, 110–118 (1997). Jan 1997.

11. R. A. Wagstaff and J. George, "A New Fluctuation Based Processor Including Phase Variations," unpublished manuscript, Apr 1996.

12. J. George, "Performance Evaluations of a Fluctuation Sensitive Processor Using Synthetic and Measured Data," submitted to *J. Acous. Soc. Am.*, Mar 1996.

13. R. A. Wagstaff and J. A. Mobbs, "Pseudo-Operational Unalerted Detection Classification Test of the WISPR Filter," unpublished manuscript, Oct 1996.

14. R. A. Wagstaff and R. F. Fisher, "Mitigating the Adverse Effects of Transients in Acoustic Parameter Estimation," submitted to *J. Acous. Soc. Am.*, Apr 1997.

15. R. A. Wagstaff, "A_kCSDM: Fluctuation Sensitive Beamformers for the Enhancement of Low-Fluctuation-Amplitude Signals," submitted to *IEEE J. of Oceanic Eng.*, Jan 1997.

16. R. A. Wagstaff and W. E. Avera, "Nonacoustic Detection of Submerged Sources Using the WISPR and AWSUM Filters to Exploit Amplitude Fluctuations," unpublished manuscript, Nov 1996.

17. R. A. Wagstaff, "Increasing the Resolution and Gain of High-Resolution Signal Processors for Low Fluctuation Amplitude Signals by Increasing Their Sensitivity to Fluctuations," submitted to *IEEE J. of Oceanic Eng.*

18. J. George, "Physical Mechanisms to Explain the Observed Features of Ambient Noise in Shallow Water," *J. Acous. Soc. Am.* **99**, 3439–3444 (1996).

19. R. A. Wagstaff and J. A. Mobbs, "Exploiting the Sequential Order-Dependence of Amplitude Fluctuations to Enhance Acoustic Parameter Estimation," submitted to *J. Acous. Soc. Am.*, Jun 1997.

B.3.0 REPORTS

1. J. George and R. A. Wagstaff, "Enhanced Shallow Water Barrier Detection Using WISPR and its Application to Dabob Bay," unpublished manuscript, 1993.

2. J. George and R. A. Wagstaff, "Variations of WISPR Levels and Average Power Levels with Standard Deviation," NRL/MR/7176--93-7077, Naval Research Laboratory, Stennis Space Center, MS, 1994.

3. J. George and R. A. Wagstaff, "Target Detection in the Fixed-Fixed III Experiment Using the WISPR Algorithm," unpublished manuscript, 1994.

4. J. George and R. A. Wagstaff, "WISPR Performance Measured by ROC Curves," NRL/MR/7176--94-7559, Naval Research Laboratory, Stennis Space Center, MS, 1994.

5. R. A. Wagstaff, "WISPR Processing of the Full Spectrum Program ROW Tape #1," unpublished manuscript, 1995.

6. R. A. Wagstaff, R. W. Fidler, and A. Kirk, "WISPR Analysis of NAVIR Sonobuoy Data," unpublished manuscript, 1995.

7. K. J. Dudley and R. A. Wagstaff, "Trend Removal to Improve the Performance of a Fluctuation Sensitive Signal Processor," NRL/MR/7176--95-7583, Naval Research Laboratory, Stennis Space Center, MS, 1995.

8. R. A. Wagstaff, "WISPR Processing: The Key to Accessing a New Source of Signal-to-Noise Gain," unpublished manuscript, Nov 1994.

9. C. A. Fisher, "A Bibliography, with Abstracts and Annotations, of Publications On and Related to Underwater Acoustic Fluctuations," NRL/MR/7176--94-7563, Naval Research Laboratory, Stennis Space Center, MS, 1995.

10. J. George, "Cumulative Distribution Functions in Shallow Water: Two Features of Signal and Noise," NRL/MR/7176--94-7563, Naval Research Laboratory, Stennis Space Center, MS, 1995.

11. R. A. Wagstaff, "Submerged Source Gram," unpublished manuscript, 1995.

12. J. George, "Simulations for Performance of a Family of Fluctuation-Sensitive Processors," NRL/MR/7176--96-7724, Naval Research Laboratory, Stennis Space Center, MS, 1996.

13. J. George and R. A. Wagstaff, "The Effects of Variable Time Window Width and Signal Position within FFT Bin on WISPR Performance," NRL/MR/7176--96-7717, Naval Research Laboratory, Stennis Space Center, MS, 1996.

14. R. A. Wagstaff and J. A. Mobbs, "WISPR Filter Detection Results for the Advanced Processor Sea Test," unpublished manuscript, Oct 1996.

15. J. George, "Choice of Computer-Generated Random Numbers Whose Statistics Match Those of Experimentally Measured Ambient Noise," NRL/MR/7176--96-0022, Naval Research Laboratory, Stennis Space Center, MS, Dec 1996.

16. S. F. Kooney, "Assessment of the Minimum Detectable Level Enhancement of the WISPR and $AWSUM_k$ Filters Using the SESAME 1 Data," Naval Research Laboratory, Stennis Space Center, MS, in prep.

17. R. A. Wagstaff and J. George, "The AWSUM III_{434} Processor," NRL/MR/7176--97-0029, Naval Research Laboratory, Stennis Space Center, MS, Mar 1997.

B.4.0 PROCEEDINGS

1. R. A. Wagstaff, "Exploitation of Fluctuations to Enhance Target Detection and to Reduce Clutter and Background Noise in the Marine Environment," Proceedings of Aerospace/Defense Sensing and Controls '96 Symposium, Targets and Background: Characterizations and Representation II Conference, Apr 1996.

2. R. A. Wagstaff and J. George, "Phase Variations in Fluctuation-Based Processor," Proceedings of Aerospace/Defense Sensing and Controls '96 Symposium, Targets and Background: Characterizations and Representation II Conference, Apr 1996.

3. G. C. Carter and R. A. Wagstaff, "Innovative Signal Processing Algorithms," Proceedings of the Workshop on Passive Sonar: Fundamental Limits and Future Opportunities for Achieving Undersea Warfare Superiority, 20–22 Mar 1996, Naval Undersea Warfare Center, Vol. 2, pp. 29-1–29-28.

4. S. F. Kooney and A. E. Leybourne, "An Orderly Approach to Setting Detection Thresholds for the $AWSUM_k$ Family Processors," Eleventh International Conference on Mathematical and Computer Modeling and Scientific Computing, Apr 1997.

5. J. George, "Shallow Water Passive Acoustic Detection Using Normal Modal Components in Fluctuation-Based Processing," SPIE Conference, Orlando, FL, Vol. 3069, Jul 1997.

B.5.0 CONFERENCE ORAL PRESENTATIONS

1. J. George and R. A. Wagstaff, "Application of Wavelet Transform to Fluctuation Based Processing," ASA Conf., Nov 1995.

2. R. A. Wagstaff, "Fluctuation Based Processing," Technical Workshop on Undersea Warfare Superiority, *Passive Sonar: Fundamental Limits and Future Opportunities*, Mar 1996.

3. J. George, "Simulations for Performance Evaluations of a Family of Fluctuation Based Processors," ASA Conf., May 1996.

4. R. A. Wagstaff, "Fluctuation Based Processing to Enhance the Detection of Low-Fluctuation Amplitude Signals in a Background of High Clutter and Noise," ASA Conf., Dec 1996.

5. S. D. Gardner and R. A. Wagstaff, "The DIET WISPR and DIET AWSUM High-Resolution and High-Gain Deconvolution Techniques," ASA Conf., Dec 1996.

6. R. A. Wagstaff and J. A. Mobbs, "Technique for Exploiting the Temporal Order in Acoustic Fluctuations to Enhance Signal Processor Performance," Jun ASA Conf., 1997.

7. R. A. Wagstaff and J. A. Mobbs, "Environmentally Sensitive Adaptive Fluctuation Based Processing," Jun ASA Conf., 1997.

8. R. A. Wagstaff and S. F. Kooney, "A Simple Technique for Converting a Conventional Processor to a Fluctuation Based Processor and Enhancing Performance," Jun ASA Conf., 1997.

9. R. A. Wagstaff, "Fluctuation Based Beamformer for the Enhancement of Low Fluctuation Amplitude Signals," Jun ASA Conf., 1997.

10. S. F. Kooney, "SESAME 1 Assessment of Enhancement in Minimum Detectable Level Using Fluctuation Sensitive Processors," Jun ASA Conf., 1997.

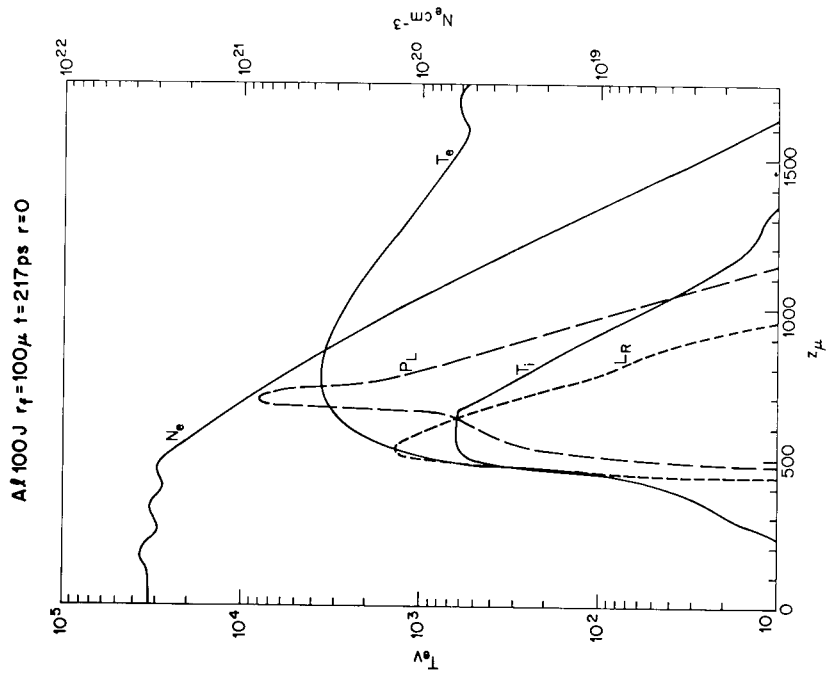

Fig. 7 — Same data as Fig. 6 for a 100 J laser pulse at t = 217 ps

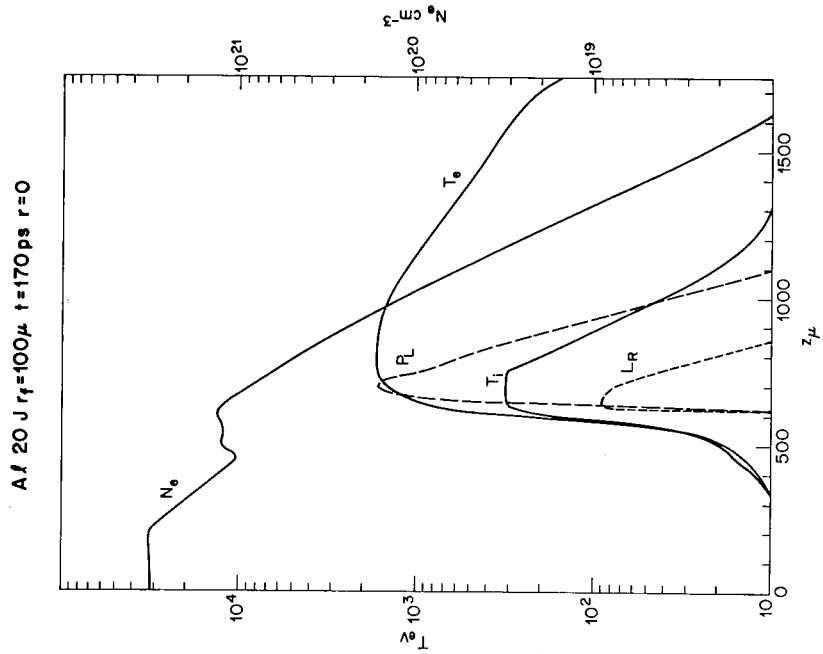

Fig. 6 — Electron density, electron and ion temperature, absorbed laser power and line radiation power as a function of distance on the axis for a 20 J, 100 μ, 250 ps laser pulse at t = 170 ps (70 ps after the peak of the laser pulse)

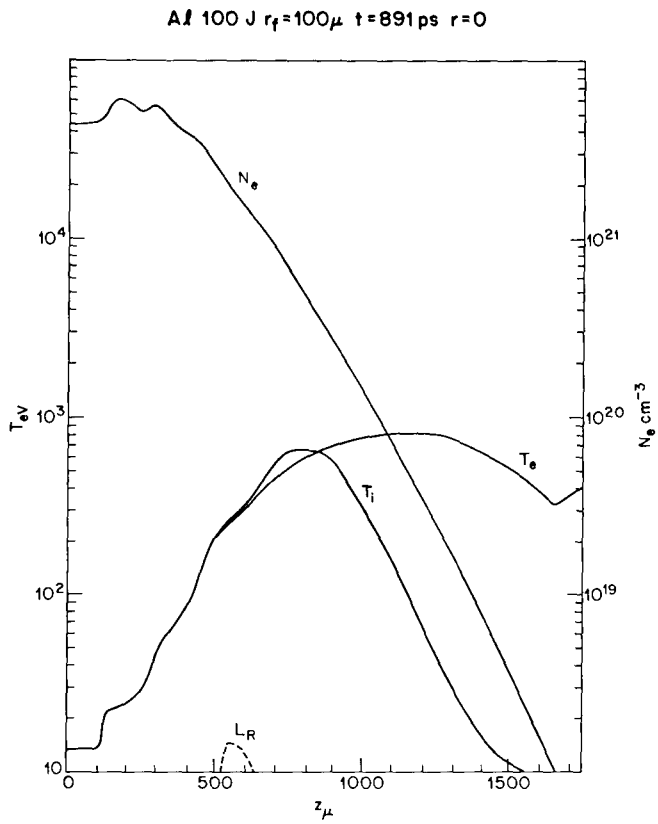

Fig. 8 — Same as Fig. 7, at t = 891 ps. The absorbed laser power is negligible at that time.

region due to the high electron thermal conductivity, and of course, in this region T_i greatly lags T_e. Maximum temperatures range from $T_e \sim 1.7$ keV to 5 keV.

The line emission has a maximum that occurs where $T_e \cong 1$ keV so that it is displaced into the overdense region beyond the maximum in P_L which occurs at the critical depth. This displacement increases with laser energy. Energy is deposited in the overdense region by direct deposition from the evanescent wave, thermal conduction, and radiation transport, and then radiates more efficiently from this region. The evanescent wave appears to penetrate more deeply as T_e increases (see the 200 J case).

The increase in electron density $N_e = ZN$ above the initial density (this is most pronounced in the late time case Fig. 8) is principally due to an increase in Z and is not ion density compression.

Fluid velocities are small in the examples shown. This is a consequence of the slow fall-off in density of the initial target as can be verified by estimating the fluid velocity from $V \sim \tau_L v_s^2/\ell$ where v_s is the sound speed and ℓ the initial gradient scale. A steeper initial gradient gives rise to higher fluid velocities. Radiation pressure was also observed to have a large effect on the fluid velocity while the pulse was on.

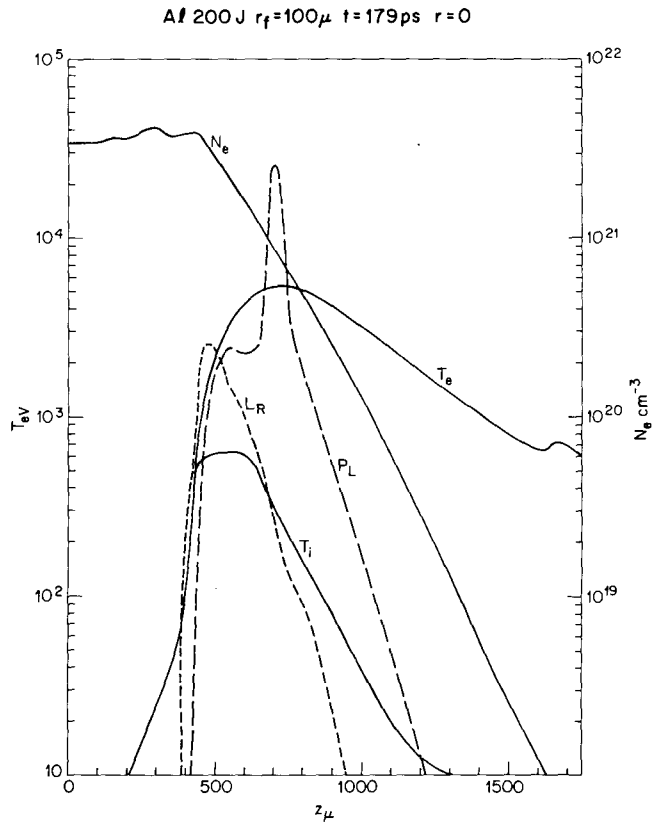

Fig. 9 — Same data and time as Fig. 6, but for 200 J laser pulse

An off-axis plot of the same parameters is shown in Fig. 10 and shows similar features. The radial dependence of T_e, P_L, and L_R is shown more clearly in Figs. 11, 12, and 13. In Figs. 11 and 12 it is interesting to note that $T_e(r)$ has a maximum for fixed z that occurs *off axis*. This can be understood as due to the magnetic field which is zero at $r = 0$ but has a maximum off axis. The reduced thermal conductivity in the high B region leads to a slower transport of deposited laser energy out of that region. This is supported by Fig. 13 in which the maximum in T_e returns to $r = 0$ if B fields are suppressed in the code. In Fig. 11 we also note that the emission L_R has a maximum displaced off axis.

Figure 14 is an illustration of a diagnostic which has been developed in order to compare experimental results with our code results. These pinhole photographs can be obtained for both main line radiation and total radiation. They are time-resolved and because of their sensitivity to both density and temperature profiles, they provide one of the most accurate comparisons between numerical and experimental results.

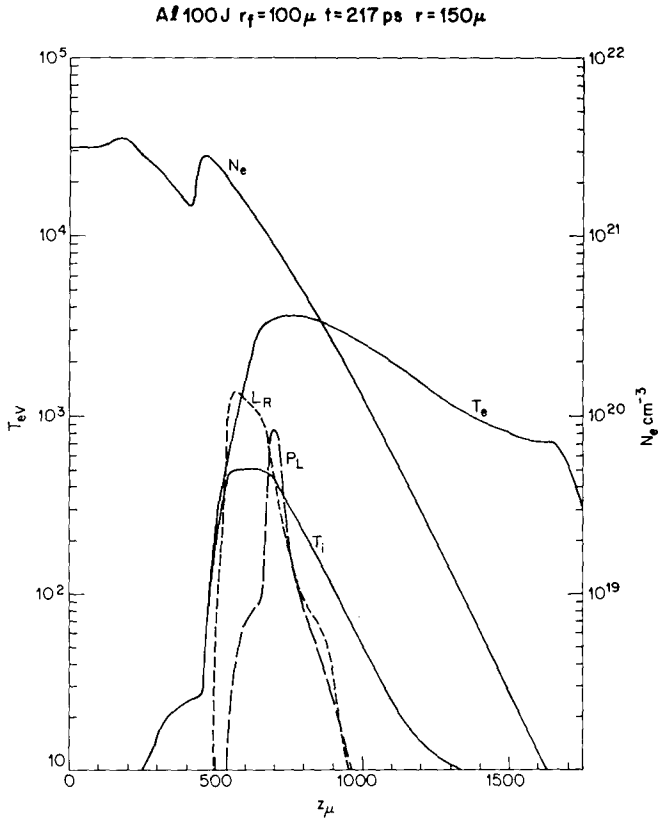

Fig. 10 — Same case as Fig. 7 viewed off-axis at r = 150 μ

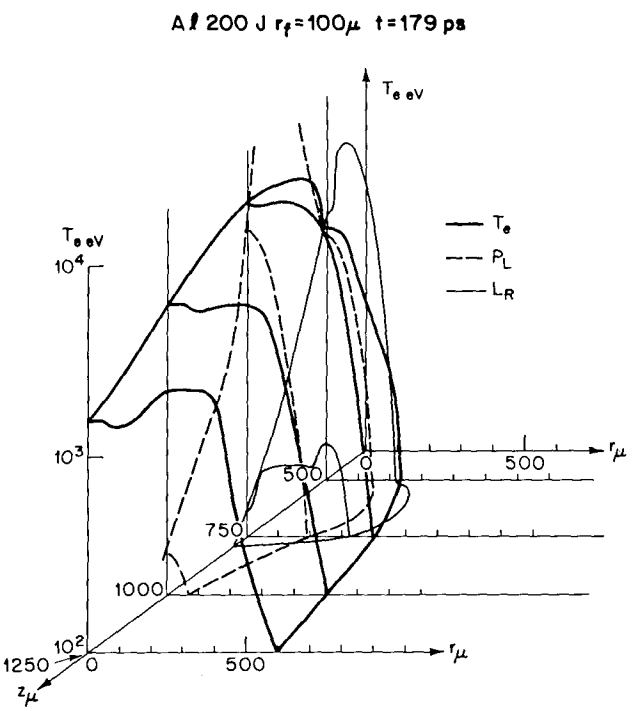

Fig. 11 — Electron temperature, absorbed laser power and line radiation power as a function of both distance along the axis and radius for case shown in Fig. 9

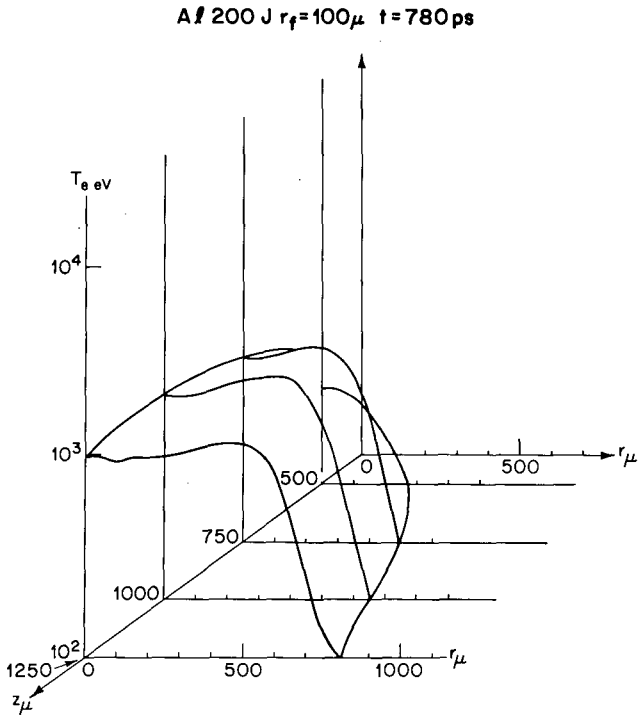

Fig. 12 — Electron temperature for the case of Fig. 9 at t = 780 ps

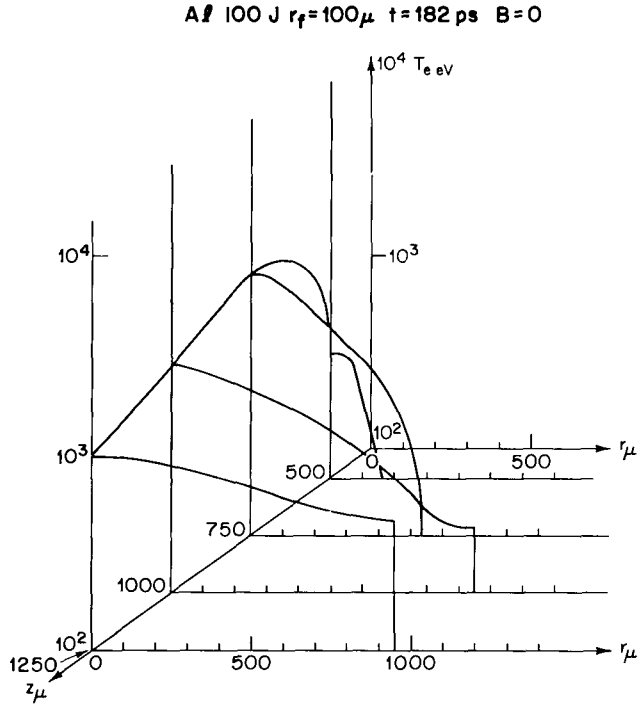

Fig. 13 — Electron temperature as a function of r and z for 100 J incident energy without any self-generated B field at t = 182 ps. Without any B field the temperature is more uniform in the radial direction.

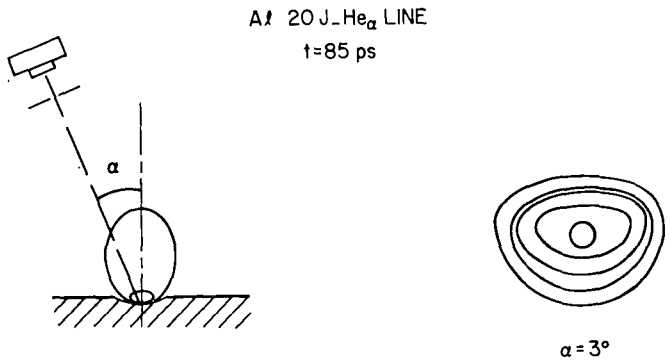

Fig. 14 — Time-resolved pinhole photograph for the He_α line at t = 85 ps. The lines shown in the photograph are contours of equal intensities.

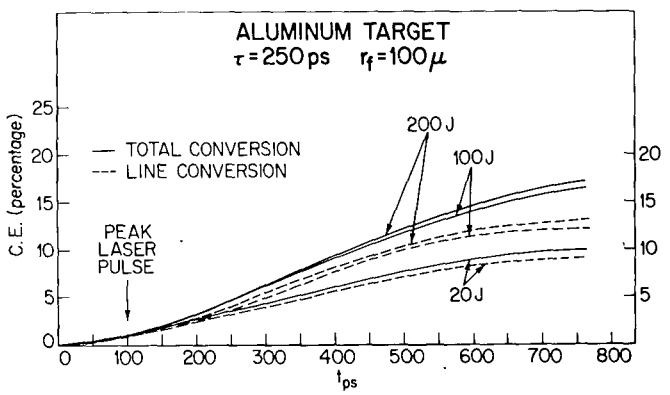

Fig. 15 — Conversion efficiencies of incident laser energy into x-ray energy as a function of laser energy and time. This is also a plot of conversion efficiencies as a function of laser intensities for a fixed focal spot radius (100 μ).

The x-ray conversion efficiency into escaping photons is plotted as a function of time and laser energy in Fig. 15. The maximum emission is delayed by about 275 ps from the maximum in the laser pulse. This delay is also a consequence of the fact that the maximum emission occurs from plasma for which $T_e \cong 1$ keV. The focal spot first overshoots this optimum temperature and only later spreads the energy sufficiently that a large emitting region of 1 keV plasma is present. The total x-ray conversion efficiency is observed to increase with laser energy and can reach values of about 20% for E_J = 200 J.

Figures 16-19 represent a series of computer runs aimed at understanding how to scale our results for the conversion efficiency to large pulses. The total energy incident in the laser pulse can be written as $W_L \cong \pi r_f^2 I_o \tau_L$ where I_o is the axial intensity, r_f the focal spot radius, and τ_L the laser pulse duration. In the limit that $W_L \to \infty$ and $r_f \to \infty$ with I_o and τ_L remaining constant, we expect the dynamics of the plasma to become one-dimensional. In this limit the conversion efficiency satisfies

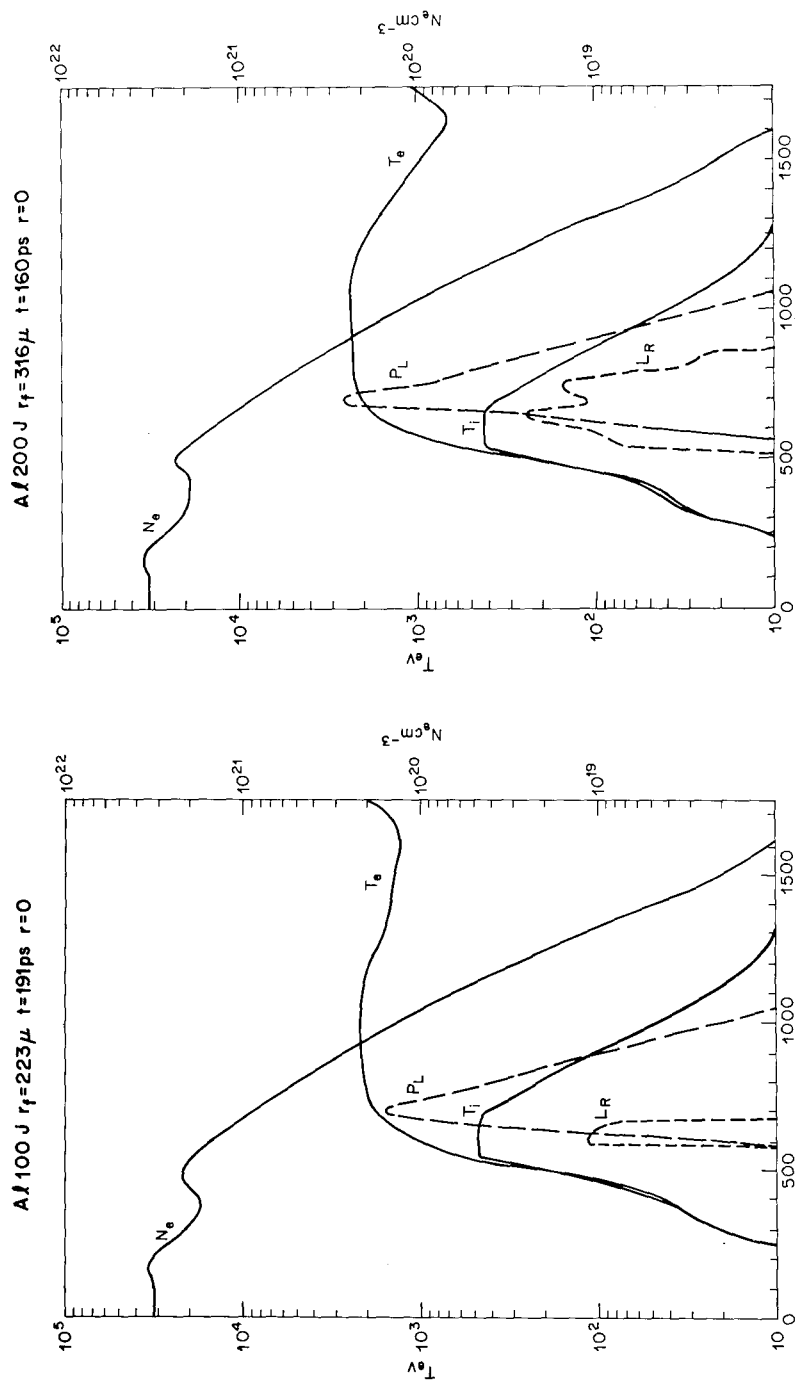

Fig. 16 — Typical quantities as a function of z for the same intensity of laser pulse as in Fig. 6, but the focal spot area has been increased by a factor of 5

Fig. 17 — Same data as Fig. 16, for focal spot area multiplied by 10

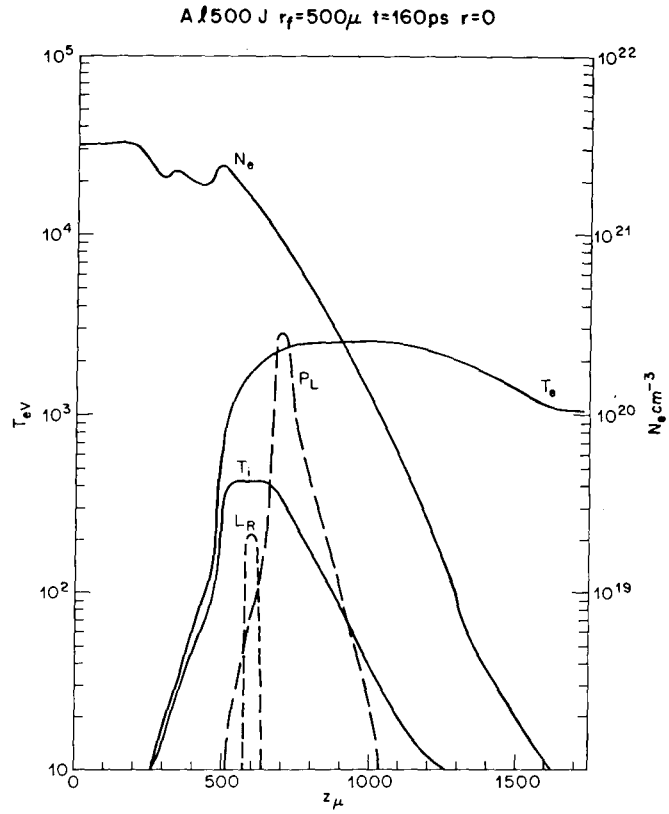

Fig. 18 — Same data as Fig. 16, for focal spot area multiplied by 25

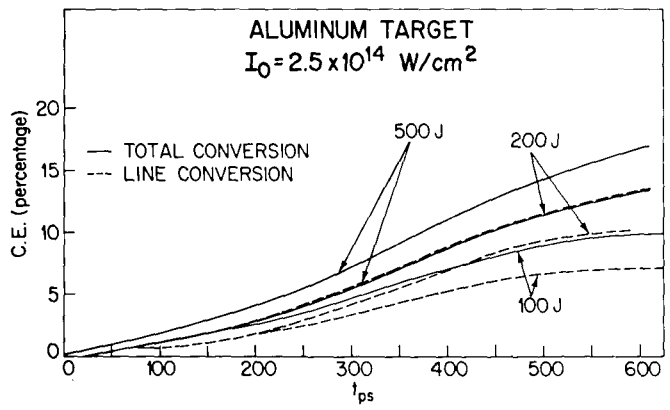

Fig. 19 — Conversion efficiencies of incident laser energy into x-ray energy for cases shown in Figs. 16-18. For the same intensity, this figure shows the variation of conversion efficiencies with focal spot size (two-dimensional effects).

$$CE^{\text{Total}}\Big|_{r_f\to\infty} = \frac{\pi r_f^2 \int I_\nu \, d\nu dt}{(\pi r_f^2 I_o \, \tau_L)} = \frac{\int_{\nu_M}^{\infty} d\nu \int_o^{\infty} dt \, I_\nu}{I_o \, \tau_L} ,$$

i.e., it becomes a function of I_o and τ_L only. If we are given this function then the conversion efficiency for very large pulses can be simply predicted as the value of CE corresponding to $I_o \tau_L = W_L/\pi r_f^2$ for the pulse in question. For a given I_o and τ_L there will of course be a minimum energy W_L^{Min} above which the system is essentially $1D$ and the above scaling applies. For $W_L < W_L^{\text{Min}}$ the dynamics is two dimensional and the scaling does not apply.

In Figs. 16, 17, and 18 we have plotted 3 profiles of several target plasma parameters for the pulses in which W_L = 100 J, r_f = 223 μ; W_L = 200 J, r_f = 316 μ; and W_L = 500 J, r_f = 500 μ, i.e., these three pulses have a constant axial intensity ($I_o = 2.5 \times 10^{14}$ W/cm^2) and pulse width τ_L = 250 ps. As expected the maximum electron temperatures reached in these 3 cases are approximately the same (they range from 2.15 keV to 2.5 keV). Further, the conversion efficiencies are shown in Fig. 19.

REFERENCES

1. S.E. Braginskii, in *Reviews of Plasma Physics*, edited by M.A. Leontovich (Consultants Bureau, New York, 1965), p. 205.
2. J.A. Stamper, K. Papadopoulos, S.O. Dean, E.A. McLean, and J.M. Dawson, Phys. Rev. Lett. **26**, 1012 (1972).
3. N.K. Winsor and D.A. Tidman, Phys. Rev. Lett. **31**, 1044 (1973).
4. J.B. Chase, J.L. LeBlanc, and J.R. Wilson, Phys. Fluids **16**, 1142 (1973).
5. K. Whitney and J. Davis, J. Applied Phys., to be published, Dec. 1974.
6. D. Colombant and N.K. Winsor to be published.
7. P.S. Julienne and J. Davis, *Radiation Escape from an Optically Thick Plasma*, Naval Research Laboratory Memo Report 2556 (1973).
8. J.D. Lindl and P.K. Kaw, Phys. Fluids **14**, 371 (1971).
9. J.W. Shearer and J.L. Eddleman, Phys. Fluids **16**, 1753 (1973).
10. J.A. Stamper and D.A. Tidman, Phys. Fluids **16**, 2024 (1973).
11. See, e.g., Bull. Amer. Phys. Soc. **18**, 684 (1973), abstracts HN5-HN14. See also J.A. Stamper, O.C. Barr, J. Davis, G.A. Doschek, C.M. Dozier, U. Feldman, B.M. Klein, W.M. Manheimer, E.A. McLean, J.M. McMahon, D.J. Nagel, D.A. Tidman, R.R. Whitlock, K. Whitney, N. Winsor, and F.C. Young, *Laser-Matter Interaction Studies at NRL*, to appear in Proceedings of the Third Workshop on "Laser Interactions and Related Plasma Phenomena," Rensselaer Polytechnic Institute (1973).

12. P.J. Mallozzi, H.M. Epstein, R.G. Jung, D.C. Applebaum, B.P. Fairand, and W.L. Gallagher, in "Fundamental and Applied Laser Physics: Proceedings of the Esfahan Symposium," ed. by M.S. Feld, A. Javan, and N.A. Kurnit (Wiley, New York, 1973).

13. P.J. Mallozzi, H.M. Epstein, R.G. Jung, D.C. Applebaum, B.P. Fairand, W.J. Gallagher, R.L. Uecker, and M.C. Muckerheide, J. Appl. Phys. 45, 1891 (1974).

14. D. Colombant and G.F. Tonon, J. Appl. Phys. 44, 3524 (1973).

15. See the Semi-Annual Report of the Laser Fusion Program, Lawrence Livermore Lab., Jan.-June 1973 p. 177 (UCRL-50021-73-1).

16. H.D. Shay, D. Bailey, S. Bodner, J. Katz, W. Kruer, J. Nuckolls, W. Slivinsky, E. Valeo, and G. Zimmerman, *Suprathermal Electron Distributions in Laser-Produced Plasmas*, paper at the 7th European Conference on Plasma Production by High Power Lasers, Garching, April 22, 1974.

17. J.P. Freidberg, R.W. Mitchell, R.L. Morse, and L.I. Rudsinski, Phys. Rev. Lett. 28, 795 (1972).

18. M.M. Wilson, Bull. Am. Phys. Soc. II 18, 1317 (1973).

19. A.A. Amsden and C.W. Hirt, LASL Report LA-5100 (Los Alamos, 1972), unpublished.

20. J.P. Boris and D.L. Book, J. Comput. Phys. 11, 38 (1973).

21. T.W. Johnston and J. Dawson, Phys. Fluids 16, 722 (1973).

22. D.J. Nagel, P.G. Burkhalter, C.M. Dozier, J.F. Holzrichter, B.M. Klein, J.M. McMahon, J.A. Stamper, and R.R. Whitlock, Phys. Rev. Lett., 33, 743 (1974).

23. M.J. Seaton in "Atomic and Molecular Processes," (D.R. Bates), Academic Press, New York and London, 1962.

24. M.J. Seaton, M.N.R.A.S. 119, 81 (1959).

25. J. Davis, J.Q.S.R.T. 14, 549 (1974).

26. E. Daltabuit and D.P. Cox, Astrophys. J. 177, 885 (1972).

IX. MODEL STUDIES

In addition to the 2-D MHD reactive flow code already discussed in Chapter VIII in detail, two additional models are in the development phase and are near completion. They will be able to treat spherical and cylindrical targets with an expanded atomic physics model coupled with a 1-D fluid, radial expansion model. An additional feature is the inclusion of a radiative transport scheme capable of exhibiting such characteristics as line inversion as well as frequency diffusion in an integrated fashion. An earlier version of one of these models is referred to as the hot-spot model and will now be described.

A. INTRODUCTION

When laser energy is deposited quickly ($\ll 1$ ns) in a cold plasma, a substantial conversion of this energy to K-line x-rays is possible in low-Z target plasmas [1]. Thus, while the absorption of laser radiation rapidly heats the electron gas and, in turn, the plasma, radiative losses can produce a comparable cooling of the plasma. The cooling rate by K-line emission depends on the degree of plasma heating and on the plasma Z.

In general, to treat the evolution of laser-heated plasmas, one must employ a fluid dynamic description that is based on equations of motion for the following fluid quantities [2-4]: $\{N_\mu\}$, the ion population densities; $\vec{B}$, the spontaneously generated magnetic field [5]; $\vec{v}$, the fluid velocity; T_e, the electron temperature; and T_i, the ion temperature. In this paper, however, a simpler model will be developed that describes specifically K-line emission from a small-volume element of *stationary* laser-heated plasma. The dynamic variables of this theory are $\{N_\mu\}$, T_e, and T_i; $\vec{v}$ and $\vec{B}$ are assumed to remain zero. The model is designed to provide first-order comparisons of the capability of different Z plasmas to convert laser energy to K-radiation. Its validity rests on the assumption that, when a cold plasma absorbs laser radiation in less than a quarter nanosecond at intensity levels between 10^{11} and 10^{16} W/cm^2, only a weak, at first neglectable, magnetohydrodynamic plasma motion will be generated over 1 to 2 ns time intervals. The justification for this assumption is that the buildup time for the B-field and fluid-motion energies is roughly a nanosecond, as estimated from the same temperature gradient used to compute conduction losses [1]. On the other hand, the plasma in our model is cooled by heat conduction and K-line emission in less than a nanosecond.

After the model is proposed in Sections B and C, a comparison of its predictions with experiment will be made in Section D. The remainder of the paper will then be devoted to a discussion of the problem of maximizing laser-energy conversion to K-line x-rays in carbon, fluorine, and aluminum plasmas. These plasmas produce K-radiation in different frequency intervals, and the ability to maximize x-ray output in a given frequency interval may be important if, for example, laser-heated plasmas are to find use as x-ray sources for the pumping of vacuum UV lasers.

B. THE MODEL

In developing our model, we envision the physical situation sketched in Fig. 1. We imagine that a sphere of uniform and stationary plasma is located in the focus of a laser beam, where it absorbs a prescribed amount of laser radiation. The sphere radius r is chosen equal to the radius of the focal spot. Since light absorption is resonant when the laser frequency ω_L equals the plasma frequency, the ion density N_i within the sphere is determined by the condition that $N_i = N_e^c/Z$, where Z is the nuclear charge of the ions and N_e^c is the critical electron number density: $4\pi e^2 N_e^c/m = \omega_L^2$. This choice of N_i ensures that the sphere remains strongly absorbing, yet translucent to the light throughout the course of the plasma heating.

Heating of the plasma will be studied by deposition of a small quantity of laser energy E_o into the volume ΔV of the sphere in a given time interval Δt. The deposition rate S_e will be taken to be Gaussian:

$$S_e = \frac{E_o}{\Delta V}\frac{1}{\sqrt{\pi}\Delta t} e^{-\left(\frac{t-t_o}{\Delta t}\right)^2} \tag{1}$$

for mathematical convenience. The exact shape of the heating pulse will depend on the shape of the laser pulse and on changes of the plasma absorption coefficient during the course of the plasma heating. The absorption length λ_{abs} for absorption by inverse bremsstrahlung is [6],

$$\lambda_{abs} = \frac{8.3 \times 10^9 \; T_e^{3/2} \left(1 - \frac{N_e}{N_e^c}\right)^{1/2}}{(N_e^2/N_i)\; \ell n\Lambda (N_e/N_e^c)}$$

where $\ell n\Lambda$ is the Coulomb logarithm. For a singly ionized Al plasma, for example, at a temperature of 3×10^4 °K ($\sim$ 3eV) and an electron density of roughly 7×10^{19} cm^{-3} ($N_e^c = 10^{21}$ electrons/cm^{-3} is the critical density for 1.06 μ neodymium laser radiation), λ_{abs} is on the order of 100 μ. When the electron temperature increases to 10^7 °K and the electron density and Coulomb logarithm increase correspondingly an order of magnitude, λ_{abs} largely maintains its value. The only large changes in λ_{abs} occur because of time lags in the changes of N_e that are brought about by changes in T_e. However, as T_e increases, collisional ionization rates of low-lying ionization stages approach values of 10^{12} sec^{-1}, so that lag times are only on the order of picoseconds. Thus, the heating and laser pulses should not differ significantly. Moreover, the laser radiation will penetrate spheres smaller than 100 μ in diameter. In this model, however, we will be concerned only with the energy actually deposited within the sphere in a given Δt in order to compute efficiencies with which it is converted to x-rays.

E_o, Δt, and r are free parameters whose values are chosen in accordance with the physics of the model. For example, since we are assuming that the plasma densities and temperatures are uniform within ΔV, r should be chosen as small as possible. A good lens can focus the laser beam to a 46-μ spot; accordingly, we have taken $r = 23$ μ ($\Delta V = 5 \times 10^{-8}$ cm^3). Then, since an ideal electron gas with a density of 10^{21} electrons cm^3 and

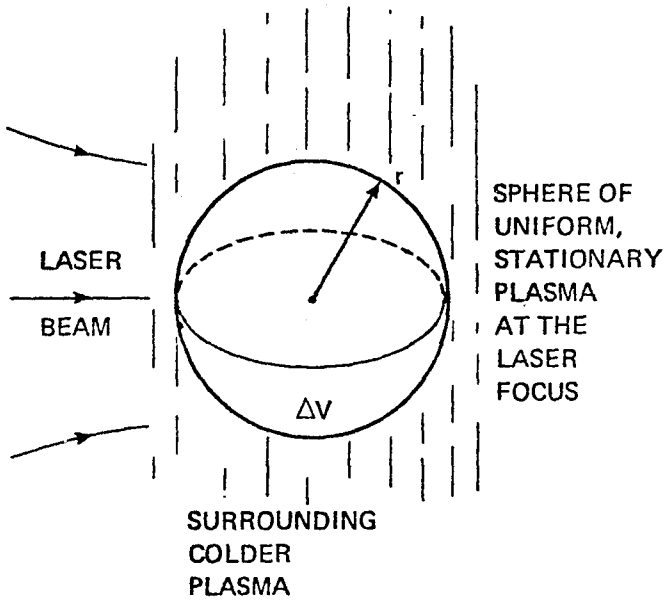

Fig. 1 — Hot-spot model geometry

a temperature of 1 keV has an energy density of 2×10^5 J/cm^3, the net absorption of only 10^{-2} Joules is sufficient to heat the plasma in a sphere of 5×10^{-8} cm^3 to keV temperatures. Moreover, since this energy is conducted outside the sphere to a larger volume of plasma, the surrounding plasma will not be heated as strongly as the sphere, where direct energy deposition is assumed. Thus, in the theory to follow, E_o will have values ranging around 10^{-2} J and will be restricted to values less than 1 or 2 J. Finally, in order to protect our assumption that there be negligible MHD motion generated in the course of the plasma heating and cooling, the laser energy will be deposited quickly, generally $\Delta t \leqslant 1/10$ ns, and the plasma internal dynamics will be studied only over 1 or 2 ns periods. (Δt = 1/4 ns will be used to compare theory to experiment in one case.)

If light is absorbed in ΔV predominantly through the process of inverse bremsstrahlung, one can assume that the laser energy is deposited directly as thermal energy into the electron gas. The electrons then share their energy with the ions through collisions that heat, excite, and ionize the ions. When the electron gas is heated to temperatures between 100 and 1000 eV, low Z ions ($Z \leqslant 13$) can be stripped to their two K-shell electrons. The excitation and subsequent radiative decay of these hydrogen-like and helium-like ionization stages will be modeled in some detail in this paper to allow computation of the K-line emission spectrum that has been observed in laser heated carbon, fluorine, and aluminum plasmas. Examples of experimental C [7], F [8], and Al [9] K-line spectra are shown in Figs. 2 through 4. The prominent lines they contain are emitted by $np-1s$ ($n \geqslant 2$) transitions in H- and He-like ions.

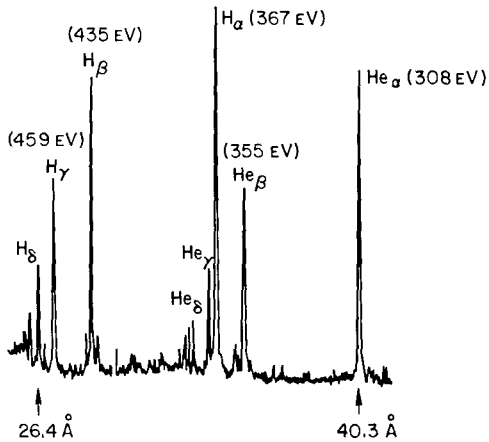

Fig. 2 — Experimental carbon K-line spectrum (C in CH_2)

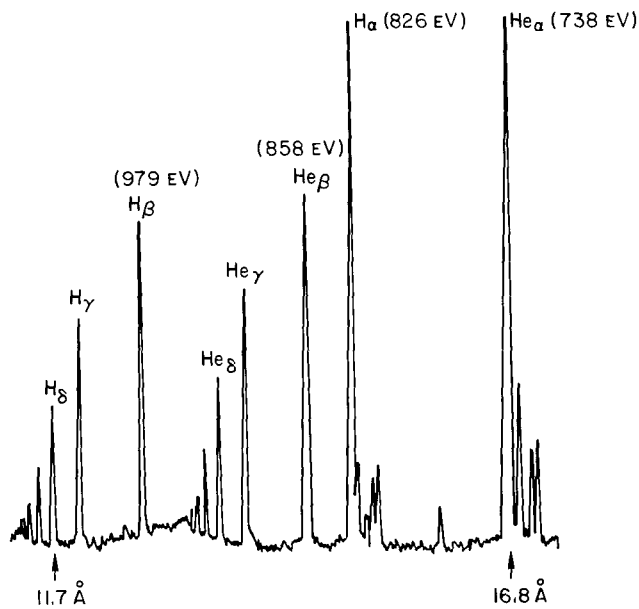

Fig. 3 — Experimental fluorine K-line spectrum (F in LiF)

Guided by the spectra in Figs. 2-4, we have set up a description of laser-heated plasma x-ray generation based on the energy level diagram of Fig. 5. The topmost state is the state of total ionization, which is alternatively CVII, FX, or Al XIV. Only four H-like and four He-like p-states are used; no other excited states are presently included in our model. The p-states emit most of the radiation recorded in Figs. 2-4. They are excited from the ground state above them by collisional and radiative recombination and from the ground state below by collisional excitation. Thus, line emission is generated in both the ionizing (or heating) and deionizing (or cooling) stages of the plasma's time evolution. Neighboring ground states are connected to each other by collisional ionization and radiative and collisional recombination processes.

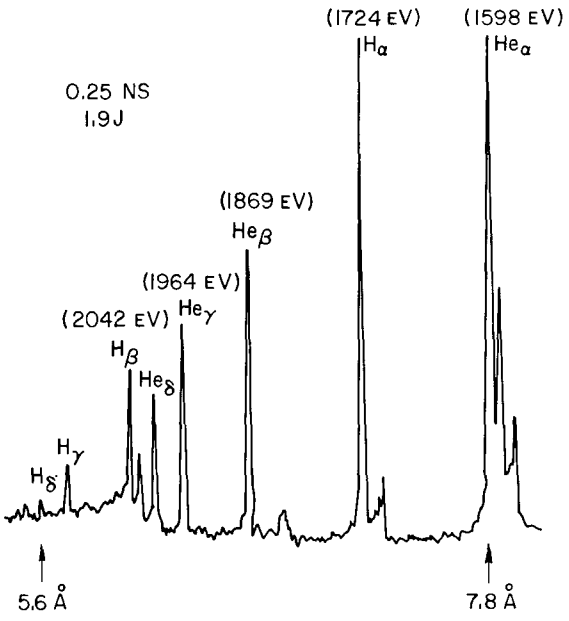

Fig. 4 — Experimental aluminum K-line spectrum

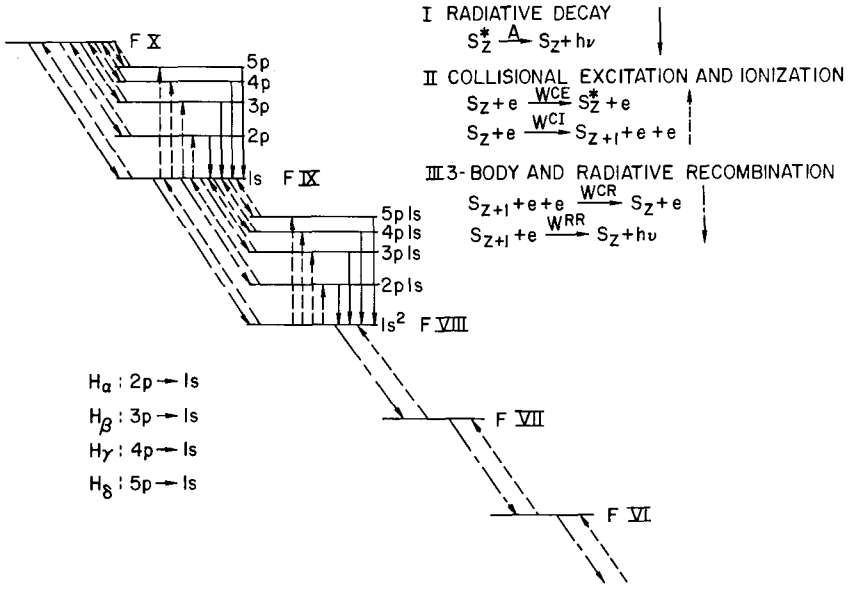

Fig. 5 — Fluorine energy level diagram showing the transitions used in the rate equation theory

C. EQUATIONS OF MOTION AND RATE COEFFICIENTS

The equations of motion of our model describe a small-volume energy flow that is representable diagrammatically, as shown in Fig. 6. Generation of internal ion energy and x-radiation is described by a set of rate equations for the ion population densities. They are based on the energy diagram of Fig. 5 and have the form:

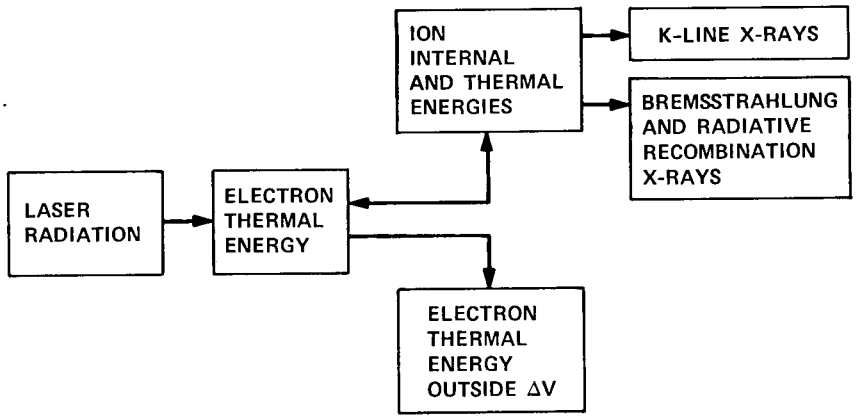

Fig. 6 — Energy flow diagram of the hot-spot model

$$\partial_t N_\mu = \sum_\nu W_{\mu\nu} N_\nu (\mu = 1, \text{---}, s) \tag{2}$$

where s is the number of energy levels in Fig. 5. The rates $W_{\mu\nu}$ for $\mu \neq \nu$ correspond to transitions from the νth to the μth energy level, and

$$W_{\mu\mu} = -\sum_\nu W_{\nu\mu}.$$

$$N_i = \sum_\mu N_\mu$$

is a constant of the motion. The rates depend on the energy density of the electron gas through the electron temperature and on the electron density,

$$N_e = \sum_\mu Z_\mu N_\mu \tag{3}$$

where $\{Z_\mu\}$ are the ionic charges.

On multiplying the equation for N_μ by E_μ, the energy of the μth ionic level, and summing over μ, one obtains an equation of motion for the plasma internal energy,

$$E_i = \sum_\mu E_\mu N_\mu:$$

$$\partial_t E_i = Q_i - R_i \tag{4}$$

where Q_i is the net rate of energy transfer from the electrons to the ions via collisional excitation and ionization less collisional recombination processes. R_i is the rate of energy loss from the ions by line and radiative recombination emission processes:

$$R_i = \sum_{\mu\nu} \left\{ N_\mu W^{RR}_{\nu\mu}(E_\mu - E_\nu) + N_\mu A^{Ein}_{\nu\mu}(E_\mu - E_\nu) \right\} . \tag{4a}$$

To obtain a complete description of the energy flow in ΔV, one must supplement the equation for E_i with equations of motion for the electron and ion thermal energies. When there is no hydrodynamic motion and therefore no generation of motional energy, these equations can be written as follows [10]:

$$\partial_t \left(\frac{3}{2} N_e k T_e \right) = S_e - \nabla \cdot \vec{q}_e - \frac{3m_e}{m_i} \frac{N_e k}{\tau_e} (T_e - T_i) - Q_i - R_b \tag{5}$$

$$\partial_t \left(\frac{3}{2} N_i k T_i \right) = \frac{3m_e}{m_i} \frac{N_e k}{\tau_e} \left(T_e - T_i \right) \tag{6}$$

where τ_e is the electron-electron $\pi/2$ collision time. The first term on the right-hand side of Eq. (5) is the laser heating term; the second, involving the heat-flow vector $\vec{q}_e$, represents thermal conduction losses; the third term describes the exchange of thermal energy between the electrons and ions; Q_i is described in Eq. (4); and R_b represents energy losses due to the emission of bremsstrahlung radiation [11]:

$$R_b = 1.2 \times 10^{-19} \sqrt{kT_e}\, N_e \sum_\mu Z^2_\mu N_\mu . \tag{7}$$

Equations (2), (5), and (6) can be solved only when an estimate for $\nabla \cdot \vec{q}_e$ in terms of N_e and T_e can be made. Since the plasma is assumed to be uniform within ΔV, Eq. (5) can be averaged over the sphere and $\nabla \vec{q}_e$ replaced by

$$\frac{1}{\Delta V} \int_{\Delta V} dV\, \nabla \vec{q}_e = \frac{3}{r} \vec{q}_e \cdot n \tag{8}$$

where $\hat{n}$ is a unit vector normal to the sphere's surface. A phenomenological estimate for $\vec{q}_e \cdot \hat{n}$, the conduction loss rate across a unit area of the sphere's surface, can be made by setting

$$\vec{q}_e \cdot \hat{n} = - \kappa_e \hat{n} \cdot \nabla T_e \simeq \kappa_e \frac{T_e}{\ell_e} \tag{9}$$

where

$$\ell_e = \begin{cases} 10^{-2} \text{ cm} & t \leqslant 10^{-10} \\ 10^3 \sqrt{t} \text{ cm} & t \geqslant 10^{-10} \end{cases} \tag{10}$$

With this choice of ℓ_e, the temperature gradient scale, the conduction losses are not allowed to exceed physically realizable values for $t \leqslant 10^{-10}$ [12]. The formulas that were used in this paper, expressing κ_e, the electron thermal conductivity, and τ_e in terms of N_e, N_i, and T_e, are found in Braginskii [10]. Thus, the addition of Eqs. (4) and (5):

$$\partial_t \left\{ \frac{3}{2} N_e k T_e + E_i \right\} = S_e - \frac{3\kappa_e T_e}{r\ell_e} - \frac{3m_e}{m_i} \frac{N_e k}{\tau_e} (T_e - T_i) - R_i - R_b \tag{11}$$

yields an equation that together with Eqs. (2) and (6) provides a closed set of equations of motion for N_μ, T_e, and T_i.

As shown in Fig. 5, rate coefficients for five different rate processes must be known as functions of T_e in order to model the atomic physics of the carbon, fluorine, and aluminum plasmas. The values of the Einstein A coefficients for spontaneous radiative decay were taken from Weise [13] when available, or, in the case of the high-lying ($4p \rightarrow 1s$ and $5p \rightarrow 1s$) He-like transitions, they were found by extrapolation of $2p \rightarrow 1s$ and $3p \rightarrow 1s$ tabulated values. All of the rates for the collisional processes were calculated by standard techniques.

The formula used to compute the ionization coefficients $S^Z \equiv W^{CI}/N_e$ was obtained by integrating Seaton's [14] electron-ion impact ionization cross-section [15] over a Maxwellian electron velocity distribution. On neglect of processes such as autoionization and inner-shell excitation, one can approximate S^Z's dependence on T_e by the expression,

$$S^Z \cong 4.5 \times 10^{-24} (kT_e)^{1/2} \xi_i X_i^{-2} e^{-(X_i/kT_e)} \tag{12}$$

where ξ_i is the number of equivalent valence electrons in the ith shell and X_i is the ionization energy of an electron in the ith shell. For the reverse process of collisional recombination, the rate coefficient $\beta^Z \equiv W^{CR}/N_e^2$ was obtained by detailed balance:

$$\beta^Z = \sqrt{\left(\frac{h^2}{2\pi m k T_e} \right)^3} e^{X_i/kT_e} S^Z. \tag{13}$$

The formula used to calculate the radiative recombination coefficient $\alpha^Z \equiv W^{RR}/N_e$ was also derived by Seaton [16]. By retaining the first three terms in the asymptotic expansion of the Kramers-Gaunt factor, he found that

$$\alpha^Z = 5.2 \times 10^{-14} Z \lambda^{1/2} (0.43 + 1/2 \ln\lambda + 0.47\lambda^{-1/3}) \tag{14}$$

where $\lambda = X_i^{(Z-1)}/kT_e$. This formula is valid for the case of an electron and nucleus recombining to form a hydrogenic ion; nevertheless, we have used it for all ion recombinations because no other simple formula is available.

Finally, the electron impact excitation coefficients, $X_{ij} \equiv W^{CE}/N_e$, for excitation from level i to level j, were evaluated using a prescription similar to Burgess' semiclassical method [17], but modified in the threshold region and extended to cover a larger range of electron temperatures [18]:

$$X_{ij} = 16\left(\frac{2\pi}{3m_e}\right)^{1/2} \frac{I_H}{(kT_e)^{1/2}} \frac{I_H}{\Delta E} e^{-\Delta E/kT_e} f\langle g\rangle \pi a_o^2 \tag{15}$$

where I_H is the ionization energy of hydrogen, ΔE is the energy separation between levels i and j, f is the absorption oscillator strength of the transition, and $\langle g\rangle$ is an average Gaunt factor given by

$$\langle g\rangle = \int_{\Delta E} dE g(E) e^{-E/kT_e} \Big/ \int_{\Delta E} dE e^{-E/kT_e}. \tag{16}$$

The evaluation of $\langle g\rangle$ for multicharged ions can very considerably from Allen's values [19] for both resonance and nonresonance transitions. However, the temperature dependence of $\langle g\rangle$ obtained from Eq. (16) is in good agreement with values obtained by considerably more detailed computational methods [20].

Because stimulated absorption and emission processes are not included in Eq. (2), our rate theory treats the plasma sphere as if it were optically thin to the x-radiation it emits. This feature of the model limits its numerical validity to the establishment of upper bounds for cooling by x-ray emission. Estimates we have made indicate, in fact, that, at ion densities corresponding to the neodymium critical density, a 46-μ sphere of carbon plasma is effectively thick to its helium-like K_α radiation, a 46-μ fluorine is effectively grey, and 46-μ aluminum plasma is effectively thin. Thus, the K-line emission cooling rates calculated in this paper for carbon and fluorine are too large. Nevertheless, by first treating the plasmas as if each were optically thin, one can make useful initial comparisons between different Z-target materials that depend primarily on the locations of their K-line spectra.

D. COMPARISON WITH EXPERIMENT

The spectrum in Fig. 4 was obtained in an experiment where 1.9-J, 0.25-ns pulse of neodymium laser radiation was focused to a 50-μ spot on a slab of solid aluminum in vacuo [9]. The average intensity at the focus of this pulse was 4×10^{14} W/cm^2. In the experiment, the conversion of incident laser energy to K-line x-ray energy was at least 0.6 percent, measured under the assumption that the emission was isotropic. The measured ratio of energies in the hydrogen-like $K\alpha$ to helium-like $K\alpha$ lines was 0.6.

We would like to compare the results of this experiment to the predictions of the hot-spot model as represented by Eqs.(1) through (16). Before making this comparison, however, we must digress momentarily to justify it.

One of the main questions that can be answered by solving Eqs. (2), (6) and (11) is what are the laser-energy converting capabilities of a *given* quantity of plasma. Because hydrodynamic motion is neglected, once energy is deposited into ΔV and the plasma is heated, only radiative and thermal conduction energy losses compete to cool the plasma. If this competition is properly described by Eqs. (1) through (16), the deposition of a

comparable amount of laser energy into ΔV with an intensity comparable to that used in the above experiment should produce comparable amounts of K-line x-rays assuming the experiment produced a plasma roughly equivalent to the plasma sphere described in the hot-spot model.

One can argue that this assumption is correct on the basis of the model for plasma generation from a solid target proposed by Kidder [21]. In this model, the absorbed light generates a Chapman-Jouguet deflagration, which drives a shock wave into the solid and a blowoff rarefaction into the vacuum. The rarefaction is self-regulated, so that the density in the blowoff plasma is maintained at or near the critical density until the time when the optical thickness of the rarefaction equals one. According to Kidder's analysis, at 4×10^{14} W/cm^3, blowoff from an aluminum target becomes opaque to the incident laser radiation only after 0.8 ns. Moreover, if the blowoff occurs at a velocity of $\sim 3 \times 10^7$ cm/sec (the sound speed, $\sqrt{(Z+1)\,kT_e/m_i}$, of a 2-keV aluminum plasma) 75 μ of the blowoff plasma would be generated in a 1/4-ns period. Thus, in the rest frame of the blowoff, a Chapman-Jouguet deflagration generates a plasma in the above experiment whose size and density resemble closely the plasma modeled by Eqs. (1) through (16).

In an attempt, therefore, to compare the above experiment with theory, Eqs. (2), (6), and (11) were solved numerically under the following conditions. One and a half Joules of laser energy were deposited into the electron gas in 0.25 ns. The plasma within ΔV was taken to be initially in equilibrium at a temperature of 10^6 °K (86 ev). Thus, the initial thermal energy stored by the electrons within ΔV at a density near 10^{21} cm^{-3} J. Since electron and ion energy densities in a plasma are comparable, only milli-Joules of energy was stored initially in ΔV. The addition of 1.5 J of laser energy is therefore a major perturbation of the plasma. Consequently, one can assume that the calculation did not depend too sensitively on the chosen equilibrium initial conditions.

Results of the numerical integration of Eqs. (2), (6), and (11) are shown in Figs. 7 through 11. The electron temperature was driven to a maximum value of 2 keV in 0.3 ns, falling with equal rapidity to values below 0.5 keV. The fact that Al XIII ions outnumber Al XII ions for only about 0.5 ns (Fig. 8) accounts for the fact that the He-like lines are more prominent than the H-like lines of the computed x-ray spectrum of Fig. 9. The emission rates for the two sets of lines, which are plotted in Figs. 10 and 11, peak slightly before (for He-like) or at (for H-like) the time when the electrons are at their peak temperature and the collisional excitation rates are largest. The double peaking of some of these rates is indicative of the fact that we have allowed for the population of the Al XIII and Al XII excited states from above by collisional and radiative recombination. Thus, as the plasma cools and Al XIV and Al XIII ground states are depopulated, excited states are formed and line emission continues. The fall of the power curves of the H-like and He-like lines are correlated, for this reason, to the fall of the Al XIV and Al XIII population curves respectively.

The computed spectrum in Fig. 9 looks qualitatively very much like the experimental spectrum of Fig. 4, which is a film densitometer tracing. The quantitative agreement between the K-line outputs in the computer and laboratory experiments was also good. In the computer experiment, 1.5 J of laser energy was converted to 7×10^{-3} J of K-line x-rays, a 0.5-percent conversion efficiency. Moreover, the computed ratio of (total)

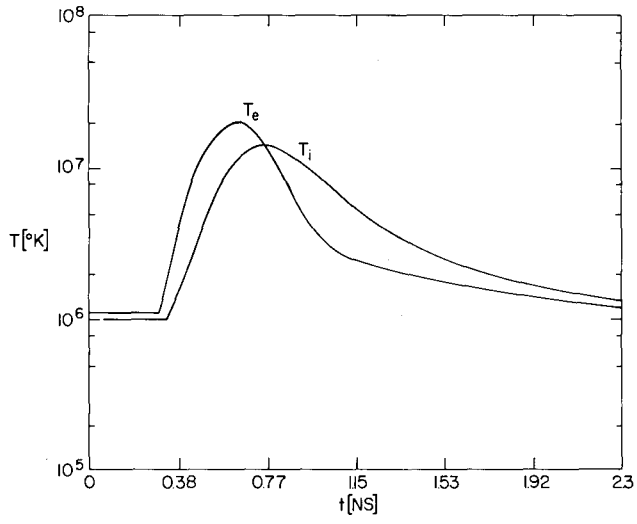

Fig. 7 — Electron and ion temperatures versus time

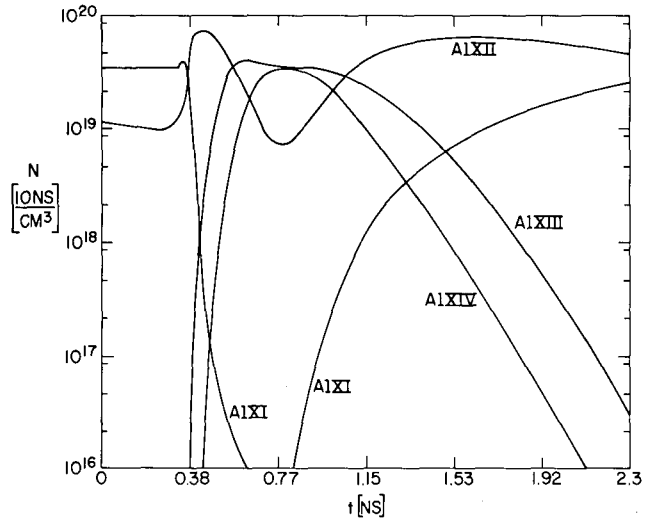

Fig. 8 — Ion population densities versus time

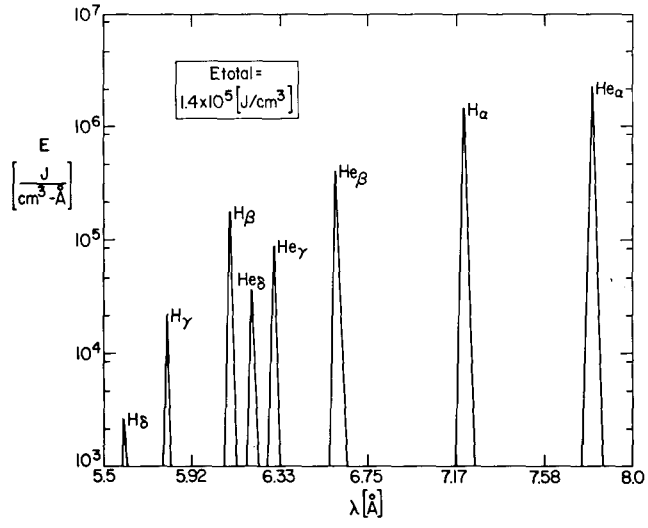

Fig. 9 — Computed time integrated K-line spectrum

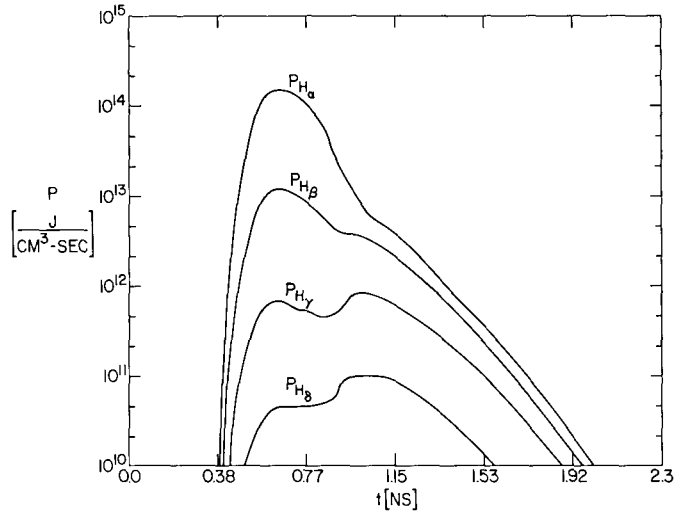

Fig. 10 — Power output from the H-like ion lines versus time

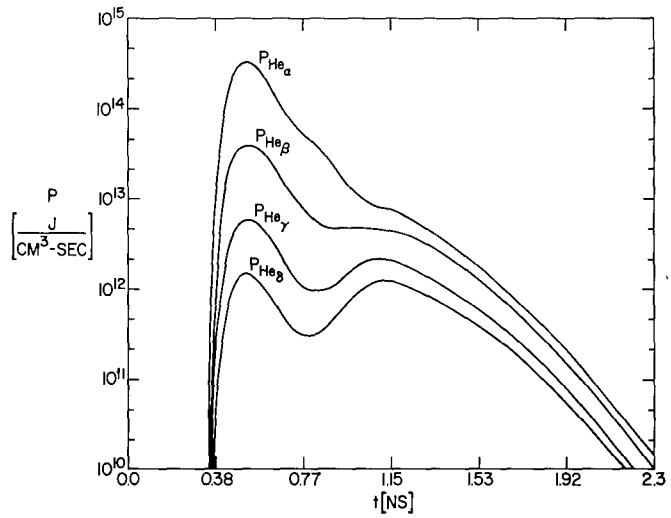

Fig. 11 — Power output from the He-like ion lines versus time

emitted hydrogen-like K_α to helium-like K_α radiation was 0.55. When a similar calculation was performed using a coronal model, in which the ion densities were determined from the requirement that they be in equilibrium with the electron gas rather than from a solution to rate equations, agreement between experiment and the hot-spot model was much worse [22].

E. COMPUTATION OF CONVERSION EFFICIENCIES

The good agreement between the predictions of the hot-spot model and experiment in the above case supports the model's further use to compute variations of the laser-light-to-x-ray conversion efficiency when the laser energy, pulse width, or conduction loss rate is changed. This conversion efficiency can also depend on the length of time (for short times < 1 ns) over which one integrates the x-ray production. For good x-ray conversion, one would like the short-time conversion efficiency to be large.

For this reason, we chose to compare the C, F, and Al plasmas using 25 ps laser pulses. The energy deposited was varied, corresponding to an equivalent variation in the average intensity of light incident on the sphere. The plasmas were initially chosen to be in equilibrium at a low plasma temperature of 10^4 °K in order to insure again that our results are independent of initial conditions for a broad range of laser energies. Maximum energy deposition occurred at t_o = 75 ps; the conversion efficiency (C.E.) to K-line x-rays was computed over the first nanosecond of plasma-time evolution. Figure 7 shows this is sufficient time for the K-line emission to go to completion. In effect, therefore, the plasma was heated by laser-energy deposition during the first 0.1 ns and cooled over the last 0.9 ns. For each plasma history, a K-line conversion efficiency was calculated. These results are plotted for carbon, fluorine, and aluminum plasmas in Fig. 12 [23].

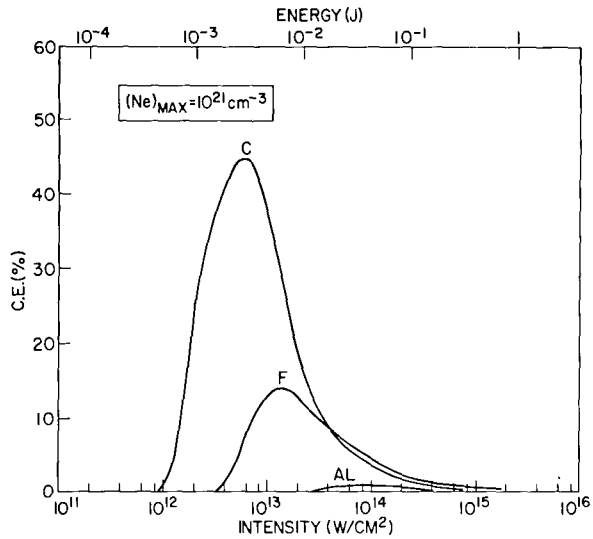

Fig. 12 — K-line conversion efficiencies in carbon, fluorine, and aluminum plasmas as a function of laser intensity

The striking differences between the conversion efficiencies of the three plasmas are due to several causes. To begin with, the energies of the K-line photons increase as Z^2. Therefore, for increasing Z, one must heat the plasma to progressively higher temperatures in order to excite K-line emission. For example, near coronal equilibrium, peak emission of the He-like K-lines occurs roughly at electron temperatures of 70, 250, and 900 eV respectively for C, F, and Al plasmas. For this reason, the peaks in the C.E. curves shift to higher intensity as the plasma Z is increased. However, since the conduction loss rate goes as $T_e^{5/2}$ [24], conduction losses also increase as the plasma becomes hotter. This is one reason why the C.E. peaks get smaller as Z increases. Another reason for the peak decrease is that, in our model, there are more emitters per cubic centimeter in the plasma with the smaller Z. For example, the requirement that $N_e = 10^{21}$ cm^{-3}, the neodymium critical density, when the plasma is fully ionized, sets the ion density at 1.67×10^{20}, 1.11×10^{20}, and 7.69×10^{19} respectively for the C, F, and Al plasmas.

The C.E. curve for carbon peaks sharply in our theory, since we do not account for the laser energy once it is conducted from the sphere. All of the computed conversion takes place within ΔV. In Fig. 13, curves showing the radiative energy input and output of the carbon sphere, which illustrate this point, are plotted. As the deposited energy is increased, the electrons are driven to higher temperatures, which in turn increases the plasma radiation loss rate. However, past the intensity for peak conversion, the plasma is overheated. The electrons get too hot, too fast, stripping the ions of their bound electrons and causing a decrease in the emission of x-rays on the ionizing side of the plasma's time evolution. It is clear that once the plasma is strongly overheated and totally ionized, it can no longer emit line or radiative recombination radiation. It cools only by thermal conduction, or more weakly by bremsstrahlung emission (which occurs at slower rates than line and radiative recombination emission). This statement explains why the total

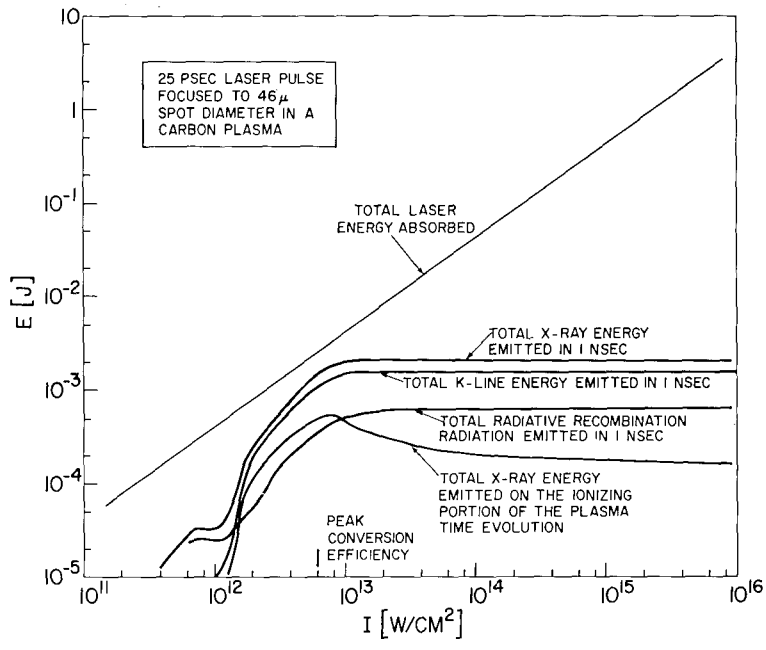

Fig. 13 — Total energies emitted and absorbed from a carbon plasma as a function of laser intensity

x-ray output saturates and why additional laser energy, in excess of 1 or 2 mJ, cannot be converted to 1 ns to x-rays within the carbon sphere. It is lost by conduction instead.

In order to convert more laser energy to x-rays within the sphere, one would be led to try to (a) speed up the line emission losses, (b) slow down the conduction losses, or (c) deposit the energy more slowly to avoid overheating the plasma. Once excited, the *p*-states radiate in 1/10 to 10 ps, that is, in times generally shorter than the laser-energy deposition time. Therefore, to increase line emission, one must increase the excitation rates of the *p*-states by heating a higher density plasma [1]. One can either heat denser plasmas by using light with a frequency higher than neodymium laser radiation or deposit excess amounts of neodymium laser radiation into a plasma with a density gradient such that, by thermal energy conduction, denser regions of plasma would be heated beyond the depository site. An example of the effect of increasing the *p*-state excitation rates is shown in Fig. 14 for a fluorine plasma at a density corresponding to the absorption of frequency-doubled neodymium laser radiation. At this density, a 46-μ sphere of fluorine plasma has a comparable optical thickness to its *K*-lines as the 46-μ sphere of carbon plasma has at the neodymium critical density.

Two conversion-efficiency curves are shown in Fig. 14. They give the efficiency of converting 0.53 μ laser energy to *K*-lines and to radiative recombination radiation which is emitted when H-like and He-like ground states are formed. Conversion to *K*-line peaks at 47 percent, in contrast to the 14-percent fluorine peak of Fig. 12. Thus, increasing the ion density fourfold, increased the peak *K*-line conversion by almost the same amount.

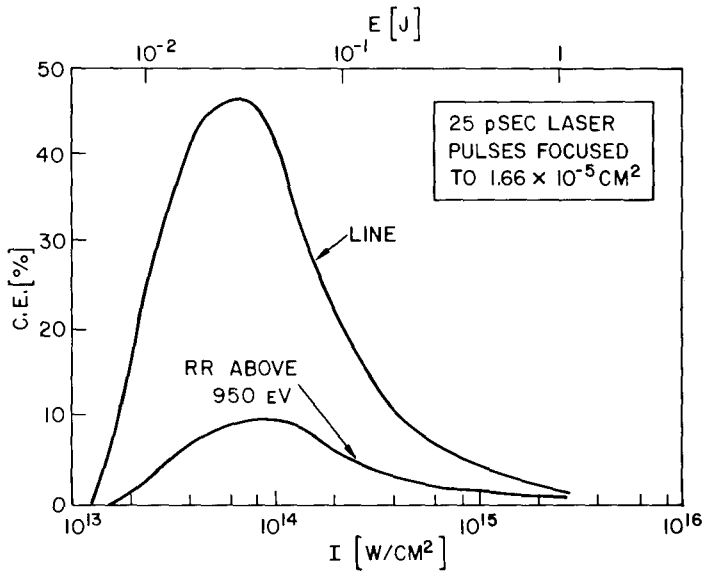

Fig. 14 — Conversion efficiencies in a fluorine plasma with an ion density corresponding to the critical density for 0.53μ radiation

The conduction-loss rate in our model can be controlled by decreasing the temperature gradient at the surface of the sphere — that is, by heating more plasma with laser energy. Figure 15 shows the effect on the C.E. curve of a fluorine plasma of changing the minimum value of ℓ_e from 10^{-2} to 2×10^{-2}, to 10^{-1}. As expected, the peak of the curve rises as ℓ_e increases. Note however that the peak is not shifted or broadened. For a fixed pulse width, good conversion is obtained for a well-defined range of pulse energies, corresponding to optimally heated plasmas.

Finally, in an effort to convert more laser energy in ΔV to K-lines, one might deposit the greater energy at a slower rate. In Fig. 16, conversion efficiency curves for fluorine, obtained by using 10-ps and 100-ps laser pulses, are compared to the fluorine curve of Fig. 12. The dashed line in Fig. 16 represents the conversion one gets in 0.6 ns using 25-ps pulses. It merges with the curve showing conversion in one or more nanoseconds of 25-ps pulses. One sees from these two curves that most of the conversion to K-line x-radiation occurs in the first 0.6 ns. Because the C.E. curves are plotted against laser intensity rather than energy, peak conversion using 100-ps pulses, for example, is displaced from peak conversion for 25-ps pulses. Both peaks occur at the same input energy and are therefore displaced in intensity by a factor of four. The range of energies over which one gets good conversion is also the same; therefore, as expected, one gets less overheating in ΔV and better conversion by lengthening the laser pulse so that the heating rate more closely equals the K-line emission cooling rate. Similar statements hold in comparing the 10-ps and 25-ps C.E. curves. Consequently, one would expect that, as the density of the increased, the pulse width used for *optimal* heating would have to decrease. In this way, one would adjust the heating rate to the increased K-line cooling rate.

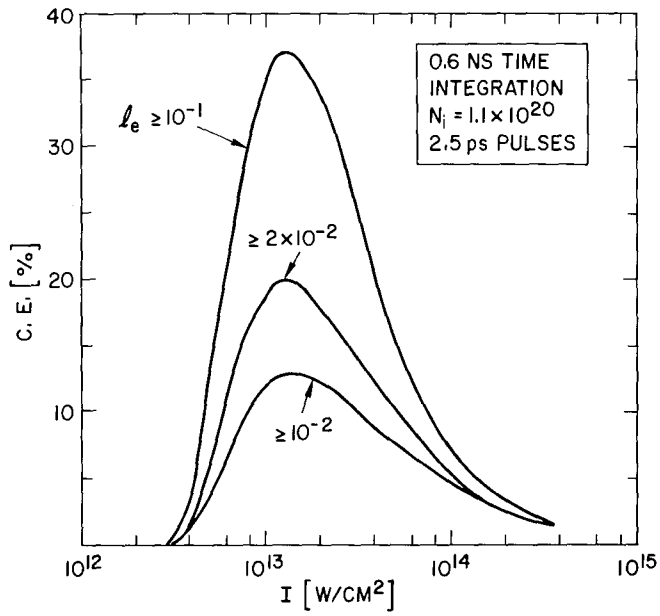

Fig. 15 — Conversion efficiencies in a fluorine plasma for different rates of heat conduction loss from the sphere

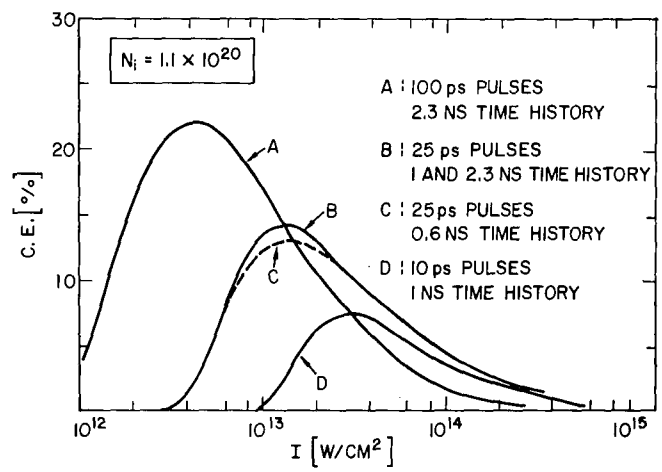

Fig. 16 — Conversion efficiencies in a fluorine plasma for different laser pulse widths

F. SUMMARY AND CONCLUSIONS

We have developed a simple, but illustrative, model describing K-line emission from laser-heated plasmas. The development proceeded along two lines. On the one hand, we established a correspondence between the physical situation described by our model and a particular set of experiments in which a blowoff plasma is generated and heated by the same (subnanosecond) laser pulse. The pulse, which is incident on a solid target, sets up a Chapman-Jouguet deflagration that expels hot plasma into a vacuum at the critical density of the laser frequency. We used the results of an experiment involving an aluminum target as a fiducial point for our model. The reasonable agreement between the predictions of the model with the experimental results indicated that our phenomenological description of the conduction losses from the sphere was adequate. On the other hand, having established contact with experiment, we used our model to make some parameter studies of the K-line conversion efficiency.

In all cases, for a fixed set of conditions, we found there was a well-defined peaking of the K-line conversion efficiency as a function of laser intensity (i.e., as a function of the plasma heating rate). Two important ideas regarding the peak location and the peak height emerged from the results of our parameter studies [25].

The location of the peak depends on the location of the K-lines, i.e., on their photon energy. As the plasma Z is increased, more energy must be deposited to heat the plasma sufficiently to excite the He-like and H-like p-states. For the same reason, the peak shifts to higher energies as the plasma density increases. However, for a given Z and given density, peak location depends on the degree and not the rate of plasma heating. For 10, 25, and 100 ps pulses, the plasma heating rate in C, F, and Al plasmas is faster than its cooling rate. In these cases, the conversion efficiencies peak at the same value of energy deposited rather than at the same value of light intensity. In other words, light energy/area and not light energy/area-time is important in determining peak location for short pulses.

Peak height depends on the competition between radiative and conduction losses. A decrease in the temperature gradient at the sphere's surface brought corresponding increases in peak height. However, the peak width remained the same, showing that the rise in the C.E. curves was associated with the achievement of high enough electron temperatures to excite the K-lines, whereas the fall in the curves was associated with overheating of the electrons, which caused total ionization of the plasma. Because conduction losses increase with T_e, peak height decreased with plasma Z for a given critical density. However, as the electron density is increased the conduction-loss rates decrease through κ_e as N_e^{-2}. Moreover, the p-states are pumped more effectively so that the radiative cooling rate increases. These two effects cause the peak height to increase with plasma density. Our estimates for C, F, and Al seem to indicate, in fact, that the peak heights of these three plasmas are comparable under conditions where they trap their K-radiation with comparable strength. Large K-line conversion is attainable in C, F, and Al plasmas only when the plasma is optically thick to this radiation. Before it escapes, therefore, it may be quenched or frequency redistributed.

REFERENCES

1. K.G. Whitney and J. Davis, Appl. Phys. Lett. 24, 509 (1974).
2. J.B. Chase, J.M. LeBlanc, and J.R. Wilson, Phys. of Fluids 16, 1142 (1973).
3. K.G. Whitney, N.K. Winsor, J. Davis, and D.A. Tidman, Bull. Am. Phys. Soc. II 18, 1317 (1973).
4. N.K. Winsor and D.A. Tidman, Phys. Rev. Lett. 31, 1044 (1973).
5. J.A. Stamper, K. Papadopoulos, R.N. Sudan, S.O. Dean, E.A. McLean, and J.M. Dawson, Phys. Rev. Lett. 26, 1012 (1971).
6. T.W. Johnston and J.M. Dawson, Phys. of Fluids 16, 722 (1973).
7. G.A. Doschek, U. Feldman, and D.J. Nagel, unpublished.
8. U. Feldman, G.A. Doschek, D.J. Nagel, W.E. Behring, and R.D. Cowan, Astrophys. J. 187, 417 (1974).
9. D.J. Nagel, P.G. Burkhalter, C.M. Dozier, J.F. Holzrichter, B.M. Klein, J.M. McMahon, J.A. Stamper, and R.R. Whitlock, Phys. Rev. Lett., to be published.
10. S.I. Braginskii, "Reviews of Plasma Physics," ed. by M.A. Leontovich (Consultants Bureau, New York, 1965, p. 205).
11. L. Spitzer, Jr., "Physics of Fully Ionized Gases," Interscience, New York (1962).
12. A more elaborate computation of ℓ_e would have to account for its dependence on temperature and density, see: J.M. Dawson, Phys. of Fluids 7, 981 (1964). For the convenience of estimating ΔT_e simply under time changing conditions, we have chosen an average value for ℓ_e.
13. W. Wiese, M. Smith, and B. Miles, "Atomic Transition Probabilities," NBS-22, Vol. II (1969).
14. M. Seaton, "Atomic and Molecular Processes," ed. by D. Bates, Academic Press (1962).
15. M. Seaton, Phys. Soc. 79, 1105 (1962).
16. M. Seaton, MNRAS 119, 81 (1959).
17. A. Burgess, Culham Conference on Atomic Collisions, AERE Rept. 4818, 63 (1964).
18. J. Davis, JQSRT, 14, 549 (1974).
19. C.W. Allen, "Astrophysical Quantities," Althone Press (London), 1965.
20. J. Davis and E. Oran, J. Appl. Phys. 45, 2480 (1974).
21. R.E. Kidder, Nucl. Fusion 8, 3 (1968); "Proceedings of the International School of Physics 'Enrico Fermi,' Course 48," ed. by P. Caldirola and H. Knoepfel, New York academic Press, 1971, p. 306.
22. J.A. Stamper, O.C. Barr, J. Davis, G.A. Doschek, C.M. Dozier, U. Feldman, B.M. Klein, W.M. Manheimer, E.A. McLean, J.M. McMahon, D.J. Nagel, D.A. Tidman, R.R. Whitlock, K. Whitney, N.K. Winsor, and F.C. Young, in the Third Workshop on "Laser Interactions and Related Plasma Phenomena," at Renssalaer Polytechnic Institute, Troy, N.Y., August 13-17 (1973).

23. The large peak conversion efficiencies computed here are for K-shell line radiation. Comparable conversion efficiencies for L-shell radiation from Fe and Cu plasmas using 1 ns neodymium laser pulses has been reported by P.J. Mallozzi, H.M. Epstein, R.G. Jung, D.C. Applebaum, B.P. Fairand, W.J. Gallagher, R.L. Uecker, and M.C. Muckerheide, J. Appl. Phys. 45, 1891 (1974).

24. Under the assumption of a constant ℓ_e.

25. The peak width will depend on the amount of plasma included in the calculation. Our model deals with the converting capabilities of a given volume of plasma under the (violatable) assumption that it constitutes the bulk of the plasma heated by E_o. X-ray production from energy conducted outside the plasma sphere is not computed.

X. LASER RADIATION FORCE

The forces exerted by laser radiation play a varied role in laser-produced plasmas. Radiative forces have been shown to contribute to such phenomena as plasma acceleration [1], self-focusing of laser radiation [2], parametric instabilities [3,4], and magnetic field generation [5,6]. These effects may be important in laser-fusion applications [7,8]. A discussion is given here of physical mechanisms involved in the radiative force, and the limitations in a particular theory (ponderomotive force) are pointed out. The discussion is concerned mainly with laser radiation (transverse waves), but much of the reasoning also applies to plasma (longitudinal) waves.

Radiative forces act primarily on the electrons, due to their small mass. Part of this force is transmitted via an irrotational electric field and collisions to the ions, so that this part of the force acts effectively on the neutral plasma. However, for typical focal-region geometries, the radiation-induced electric field has a large solenoidal component which drives currents and generates magnetic fields. The solenoidal nature is dependent on the net field momentum carried by the laser beam and on the different directions of the electron density and laser intensity gradients. Both effects are ignored in the ponderomotive theory of radiative forces. A general description of radiative forces must include both the plasma force and the electric field.

The radiative force involves a time-averaged momentum transfer in the electron fluid. One contribution, a direct transfer of field momentum (e.g., due to absorption), could occur with initially homogeneous fields. However, with the resulting inhomogeneous fields, there is another contribution which does not depend on a net field momentum. This contribution involves a momentum transfer within the electron system and is due to the electron quiver motion in the inhomogeneous fields. The quiver force is analogous to the force on the electron fluid resulting from a thermal pressure gradient. From these considerations, one can see why [6] the effective radiation pressure (time-averaged momentum flux associated with the laser radiation) in a laser-produced plasma is the sum of a field and quiver pressure.

Field momentum and energy, being quadratic in the fields, are transported at the group velocity. Purely sinusoidal fields, i.e., a single Fourier component, do not allow the definition of group velocity and thus cannot account implicitly for the transport of field energy and momentum. Thus, the finite bandwidth of laser radiation must be included if a microscopic theory is to account for field momentum.

Field momentum is implicitly accounted for when the wave spectrum is given, and it can be expressed in terms of the group velocity $\underline{v}_g$. It is also possible to explicitly account for a net field momentum density $\underline{g}$ in the form of the radiation pressure $\underline{\underline{P}}^r$

$$\underline{\underline{P}}^r = P_o^r \underline{\underline{I}} + \underline{v}_g \underline{g} \tag{1}$$

where there is a scalar radiation pressure P_o^r and a directed part $\underline{v}_g\underline{g}$. Field momentum produces an anisotropy in $\underline{\underline{P}}^r$ which is essential to the nature of the radiation-induced forces and fields.

The radiative force considered here is a time-averaged, nonrelativistic force density on the electrons due to high-frequency electromagnetic fields having a weak spatial inhomogeneity. Two types of descriptions are discussed: that derived from the radiative force on a single electron, and the radiative force on the electron fluid.

The term "pondermotive force" is used here to denote the radiative force density derived by considering the force on a single electron due to fields having a purely sinusoidal time variation [3,4,9]. The amplitudes of the fields are assumed to be arbitrary functions of space, so that the theory could apply to both macroscopic and microscopic phenomena. However, one should note how time averaging the product of fields places restrictions on the spatial description [10].

The force on a single electron can be expressed [11] as $-(e^2/2m\omega^2)\nabla\langle(\delta\underline{E})^2\rangle$. The ponderomotive force, or radiative force density, can thus be written as

$$\underline{f}_o^r = -\frac{1-\epsilon}{8\pi}\nabla\langle(\delta\underline{E})^2\rangle . \tag{2}$$

The time-averaged force density or the electron fluid due to high-frequency electromagnetic fields can be derived by taking the first velocity moment of the electron kinetic equation [5,6]. This force density will be referred to simply as the radiative force in order to distinguish it from the ponderomotive force. It can be expressed as [5,6],

$$\underline{f}^r = -\nabla\cdot\underline{\underline{P}}^r - \frac{\partial\underline{g}}{\partial t} \tag{3}$$

where $\underline{\underline{P}}^r$ is an effective radiation pressure or time-averaged momentum flux associated with the high-frequency fields and where $\underline{g} = \langle\delta\underline{E}\times\delta\underline{B}\rangle/4\pi c$ is the field momentum density.

The ponderomotive formulation has implicit in it several restrictions. It ignores field momentum, since field momentum cannot be represented explicitly in a scalar radiation pressure, and it cannot be represented implicitly by purely sinusoidal variations (i.e., there is no wave spectrum). Note that the force per particle is conservative (derivable from a potential) and hence cannot represent dissipative effects such as absorption by collisions or plasma turbulence. Field momentum is transferred to the electrons during the absorption of directed laser energy. Recall that the rate per unit volume at which field momentum is transferred to the plasma is given by $\langle\delta\rho\ \delta\underline{E} + c^{-1}\ \delta\underline{J}\times\delta\underline{B}\rangle$ where, for laser-produced plasmas, the coupling is due almost entirely to the oscillating current $\delta\underline{J}$ associated with electron quiver motion. Ignoring field momentum is thus equivalent to setting $\langle\delta\underline{J}\times\delta\underline{B}\rangle$ equal to zero.

Since the ponderomotive force is derived from a single particle theory, it refers, in effect, to a homogeneous, neutral plasma. If one calculates the force on a single particle and then multiplies this result by the particle number density, the resulting force density does not correctly include the effects of density variations. In effect, it refers to the force

density in a homogeneous ($\nabla n = \underline{0}$) plasma. Similarly, one cannot correctly account for charge-density effects in the force density by multiplying the unit charge in the single particle force equation by number density.

The ponderomotive description is valid for purely sinusoidal fields in a neutral, homogeneous, nonabsorbing plasma. In fact [10], applying these restrictions to Eq. (3) yields Eq. (2).

The electric field in a plasma is commonly evaluated from a generalized Ohm's law which is dependent on various forces acting on the electron fluid [12]. This is reasonable since, due to the small electron inertia, various forces acting on the electron fluid tend to be balanced by the electrical force. For example, a thermal pressure gradient produces a contribution $-(1/ne)\nabla P_e$ to the electric field which primarily drives the thermally generated magnetic fields [13,14]. When the radiative force density is included in the electron equation of motion [5,6], then it appears as a contribution $\underline{E}^r = \underline{f}^r/ne$ to the slowly varying electric field.

Little thought is usually given to this electric field since, in many circumstances, it is primarily of an irrotational nature, so that it merely represents an electrostatic transmission of the radiative force from the electrons to the ions. The effective radiation force is then on the neutral plasma. However, for the case of highly focused laser radiation, the solenoidal component of $\underline{E}^r$ is large so that, in addition to the force on the neutral plasma, electric currents are produced and magnetic fields are generated [5,6].

The contributions to $\nabla \times \underline{E}^r$ can be seen by considering $\underline{E}^r = -(1/ne)\nabla \cdot \underline{\underline{P}}^r$ where $\underline{\underline{P}}^r$ has the form given in Eq. (1) with P_o^r equal to $(1-\epsilon)\langle(\delta \underline{E})^2\rangle/8\pi$

$$ne\underline{E}^r = \nabla P_o^r + (\underline{v}_g \cdot \nabla)\,\underline{g} + (\nabla \cdot \underline{v}_g)\,\underline{g}. \tag{4}$$

One can see from Eq. (4) that there are two major contributions to $\nabla \times \underline{E}^r$. For simplicity, these are considered separately. One is due to density variations and would exist even when the field momentum $\underline{g}$ vanishes so that $\underline{\underline{P}}^r$ is isotropic.

Setting $\underline{g} = \underline{0}$ gives

$$\nabla \times \underline{E}^r = (8\pi en^*n)^{-1}\,\nabla\langle(\delta \underline{E})^2\rangle \times \nabla n. \tag{5}$$

Since the gradient of $\langle(\delta \underline{E})^2\rangle$ or laser intensity has, due to absorption, a large component in the direction of the laser beam, and since ∇n is not so constrained, it is seen that the density effect will generally make a large contribution.

Next assume the density is constant and consider the effect of field momentum. Setting $\nabla n = \underline{0}$ shows that this is a direct result of the anisotropy of $\underline{\underline{P}}^r$, depending on the structure of $\underline{\underline{P}}^r$ and not on the relative variation of different quantities in $\underline{\underline{P}}^r$. For example, one term is proportional to $\nabla(\nabla \cdot \underline{v}_g) \times \underline{g}$ and thus depends on the variation of a single quantity.

Since ∇n and $\underline{g}$ are both assumed to be zero in the ponderomotive description, the ponderomotive theory cannot account for solenoidal contributions to $\underline{E}^r$.

REFERENCES

1. H. Hora, Phys. Fluids 12, 182 (1969). See also H. Hora, *Laser Interaction and Related Plasma Phenomena*, (H. Schwarz and H. Hora, Eds.) Plenum, New York; Vol. 1, p. 383 (1971) and Vol. 2, p. 341 (1972).
2. J.W. Shearer and J.L. Eddleman, Phys. Fluids **16**, 1753 (1973).
3. Francis P. Chen, chapter in *Laser Interaction and Related Plasma Phenomena*, Vol. 3 (H. Schwarz and H. Hora, Eds.) Plenum, New York (1973). See also Chen's University of California Report, PPG-160, Aug. 1973.
4. W.M. Manheimer and E. Ott, to be published in Phys. Fluids (June or July 1974).
5. J.A. Stamper and D.A. Tidman, Physics of Fluids **16**, 2024 (1973).
6. J.A. Stamper et al., chapter in *Laser Interaction and Related Plasma Phenomena*, Vol. 3 (H. Schwarz and H. Hora, Eds.) Plenum, New York (1973).
7. J. Nuckolls, L. Wood, A. Thiessen and G. Zimmerman, Nature **239**, 133 (1972).
8. J.S. Clarke, H.M. Fisher and R.J. Mason, Phys. Rev. Lett. **30**, 89 (1973).
9. G. Schmidt, *Physics of High Temperature Plasmas* (Academic Press, New York 1966), p. 47ff.
10. J.A. Stamper, submitted to Phys. Fluids; see also NRL Memorandum Report 2775.
11. Most observable quantities are time averages (designated by $\langle\ \rangle$) of quantities (designated by a prefix δ) oscillating at the frequency of the laser radiation.
12. S.I. Braginskii, *Reviews of Plasma Physics*, ed. by Acad. M.A. Leontovich, Vol. 1, p. 267ff (1965).
13. J.B. Chase, J.L. LeBlanc and J.R. Wilson, Phys. Fluids **16**, 1142 (1973).
14. J.A. Stamper, NRL Report 7411, June 1972, p. 2,3.

XI. PUBLICATIONS AND REPORTS

"A Large Aperture High Extinction Ratio Faraday Rotator Isolator," O.C. Barr, J.M. McMahon, IEEE Jour. Quant. Elect., Nov. 1973, p. 1124.

"Analysis of Discrete Pulse Forming Networks Driving Nonlinear Flashlamps Loads," O.C. Barr, NRL Memorandum Report 2808, June 1974.

"Optical Isolation and the Design of Large Aperture, High Extinction Ratio Faraday Rotators for High Power Glass Lasers," O.C. Barr, NRL Memorandum Report 2817, June 1974.

"Design of Fanned and Wedged Stacked Plate Polarizers for High Power Lasers," O.C. Barr and J.M. McMahon, NRL Memorandum Report 2830, July 1974.

"Laser-Produced Rare Earth X-Ray Spectra," P.G. Burkhalter, D.J. Nagel and R.R. Whitlock, Phys. Rev. A 9, 2331 (1974).

"Transitions in Highly Ionized Sn Spectra from a Laser-Produced Plasma," P.G. Burkhalter, U. Feldman and R.D. Cowan, J. Opt. Soc. Am. 64, 1058-1062 (1974).

"The Influence of High Density Plasmas on Series Merging," J. Davis, NRL Memorandum Report 2655, October 1973.

"Effective Gaunt Factors for Electron Impact Excitation of Multiply Charged Nitrogen and Oxygen Ions," J. Davis, J. Quant. Spectrosc. Radia. and Transfer 14, 549 (1974).

"Electron Impact Cross Sections and Rates for One- and Two-Electron Aluminum Ions," J. Davis, and E. Oran, J. Appl. Phys. 45, 2480 (1974).

OI Isoelectronic Sequence: Transitions $2p^4$-$2p^3 2s$, by G.A. Doschek et al., J.O.S.A. 63, 1463 (1973).

"X-Ray Emission from Laser-Produced Plasmas," C.M. Dozier, P.G. Burkhalter, B.M. Klein, D.J. Nagel and R.R. Whitlock in *Advances in X-Ray Analysis*, Vol. 17 (Plenum Press, N.Y., 1974), p. 423.

"X-Ray Point Source Projection Photography with a Laser-Produced Plasma," J.F. Holzrichter, C.M. Dozier and J.M. McMahon, Appl. Phys. Lett. 23, 687-689 (1973).

"Variation of the Temperature of Laser-Produced Plasmas with Laser-Pulse and Target Parameters, by B.M. Klein et al., Proc. European Conf. on Contr. Fusion and Plasma Physics, Moscow (1973).

"The Effect of Sidescatter Instabilities on the Propagation of an Intense Laser Beam in Inhomogeneous Plasma," H. Klein, W. Manheimer and E. Ott, Phys. Rev. Lett 31, 1187 (1973).

"The Effect of Trapping on the Saturation of the Raman Backscatter Instability," H.H. Klein, E. Ott and W. Manheimer, accepted for Physics of Fluids.

"Parametric Decay of Intense Radiation into a Whistler Wave," H.H. Klein, W.M. Manheimer and E. Ott, accepted for Phys. Fluids.

"The Effects of Plasma Inhomogeneity on the Production of Energetic Electrons," H.H. Klein and W. Manheimer, submitted to Physical Review Letters.

"Compression and Shaping of Pulses from High Power Solid State Lasers," R.H. Lehmberg, PROC-IEEE Electron Devices Meeting (Nov. 1973).

"Two Photon Resonantly Enhanced Self Defocusing in Cs Vapor at 1.06 μ," R.H. Lehmberg, J. Reintjes and R.C. Eckardt, accepted for publication in Appl. Physics Letters.

"Stripline Pockels Cell Assembly," J.P. Letellier, NRL Memorandum Report 2716, Jan. 1974.

"Passively Mode-Locked Nd:YAG Laser Stability Study," J.P. Letellier, NRL Memorandum Report 2684, Nov. 1973.

"Parametric Instabilities Induced by the Coupling of High and Low Frequency Plasma Modes," W. Manheimer and E. Ott, Phys. Fluids, July 1974. This was in last RPI report.

"A Connection Between the Linear and Nonlinear Theory of Anomalous Reflection from a Plasma Slab," W. Manheimer, Phys. Fluids, Sept. 1974.

"The Coherent Production of Energetic Electrons in Anomalous Reflection and Absorption of Intense Laser Light," W. Manheimer and H. Klein, accepted for Physics of Fluids.

"A Glass Disc Laser Amplifier," J.M. McMahon, J.L. Emmett, J.F. Holzrichter and J.B. Trenholme, IEEE J. QE, Oct. 1973, p. 992.

"A Glass Laser System Designed for Target Irradiation," J.M. McMahon, and O.C. Barr, Proc. SPIT (Aug. 1973).

"A Helically Pumped Disc Laser Amplifier," J.M. McMahon, O.C. Barr, Proc. IEDM (Nov. 1973).

"Suppression of Parasitic Oscillation in Laser Rod Amplifiers," J.M. McMahon, R.P. Burns, and T.H. DeRieux, Proc. ASTM-NBS Sym. on Damage in Laser Materials, May 1974.

"X-Ray and UV Emission of Laser Produced Plasmas," by D.J. Nagel et al., Proc. Eur. Conf. on Controlled Fusion and Plasma Phys., Moscow 1973.

"X-Ray Diagnostics of Laser-Compressed Plasmas," D.J. Nagel, Physica Fennica, 9(S1), 403-405 (1974).

"Power Dependence of Laser-Plasma X-Ray Emission," D.J. Nagel, P.G. Burkhalter, C.M. Dozier, B.M. Klein, and R.R. Whitlock, Bull. Am. Phys. Soc. **19**, 557 (1974).

"Transitions of Fe XVIII and Fe XIX Observed in Laser-Produced Plasmas," U. Feldman, G.A. Doschek, D.J. Nagel, W.E. Behring, and L. Cohen, Astrophys. J. **183**, L430 (1973).

"Laser-Plasma Spectra of Highly Ionized Fluorine," U. Feldman, G.A. Doschek, D.J. Nagel, W.E. Behring, and R.D. Cowan, Astrophys. J. **187**, 417 (1974).

"Satellite Line Spectra from Laser-Produced Plasmas," by U. Feldman, G.A. Doschek, D.J. Nagel, R.D. Cowan, and R.R. Whitlock, Astrophys. J., **192**, 213 (1974).

"X-Ray Emission from Laser-Produced Plasmas," D.J. Nagel, P.G. Burkhalter, C.M. Dozier, J.F. Holzrichter, B.M. Klein, J.M. McMahon, J.A.Stamper and R.R. Whitlock, Phys. Rev. Lett. **33**, 743 (1974).

"Time-Resolved Laser-Plasma Backscatter Studies," B.H. Ripin, J.M. McMahon, E.A. McLean, W.M. Manheimer and J.A. Stamper, Phys. Rev. Lett. 33, 634 (1974).

"Picosecond Diagnostics of Laser Light Scattered from Laser-Produced Plasmas," B.H. Ripin and J.A. Stamper, Proceedings of the Electro-Optical Systems Design Conference, 1974 West (to be published).

Laser-Matter Interaction Studies at NRL, John Stamper, et al., Proc. of Third Workshop on "Laser Interactions and Related Plasma Phenomena," at Renssalaer Polytechnic Institute, Troy, N.Y. Aug. 1973.

"Magnetic Field Generation due to Radiation Pressure in a Laser-Produced Plasma," J.A. Stamper and D.A. Tidman, Phys. of Fluids **16** (1973).

"Role of Magnetic Fields in Suprathermal Particle Generation by Laser-Produced Plasmas," D.A. Tidman and J.A. Stamper, Appl. Phys. Lett. **22**, 498 (1973).

"Field-Generating Thermal Instability in Laser-Heated Plasmas," D.A. Tidman and R.A. Shanny, NRL Memorandum Report 2667, Oct. 1973.

"Conversion Efficiencies of Laser to X-Ray Energy in C, F, Al Plasmas," K. Whitney and J. Davis, Appl. Phys. Lett. **24**, 509 (1974).

"K-Shell Line Radiation from Laser-Produced Aluminum Plasmas," K. Whitney, J. Davis, and E. Oran, NRL Memorandum Report 2644, June 1973.

"Laser Target Model," N.K. Winsor and D.A. Tidman, Phys. Rev. Lett. **31**, 1044 (1973).

"Measurements of Energetic X-Rays from Laser-Produced Plasmas," F.C. Young, Phys. Rev. Lett. **33**, 747 (1974).